

Cucurbit[n]uril-engineered Nano-constructs for Molecular Sensing

Author:

Xiaohe Ren

Supervisor:

Prof. Oren A. Scherman

This dissertation is submitted for the degree of Doctor of Philosophy
August 17, 2018

Abstract

Surface-enhanced Raman scattering (SERS) spectroscopy is a powerful analytical technique for ultrasensitive detection of chemicals and biomolecules. As the high sensitivity of SERS requires analytes to be in close contact with a plasmonic substrate, the detection of analyte molecules with low chemical affinity towards the substrate is thus limited. Cucurbit[n]uril (CB[n]) exhibits strong and selective encapsulation of various guest molecules into its barrel-shaped cavity. In addition, it can function as a precise rigid spacer between metallic nanoparticles (NPs). The larger homologue CB[8] can simultaneously sequester two guest molecules to form ternary complexes, allowing for tailoring of the chemical environment of its cavity to trap specific analytes. CB[n] aggregated metallic NPs provide a powerful platform for the detection of a wide variety of molecules. However, the colloidal instability of this system requires the measurement to be finished within 60 min after the preparation of the substrate. In addition, *in situ* measurements may involve environments that affect such self-assembly processes. For example, the possible displacement of analytes in the nanogap by non-analyte moieties can give rise to fluctuating backgrounds. Therefore, a SERS substrate that can provide the same levels of detection and functionality but eliminates the need for aggregation is of great demand. This thesis mainly focuses on the preparation and characterisation of CB[n]-engineered nanostructures as SERS substrates with great colloidal stability, high SERS enhancements and sensitivities. Other applications of the prepared nanostructures such as peptide separation and high-performance catalysis are also discussed.

In the first chapter, the historical development and the remaining challenges in the field of SERS are discussed. Three types of the most commonly used SERS substrates are introduced, followed by the introduction of rationally designed nanoplatforms for

molecules with low chemical affinity towards metallic surfaces. In addition, CB[*n*] host-guest complexation, examples of CB[*n*]-engineered nanostructures and the application of these nanostructures in SERS sensing are also discussed.

The second chapter demonstrates the preparation of surface-bound CB[8] catenanes on silica NPs, where CB[8] is employed as a tethered supramolecular "receptor" to selectively capture target guest molecules. More specifically, CB[8] is threaded onto a methyl viologen (MV²⁺) axle and immobilised onto silica NPs with a surface density up to 0.56 nm⁻². Its use as an efficient and recyclable nanoplatform for peptide separation is demonstrated. The peptides captured by the catenanes can be released by reversible single-electron reduction of MV²⁺. The entire process demonstrates high recoverability.

Continued in the third chapter, a highly stable free-standing molecular sensor that exploits a catenane-engineered nanostructure is described. CB[8] is tethered onto spiky γ -Fe₂O₃@Au NPs in a similar approach, to collect target analytes from aqueous media. These target analytes can be detected with high sensitivities, on account of the high SERS enhancement (on the order of 10⁸) of the spiky NPs. This CB[8] catenane-based molecular sensor provides a powerful SERS substrate that shows great promise in the detection of versatile chemicals, biomolecules, controlled substances and auxiliary diagnostics of various diseases.

The fourth chapter introduces a facile preparation of monodispersed γ -Fe₂O₃@Au magnetic nanoraspberry NPs using a one-pot seeded growth method. The obtained nanoraspberry NPs show excellent colloidal stability and high SERS enhancement factors (on the order of 10¹⁰). By immobilising a dense layer of CB[*n*]s onto the surface of nanoraspberry NPs, a new type of CB/Au NP SERS substrate is obtained. CB[*n*]s are located perpendicularly to the NP surface and their cavity maintain the capability to sequester guest molecules from aqueous media. More versatile molecules (both electron rich and electron deficient molecules) can thus be detected with high sensitivities. We envisage that this nanoraspberry-based molecular sensor will provide a powerful platform for SERS detection in various fields, such as chemical and biomolecule analysis, illegal drug detection and pre-clinical/clinical diagnosis.

The fifth chapter focuses on the preparation of CB[7]-based catalytic microreactors, where metallic NPs are immobilised onto microchannels *via* supramolecular interaction of methyl viologen@CB[7]. This microreactor exhibits remarkable catalytic activity on account of the high surface area to volume ratio of the microchannels and metallic NPs. Superior to most conventional heterogeneous catalytic reactions, separation post reaction and complicated recycling steps of the catalysts are not required. Moreover, CB[7] can complex a variety of metallic NPs onto its portal (e.g. gold, silver, palladium, quantum dot), providing a multifunctional *in situ* catalysis platform.

In the end, a concluding chapter summarises the presented work, also giving a brief outlook of the potential future work.

Contents

1	Introduction	1
1.1	Nanoplatforms for SERS Technique	1
1.1.1	SERS: an ultrasensitive analytical technique for molecular sensing	1
1.1.2	Commonly used SERS substrates	4
1.1.3	Nanoplatforms for SERS detection of "inert" analytes	9
1.2	Cucurbit[<i>n</i>]uril Host-Guest Chemistry	15
1.2.1	Macrocyclic host-guest complexation	15
1.2.2	CB[<i>n</i>]-engineered nanostructures	21
1.2.3	CB[<i>n</i>]-engineered nanostructures in SERS sensing applications . .	27
1.3	Objectives	30
2	Cucurbit[8]uril Catenanes on Silica Nanoparticles Exhibiting Molecular Recognition	32
2.1	Introduction	33
2.2	Results and Discussion	35
2.2.1	Synthesis and complexation study of MV-disilane guest molecule .	35
2.2.2	Preparation of surface-bound CB[8] catenanes on silica NPs	38
2.2.3	UV-vis titration study	39
2.2.4	Lithography characterisation	42
2.2.5	Preparation of CB[8] catenanes on magnetic silica nanoparticles . .	43
2.2.6	Peptide separation using CBC-MNPs	43
2.3	Conclusion and Outlook	47

2.4	Experimental Appendix	47
2.4.1	Materials and general methods	47
2.4.2	Synthesis and characterisation of MV-disilane guest molecule . . .	48
2.4.3	Preparation of silica nanoparticles	48
2.4.4	Preparation of CB[8] catenanes on silica nanoparticles	49
2.4.5	UV-vis titration	49
2.4.6	Lithography characterisation	50
2.4.7	Preparation of magnetic silica nanoparticles	51
2.4.8	Preparation of CB[8] catenanes on magnetic silica nanoparticles . .	51
2.4.9	Preparation of peptides	52
2.4.10	Peptide separation using CBC-MNPs and recovery of CBC-MNPs .	52
2.4.11	Quantification of the CB[8] on the silica nanoparticle surface	53
2.4.12	Peptide separation using CBC-MNPs	55
2.4.13	Quantification of the peptide separation using CBC-MNPs	58
3	Advanced Molecular Sensing Exploiting Catenane-Engineered Nanostructures	60
3.1	Introduction	61
3.2	Results and Discussion	64
3.2.1	Trials of CB[8] catenanes on spherical Au NPs	64
3.2.2	Synthesis and characterisation of spiky γ -Fe ₂ O ₃ @Au NP core . . .	66
3.2.3	Preparation of CB[8] catenanes on spiky magnetic Au NPs (CBCat)	68
3.2.4	Detection of target analytes	72
3.2.5	Detection of controlled substances	75
3.3	Conclusion and Outlook	77
3.4	Experimental Appendix	77
3.4.1	Materials and general methods	77
3.4.2	Synthesis and characterisation of HS-MV-SH	78
3.4.3	Preparation of spiky γ -Fe ₂ O ₃ @Au NPs	79
3.4.4	Preparation of CB[8] catenanes on spiky γ -Fe ₂ O ₃ @Au NPs (CBCat)	80

3.4.5	Molecular detection using CBCat by SERS	80
3.4.6	Powder Raman spectra of investigated molecules	82
3.4.7	Binding constants of ternary complexes	89
3.4.8	UV-vis study of spherical Au NPs aggregation	93
3.4.9	Quantification of CB[8] surface density on spiky γ -Fe ₂ O ₃ @Au NP .	94
3.4.10	Calculation of SERS enhancement factor	95
4	γ-Fe₂O₃@Au Nanoraspberry Particles for High-performance SERS	97
4.1	Introduction	98
4.2	Results and Discussion	100
4.2.1	Synthesis and characterisation of γ -Fe ₂ O ₃ @Au nanoraspberry particles	100
4.2.2	Detection of target analytes using CB[7]-functionalised NRSP . . .	106
4.2.3	Detection of target analytes using CB[8]-functionalised NRSP . . .	109
4.2.4	Detection of ephedrine	112
4.3	Conclusion and Outlook	113
4.4	Experimental Appendix	114
4.4.1	Materials and general methods	114
4.4.2	Synthesis of γ -Fe ₂ O ₃ nanoparticles	114
4.4.3	Synthesis of γ -Fe ₂ O ₃ @Au nanoraspberry particles	115
4.4.4	Modification of growth conditions	116
4.4.5	Surfactant exchange	117
4.4.6	Detection of target analytes using CB[7]-functionalised NRSP . . .	117
4.4.7	Guest displacement	118
4.4.8	Powder Raman spectra of investigated molecules	119
4.4.9	Binding constants of complexes	120
4.4.10	Calculation of SERS enhancement factor	124
5	Cucurbit[7]uril-based High-performance Catalytic Microreactors	126
5.1	Introduction	127

5.2	Results and Discussion	128
5.2.1	Fabrication of the catalytic microreactor	128
5.2.2	Characterisation of the catalytic microreactor	130
5.2.3	Catalytic activity investigation	136
5.3	Conclusion and Outlook	140
5.4	Experimental Appendix	140
5.4.1	Materials and general methods	140
5.4.2	Preparation of metallic catalyst nanoparticles	141
5.4.3	Synthesis and characterisation of MV-silane	142
5.4.4	Preparation of PDMS microfluidic devices	143
5.4.5	Preparation of CB[7]-based catalytic microreactors	143
5.4.6	Au NP catalytic microreactors reaction conditions	144
5.4.7	Pd NP catalytic microreactors reaction conditions	145
5.4.8	UV-vis and HPLC spectra for examined reactions	146
5.4.9	Turnover frequency calculation	153
6	Conclusion and Outlook	155
	Bibliography	158

List of Abbreviations and common units

- ADA - adamantane amine
- Ag - silver
- Au - gold
- CB[*n*]s - cucurbit[*n*]urils
- CBCat - CB[8] catenanes on spiky magnetite@Au NPs
- CDs - cyclodextrins
- CBC-NPs - surface-bound CB[8] catenanes on silica nanoparticles
- CBC-MNPs - surface-bound CB[8] catenanes on magnetic silica nanoparticles
- CB[*n*]-NRSP - CB[*n*]-functionalised nanoraspberry particles
- Cu - copper
- DCM - dichloromethane
- DI - deionized water
- DFT - density functional theory
- DLS - dynamic light scattering
- DMF - dimethylformamide
- DMSO - dimethyl sulfoxide
- DNA - deoxyribonucleic acid

- EBL - electron beam lithography
- EDL - electronic double layer
- EDX - energy dispersive X-ray
- EF - enhancement factor
- FTIR - Fourier-transform infrared spectroscopy
- GPC - gel permeation chromatography
- HAADF - high-angle annular dark-field imaging
- HPLC - high-performance liquid chromatography
- HRTEM - high resolution transmission electron microscopy
- ITC - isothermal titration calorimetry
- LSPRs - localised surface plasmon resonances
- MV - methyl viologen
- MS - mass spectrometry
- NIPAM - N-isopropylacrylamide
- NMR - nuclear magnetic resonance
- Np - 2-naphthol
- NPs - nanoparticles
- NSL - nanosphere lithography
- NRSP - nanoraspberry particles
- PDi - perylene bis(diimide)
- PDI - polydispersity

- PDMS - polydimethylsiloxane
- PS - polystyrene
- r.t. - room temperature
- r.p.m - revolutions per minute
- SEM - scanning electron microscopy
- SERS - surface-enhanced Raman scattering spectroscopy
- STEM - scanning transmission electron microscopy
- TEM - transmission electron microscopy
- TEOS - tetraethyl orthosilicate
- TDL - dibutyltin dilaurate
- THF - tetrahydrofuran
- 3D-FDTD - three dimensional finite distance time domain
- UV - ultraviolet
- XPS - X-ray photoelectron spectroscopy

Declaration

This report is submitted in the fulfilment for the PhD Study in Chemistry. Except where indicated to the contrary, either directly or by reference, the work described in this dissertation is solely the work of the author. This work by no means surpasses the word limit of 60000.

Signed,

Number of words: 31261

Xiaohe Ren,
University of Cambridge

Acknowledgements

I would like to express my gratitude to many people who have provided encouragement, support and help to me during my four years PhD study.

Firstly, I would like to thank my supervisor, Prof. Oren A. Scherman, for giving me the opportunity to study in the world's best university and conduct research in such an excellent group. He offered great support for my research, guiding me to grow up as a mature researcher gradually.

Next, I would like to acknowledge my co-workers as well as my colleagues in/outside the Scherman group, who helped me and let me work in such enjoyable environment. To thank them in turn: special thanks must go to my senior fellow Dr. Yuchao Wu, who has been a strict yet nice mentor to me, for his careful guidance during my first year and selfless help throughout my PhD study. I am also very thankful to Dr. Ji Liu, who has given me a lot of valuable advice on both life and research. Yuchao and Ji gave me many useful tips on how to be a competent independent researcher, how to deal with collaborations and promote working efficiency, as well as many manuscript writing skills. Third, I want to thank Dr. Marlous Kamp, who has offered great support during my hardest time. I've been suffered a difficult time in both research, funding and health in the beginning of my third year, during which Marlous offered kind support and helped me heartily, making me feel extremely warmhearted. Then I want to express my gratitude to Dr. Bart de Nijs and Dr. Rohit Chikkaraddy, who have been really great collaborators and have offered enthusiastic help. I admire the way they conduct themselves quite a lot. I am also thankful to Dr. Ziyi Yu, who has been a great senior, mentor, collaborator, and friend during the four years. Sixth, I want to thank Domnique Hoogland and Magda Olesinska, who joined the group the same year with me. We have shared a lot of happiness and sorrow,

witnessing the gradual growth of each other. It is really lucky to have them accompanied. In addition, I am very thankful to Dr. David Clarke, who has been a nice friend and collaborator. He helped a lot with the peptide synthesis and we had nice discussions and brainstorming about the catenane structure. Then I also want to thank Kamil for inviting me to join the edition of the RSC book chapter; Vijay for being a nice lab buddy and sharing some useful information about his PhD study; Qifeng, Baoyuan, Chenyan, Rui Li, and Yaan for the enjoyable leisure time together.

I am also grateful to the supervisor of my collaborators: Prof. Jeremy Baumberg for the support and suggestions on my SERS sensing projects and giving access to most equipment in his lab; Prof. Chris Abell for the support on the microreactor project.

In addition, I am indebted to China Scholarship Council and Cambridge Trust, which offered me financial support and the chance to dig out more in the field of materials. I want to thank all the support staff in the lab: secretaries Glenda, Ishita and Alex, technician Matt and lab manager Elisabetta. They are incredibly helpful and so crucial to keep the lab operating properly on a day-to-day basis. I am also very grateful to the graduation supporting staff in the Chemistry Department, Mrs. Rachel MacDonald, Dr. Nick Bampos, Dr. Deborah Longbottom, for always being a strong back support and giving careful guidance throughout my PhD.

Finally, and most crucially, I owe my deepest gratitude to my father Fei Ren and my mother Chunzhi Liang, for their constant concern and inspiration. They always give me unconditional love and the strongest support for whatever I pursue. I really love them.

List of Publications

Publication

- **Ren, X.**; Wu, Y.; Kamp, M.; Liu, J.; Chikkaraddy, R.; Nijs, B. D.; Yu, Z.; Baumberg, J. J.*; Scherman, O. A.* “ γ -Fe₂O₃@Au core-shell magnetic nanoraspberry particles for high-performance SERS”, *submitted*.
- **Ren, X.**; Clarke, D. E.; Kamp, M.; Wu, Y.; Chikkaraddy, R.; Nijs, B. D.; Liu, J.; Barrow, S. J.; Yu, Z.; Baumberg, J. J.*; Scherman, O. A.*, "Advanced molecular sensor exploiting catenane-engineered nanostructures", *submitted*.
- **Ren, X.**; Yu, Z.; Wu, Y.; Liu, J.; Abell, C.; Scherman, O.A.*, "Cucurbit[7]uril-based high-performance catalytic microreactor", *Nanoscale*, *in press*.
- Wu, Y.; Shah, D. U.; Wang, B.; Liu, J.; **Ren, X.**; Ramage, M.H.; Scherman, O. A.*, "Biomimetic supramolecular fibers exhibit water-induced supercontraction", *Adv. Mater.*, **2018**, 30, 1707169.
- Wu, Y.[‡]; Shah, D. U.[‡]; Liu, C.; Yu, Z.; Liu, J.; **Ren, X.**; Rowland, M. J.; Abell, C.; Ramage, M. H.; Scherman, O. A.* “Bioinspired supramolecular fibers drawn from a multi-phase self-assembled hydrogel”, *Proc. Natl. Acad. Sci. U.S.A.*, **2017**, 114(31), 8163.
- **Ren, X.**[‡]; Wu, Y.[‡]; Clarke, D. E.; Liu, J.; Wu, G.; Scherman, O. A.*; “Surface-bound cucurbit[8]uril catenanes on magnetic nanoparticles exhibiting molecular recognition”, *Chem. Asian J.*, **2016**, 11, 2382.

[‡]These authors contributed equally to this work

Chapter 1

Introduction

1.1 Nanoplatforms for SERS Technique

1.1.1 SERS: an ultrasensitive analytical technique for molecular sensing

Surface-enhanced Raman scattering (SERS) spectroscopy is a surface-sensitive technique that enhances the Raman scattering of molecules by adsorbing them on roughened metal surfaces or nanostructures.¹⁻⁶ The specific vibrational modes of the molecules result in different frequency shifts of the scattering energy from the incident light, so that virtually all polyatomic molecules display characteristic Raman/SERS spectral peaks.¹⁻⁶ Ultrahigh SERS sensitivity even down to the few or single molecule level can be achieved with well-designed nanostructures.^{1,4,7,8} SERS has been established as an ultrasensitive and ultra-rapid analytical technique widely applied in various fields, ranging from analytical chemistry,⁹ surface science,^{10,11} biomolecule and pharmaceutical drug diagnostics,^{12,13} to environmental monitoring.¹

After decades of debate, it is now generally accepted that the predominant contributor to most SERS processes is the electromagnetic field enhancement.^{1-6,14} The enhanced SERS signals are largely due to the amplification of electromagnetic field by the excitation of localised surface-plasmon resonances.^{1,2,14} This amplification occurs preferentially in the sharp features, gaps, or crevices of plasmonic materials, which are commonly noble and coinage metals (e.g. silver, gold and copper) with nanoscale features.^{1,2,14}

The sensitivity and resolution of SERS are strongly influenced by several factors, in-

cluding the characteristics of the laser excitation (e.g. wavelength, incident direction and polarization), the dielectric properties of the ambient environment, the intrinsic Raman cross-section of probe molecules, and more importantly, the optical properties of SERS substrates.¹⁻⁵ Over the past decades, great efforts have been devoted to developing optimized SERS substrates for high enhancement and sensitivity.^{10,15-22} The pioneering discovery can be traced back to the 1970s for pyridine adsorbed on roughened silver electrodes.^{23,24} Thereafter, the history of SERS is largely governed by the development of SERS substrates (as illustrated in Figure 1.1). Early research focused on the fundamental theory and increasing the field enhancement exploring substrates mainly consisting of roughened Au/Ag electrodes, colloidal aggregates, island films and microlithographic-manufactured surface structures.^{16,18,24} The 1990s witnessed the rapid development of nanoscience and nanotechnology.¹⁷ Emerging synthetic methods of nanoparticles (NPs) and nanofabrication methods of structured surfaces significantly benefited the development of SERS substrates.⁵ Au and Ag NPs with nanometre-sized tips, shells or gaps as well as structured surfaces with nanometre-sized holes, bumps or ridges were manufactured for high-sensitivity SERS.^{10,15,17,19-22}

Challenges still remain in the SERS field, namely, limited detectable analyte species, degradation of the substrates with time which leads to a decrease in signal and limited re-usability of the substrates.¹⁻⁶ Since the high sensitivity of SERS is dependent on the optimization of local enhanced electromagnetic field at the metal surface, the adsorption of the analyte molecules onto the SERS substrates is required.¹⁻⁶ As a result, the applications of SERS in liquid environments are largely restricted to analyte molecules with chemical affinity for the common plasmonic substrates (e.g. thiolated or aminated molecules).¹⁻⁶ Therefore, one of the key challenges is the rational design of efficient and flexible substrates for a broader collection of chemical analytes.¹

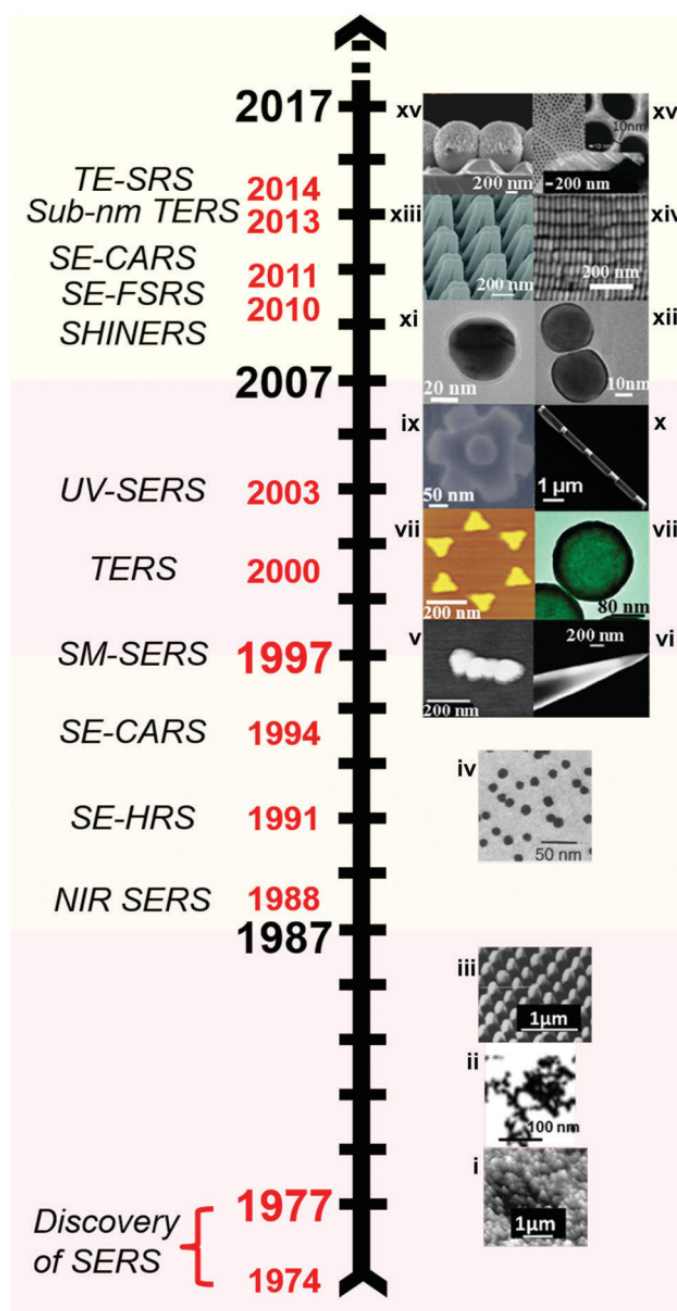


Figure 1.1: Milestones of the development of SERS, adapted from reference.⁵ Development of new methods of surface-enhanced Raman spectroscopies (left), and representative SERS substrates (right) in the past four decades. Image (ii-xvi) are adapted from references.^{10,15-22} Full names of abbreviations in the figure: near infrared SERS (NIR SERS), surface-enhanced hyper-Raman spectroscopy (SE-HRS), surface-enhanced coherent anti-Stokes Raman spectroscopy (SE-CARS), single-molecule SERS (SM SERS), tip-enhanced Raman spectroscopy (TERS), ultraviolet SERS (UV SERS), shell-isolated nanoparticle-enhanced Raman spectroscopy (SHINERS), surface-enhanced femtosecond stimulated Raman spectroscopy (SE-FSRS) and tip-enhanced stimulated Raman spectroscopy (TE-SRS).

1.1.2 Commonly used SERS substrates

Most SERS-active substrates are based on noble and coinage metals (i.e. Au, Ag or Cu).^{1,2} In general, Au and Ag are most often used because they are air stable while Cu is more reactive.² All three metals have localised surface-plasmon resonances covering most of the visible and near infrared wavelength range, where most Raman measurements are conducted (Figure 1.2).² The most common SERS substrates can be arbitrarily classified into three generic categories:^{2,3,6} (1) metal NPs in suspension; (2) metal NPs immobilised on solid substrates; (3) solid substrates with well-designed nanostructures, often fabricated by nanolithography and/or template based synthesis.

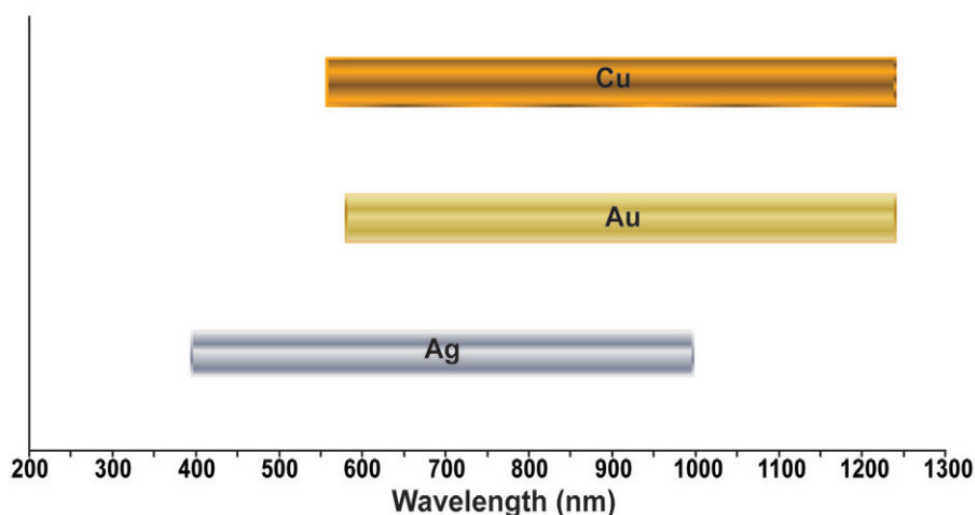


Figure 1.2: Approximate wavelength ranges which the localized surface-plasmon resonances of Au, Ag and Cu cover. Adapted from reference.²

1.1.2.1 Metal NPs in suspension

Metal NPs in suspension are used extensively as SERS substrates due to their high SERS-performance and developed fabrication methods.^{2,3,6} Various sizes and shapes of NPs can be obtained by both physical and chemical strategies,^{25,26} typically wet chemical synthesis using specific surfactants to direct the growth process.²⁵ It is well recognised that besides particle size, the shape of NPs also plays an important role in the magnitude of SERS enhancement.^{1,4,6,8,9} The overall SERS enhancement factor increases with shape

as follows: nanospheres < nanorods < nanogap (dimers, aggregates) <= nanostars, attributed to the number of intrinsic hot-spots per particle.^{1,5,6,27–29} Hot-spots are locations in the vicinity of the plasmonic nanostructures where the local optical field is tremendously enhanced compared to its surrounding.^{3,6} Consequently, molecules present in the hot-spots exhibit an immense enhancement in its Raman scattering signals.^{3,6} Nanostars are star-shaped NPs with sharp edges and tips, possessing much denser hot-spots in a single NP, thus giving rise to higher SERS enhancement in comparison to nanospheres, nanorods and aggregated nanospheres.^{3,6}

The simplest SERS measurement using metal NPs in suspension is conducted by direct mixing of NPs with analytes in solution.³ Other means of mixing NPs with analytes including microfluidics,³⁰ slippery liquid-infused porous SERS,³¹ as well as depositing and drying the analytes in NP colloidal suspensions on a solid optical substrate.^{22,32} For example, Figure 1.3 shows a flow-focusing microfluidic device for controlled Ag NP aggregation and SERS measurement.³⁰ The system was designed to firstly diffuse the analyte into the side stream containing Ag NPs, followed by the introduction of salt ions which caused the aggregation of Ag NPs, creating species with strong SERS signals.³⁰

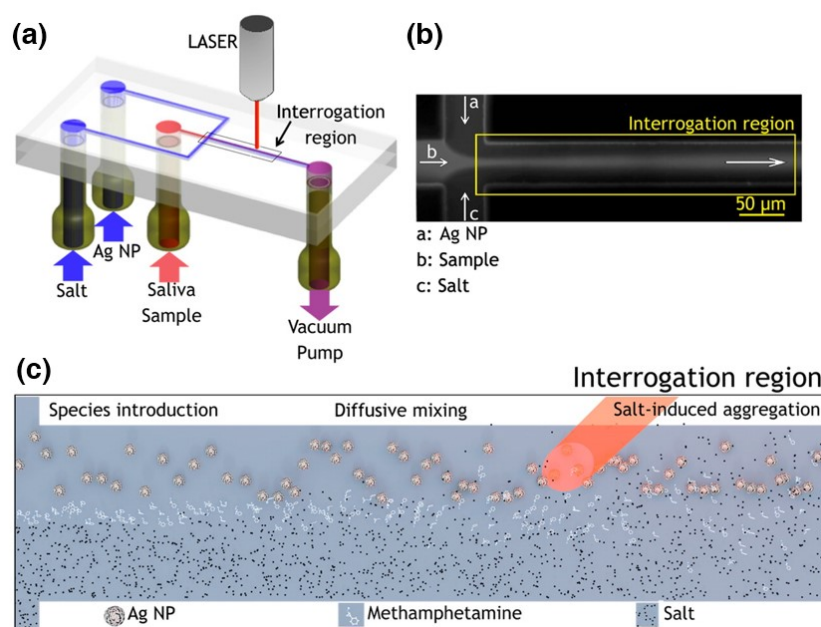


Figure 1.3: (a) Schematic illustration of the flow-focusing microfluidic device; (b) microphotograph of the flow-focusing junction; (c) schematic of the reaction between the Ag NP, analyte, and salt ions. Adapted from reference.³⁰

SERS measurements using metal NPs in suspension usually require the aggregation of NPs for enhanced fields.³ However, aggregation reduces the reproducibility and colloidal stability of the substrate systems, which is a remaining challenge.^{3,6} One of the solutions developed by the Tian group is the shell-isolated nanoparticle-enhanced Raman spectroscopy (SHINERS), in which the Raman signal amplification is provided by Au NPs covered with an ultrathin silica or alumina shell.^{7,22} As illustrated in Figure 1.4, a monolayer of such NPs is spread as 'smart dust' over the surface to be probed, where the jointly enhanced Raman signals contributed by all of these NPs are collected.^{7,22} The ultrathin coating keeps the NPs from agglomerating, separating them from direct contact with the probed surface.^{7,22} The SHINER substrate has been demonstrated to successfully probe hydrogen adsorbed on a single crystal Pt surface, detect pesticides that contaminated citrus fruits and dynamically track heterogeneous nanocatalytic processes.^{7,22}

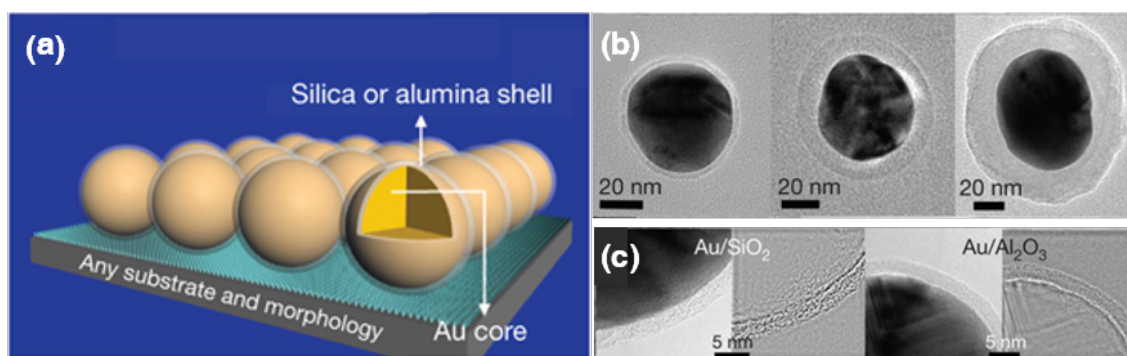


Figure 1.4: (a) Schematic illustration of the shell-isolated nanoparticle-enhanced Raman spectroscopy (SHINERS); (b) high resolution TEM images of Au/silica core-shell NPs with different shell thicknesses; (c) high resolution TEM images of Au/silica NPs and Au/alumina NPs with a continuously and completely packed shell of 2 nm. Adapted from reference.^{7,22}

1.1.2.2 Metal NPs immobilised on solid substrates

Immobilisation of the metal NPs on solid substrates provides an approach to bring the NPs into close contact while avoiding aggregations.⁶ Several strategies have been employed to immobilise NPs on solid substrates. The most common strategy is by chemical attachment of prepared metal NPs to solid substrates using bifunctional molecules.^{19,33,34} The first self-assembled metal NPs on solid support used as SERS-active substrate was re-

ported by the Natan group in 1995 (Figure 1.5).¹⁹ The procedure was straightforward: the surface of glass slides were firstly functionalised with either aminated or thiolated molecules, followed by immersing of the functionalised slides into metal NP suspensions. Numerous works have been published based on this fabrication principle, for example, Au nanorods immobilised on amine modified quartz slides and Ag NP monolayers immobilised on 1,10-phenanthroline modified Ag plates.^{19,33,34} Many fabrication parameters, e.g. metal NP concentrations, incubation time, temperature and centrifugal forces, have been examined to tune the properties of the substrate.^{19,33,34} This principle can also be applied to immobilise metal NPs on non-flat materials. For example, Ag NPs were immobilised onto Ag nanowires using a bifunctional molecule 4-aminobenzenethiol.³⁵



Figure 1.5: Assembly strategy for Au and Ag monolayers on glass slides. X = CN, NH₂, 2-pyridyl, P(C₆H₅)₂, or SH; R = CH₃ or CH₂CH₃. Adapted from references.^{3,19}

Other methods, such as self-assembly of metal NPs onto solid surfaces based on electrostatic attraction using polymers and biomolecules,³⁶ direct transfer of pre-assembled metal NP film onto a solid support,³⁷ chemically and photochemically grown metal NPs on solid supports,³⁸ have also been reported.

1.1.2.3 Solid substrates with well-designed nanostructures

Solid substrates with highly-ordered SERS-active metallic nanostructures are generally fabricated using nanolithography and/or template-assisted techniques.^{3,6} Electron beam lithography (EBL) is one of the mostly used nanolithographic method.^{3,6,39,40} It consists of a 10-50 keV electron beam focused on a solid support, generally electro-resist covered silica wafer, as illustrated in Figure 1.6.^{3,6,39,40} The electro-resist covers can be either positive or negative resist. For the positive resist cover, the electron beam selectively etches off the covered region, leaving the surface in the predetermined architecture, and vice versa.^{3,6,39,40} The advantages of EBL are the possibility of controlling the NP sizes and

shapes as well as the interparticle distance with great accuracy.³ Another common nanolithographic method, nanosphere lithography (NSL), is an effective and high-throughput technique to produce highly-ordered 2D periodic arrays of NPs.^{6,41} NSL can fabricate three types of ordered substrates: metal films over nanospheres, periodic NP arrays and nanovoid arrays (Figure 1.7). In addition, flexible SERS substrates which can be used on irregular surfaces to detect analytes can also be prepared by NSL.⁴²

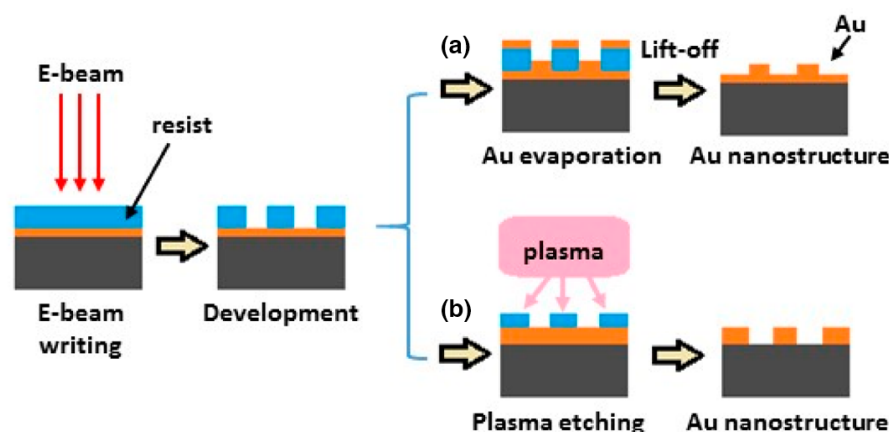


Figure 1.6: Schematic diagram of two fabrication strategies for SERS substrates using electron beam lithography (EBL): (a) using a positive resist cover and (b) using a negative resist cover. Adapted from references.^{6,39}

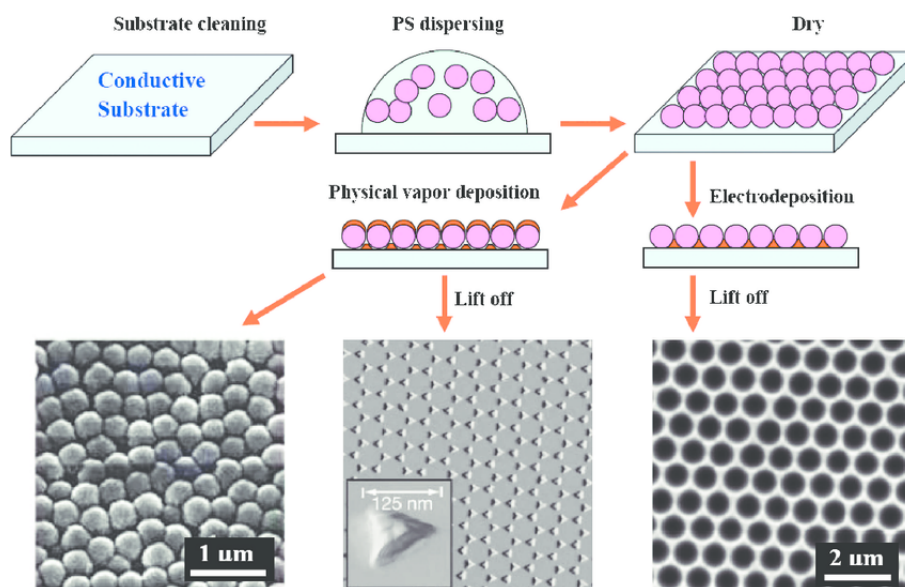


Figure 1.7: Schematic diagram of template methods using nanosphere lithography to fabricate SERS-active substrates: metal films over nanospheres, periodic NP arrays, and nanovoid arrays. Adapted from references.^{41,43,44}

Although SERS substrates using metal NPs immobilised on solid substrates or metallic nanostructures fabricated directly on solid substrates can prevent the aggregation of NPs, they are generally too expensive and substrates can hardly be reused.^{1,4,5,8,45,46}

1.1.3 Nanoplatforms for SERS detection of "inert" analytes

Analytes need to be adsorbed efficiently onto the substrate surface to obtain high sensitivity SERS signals, as the SERS enhancement decreases exponentially with the separation distance (r^{10} for spheres) and the Raman signal is only amplified at distances no larger than 5 nm from the substrate surface.¹⁻⁶ Consequently, most of the SERS measurements are carried out with thiolated or aminated molecules, which can be attached chemically onto the metal surface (i.e. Au or Ag surfaces).^{1,4,5,8,45,46} For analytes without a clear metal binding group (hereinafter referred to as "inert"), SERS signals become weaker owing to fewer molecules binding to the substrate.^{1,4,5,8,45,46} A range of solutions have been presented to trap "inert" analytes in the plasmonic hot-spots, including electrostatic and hydrophobic interactions,^{1,47} mechanical trapping,^{1,48,49} antibody receptors,⁵⁰ and host-guest interactions.^{28,51-56}

1.1.3.1 Electrostatic and hydrophobic interactions

Molecules can be attracted to metallic surfaces by electrostatic or hydrophobic interactions.¹ However, the hydrophobic nature of metallic surfaces is questionable when dealing with colloidal metal NPs in solution, as they are solvated and surrounded by an electrostatic double layer (EDL).¹ For most of common colloidal metal NP SERS substrates (i.e. citrate or borohydride reduced Au/Ag NPs), the capping agents are citrate ions and the NPs are negatively charged.¹ Since conventional charged organic molecules are generally negatively-charged, the interaction between the EDL and analyte gets hindered.¹ This problem was partially solved by using a "colloidal activation" method.^{1,47} An electrolyte solution such as nitrates, sulfates or halides was added to the system to increase the ionic strength and reduce the surface charge, leading to a smaller electrostatic repulsion between the metallic surface and the analytes. Acidic solution (e.g. HNO_3 , H_2SO_4

or HClO_4) was then added to increase the proton concentration, thereby decreasing the negative charge of the carboxylate groups.^{1,47} In addition, these acidic agents may also interact with the analytes, making them less negative or even neutral, thus improving their electrostatic interaction with the metallic surface. This method, however, compromises the colloidal stability of the system.^{1,47}

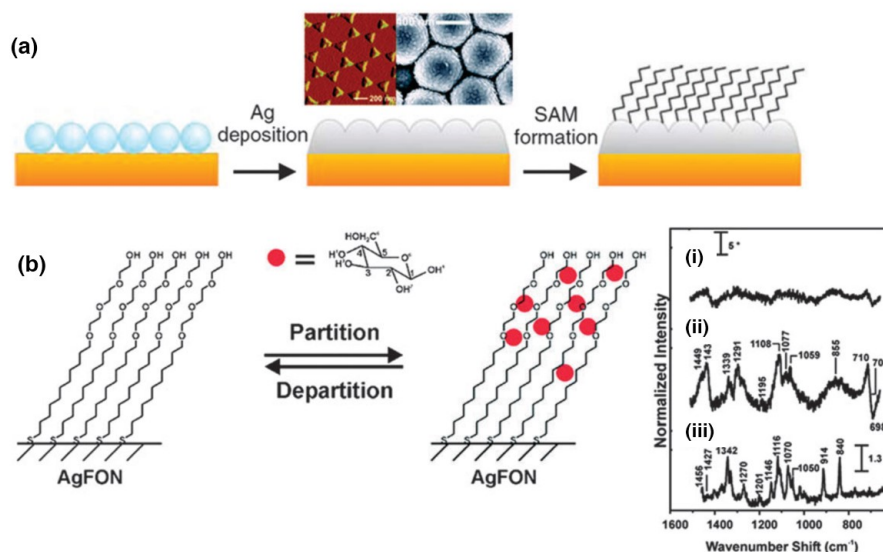


Figure 1.8: (a) Schematic illustration of the fabrication process of partition-layer modified Ag film over nanostructured substrate; (b) schematic representation of a hypothetical glucose concentration gradient created by a (1-mercaptoundeca-11-yl)tri(ethylene glycol) partition layer. SERS spectra of serum albumin (i), serum albumin with glucose (ii), Raman spectrum of glucose (iii). Adapted from references.^{1,57}

Another method developed using hydrophobic interactions is by creating a dense partition layer to increase the surface-to-solution partition coefficient. This method relies on the functionalisation of the metallic surface with hydrophobic molecular monolayers (e.g. amino- or thio-aliphatic chains), as shown in Figure 1.8.^{1,57} Since these hydrophobic molecules are generally insoluble in water, nanostructured solid substrates are preferred in this case.¹ The monolayer can be subsequently functionalised onto the substrate and increase the surface-to-solution partition, thereby detecting hydrophobic "inert" analytes.^{1,58} For example, the detection of polycyclic aromatic hydrocarbons (PAHs)⁵⁹ and polychlorinated biphenyls⁶⁰ using alkyl monolayers has been reported.

1.1.3.2 Mechanical trapping

Mechanical trapping relies on the metalsurface being surrounded by a responsive matrix which is able to trap and release target analytes upon a chemical or physical stimulus.¹ The most commonly used stimuli are temperature and pH.^{1,48} For temperature-responsive matrix, poly-N-isopropylacrylamide (pNIPAM) has been the most popular choice, on account of its reversible phase transition at its lower critical solution temperature (LCST) around 32 °C.^{1,48} Figure 1.9a shows an example of using pNIPAM to trap analytes for SERS detection, utilizing core-shell colloids consisting of a Au NP core coated with a pNIPAM shell.^{1,48} Small molecules can be trapped and released reversibly towards the Au surface, yielding SERS signals. However, the pNIPAM shell prevents close contact between the metal NPs and thus limits the enhancement factor.^{1,48,49,61} Therefore, alternative composite materials were developed, using multiple plasmonic NPs inside each pNIPAM bead (Figure 1.9b).^{1,48,49,61} In these materials, the collapse of the pNIPAM bead at high temperature makes the NPs approach each other, generating higher SERS enhancements between them.^{1,48,49,61}

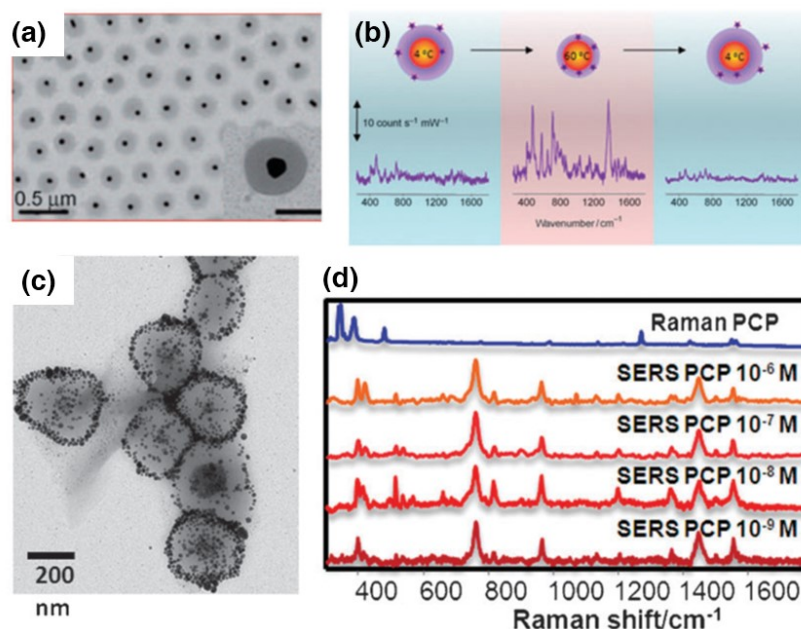


Figure 1.9: (a) Spherical Au NPs coated with pNIPAM and (b) SERS spectra of 1-naphthol with various temperature (from 4 to 60 °C and back to 4 °C); (c) magnetite-Ag@pNIPAM composite microgels and (d) the SERS detection of pentachlorophenol (PCP). Adapted from references.^{1,48,49}

Regarding pH responsive matrices, the driving force to collapse or expand the polymer matrix is the electrostatic force generated at the functional groups (typically carboxylic or amino groups) as a function of proton concentration.⁶² For example, the most widely used polymers to detect cationic analytes (amines) are polyacrylic acid^{63,64} and its block-copolymers with polyethylene glycol.¹ These polymers expand at high pH due to the electrostatic repulsion between the differently ionized carboxylate groups. When pH is decreased, the polymers collapse due to the protonation of the carboxylates and formation of intramolecular hydrogen bonds.¹

1.1.3.3 Detection *via* molecules with selective ligands

Indirect methods using molecules with selective ligands have also been investigated. Here, SERS spectra changes of the ligand molecules induced by target analytes are detected.¹ These methods are particularly suitable for the detection of atomic cations, including metallic ions, inorganic oxoanions and organic aliphatic molecules, as well as the direct detection of analytes in complex matrices such as biological fluids and waste waters.¹⁻⁶

Molecules with selective ligands can be used for the detection of organic molecules, for example, the detection of sugars (glucose) using boronic acids.⁶⁵ The most active current research direction is the use of biosensors.¹⁻⁵ Although the use of biological interfaces is expensive, they provide extraordinary chemical selectivity and highly specific binding of target analytes, thus are capable of detecting minute amounts of analytes in highly complex media such as biological fluids or natural and waste waters directly.¹ Such biosensors include antibody receptors,^{50,66} as well as nucleic acid interactions and peptidic or nucleic acid aptamers.

The use of antibody receptors is based on the antibody-antigen recognition, where structural differences induced by the antigen upon complexation lead to changes in the SERS spectrum of the antibody.^{1,50,66} The antibody receptor has been used for the detection of exogenous proteins in milk⁵⁰ and the analysis of small metabolites such as benzoylecgonine,⁶⁶ on account of its high sensitivity and specificity. As an example, the

ultrasensitive SERS detection of ovalbumin (OVA) in milk based on antibody modified Ag dendrite complexes is shown schematically in Figure 1.10.⁵⁰

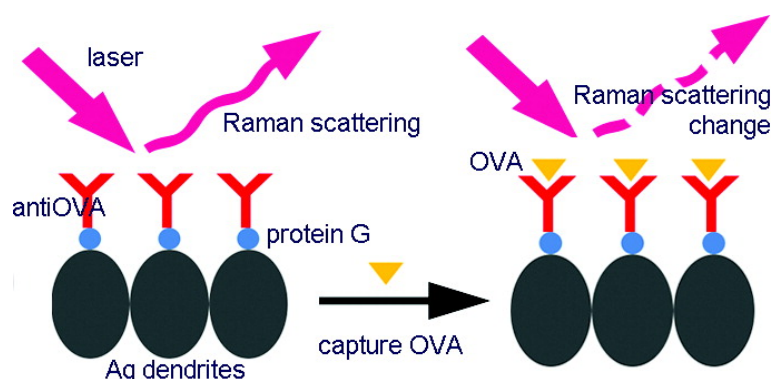


Figure 1.10: Schematic illustration of SERS detection of ovalbumin (OVA) based on antibody modified Ag dendrite complexes. Adapted from reference.⁵⁰

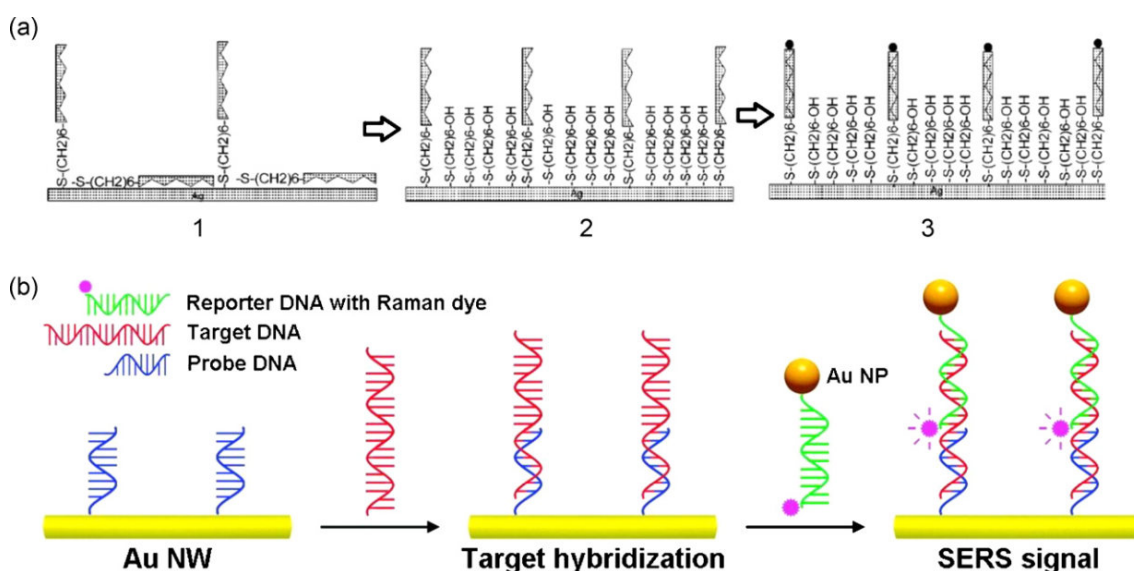


Figure 1.11: (a) Illustration of the Vo-Dinh's DNA detection scheme; (b) illustration of the detection of target DNAs by Au NP-on-nanowire system. Adapted from references.^{67,68}

The use of DNA/RNA fragments as the sensitive layer is also of great interest. The purine and pyrimidine bases composing the nucleic acids specifically recognise their corresponding pairs, contributing to the specific recognition of a given DNA or RNA sequence.^{1,67,68} As shown in Figure 1.11a, the early concept (developed in 1994 by the Vo-Dinh group) comprised immobilising single stranded DNA onto a nitrocellulose filter, followed by the exposure to a complementary DNA, which was labeled with a strong

Raman active dye molecule that yields strong SERS signals.^{67,69,70} This technique was applied to the detection of HIV gene and cancer markers.⁶⁷ Detection of pathogens using DNA probes immobilised on Au nanowires has also been reported (Figure 1.11b).⁶⁸

1.1.3.4 Host-guest interactions

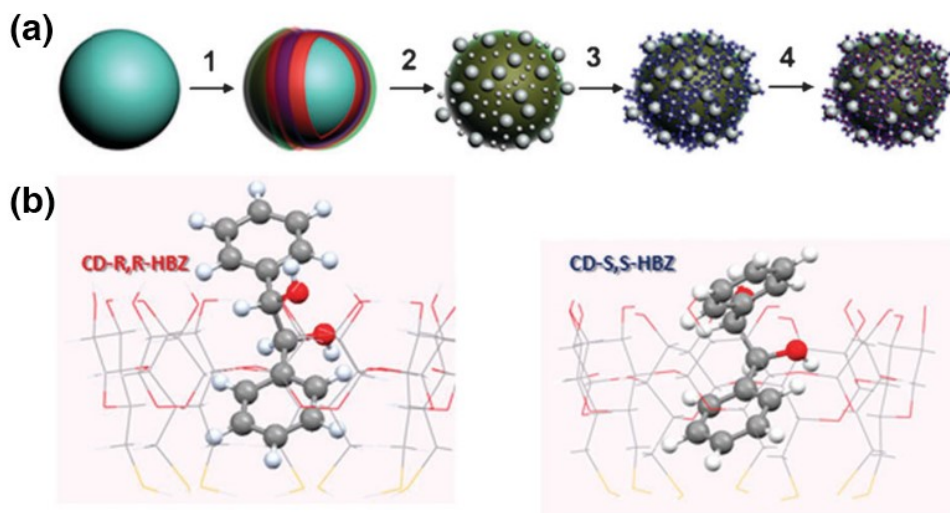


Figure 1.12: (a) Schematic of the formation of Ag NP-coated microspheres functionalised with thiolated cyclodextrin ($T\beta$ -CD). In the step 1, micron-sized polystyrene beads (PS) were wrapped with polyelectrolytes consisting of layer-by-layer assembly of poly(diallyldimethylammonium chloride) [PDPA], polystyrene sulfonate (PSS), and poly(allylamine hydrochloride) [PAH]. The functionalised beads were then coated with Ag NPs (PS@AgNPs) in the step 2, followed by functionalisation with $T\beta$ -CDs of the Ag surface (PS@AgNPs@ $T\beta$ -CD) (step 3). Finally, the addition of hydrobenzoin enantiomers led to the formation of supramolecular complexes; (b) density functional theory (DFT) calculated molecular models for the most probable conformation of each enantiomer within the CD. Adapted from references.⁷¹

Host-guest interactions of macromolecular cages (host) showing specific supramolecular interactions towards target analytes (guest), have also been applied to ultrasensitive SERS measurements.^{1,71–74} This approach imparts preferential orientations with respect to the surface on the molecules and increases the level of SERS sensitivity.^{1,71–74} For example, as shown in Figure 1.12, by using the host molecule cyclodextrin (CD), analytes are retained in a confined geometry compared to an open surface (the aromatic rings of the R,R isomer are more perpendicular to the surface than those of the S,S isomer); there-

fore, the R,R- and S,S-hydrobenzoin enantiomers can be differentiated and quantified.⁷¹ CDs show extremely low SERS cross-sections, and are therefore capable of trapping analytes while avoiding spurious background signals in the spectra.^{1,71–74} Consequently, CDs have been applied to the ultrasensitive detection of poly(allylamine hydrochloride) (PAH),⁷² explosives⁷³ and pollutants (e.g. carbendazim and parathion).⁷⁴ Other host systems of different nature have also been successfully exploited, including calixarenes⁷⁵ and cucurbit[*n*]urils (CB[*n*]s, where *n* = 5, 6, 7 or 8).^{28,51–56} The latter, CB[*n*], is of particular interest as it not only exhibits low SERS cross-sections and selective encapsulation of various guest molecules into its barrel-shaped cavity, but also functions as a precise rigid spacer between nanoparticles.^{53,76–78}

1.2 Cucurbit[*n*]uril Host-Guest Chemistry

1.2.1 Macrocyclic host-guest complexation

Macrocyclic host-guest complexation is a typical process of molecular self-assembly where molecules bind selectively through supramolecular interactions. A host-guest complex is composed of at least one host and one guest molecule held together in a unique structure by non-covalent interactions.⁷⁹ Generally, the host component is a larger molecule, which is able to encompass a smaller guest molecule.⁷⁹ Figure 1.13 shows an example of host-guest complexation between β -cyclodextrin (host) and polyaromatic hydrocarbons (PAHs, guest). A complementarity in molecular shape and binding sites location is the key to the host-guest complexation.⁷⁹

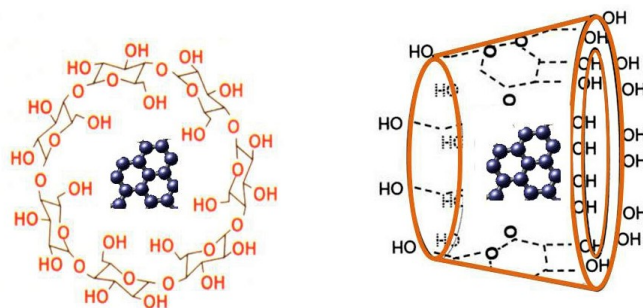
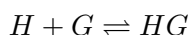


Figure 1.13: Illustration of β -cyclodextrin and polyaromatic hydrocarbon molecule host-guest complexation. Adapted from reference.⁸⁰

Host-guest complexes form reversibly, achieving an equilibrium:⁸¹



where H , G and HG represent "host", "guest" and the "host-guest complex", respectively. The thermodynamic benefit of the formation of a host-guest complex is that there is a lower overall Gibbs free energy due to the interaction between the host and guest molecules.^{81,82}

Common macrocyclic host molecules include cyclodextrins,⁸⁰ calixarenes,^{83,84} crown ethers^{85,86} and cucurbiturils^{77,87–89}. Cyclodextrin is a toroidal-shaped polycyclic glucose oligomer with a hydrophilic exterior and a hydrophobic cavity and has been investigated as a promising cargo carrier in drug delivery.^{80,90} Calixarenes are macrocycles obtained from hydroxyalkylation between aldehyde and phenol.^{83,84} Their shape resembles a bucket or a cup. Calixarenes have been applied as chemical sensors and sodium selective electrodes.⁹¹ A crown ether is a macrocycle consisting of several ether groups, among which the most common group is ethylene oxide.⁸⁶ It is able to bind strongly to certain cations, such as potassium cations (K^+).⁸⁵ The supramolecular hosts mentioned above are good choices for industrial applications due to their low cost and commercial availability, however, they also exhibit several limitations, such as low selectivity and low affinity.⁹²

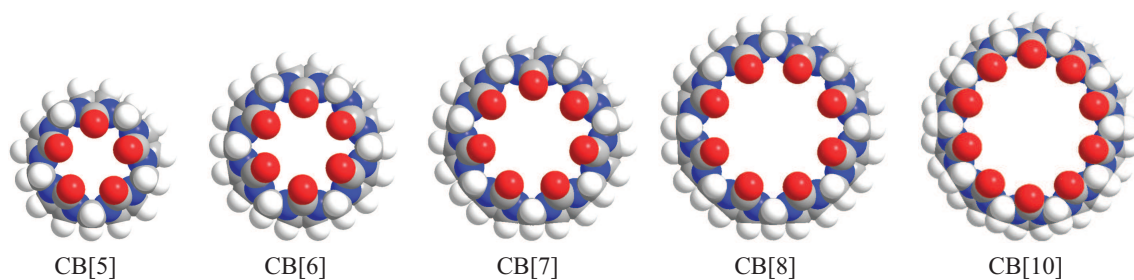


Figure 1.14: X-ray crystal structures of $CB[n]$ homologues ($CB[5]$ - $CB[8]$, $CB[10]$). Colour codes: carbon, gray; nitrogen, blue; oxygen, red. Adapted from reference.⁷⁶

Cucurbit[n]urils (Figure 1.14) are cage-like macrocyclic molecules consisting of glycoluril monomers linked by methylene bridges.⁹³ These macrocycles were named "cu-

cucurbiturils" for their resemblance to a pumpkin, which belongs to the *Cucurbitaceae* family.⁹⁴ Cucurbiturils are commonly written as cucurbit[*n*]urils, or CB[*n*], where *n* represents the number of glycoluril units. CB[6] was first synthesised in 1905 by Behrend and coworkers,⁹⁵ by acid-catalysed condensation of glycoluril and formaldehyde (Figure 1.15). However, the chemical nature and molecular structure were not identified until 1981, when a thorough investigation of CB[*n*]s was carried out by Mock and coworkers.⁹⁴ The research on the CB[*n*] family was largely promoted by the research groups of Kim, Day and Isaacs, who discovered and isolated four other homologues, (CB[5], CB[7], CB[8] and subsequently CB[10]).^{77,87–89} Recently, the largest family member, CB[14], was reported with 14 glycoluril units linked by 28 methylene bridges and aroused great interests.⁹⁶ The CB[*n*] homologues can be isolated based on their different solubility in various solvents, e.g. methanol-water and acetone-water mixtures,^{77,87} or by column chromatography with harsh acidic eluents.⁹⁷ The Scherman group has recently reported an environmentally friendly method for the isolation of CB[5] and CB[7], *via* ionic liquid binding and a solid state metathesis reaction.⁹⁸

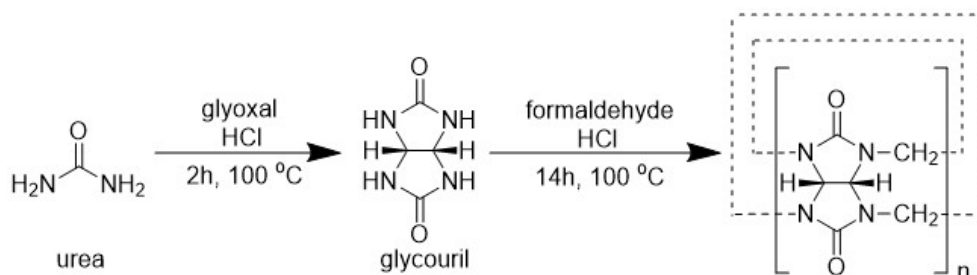


Figure 1.15: Synthetic scheme of CB[*n*]s homologues.

The structural dimensions of CB[*n*] homologues are shown in Figure 1.16 and Table 1.1.^{93,99} The height for all CB[*n*]s is $9.1\text{ }\text{\AA}$, since the height of a single glycoluril unit is fixed. The mean internal cavity diameter increases progressively from $4.4\text{ }\text{\AA}$ for CB[5] to $12.4\text{ }\text{\AA}$ for CB[10], and the portal diameter also increases from $2.4\text{ }\text{\AA}$ to $10.6\text{ }\text{\AA}$, contributing to an increase of the overall cavity volume from $83\text{ }\text{\AA}^3$ to $870\text{ }\text{\AA}^3$.

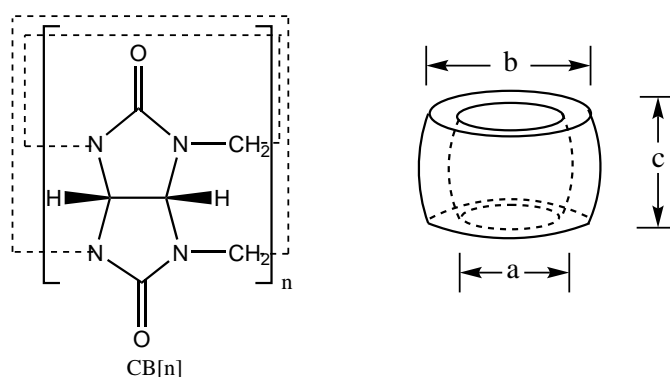


Figure 1.16: Illustration of the chemical framework (left) and dimensional structure (right) of CB[n]. Adapted from references.^{93,99}

Table 1.1: Dimensions and solubility of CB[n] homologues.^{93,99}

CB[n]	a [Å]	b [Å]	c [Å]	d [Å]	V [Å ³]	S _{H₂O} [mM]
CB[5]	13.1	4.4	2.4	9.1	82	20-30
CB[6]	14.4	5.8	3.9	9.1	164	0.018
CB[7]	16.0	7.3	5.4	9.1	279	20-30
CB[8]	17.5	8.8	6.9	9.1	479	<0.01
CB[10]	-	11.3-12.4	9.5-10.6	9.1	870	<0.05

a: outer diameter; b: internal cavity diameter; c: portal diameter; d: total CB[n] depth; V: volume of the cavity; S_{H₂O}: solubility in water.

The water solubility (Table 1.1) of CB[n]s is generally low (< 0.05 mM), except for CB[5] and CB[7], which have moderate solubility in water around 20-30 mM.^{93,99} All the CB[n]s are soluble in acidic solutions as a function of protonation.⁹³ CB[n]s are insoluble in most organic solvents, with a few exceptions. Sindelar *et al.*¹⁰⁰ first reported a CB[7]-based rotaxane, which is soluble in acetonitrile and dimethyl sulfoxide. Monhaphol *et al.*¹⁰¹ have reported a CB[8] interlocked assembly partially soluble in a non-aqueous solvent, i.e. a viologen unit linked to two tris(2,2'-bipyridine)ruthenium substitutes in acetonitrile. In most studies, CB[n] complexes are investigated in aqueous solutions.^{102,103}

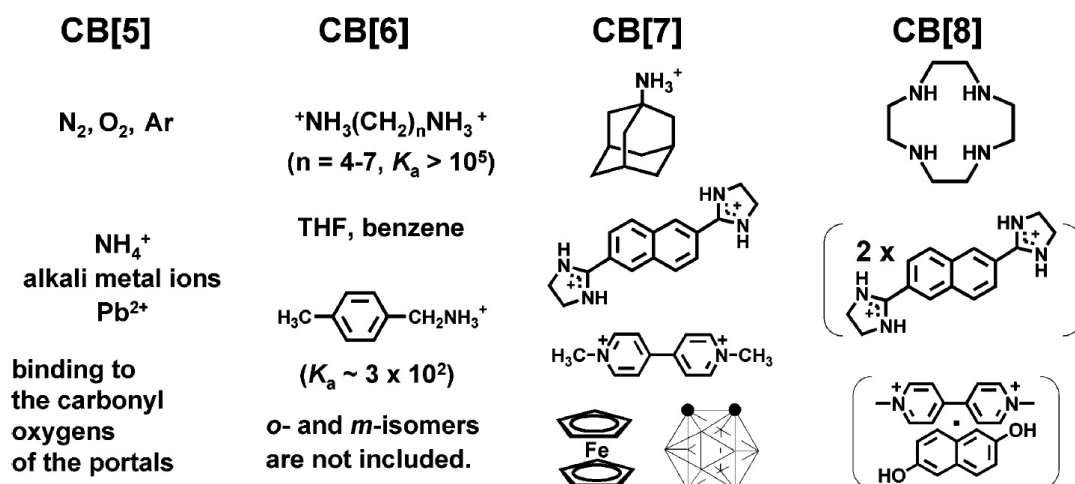


Figure 1.17: Examples of different guest molecules for CB[*n*]s. Adapted from reference.⁹³

CB[*n*]s exhibit remarkable guest binding properties attributed to their hydrophobic inner cavity and polar carbonyl portals.⁹² The main driving forces of CB[*n*] complexation include hydrophobic effect as well as ion-dipole and dipole-dipole interactions stemming from the electronegative carbonyl portals.^{104–106} This host-guest complexation has also been studied from the energy point of view, which counts for the release of ‘high-energy’ water molecules upon the inclusion of nonpolar organic guests.¹⁰⁷ More specifically, the guest molecule entering the CB[*n*] cavity leads to a energy loss from the reconstruction of hydrogen bonding network, which is due to the occupation of the guest and the release of trapped water molecules inside the cavity.¹⁰⁷ The differences in cavity and portal sizes of CB[*n*]s lead to different molecular recognition properties, as shown in Figure 1.17.⁹³ CB[5], the smallest member in the CB[*n*] family, only binds to protons, alkali metal ions and ammonium ions or encapsulates gas molecules (e.g. Ar, O₂, N₂, N₂O, CO₂, CH₄) and some solvent molecules (e.g. acetonitrile and methanol).¹⁰⁸ CB[6] is able to form stable complexes with protonated diaminoalkanes ($^+\text{NH}_3(\text{CH}_2)_n\text{NH}_3^+$, $n=4-7$) and protonated aromatic amines, e.g. *p*-methylbenzylamine, etc.⁹³ It is also able to encapsulate neutral molecules such as benzene and tetrahydrofuran in aqueous solution.⁹³ CB[7] can bind larger guest molecules that cannot fit into CB[6]. For example, CB[7] forms 1:1 complexes with protonated adamantane amine (ADA) and methyl viologen dication (*N,N'*-dimethyl-4,4'-bipyridinium, MV²⁺), and can easily encapsulate neutral molecules such

as carborane and ferrocene.⁹³ CB[8], with a much larger cavity volume (479 Å³), displays an unique ability to bind two guests at the same time.^{92,109,110} It is able to encapsulate two 2,6-bis(4,5-dihydro-1*H*-imidazol-2-yl) naphthalene molecules to form a 1:2 complex, or two complementary guest molecules (a charge transfer complex) such as MV²⁺ and 2,6-dihydroxynaphthalene to form a 1:1:1 ternary complex.⁹³ The electron-deficient MV²⁺ allows for the encapsulation of a second guest inside the CB[8] hydrophobic cavity and has been investigated mostly as the first guest for CB[8].⁹² The formation of the stable 1:1:1 ternary complex is reversible and the complex can be dissociated under certain circumstances. For example, the addition of a competitive guest ADA can expel both first and second guests from the CB[8] cavity (Figure 1.18).¹¹¹

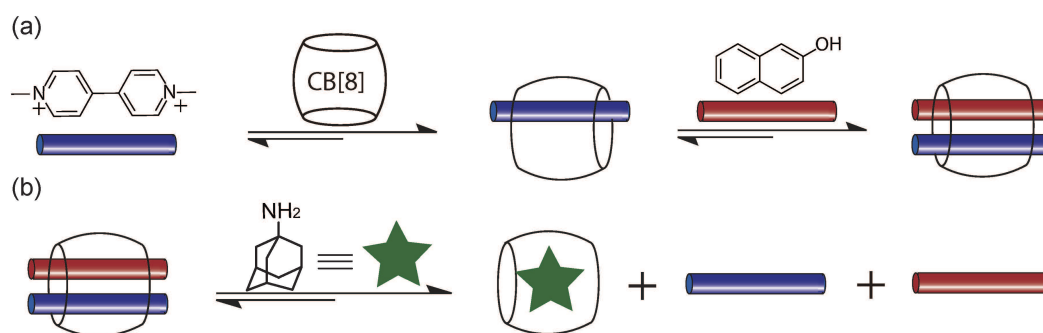


Figure 1.18: Schematic illustration of (a) CB[8] binding with MV²⁺ and naphthol, (b) disassembly of the ternary complex upon addition of ADA. Adapted from reference.¹¹¹

Moreover, the electronegative carbonyl portals of CB[*n*]s show strong binding affinity towards metal surfaces. The direct interaction of CB[*n*]'s portal with the Au surface was firstly reported by An and co-workers (Figure 1.19).¹¹² CB[*n*]s acted as direct molecular junctions between adjacent Au NPs, resulting in the formation of coagulates.¹¹² The CB[*n*] molecules were oriented perpendicular to the Au surface, and the NPs were separated by CB[*n*] molecules at a precise distance of 0.9 nm, as shown in Figure 1.19b and c.¹¹² The strong and irreversible binding between CB[*n*]s and the Au surface is attributed to the electrostatic interactions between their electronegative carbonyl portals and the metal surface, as well as the chelation.¹¹²

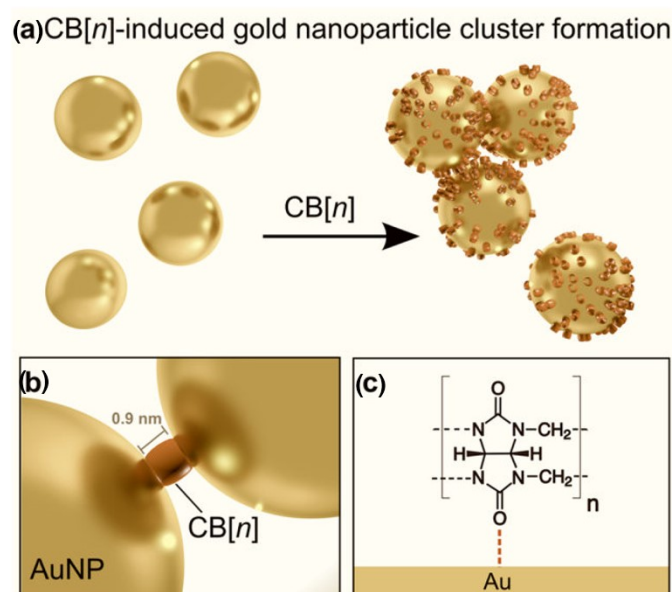


Figure 1.19: (a) CB[n]s act as direct molecular junctions in between Au NPs, forming NP coagulates; (b) NPs are separated by CB[n] molecules at a precise distance of 0.9 nm; (c) CB[n] binds to the Au surface through its carbonyl portals, orienting perpendicular to the surface. Adapted from references.^{112,113}

1.2.2 CB[n]-engineered nanostructures

CB[n]s have been widely applied in aqueous supramolecular polymers,¹⁰² polymeric networks¹⁰³ and nanoscience.^{111,114–116} CB[n]-engineered nanostructures can be arbitrarily classified into two categories according to their fundamental interactions: (1) CB[n]s as molecular junctions for metallic NPs, based on electrostatic interactions between the electronegative portals of CB[n]s and the metallic surface; (2) CB[n]-mediated supramolecular decoration and assembly of NPs/interfaces, based on supramolecular host-guest interactions between CB[n]s' cavity and guest molecules.

1.2.2.1 CB[n]s as molecular junctions for metallic NPs

Taking advantage of the strong binding affinity between CB[n]'s portal and metallic surfaces, CB[n]s have been shown to be useful in the synthesis of metallic NPs, mainly as "capping agents".^{52,114,117–120} For example, the Scherman group have reported the formation of dynamic Au NP aggregates using CB[5] in the presence of a reducing agent sodium borohydride, where CB[5] acted as a capping agent.^{52,114} The size of the result-

ant aggregates could be controlled by changing the ratio between CB[5] and the gold precursor, forming aggregates consisting of singly and doubly capped CB[5], as shown in Figure 1.20.¹¹⁴ The use of CB[5], CB[7], and the less water-soluble homologues, CB[6] and CB[8], as capping agents for metastable Au NPs and Ag NPs have also been reported.^{118,119,121}

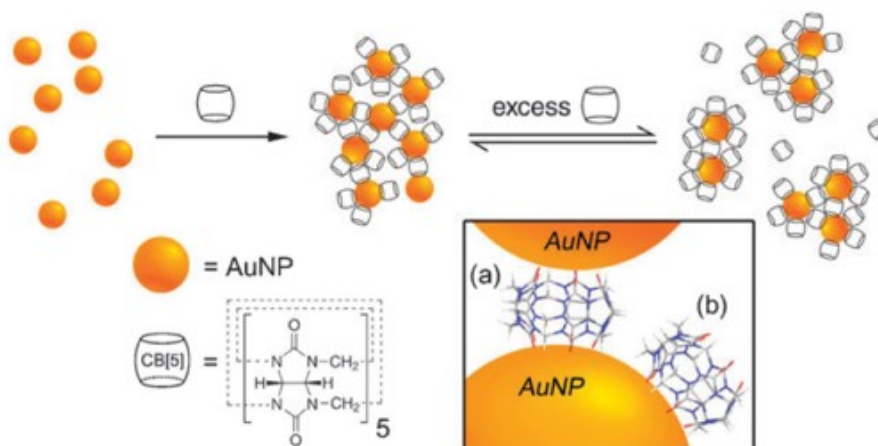


Figure 1.20: Schematic illustration of the formation of Au NP aggregates mediated by CB[5] in solution. Inset showing CB[5] doubly (a) and singly (b) capped by Au NPs. Adapted from reference.¹¹⁴

CB[*n*]s can also mediate the self-assembly of metallic NPs when using sophisticated strategies.^{54,122–124} For example, as shown in Figure 1.21, well-defined growth of one-dimensional (1D) Au NP chains with fixed and rigid CB[*n*] nanojunctions of 0.9 nm was achieved by using a nanoporous polycarbonated membrane. The process was accomplished electrokinetically by controlling the applied voltage, time, temperature, and the NP/CB[*n*] concentration ratio. Nano-assembly through plasmon-induced laser threading of Au NP strings has also been reported, producing conducting threads of 12 ± 2 nm width using CB[7].¹²³ The high field intensities in the gap junctions between NPs drew the surface atoms into the gaps through optical forces, leading to nonthermal melting, thereby forming solid metal threads among the NPs.^{113,123} The highly enhanced fields in the crevices of the threads allow for applications of these metamaterials in photovoltaics and the construction of sensing probes.¹²³ Besides self-assembly of spherical NPs, the end-to-end assembly of Au nanorods mediated by CB[*n*] has also been reported, where

Au nanorods were separated and assembled by CB[5] and CB[7].⁵⁴ Centrifugation of CTAB-coated Au nanorod solutions preferentially destabilised the CTAB bilayer at the curved 111 end facets of the nanorods. Therefore, CB[5] could only interact with the nanorod ends, forming nanorod chain-like morphologies.^{54,113}

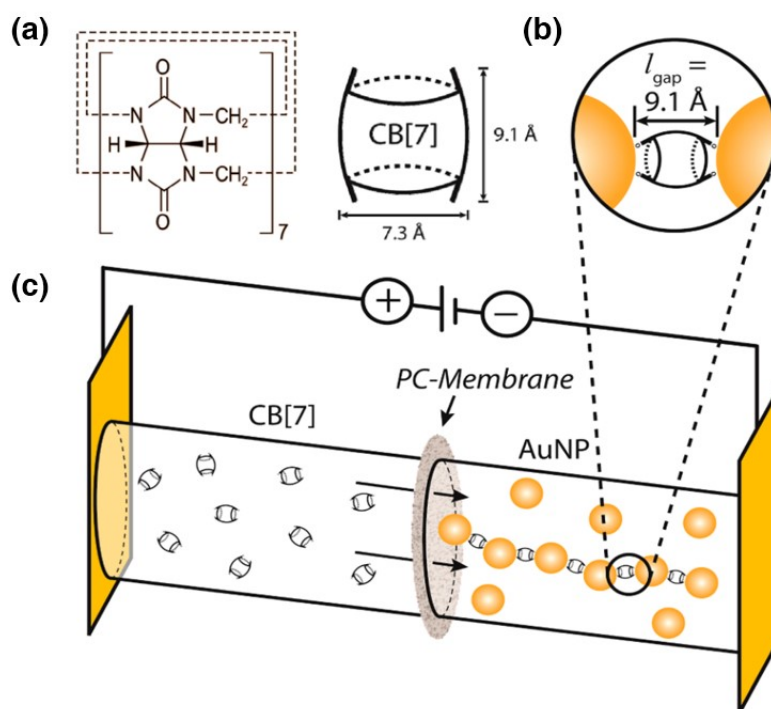


Figure 1.21: Schematic illustration of the formation of 1D Au NP chains using an electrophoresis cell, where a nanoporous polycarbonate membrane separates two compartments containing Au NPs and CB[7], respectively. The application of a small potential difference triggers the formation of chain-type objects in the Au NP compartment. Adapted from reference.¹²²

CB[*n*] molecules on flat metallic surface have also attracted research interests on account of their ability to simply manipulate and separate molecules from detection media.^{112,125,126} One of such work employed a monolayer of CB[7] deposited onto a Au flat surface, complexing with ferrocenemethylammonium (FA), a molecule which can specifically bind to thrombin.¹²⁵ This FA@CB[7] on Au surface platform can be used as an aptasensor chip for the detection of thrombin.¹²⁵

Although it has not been investigated widely, CB[*n*]'s capability to interact with metal oxide NP surfaces (e.g. copper oxide, iron oxide) has also been reported.^{127–130} The Tra-

bolsi group reported the efficient coating of $\gamma\text{-Fe}_2\text{O}_3$ NPs with CB[7] by microwave heating and its application for drug delivery and magnetic resonance imaging.¹²⁸ They later reported nano-catalysts using CB[7] coated $\gamma\text{-Fe}_2\text{O}_3$ NPs further loaded with palladium, as shown in Figure 1.22.¹³⁰ They demonstrated catalysed Suzuki-Miyaura, Sonogashira, and Mizoroki-Keck cross-coupling reactions with uniformly high yields and turnover frequencies.¹³⁰

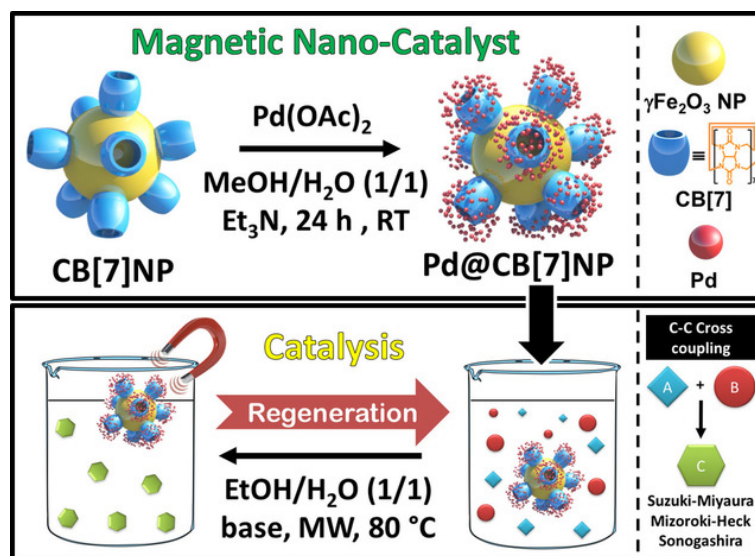


Figure 1.22: Schematic illustration of the loading of Pd^{II} onto CB[7] coated $\gamma\text{-Fe}_2\text{O}_3$ NPs (top) and their catalytic activity studies (bottom). Adapted from reference.¹³⁰

1.2.2.2 CB[n]-mediated supramolecular decoration and assembly of NPs and interfaces

The host-guest interactions of CB[n]s and guest molecules provide a versatile tool for the organisation of molecular systems into functional structures.¹³¹ CB[n]-mediated supramolecular decoration of NP surfaces has been extensively studied.^{111,113,116,131} Generally, the surface of the NPs are first functionalised with a bifunctional guest molecule, which is then complexed with CB[n] and allows further decoration of the NP surface.^{111,116,131} For example, Lan *et al.* reported the preparation of photoresponsive hybrid raspberry-like colloids (HRCs, Figure 1.23), where MV-functionalised polymeric NPs were anchored onto a azo-benzene functionalised silica core by CB[8].¹¹⁶ This assembly could be revers-

ibly disassembled upon light irradiation.¹¹⁶

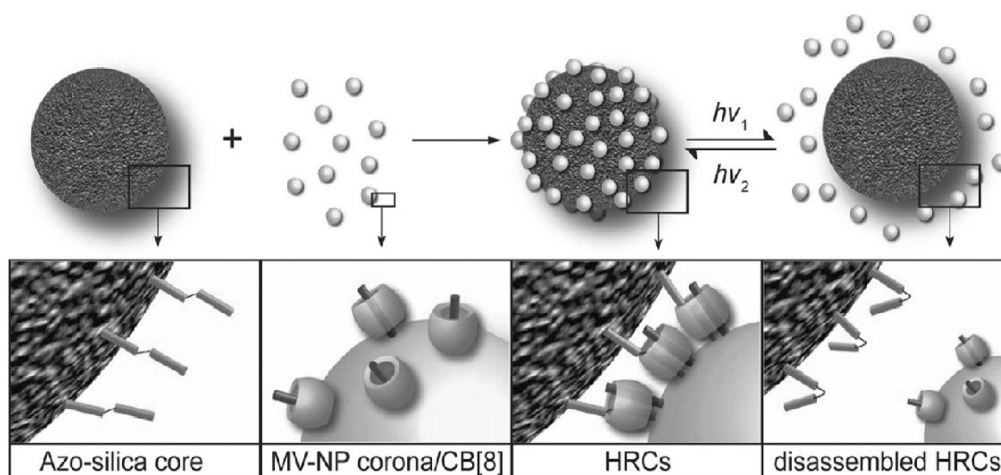


Figure 1.23: HRCs obtained by the formation of (MV/*trans*-Azo)@CB[8] ternary complexes. Adapted from reference.¹¹⁶

End-to-end Au nanorod alignments can also be formed through host-guest interactions.¹³² As illustrated in Figure 1.24, viologen end-functionalised Au nanorods were prepared, which were capable of binding with CB[8], forming 1 : 1 : 1 ternary complexes with synthesised ditopic linker molecules bearing second guest moieties.¹³² Different from the previously discussed native CB[*n*] linkers, this host-guest system allows for various length and rigidity of the nanorod alignments by adjusting the telechelic linker.¹³² In addition, the alignment was reversible. Upon adding a competing guest ADA, the nanorod filaments could be disassembled.¹³² Flat surfaces functionalised with CB[*n*]s through host-guest interactions have also been reported.^{133–135} For example, CB[8] was first complexed with a first guest molecule, bis-aminoethyl viologen, followed by the immobilisation of the inclusion complexes onto the Au surface to form a CB[8]-based rotaxane structure on Au surface.¹³³

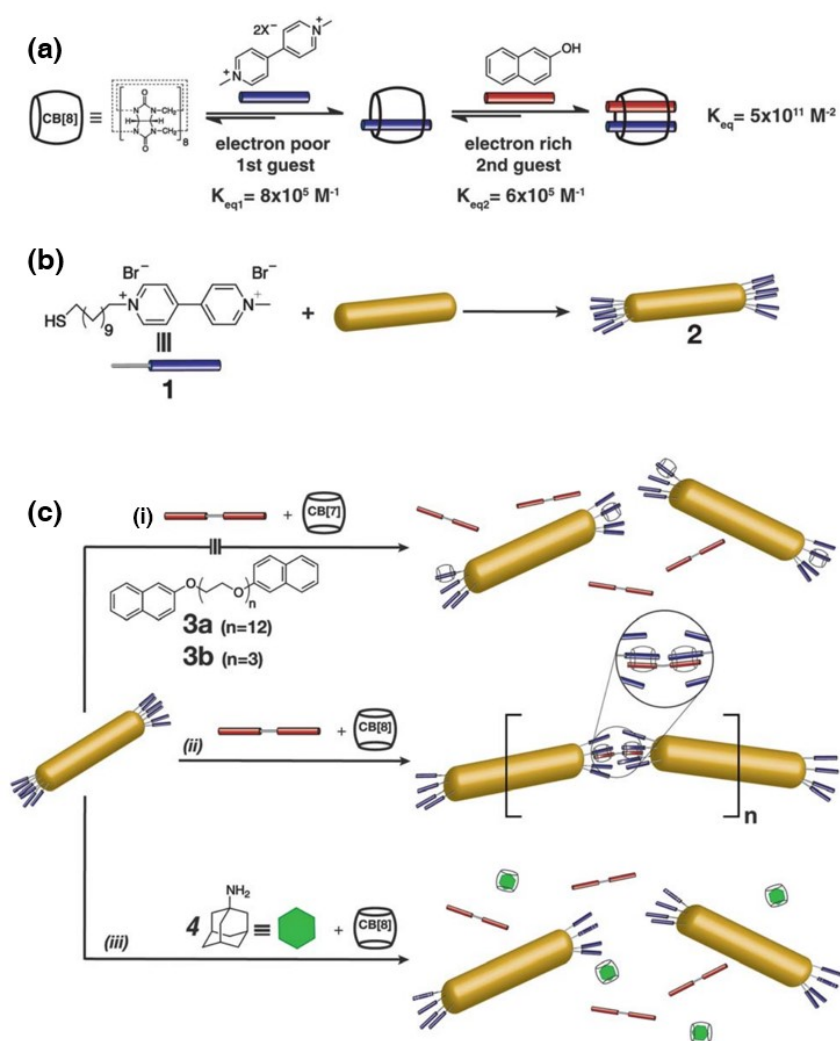


Figure 1.24: (a) Formation of a ternary complex between methyl viologen (MV), 2-naphthol and CB[8]; (b) functionalisation of Au nanorods with MV moieties to produce MV²⁺-Au nanorods; (c) addition of either ditopic naphthol linker (3a or 3b) (i) with CB[7], (ii) with CB[8], or (iii) with CB[8] in the presence of ADA. Adapted from reference.¹³²

1.2.3 CB[n]-engineered nanostructures in SERS sensing applications

In SERS measurements, analytes need to be in close contact with the substrate surface to achieve high sensitivities.¹⁻⁶ Therefore, most of the SERS applications are restricted to molecular analytes with chemical affinity towards the metallic substrates (e.g. thiolated or aminated molecules).^{1,4,5,8,45,46} However, for analytes without a clear metal binding group, exploiting SERS becomes difficult on account of weak signals.¹⁻⁶ CB[n] molecules can bind to metallic NPs *via* their portals, functioning as a rigid spacer between NPs.^{28,51-55} The symmetrical geometry of CB[n] ensures that the NPs are held apart at a precise distance of 0.9 nm, providing significantly high and reproducible local field enhancements in the gap junctions.^{28,51-55,136,137} Meanwhile, CB[n] retains its molecular recognition properties when it binds towards metallic surfaces, thus can bind guests from the bulk solution to the metal-liquid interface by acting as a "receptor".¹¹³

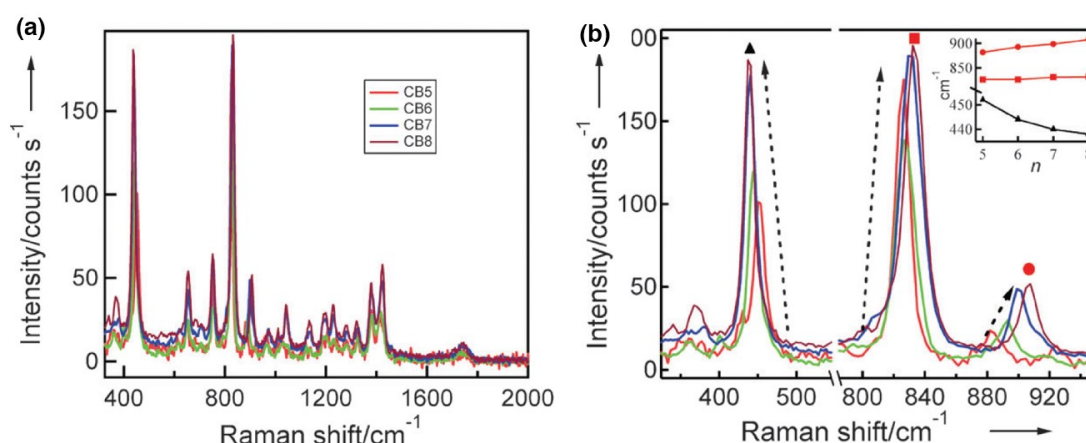


Figure 1.25: (a) Raman spectra of CB[n = 5-8] in the "fingerprint" region. (b) Peaks shift systematically with an increase in n . The variation of the marked peaks is shown in the inset. Adapted from reference.⁵¹

The first detailed study of the Raman and SERS signatures of CB[n] was reported in 2010 (Figure 1.25).⁵¹ Clearly identifiable peaks of CB[n] were observed for both the Raman spectra and SERS spectra (utilizing both the nanostructured surface and CB[n]-aggregated NP substrates), showing the same signals and a similar trend. The two intense characteristic peaks at approximately 450 and 830 cm⁻¹ were assigned to the ring scissor and ring deformation modes of the CB[n] molecules. These two peaks showed

slight upfield and downfield shifts respectively, with the increase of the ring size (n) in different CB[n] homologues.

CB[n]-engineered nanostructures applied for SERS sensing are generally carried out using CB[n]-aggregated NPs^{46,52,53,138–140} and the "nanoparticle on mirror geometry" (NPoM).^{28,141} The SERS sensing of a dye molecule Rhodamine 6G exploiting the CB[5]-aggregated Au NPs was first demonstrated by the Scherman group in 2011.⁵² It was concluded that the surface modification of Au NPs by CB[5] produces partially controllable and highly consistent fractal coagulates, following the well-known reaction kinetics as a function of CB[5] concentration.⁵² Importantly, the aggregates maintain interparticle distance, which is defined by the height of CB[5] (0.9 nm), regardless of the concentration of CB[5].⁵² This allows for the consistent formation of distinct plasmon resonances, producing strong and reproducible SERS signals.⁵² Besides acting as a "glue" to create plasmonic junctions, CB[n] can also position the guest analytes (Rhodamine 6G) precisely in the hot-spots, enabling ultrasensitive detection. The authors later reported a SERS-nanoreactor concept exploiting CB[n]-aggregated Au NPs.¹³⁸ As illustrated in Figure 1.26, CB[n]s functioned simultaneously as nanoscale reaction vessels, sequestering and templating a photoreaction within, and also as "glues" to bridge Au NPs with subnanometre distances for enhanced electromagnetic fields.¹³⁸ Selective photoisomerism or photodimerisation could be monitored *in situ* within the Au NP-CB[n] nanogap by choosing the appropriate CB[n] nanoreactor.¹³⁸ The CB[n]-aggregated metal NPs have demonstrated efficient and quantitative detection of analytes at clinical levels and hence holds great promise for use in medical applications and drug screening.^{46,53,139,140}

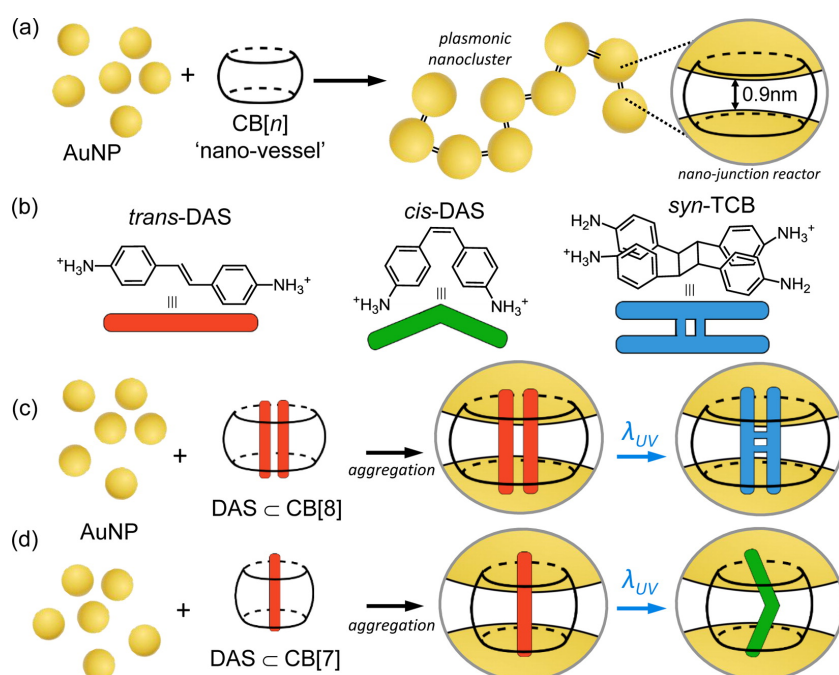


Figure 1.26: (a) Au NPs self-assemble into dendritic nanoclusters with the sub-nm $CB[n]$ linker; (b) upon UV irradiation in solution, *trans*-DAS predominantly undergoes photoisomerisation into *cis*-DAS, and into *syn*-TCB with photodimerisation in a minor pathway; (c) when complexed within $CB[8]$, the photoreaction of DAS is templated to yield almost exclusively *syn*-TCB, which can be measured *in situ* by SERS; (d) when complexed within $CB[7]$, the photoreaction of DAS is templated to produce *cis*-DAS. Adapted from reference.¹³⁸

Another widely investigated $CB[n]$ -engineered nanostructure is the NPoM system, where a metal NP is placed above a flat metal surface by a single layer of molecules.¹⁴¹ The resulting plasmonic gap of only a few nanometres contributes to a strong field confinement.^{142–144} Since the metal NP induces image charges within the metal surface, plasmonic coupling similar to a NP dimer is created.^{141–144} This self-assembled system thus provides a robust and reproducible SERS sensing platform with ultrahigh sensitivities. $CB[n]$ adsorbs spontaneously on Au surfaces with the perpendicular orientation.¹¹² Therefore, an NPoM system using $CB[n]$ as the single molecular layer to separate the Au NP and Au surface with a fixed gap distance of 0.9 nm can be readily obtained.¹⁴¹ In addition, guest molecules complexed within $CB[n]$ can be detected with high sensitivities since they are sequestered in the highest field enhancement region.¹⁴¹ Figure 1.27 shows an example of NPoM system exploiting $CB[7]$ as the spacer and detecting guest

molecules on a few-to-single-molecule level.¹⁴¹ CB[n]-based NPoM system has further been exploited to catalyse chemical reactions or induce redox processes in molecules located within the plasmonic hot-spots.¹⁴⁵ The hot-electron-induced chemical reduction processes in various aromatic molecules can be tracked *in situ* by SERS.¹⁴⁵

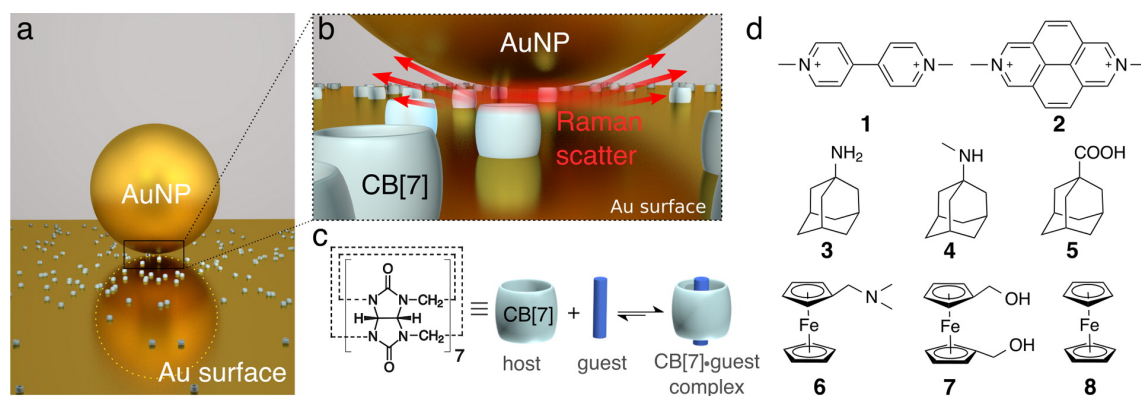


Figure 1.27: (a) Nanoparticle on mirror (NPoM) assembly, where the Au NP is spaced from a Au surface by CB[7]; (b) the plasmonically enhanced field in NPoM is confined to only a few nm³; (c) complexation between CB[7] and a guest molecule; (d) guest molecules investigated. Adapted from reference.¹⁴¹

1.3 Objectives

Cucurbit[n]urils (CB[n]s) are able to self-assemble sodium citrate-capped metallic NPs into chains or fractal-like aggregates, forming a powerful SERS substrate to detect a wide variety of molecules with low chemical affinity towards the metallic surface.^{28,51–56} However, when left uninhibited, CB[n] will continue to aggregate the metallic structures, leading to the colloidal instability of the system.^{28,51–55,122,140} In addition, *in situ* measurements may involve environments that affect such self-assembly processes. For example, the possible displacement of analytes in the nanogap by non-analyte moieties may give rise to fluctuating backgrounds.^{53,55,140} Therefore, there is great demand to design SERS substrates which can provide the same levels of detection and functionality but eliminate the need for aggregation. The objective of this thesis is to investigate CB[n]-engineered nanostructures for molecular sensing avoiding the aggregation of metallic NPs, thereby improving the colloidal stability of the SERS substrate, meanwhile increasing high SERS

enhancement factor and detection sensitivities.

Chapter 2 investigates the preparation of surface-bound CB[8] catenanes on magnetic silica nanoparticles, where CB[8] is tethered by a first guest molecule axle (disilane functionalised methyl viologen) onto the surface of a magnetic silica nanoparticle. This CB[8] catenane system exhibits specific molecular recognition towards certain aromatic molecules, providing an efficient and recyclable nanoplatform for peptide separation.

Chapter 3 describes the follow-up work to these CB[8] catenanes on silica nanoparticles: the preparation of CB[8] catenanes on spiky γ -Fe₂O₃@Au NPs as a powerful SERS substrate is investigated. Instead of using CB[8] to aggregate metal NPs, CB[8] is mechanically locked onto the spiky NP surface by a dithiol functionalised methyl viologen molecule. This catenane nanostructure exhibits excellent colloidal stability and the spiky shape gives rise to a high SERS enhancement (enhancement factor of 2.3×10^8), allowing SERS detection of target analytes with high sensitivities.

In the fourth chapter, a new type of CB[n]/Au NP SERS nanoplatform is investigated, exploiting a stable nanoraspberry NPs with CB[n]s densely immobilised on the NP surface *via* their portals. On account of the high curvature of the nanoraspberry surface and good colloidal stability, this nanoraspberry NPs can act as a free-standing SERS substrate with enhancement factor on the order of 10^{10} . By functionalising the nanoraspberry using CB[n]s in the perpendicular orientation, a wide variety of molecules could be detected with high sensitivities.

In the fifth chapter, a facile fabrication method of CB[7]-based microreactors is described, where metallic nanoparticles are immobilised in microchannels *via* supramolecular inclusion complexes methyl viologen-silane@CB[7]. This microreactor exhibits remarkable catalytic activity on account of the substantially high surface area-to-volume ratio of the microchannels and metallic nanoparticles. This type of construct is also applicable as a CB[n]-based microchannel-sensor, promising to detect analytes of extremely low concentrations on account of the accumulation effect of microchannels.

Finally, a concluding chapter summarises the work presented in this thesis, whilst also giving some perspectives on the future of the work.

Chapter 2

Cucurbit[8]uril Catenanes on Silica Nanoparticles Exhibiting Molecular Recognition

We demonstrate the preparation of surface-bound cucurbit[8]uril (CB[8]) catenanes on silica nanoparticles (NPs), where CB[8] is employed as a tethered supramolecular "handcuff" to selectively capture target guest molecules. CB[8] is threaded onto a methyl viologen (MV^{2+}) axle and immobilised onto silica NPs with a surface density of 0.56 nm^{-2} . This CB[8] catenane system exhibits specific molecular recognition towards certain aromatic molecules such as perylene bis(diimide), naphthol and aromatic amino acids, therefore, can act as a nanoscale molecular receptor for target guests. Furthermore, its use as an efficient and recyclable nanoplatform for peptide separation has also been demonstrated. By embedding magnetic NPs inside silica NPs, separation could be achieved by simply applying an external magnetic field. Moreover, the peptides captured by the catenanes could be released by reversible single-electron reduction of MV^{2+} . The entire process demonstrates high recoverability.

This work has been published in the following peer-reviewed journal articles:

- Ren, X.[‡]; Wu, Y.[‡]; Clarke, D. E.; Liu, J.; Wu G.; Scherman, O. A.*; "Surface-bound cucurbit[8]uril catenanes on magnetic nanoparticles exhibiting molecular recognition", *Chem. Asian J.*, 2016, 11, 2382.

[‡]These authors contributed equally to this work

2.1 Introduction

A catenane (Figure 2.1) is a mechanically-interlocked molecular architecture consisting of two or more interlocked macrocycles, which cannot be separated without breaking their covalent bonds.^{146,147} Catenanes have attracted great attention in the past few decades on account of their special mechanically-interlocked structure.^{146,147} The relative positions of their components can be controllably changed without breaking the interlocked structure, allowing catenanes to be readily used as molecular machines,^{148,149} switches,^{150–152} sensors^{153,154} and rotors.^{148,155}

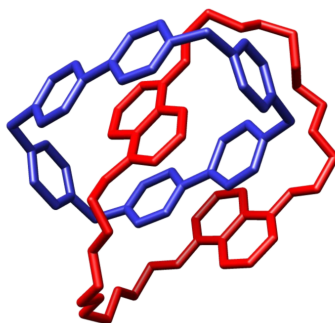


Figure 2.1: An illustration of catenane structure: crystal structure of a catenane with a cyclobis(paraquat-*p*-phenylene) macrocycle. Adapted from reference.¹⁵⁶

Macrocyclic host molecules such as crown ethers and cyclodextrins (CDs) are of interest in the preparation of catenanes, on account of their intrinsic cyclic structure and host-guest complexation capability.^{133,146,147} Catenanes based on crown ethers were extensively investigated, mainly prepared by template-directed synthesis.^{146,157} CD was also studied in the preparation of catenanes on account of its improved binding behaviour.^{147,158–161} However, crown ether and CD host complexation are both limited to relatively low affinity towards certain guest molecules ($K_a \leq 10^5 \text{ M}^{-1}$).^{92,162} Cucurbit[*n*]urils (CB[*n*]s), a family of symmetric barrel-shaped host molecules, which exhibit stronger and selective encapsulation of small guest molecules, emerged as more promising hosts for supramolecular applications (K_a up to 10^{15} M^{-1}).^{77,92,116,163–165} Cucurbit[8]uril (CB[8]), a larger member of the CB family possessing a larger cavity volume of 479 \AA^3 , can simultaneously encapsulate two guest molecules to form a dynamic yet stable heterotern-

ary complex.^{77,87,103} Owing to its excellent host-guest properties, CB[8] has been utilized as a versatile receptor and building block for various supramolecular architectures and systems.^{92,116,133,163–165} Catenanes containing CB[*n*] were explored by Kim^{166,167} and others,¹⁶⁸ but research has mainly focused on CB[6]-based catenanes. Few investigations have been conducted on CB[8]-based catenanes despite its unique host-guest properties to simultaneously bind two guests in its cavity.^{133,169}

Catenanes have been mainly studied in solution, however, to fully develop their potential practical applications, they must be interfaced with the macroscopic world.^{147,170} In recent years, effort has been made to attach catenanes on solid surfaces such as gold and glass to achieve this objective.^{150,171,172} Previously, the preparation of CB[8]-based interlocked structures immobilised on gold surfaces have been reported.¹³³ Little attention, however, has been paid to the attachment of catenanes on nanoparticles (NPs)^{151,160} in spite of their superb properties of large surface area and highly tunable physical and chemical characteristics.^{147,173}

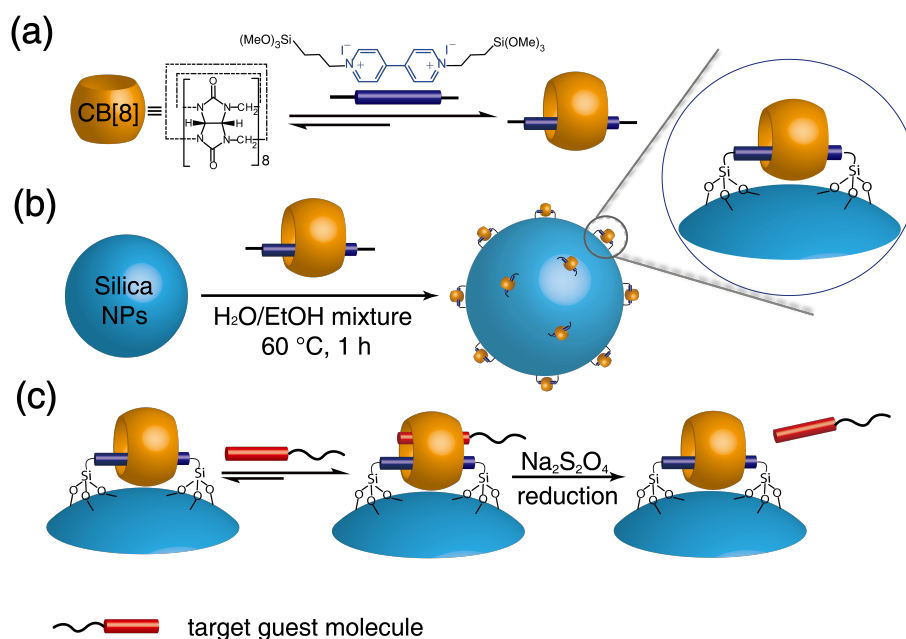


Figure 2.2: (a) Complexation between CB[8] and a first guest molecule MV-disilane; (b) surface-bound CB[8] catenanes on silica NPs (CBC-NPs) obtained by immobilising MV-disilane@CB[8] inclusion complexes onto silica NPs; (c) capture and release of a target guest by CBC-NPs.

Herein, for the first time, we demonstrate the preparation of surface-bound CB[8]

catenanes on silica NPs (CBC-NPs), where CB[8] is employed as a supramolecular “hand-cuff” to selectively capture target guests, as shown in Figure 2.2. This CB[8] catenane system can act as a nanoscale molecular receptor for target guests on account of the specific molecular recognition of the $MV^{2+}@CB[8]$ inclusion complex on silica NPs towards various second guest molecules, including perylene bis(diimide), naphthol and aromatic amino acids, such as tryptophan,^{110,174,175} phenylalanine^{110,176} and tyrosine,¹¹⁰ with the K_a of $10^3 - 10^5 \text{ M}^{-1}$.¹¹⁰ As a result, this supramolecular system can also act as a highly effective and recyclable nanoplatform for the separation and purification of peptides. The silica NPs can be endowed with magnetism by incorporating superparamagnetic iron oxide NPs into their cores, providing an easy and straightforward magnetic separation method.

2.2 Results and Discussion

2.2.1 Synthesis and complexation study of MV-disilane guest molecule

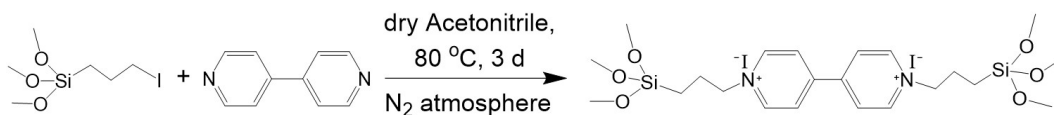


Figure 2.3: Reaction scheme of the synthesis of 1,1'-bis[3-(trimethoxysilyl)propyl]-4,4'-bipyridine (MV-disilane).

1,1'-bis[3-(trimethoxysilyl)propyl]-4,4'-bipyridine (MV-disilane) was synthesised by the reaction between (3-iodopropyl)trimethoxysilane and 4, 4'-bipyridine, as shown in Figure 2.3. The complexation of the MV-disilane guest molecule and CB[8] was investigated by ¹H NMR and isothermal titration calorimetry (ITC). Figure 2.4 shows the ¹H NMR spectra of MV-disilane alone (b) and its complexation with CB[8] (a), where CB[8] peaks at 4.2, 5.5 and 5.8 ppm can be observed. In addition, a shift of the MV^{2+} proton peaks from 9.17 and 8.63 ppm to 8.83 and 7.59 ppm, respectively, is also observed. These results indicate the complexation of the MV-disilane guest molecule with CB[8].

To further confirm the complexation, ITC was carried out and the result is shown in Figure 2.5. The measurements were repeated three times and the results indicate good

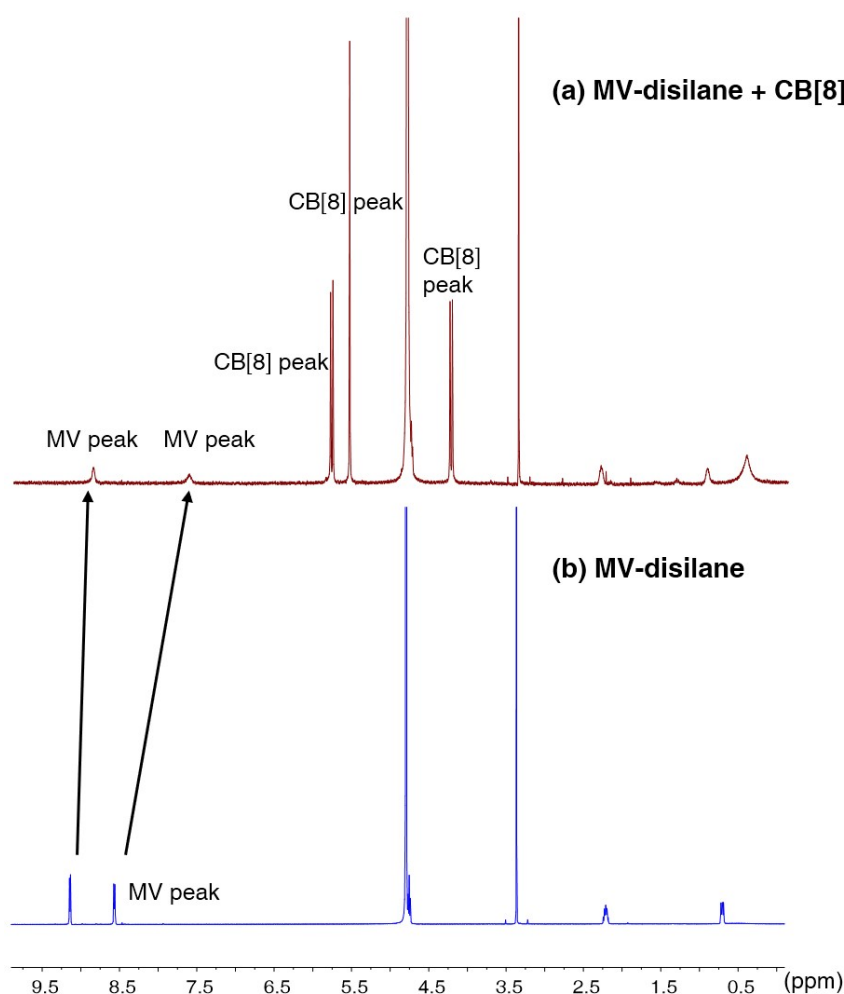


Figure 2.4: ¹H NMR spectra of (a) MV-disilane@CB[8] complex; (b) MV-disilane.

reproducibility, suggesting 1:1 complexation of MV-disilane and CB[8]. The average association constant K_a is $3.25 \times 10^5 \text{ M}^{-1}$. The high association constant of the MV-disilane and CB[8] confirms strong complexation. It lays the foundation for the post-functionalisation of MV-disilane@CB[8] complexes onto silica nanoparticles.

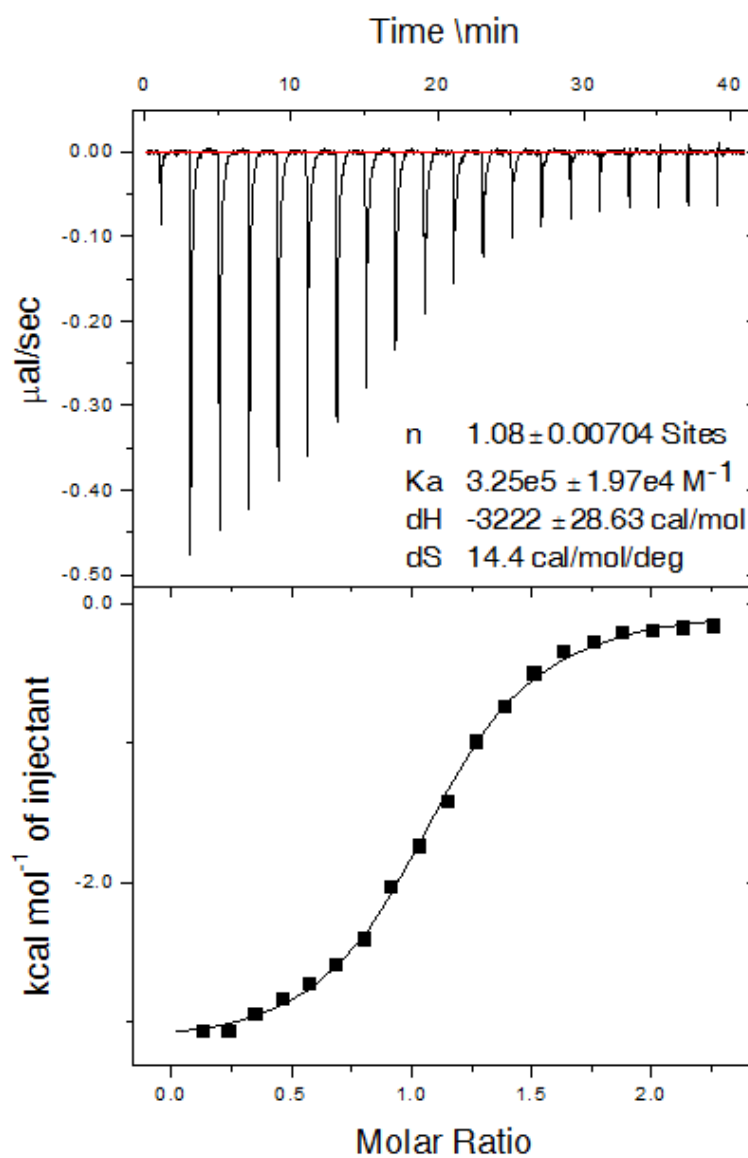


Figure 2.5: ITC results of the complexation between MV-disilane and CB[8]. 1 mM MV-disilane was injected into 0.05 mM CB[8] in buffer solution at 25 °C. 50 mM sodium acetate buffer, pH=4.6, was used.

2.2.2 Preparation of surface-bound CB[8] catenanes on silica NPs

The surface-bound CB[8] catenanes on silica NPs (hereafter referred to as “CBC-NPs”) were prepared by immobilising MV-disilane@CB[8] inclusion complexes onto silica NPs. The reaction was conducted in a mixture of water and ethanol (3:2 *v/v*) at 60 °C for 1 h. In the meantime, control NPs were prepared using the same reaction conditions, in absence of CB[8].

The average hydrodynamic diameter (D_h) and zeta potential of the silica NPs, CBC-NPs and control NPs obtained from dynamic light scattering (DLS) are listed in Table 2.1 and Figure 2.6a. The average diameter of the CBC-NPs increases to 337 nm compared to the bare silica NPs, which is 286 nm. The moderate rise of the diameter indicates that crosslinks between the silica NPs by MV-disilane molecules do not exist, which would happen if the end groups of the MV-disilane molecule reacted with two different silica NPs. Zeta potential is the potential difference between the dispersion medium and the stationary fluid layer stucked to the dispersed particles.¹⁷⁷ The negative zeta potential of silica NPs is attributed to the hydroxyl groups on the surface of the NPs. The zeta potential of the CBC-NPs turns to be positive, 35.5 mV, which suggests that the positively charged MV-disilane molecules have been functionalised onto the silica NPs. In comparison, the control NPs show similar size and zeta potential with CBC-NPs. TEM images (Figure 2.6b-d) show that all the NPs have homogeneous sizes and can be well dispersed in water.

Table 2.1: DLS data of the bare silica NPs, CBC-NPs and control NPs.

	Average diameter (nm)	PDI	zeta Potential (mV)
Silica NPs	286	0.07	-44.2
CBC-NPs	337	0.24	35.5
Control NPs	343	0.22	37.5

Note: The positive zeta potential of CBC-NPs suggests that the positively charged MV-disilane molecules have been successfully functionalised onto the silica NPs.

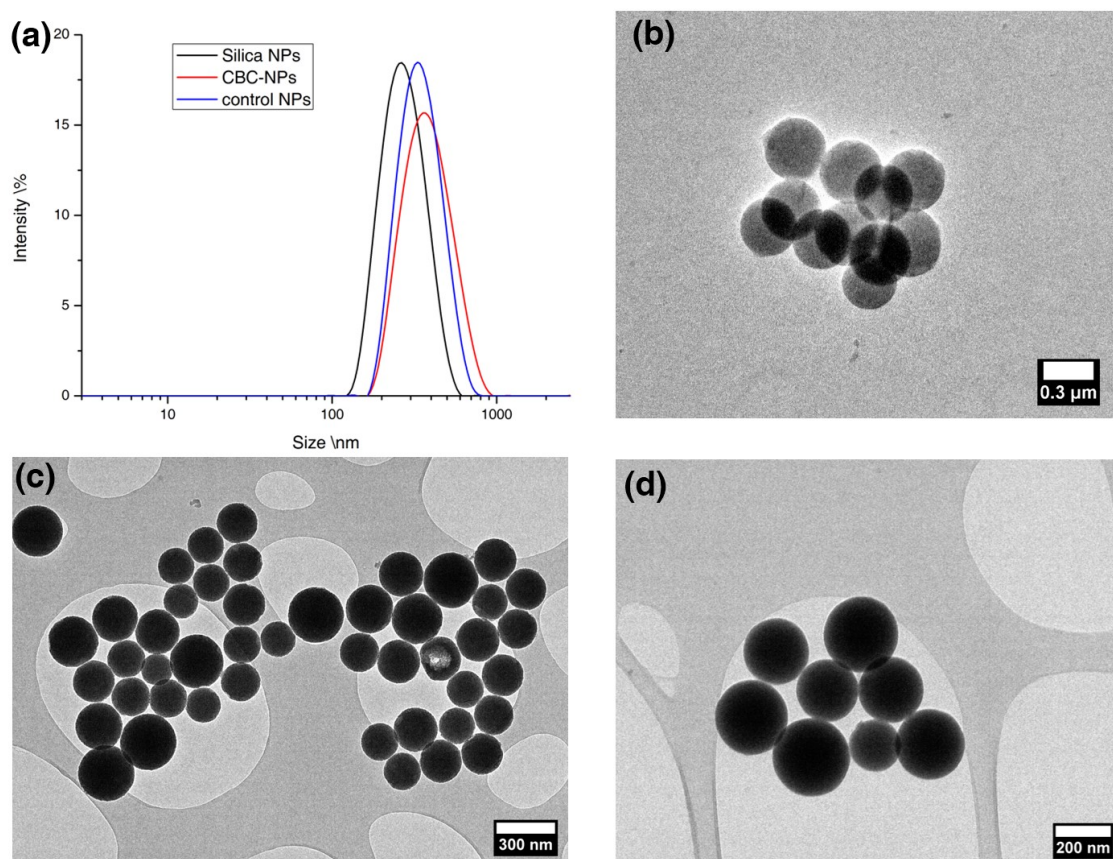


Figure 2.6: (a) Hydrodynamic diameter distribution of silica NPs, CBC-NPs and control NPs in water. TEM images of the silica NPs (b), CBC-NPs (c) and control NPs (d).

2.2.3 UV-vis titration study

To confirm the formation of catenanes on silica NPs and quantify the amount of CB[8] incorporated into the CBC-NPs, UV-vis titration of substituted perylene bis(diimide) (PDi) was conducted. PDi was employed on account of its good binding affinity towards the $MV^{2+}@CB[8]$ complex.^{178,179} A UV-vis calibration of PDi/CB[8] solution is shown in Figure 2.7. The absorption of a PDi/CB[8] solution was measured because sole PDi molecules tend to form π - π stacks in water, which would cause a decline in the UV-vis absorption. Upon addition of excess CB[8], PDi stacks disassemble and form strong host-guest inclusion complexes with CB[8], giving the maximum absorption.

The basic idea of the UV-vis titration is briefly illustrated in Figure 2.8a. The addition

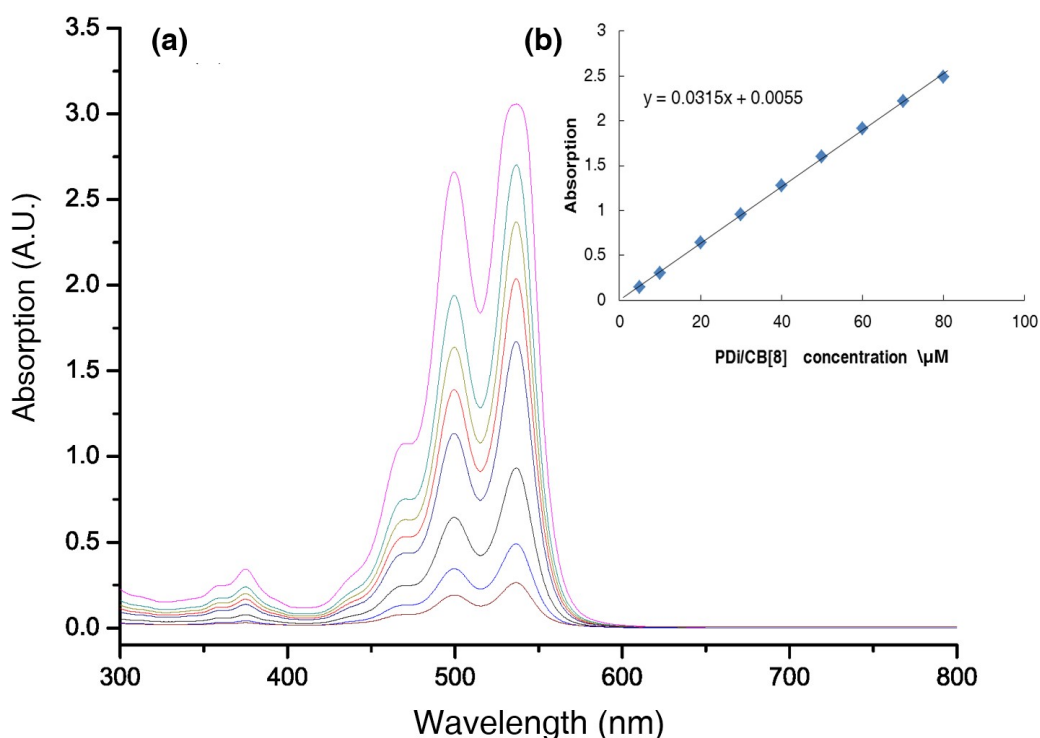


Figure 2.7: UV-vis calibration plot of PDi/CB[8] solution. (a) UV-vis absorption spectra; (b) calibration line.

of CBC-NPs into PDi solution induced the formation of CB[8]/PDi/MV-disilane ternary complexes on the silica NPs, leaving the uncomplexed PDi molecules in the solution, which were then separated and quantified. The same procedure was repeated for the control NPs, whereas no PDi molecule was complexed. As shown in Figure 2.8b, the absorption of PDi solution showed little change after mixing with the control NPs. In comparison, its absorption decreased linearly with an increasing amount of CBC-NPs added, from 0.165 to 0.074, which confirms the formation of the catenane structures on the silica NPs. The mass fraction of CB[8] was calculated to be $11.65 \mu\text{g}/\text{mg}$ and the density of CB[8] on the silica NPs surface was 0.56 nm^{-2} (more details are shown in the Experimental Appendix).

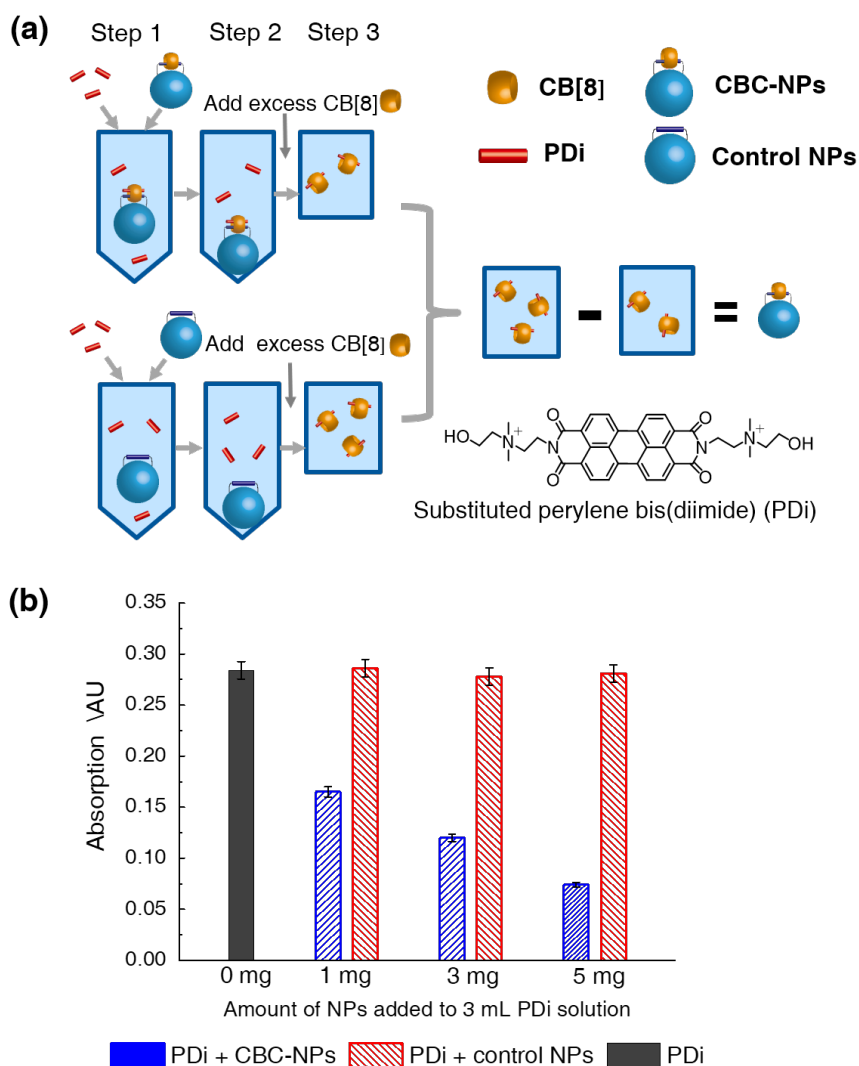


Figure 2.8: (a) Schematic illustration of the UV-vis titration experiment between PDI and CBC-NPs. The addition of CBC-NPs into PDI solution induced the formation of CB[8]/PDI/MV-disilane ternary complexes on the silica NPs. After centrifuging and removing the sediments, the uncoordinated PDI molecules were left in the solution and quantified. Upon addition of excess CB[8], PDI stacks disassembled and formed complexes with CB[8], giving the maximum absorption. The same procedure was repeated for the control NPs, whereas no PDI molecule was bound. (b) PDI UV-vis absorption (501 nm) after mixing with different NPs with various mass. 0, 1, 3, 5 mg NPs solid were added to 3 mL 16 μ M PDI solutions. The absorption decreased linearly with the amount of CBC-NPs added, whereas remained unchanged after mixing with control NPs.

2.2.4 Lithography characterisation

Lithography was further examined to confirm the formation of CB[8] catenane structures on the NP surface. The principle of lithography is shown in Figure 2.9a, where microscale patterns of a second guest molecule (naphthol-silane) were prepared on a glass surface. The silane groups in naphthol-silane molecules bind covalently to the glass surface and the naphthol groups could bind with MV-disilane@CB[8] complex. The patterned surfaces were immersed in aqueous suspensions of fluorescent rhodamine B (RhB)-labelled CBC-NPs and control NPs, respectively. After extensive washing, patterned surfaces were observed under a fluorescence microscope. As shown in Figures 2.9b and c, the fluorescent CBC-NPs aligned in a patterned manner on account of the complexation between the CB[8] catenane on the CBC-NP surface and naphthol-silane on the glass substrate. In comparison, the fluorescent control NPs could not be observed as they were all washed away (Figure 2.9d).

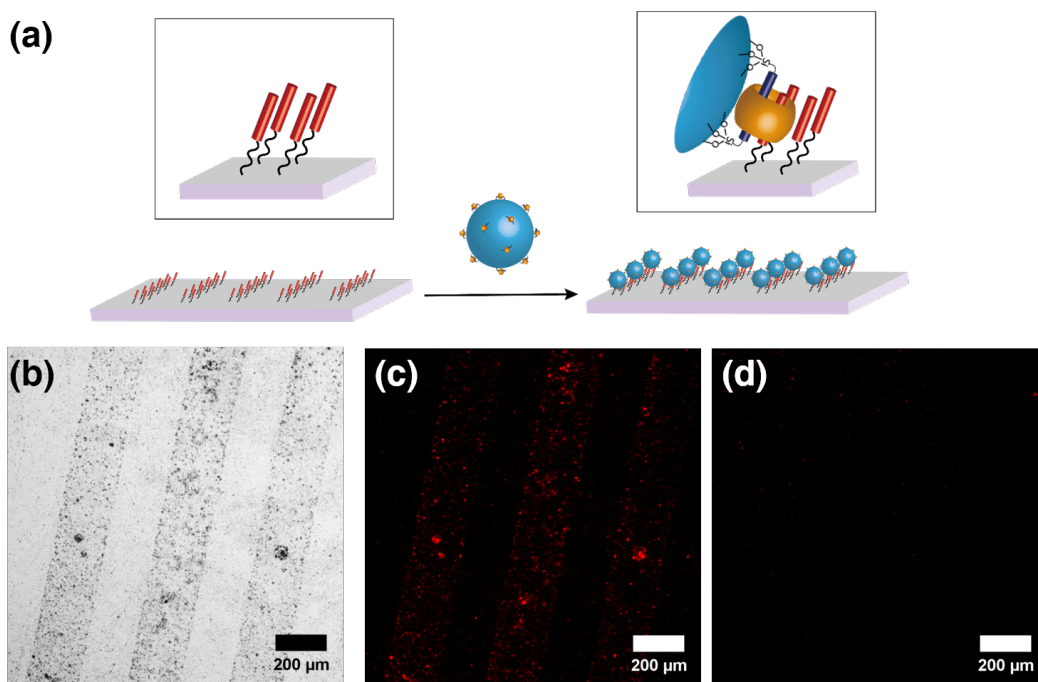


Figure 2.9: (a) Schematic illustration of the lithography characterisation of CBC-NPs. Fluorescence microscope images of RhB-labelled CBC-NPs on the patterned glass, (b) bright field, (c) dark field. In the control experiment (d) using RhB-labelled control NPs, patterned structure can be barely observed as they were all washed away.

2.2.5 Preparation of CB[8] catenanes on magnetic silica nanoparticles

To endow magnetic responsiveness to the CBC-NPs so that it can be easily separated and recycled, the silica core of CBC-NPs was incorporated with superparamagnetic iron oxide NPs. The magnetic silica NPs (MNPs) were prepared by the reaction of iron oxide NP ferrofluids and tetraethyl orthosilicate in a 2-propanol/water mixture. Surface-bound CB[8] catenanes on magnetic silica NPs (CBC-MNPs) were prepared by a similar method as CBC-NPs. The TEM images clearly show the incorporation of iron oxide NPs into the silica NPs (Figure 2.10a and b). The CBC-MNPs exhibit strong magnetic responsiveness. As shown in Figure 2.10c, the cloudy solution turned clear within 20 min with almost all CBC-MNPs attracted and accumulated in the corner by a magnet.

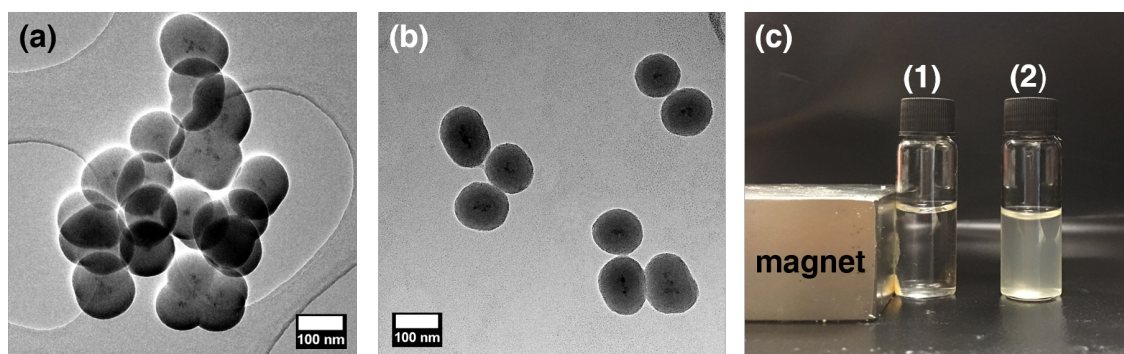


Figure 2.10: TEM images of magnetic silica NPs (MNPs, a) and CB[8] catenanes on magnetic silica NPs (CBC-MNPs, b); (c) picture of CBC-MNPs suspensions before (2) and after (1) separation by a magnet. After separating by a magnet for 20 min, the cloudy suspension of CBC-MNPs turned clear, with most of CBC-MNPs attracted and settled by the magnet.

2.2.6 Peptide separation using CBC-MNPs

The molecular recognition capability of the $MV^{2+}@CB[8]$ inclusion complexes within the CB[8] catenane system makes it promising to act as a nanoscale molecular receptor for various target guest molecules. Also, as $MV^{2+}@CB[8]$ inclusion complexes exhibit strong binding towards some aromatic amino acids such as tryptophan (Trp),^{110,174,175} phenylalanine (Phe)^{110,176} and tyrosine,¹¹⁰ the selective capture and separation of target peptides containing such residues from peptide mixtures with our CB[8] catenane sys-

tem was investigated. The schematic illustration of the peptide separation and recycling cycle is shown in Figure 2.11.

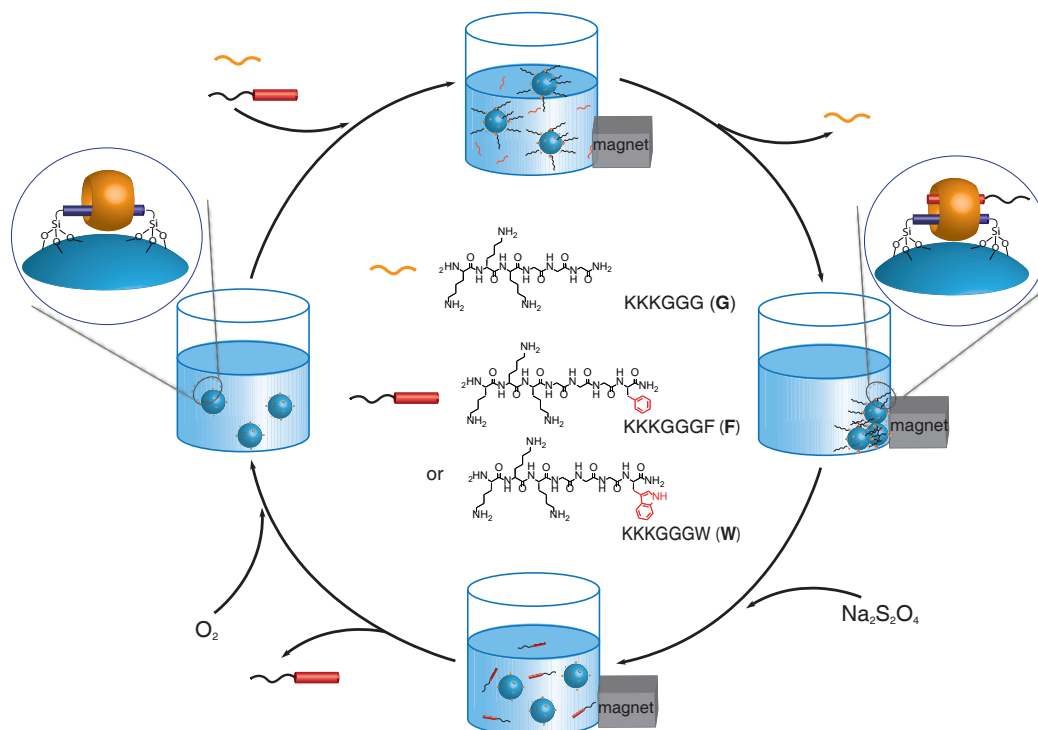


Figure 2.11: Schematic illustration of the peptide separation using CBC-MNPs and molecular structures of peptides **G**, **F** and **W**. After the addition of CBC-MNPs into a peptide mixture, peptides with recognisable residues such as Phe and Trp (i.e. **F** and **W**) would complex with CBC-MNPs and sediment upon an external magnetic field. Peptides without recognisable residues such as **G**, would remain in the solution and be separated. The complexed peptides **F** and **W** can be released upon one-electron reduction of MV^{2+} using $Na_2S_2O_4$ and CBC-MNPs can be reused after the oxidation of $MV^{\cdot+}$.

To investigate the efficiency of peptide separation using CBC-MNPs, model peptide sequences **KKKGGGF** (**F**), **KKKGGGW** (**W**) and **KKKGGG** (**G**) (molecular structures are shown in Figure 2.11) were synthesised and explored, as illustrated in Figure 2.11. Peptide **F** and **W** contain Phe and Trp residues, respectively, and can be recognised by CBC-MNPs. Peptide **G** was prepared as a control peptide. The UV absorptions of peptide solutions before and after mixing with CBC-MNPs were measured by high-performance liquid chromatography (HPLC). After mixing with CBC-MNPs, the absorption of **F** and **W** solutions at both 20 and 40 μM decreased significantly, while remaining unchanged

for **G** solutions, indicating efficient peptide separation by CBC-MNPs (Table 2.2 and Figure 2.12). The concentration decreased 60% and 30% for 20 and 40 μM solutions, respectively, as calculated. The decrease of concentration for both solutions of **F** and **W** at both 20 and 40 μM were similar, around 12 μM as calculated, which indicates good reproducibility (Table 2.2). The peptide separation efficiency, which is the absorption of peptides per gram CBC-MNPs, was estimated to be 12.5 and 12.2 $\mu\text{mol/g}$ for **F** and **W**, respectively. In addition, the peptides complexed with $\text{MV}^{2+}@\text{CB}[8]$ on CBC-MNPs can be easily released upon one-electron reduction of MV^{2+} to its radical cation ($\text{MV}^{\cdot+}$) by sodium dithionite ($\text{Na}_2\text{S}_2\text{O}_4$) under nitrogen,¹³³ exhibiting high release efficiency (up to 11.6 $\mu\text{g/mol}$). Moreover, CBC-MNPs can be recovered by the oxidation of $\text{MV}^{\cdot+}$ to MV^{2+} , simply by purging the solution with oxygen for 1 min. A subsequent separation cycle showed almost no loss in the separation efficiency, up to 11.1 $\mu\text{mol/g}$, suggesting good recoverability (Table 2.2 and Figure 2.12).

Table 2.2: Peptide separation using CBC-MNPs and recovery of CBC-MNPs

	c(pep) [μM]	Δc with CBC- MNPs [μM]	c (released pep) [μM]	Δc with recovered CBC-MNPs [μM]	separation efficiency [$\mu\text{mol/g}$]
F	20	12.6	11.3	8.7	12.5 ± 0.1
	40	12.4	11.6	8.8	
W	20	12.3	9.7	10.2	12.2 ± 0.2
	40	12.0	9.9	11.1	

note: c stands for concentration of peptides, Δc stands for change of peptide concentration .

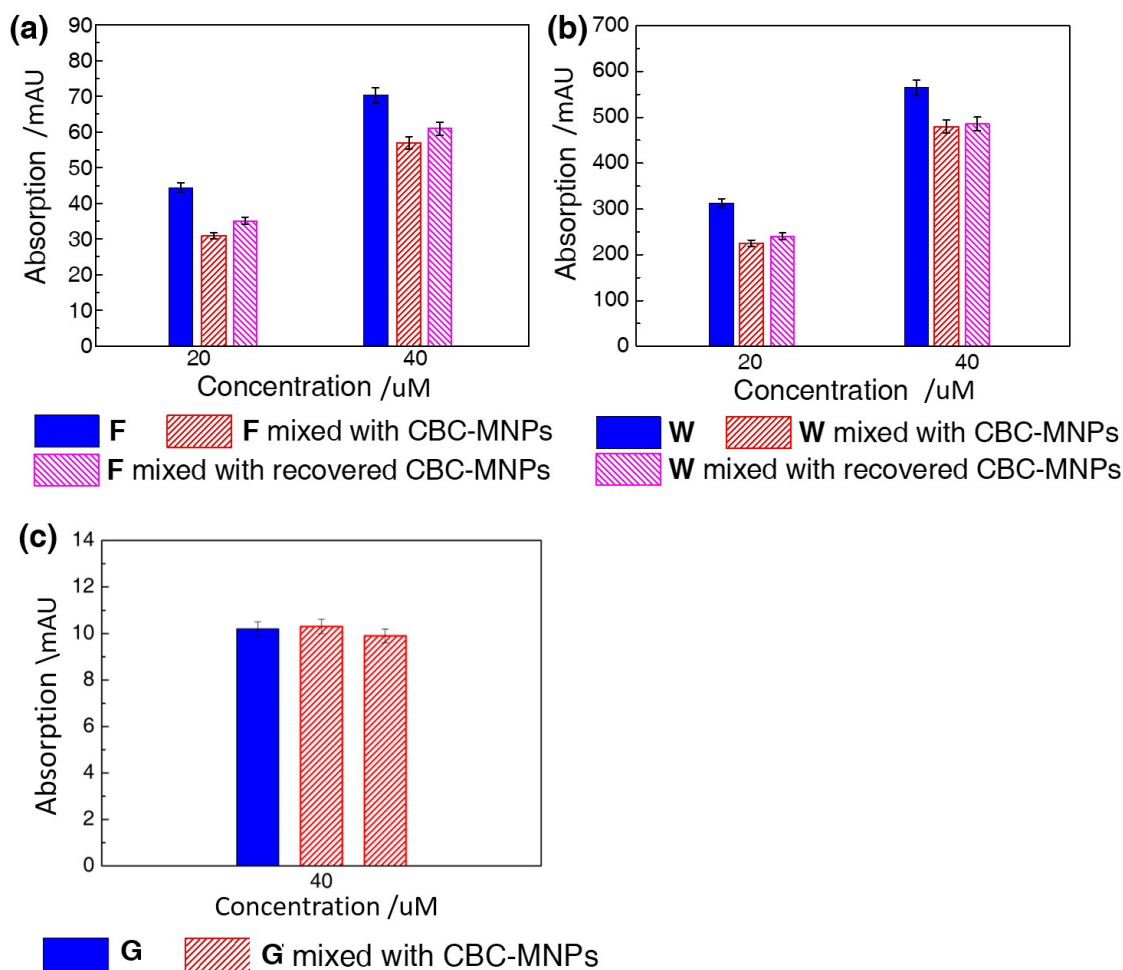


Figure 2.12: HPLC UV absorption of solutions of (a) **F** and (b) **W** at 20 μM and 40 μM before and after mixing with CBC-MNPs. 1.5 mL peptide solutions in acidic mobile phase (95 *vol%* water, 4.9 *vol%* acetonitrile and 0.1 *vol%* trifluoroacetic acid) were mixed with 1.5 mg CBC-MNPs. The decrease of concentration for both solutions of **F** and **W** at 20 and 40 μM were similar, around 12 μM according to calculation. While remaining unchanged for solutions of **G** (c). In addition, after recycling of the CBC-MNPs, a subsequent separation cycle showed almost no loss in the separation efficiency (a, b), suggesting good recoverability.

2.3 Conclusion and Outlook

In conclusion, a novel and facile method for the preparation of surface-bound CB[8] catenanes on silica NPs was developed. The formation of catenanes on silica NPs was confirmed by UV-vis titration experiments and lithography characterisation. The CB[8] catenane system acts as a nanoscale molecular receptor for certain aromatic molecules such as PDi, naphthol and aromatic amino acids. We further demonstrated a simple and efficient peptide separation approach using surface-bound CB[8] catenanes on magnetic NPs, whereby the target peptides could be selectively captured and separated from a peptide mixture and released by the single-electron reduction of MV^{2+} . Moreover, the CB[8] catenane NPs could be readily recycled after use. The introduction of CB[8] catenane structures onto NPs allows for single molecule recognition on a micromolar scale, providing potential opportunities in biological sensing and separation.

2.4 Experimental Appendix

2.4.1 Materials and general methods

All the starting materials were purchased from Alfa Aesar and Sigma Aldrich and used as received unless stated otherwise. CB[8] was prepared according to literature protocols.⁷⁷

^1H NMR (400 MHz) spectra were recorded using a Bruker Avance QNP 400. FTIR spectra was recorded using a Perkin-Elmer Spectrum 100 series FTIR spectrometer, which is equipped with a universal ATR sampling accessory. DLS and zeta potential measurements were performed on a Malvern Zeta-sizer NS90. UV-*vis* spectra were obtained on a Varian Cary 4000 UV-*vis* spectrophotometer. TEM images were obtained on a FEI Philips Tecnai 20 TEM under an accelerating voltage of 80 kV. Samples were prepared by applying one drop of the sample solutions onto a Holey R carbon coated copper TEM grid (400 mesh), followed by drying overnight at room temperature. Fluorescence images were obtained using an Olympus IX81 inverted optical microscope coupled with a camera of Andor Technology EMCCD iXonEM + DU 897. Titration experiments were carried out on a MicrocalTM ITC₂₀₀. Peptides were synthesised using LibertyBlue peptide synthesiser,

purified and analysed by high-performance Liquid Chromatography (HPLC) performed on a Varian 940-LC system. The semi-preparative and analytical columns used were Agilent ZORBAX 300SB C18 5 μm 9.4 x 250 mm column and Agilent Eclipse Plus C18 5 μm 4.6 x 150 mm column. The gradient applied was from 95:5 water (0.1% trifluoroacetic acid): acetonitrile to 100% acetonitrile. Electrospray ionisation mass spectrometry (ESI-MS) was performed on a Thermo Scientific LTQ Orbitrap Velos mass spectrometer with an electrospray ion source in the positive ion mode.

2.4.2 Synthesis and characterisation of MV-disilane guest molecule

4, 4'-bipyridine (2 g, 13 mmol) was dissolved in 200 mL dry acetonitrile under nitrogen, after which (3-iodopropyl)trimethoxysilane (8 mL, 41 mmol) was added. The mixture was then refluxed at 80 °C for 3 days under nitrogen. The resultant product was filtered and washed with copious amount of acetonitrile and diethyl ether. The product obtained was a redish-orange powder (5.19 g, yield of 55%). ^1H NMR (400 MHz, D_2O), 9.17 (*d*, 4H), 8.63 (*d*, 4H), 3.63 (*s*, 15H), 3.38 (*s*, 2H), 2.24 (*t*, 4H), 0.9 (*t*, 4H). ^{13}C NMR (400 MHz, D_2O), δ = 145.4, 126.9, 63.9, 48.8, 24.7, 8.2 ppm. Mass Spectra, m/z =482.2243 g/mol. FTIR spectrum (Figure 2.13) shows characteristic peaks around 3056 and in the range of 1450 to 1640 cm^{-1} , corresponding to the aromatic rings; and the peak in 1077 cm^{-1} , indicating the C-N stretches attached to the nitrogen cations. In addition, peaks around 1270 and 760 cm^{-1} are attributed to the methoxysilane segments.

2.4.3 Preparation of silica nanoparticles

The silica nanoparticles were prepared using Stöber's method.¹⁸⁰ A mixture containing NH_4OH (3 mL), H_2O (20 mL), and ethanol (70 mL) was prepared in a 150 mL round-bottomed flask. Tetraethyl orthosilicate (TEOS, 2.08 g, 10 mmol) was dissolved in 10 mL ethanol and added into the mixture, stirring vigorously for 2.5 h. The resultant silica NPs were washed by ethanol several times and dried in air.

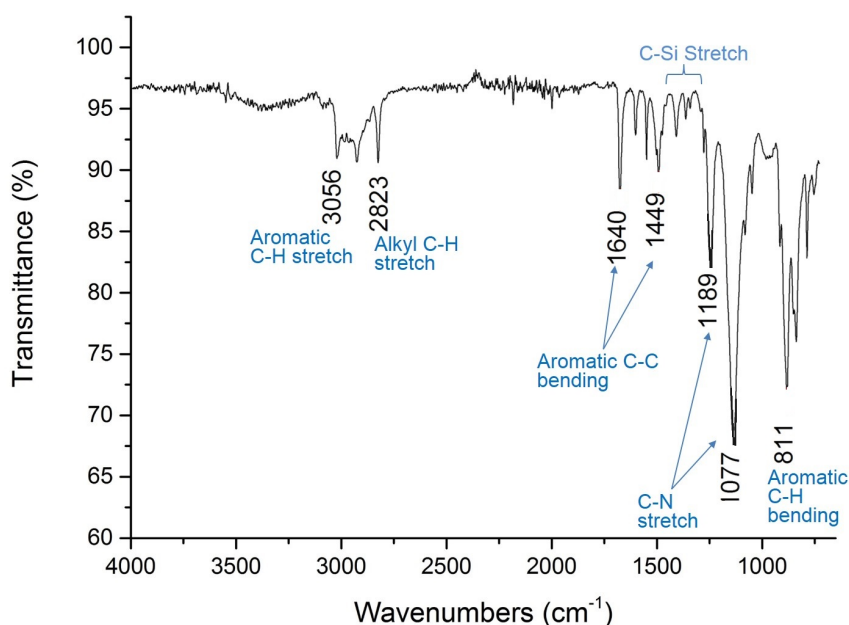


Figure 2.13: FTIR spectrum of MV-disilane.

2.4.4 Preparation of CB[8] catenanes on silica nanoparticles

MV-disilane (36.8 mg, 0.05 mmol) and CB[8] (85 mg, 0.05 mmol) were mixed and dissolved in 330 mL water in a 1 L round-bottomed flask to form a homogenous solution, after which 130 mL ethanol was added. Silica NPs (100 mg) were dispersed evenly in 10 mL water and then added to the mixture. Subsequently, the mixture was reacted at 60 °C for 1 h. The resultant colloids were washed with copious amount of water before being redispersed in water, with addition of excess adamantane amine (11.3 mg, 0.75 mmol), followed by dialysis for 3 days and lyophilization. Similarly, control NPs were prepared by the same procedure, without the addition of CB[8]. The resultant NPs were washed with copious amount of water and then lyophilized.

2.4.5 UV-vis titration

1 mg, 3 mg, and 5 mg NPs solids (CBC-NPs and control NPs) were dispersed in 3 mL 80 μ M PDi solutions and ultrasonicated for 5-10 min. After that, the suspensions were centrifuged at 13000 rpm for 10 min, and the top clear solutions (600 μ L) were taken out and diluted to 3 mL PDi solutions (16 μ M). Excess CB[8] was added to the solutions,

followed by ultrasonication for 5-10 min. The UV-vis absorption was then measured.

2.4.6 Lithography characterisation

2.4.6.1 Preparation of naphthol-silane guest molecule

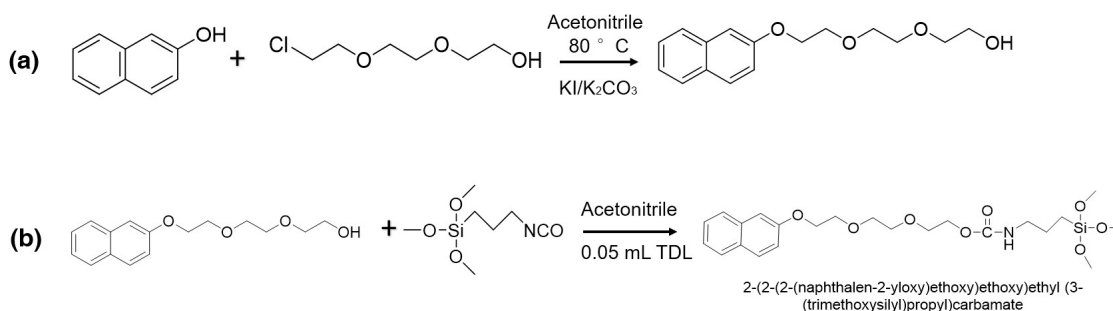


Figure 2.14: Reaction scheme of the synthesis of naphthol-silane guest molecule.

(a) 2-naphthol (11.2 g, 0.08 mol) was added to a solution of 2-[2-(2-chloroethoxy)ethoxy]-ethanol (10.1 g, 0.06 mol) with potassium iodide (5 g, 0.03 mol) and potassium carbonate (8.3 g, 0.06 mol). The resulting solution was heated and refluxed for 36 h under nitrogen, after which KI and K_2CO_3 was filtered and the solvent was removed by rotary evaporation. The resultant product was purified by column chromatography using 1:3 hexane and ethyl acetate as the eluent. Dark red 2-(2-(2-(naphthalene-2-yloxy)ethoxy)ethoxy)ethanol was obtained after the removal of the solvent.

(b) 2-(2-(2-(naphthalene-2-yloxy)ethoxy)ethoxy)ethanol (3.1 g, 3.7 mmol), 3-(triethoxysilyl)-silane propyl isocyanate (1.39 g, 5.6 mmol) and a catalytic amount of dibutyltin dilaurate (TDL) were added to a 100 mL dry round-bottomed flask. 30 mL of dry acetonitrile was then added. The reaction mixture was left to stir for 48 h at room temperature.

2.4.6.2 Preparation of fluorescent nanoparticles

Rhodamine B isothiocyanate (26.8 mg, 0.05 mmol) was mixed with (3-aminopropyl) triethoxysilane (11.7 μL , 0.05 mmol) in 100 mL absolute ethanol, stirred in the dark for 24 h at 42 $^\circ\text{C}$. The solvent was then removed by rotary evaporation to obtain the RhB-silane precursor (around 6 mL). Next, TEOS (3 g, 14 mmol), ethanol (11.4 mL) and RhB-silane precursor (3 mL) were mixed and added to the mixture of NH_4OH (4.3 mL), water (28.8 mL)

and ethanol (103.8 mL), and left to react for 2 h. The resultant product was centrifuged and washed with copious amount of ethanol.

2.4.6.3 Preparation of pattern on glass plates

First, glass plates were washed with a successive of water, ethanol and acetone, before being oxidised in a plasma oxidiser. The previously synthesised naphthol-silane guest molecule was dissolved in ethanol to obtain a final concentration of 10 mM. This solution was then used to transfer the naphthol-silane guest molecule to the PDMS stamp by swapping the patterned side using cotton for 15 s and drying under stream of nitrogen. Subsequently, the PDMS stamp was then brought into contact with the glass plates for 20 s and separated carefully to prevent any dragging, generating the desired pattern. Following the patterning procedure, the glass plates were washed first with water and ethanol, before being exposed to a fluorescent CBC-NPs suspension (0.75 mg/ml) for 15 min. After that, the glass plates were washed again with a series of water, ethanol and acetone.

2.4.7 Preparation of magnetic silica nanoparticles

Water (12 mL) and 2-propanol (60 mL) were mixed and stirred in a 150 mL round-bottomed flask. 1 mL 1 g/L ferrofluid (7.5 nm iron oxide NPs dispersed in water) was added to the mixture, followed by the addition of 1.2 mL NH_4OH and TEOS (0.4 g, 2 mmol). The mixture was left to react for 3 h at room temperature. The resultant nanoparticles were centrifuged and washed by copious amount of water and 2-propanol, before being redispersed in 50 mL water.

2.4.8 Preparation of CB[8] catenanes on magnetic silica nanoparticles

MV-disilane (12.3 mg, 0.02 mmol) and CB[8] (28 mg, 0.02 mmol) were mixed and dissolved in 110 mL water to form a homogenous solution, after which 45 mL ethanol was added. A previously prepared magnetic silica nanoparticles solution (40 mL) was then added and the mixture was left to react at 60 °C for 1 h. The resultant colloids were

washed with copious amount of water and then redispersed in water, with addition of excess adamantane amine (3.8 mg, 0.25 mmol), followed by dialysis for 3 days and lyophilized.

2.4.9 Preparation of peptides

All peptide sequences were synthesised on a 0.25 mmol scale using a standard solid phase Fmoc/tBu strategy and NovaPEG Rink amide resin, performed by a LibertyBlue peptide synthesiser. After synthesis and cleavage from the resin, the products were precipitated in cold diethyl ether, centrifuged, washed with an excess of diethyl ether three times, re-centrifuged and dried under vacuum overnight. The product was then re-dissolved in distilled water and lyophilized. Molecular weight and purity of the peptide sequences were determined by HPLC and mass spectrometry. ESI-MS: **G**: (M+H)⁺ 573.84 g/mol; **F**: (M+H)⁺ 721.09 g/mol; **W**: (M+H)⁺ 760.09 g/mol.

2.4.10 Peptide separation using CBC-MNPs and recovery of CBC-MNPs

The characterisation using HPLC was carried out using an analytical column C18 with a flow rate of 1.0 mL/min. Take the investigation of the peptide **F** as an example. 20 μ M and 40 μ M **F** solutions in acidic mobile phase were prepared and analysed using HPLC. 1.5 mg CBC-MNPs solid was mixed with 1.5 mL the above solutions respectively, ultrasonicated for 5 min, separated by a magnet for 20 min, and then the top supernatant solution 600 μ L was taken out and analysed by HPLC. The differences of the spectra before and after mixing with catenanes were compared.

1 mM sodium dithionite solution in a solvent mixture of 95 vol% water and 5 vol% acetonitrile was prepared under nitrogen. The sedimented CBC-MNPs together with the complexed peptides (**F**) were washed by water and redispersed in 1.44 mL solvent mixture, after which 60 μ L sodium dithionite solution was added and stirred for 3 min under nitrogen. The suspension was then separated by a magnet and the supernatant solution was taken out and analysed by HPLC.

The sedimented nanoparticles in the above procedure were washed by water and

mixed with 1.5 mL 20 μ M and 40 μ M F solutions in acidic mobile phase respectively, purging oxygen for 1 min. Then the suspensions were ultrasonicated for 1 min and separated by a magnet. The measurement of the supernatant solution by HPLC was repeated.

The procedures were repeated for **G** and **W**. The UV-vis trace was followed at 220 and 254 nm for **G** and **F**, 220 and 280 nm for **W**.

2.4.11 Quantification of the CB[8] on the silica nanoparticle surface

The calculation shown in this section is based on the UV-vis titration experiment results of the CBC-NPs prepared at 60 °C for 1 h. The first step is to calculate the mass fraction of CB[8] in the CBC-NPs, shown in Table 2.3.

Table 2.3: Calculation of the mass fraction of CB[8] in the CBC-NPs

Aomount of CB[8] added to PDi solution	$\Delta Abs.(PDi)$	$\Delta c(PDi)$ [μ M]	$n(CB[8])$ [nmol]	Average $n(CB[8])$ [nmol/mg]	$m(CB[8])/mg$ CBC-NPs [μ g/mg]
1 mg	0.119	3.78	11.34		
3 mg	0.164	5.21	15.63	6.85 ± 3.9	11.65 ± 6
5 mg	0.21	6.67	20.01		

Take the calculation of 1 mg CBC-NPs added to 3 mL 16 μ M PDi solution as an example.

The absorption of PDi solution without any addition of NPs is 0.284, 0.165 after adding CBC-NPs. The change of PDi absorption:

$$\Delta Ab.(PDi) = 0.284 - 0.165 = 0.119$$

According to the UV-vis calibration plot of PDi/CB[8] solution, the calibration equation is:

$$y = 0.0315x + 0.0055$$

so the change of concentration of PDi solution is:

$$\Delta c(PDi) = \frac{\Delta Ab.(PDi)}{0.0315} = \frac{0.119}{0.0315} = 3.78 \mu M$$

The change of mole of PDi:

$$\Delta n(PDi) = \Delta c(PDi) \times V_{oulme} = 3.78 \mu M \times 3 mL = 11.34 nmol$$

which is equal to the mole of CB[8] in the 1 mg CBC-NPs added. The moles of CB[8] in the 3 mg and 5 mg CBC-NPs are calculated in the same way.

The average mole of CB[8] per mg CBC-NPs can then be calculated and the mass fraction of CB[8] in the CBC-NPs is:

$$m(CB[8]) = n(CB[8]) \times Mw(CB[8]) = 6.85 nmol/mg \times 1700 g/mol = 11.65 \mu g/mg$$

The total volume of NPs in 1 mg CBC-NPs is:

$$V_{total} = \frac{m}{\rho} = \frac{1 mg}{2.4 g/cm^3} = 0.417 \times 10^{-3} cm^3 = 4.17 \times 10^{17} nm^3$$

where ρ is the density of silica nanoparticles, 2.4 g/cm³.

The volume of a single CBC-NPs nanoparticle is:

$$V_{single} = \frac{4}{3} \pi r^3 = \frac{4}{3} \times \pi \times \left(\frac{337 nm}{2}\right)^3 = 2.004 \times 10^7 nm^3$$

where r is the radius of the CBC-NPs nanoparticle, which is equal to 337 nm/2 = 168.5 nm, according to DLS results.

The total number of the CBC-NPs nanoparticle in 1 mg CBC-NPs is:

$$N = \frac{V_{total}}{V_{single}} = \frac{4.17 \times 10^{17} nm^3}{2.004 \times 10^7 nm^3} = 2.08 \times 10^{10}$$

The total surface area of the CBC-NPsnanoparticle in 1 mg CBC-NPs is:

$$S = 4\pi r^2 N = 4 \times \pi \times 168.5^2 nm^2 \times 2.08 \times 10^{10} = 7.42 \times 10^{15} nm^2$$

The average number of CB[8] in 1 mg CBC-NPs is:

$$N(CB[8]) = n(CB[8])NA = 4.13 \times 10^{15}$$

The density of CB[8] on the silica NP is:

$$\frac{N(CB[8])}{S} = \frac{4.13 \times 10^{15}}{7.42 \times 10^{15} nm^2} = 0.56 nm^{-2}$$

2.4.12 Peptide separation using CBC-MNPs

The calibration plots of KKKGGG (G), KKKGGGF (F) and KKKGGGW (W) of a range of concentrations in acidic mobile phase (95 vol% water, 4.9 vol% acetonitrile and 0.1 vol% TFA) are shown in Figure 2.15 to 2.17.

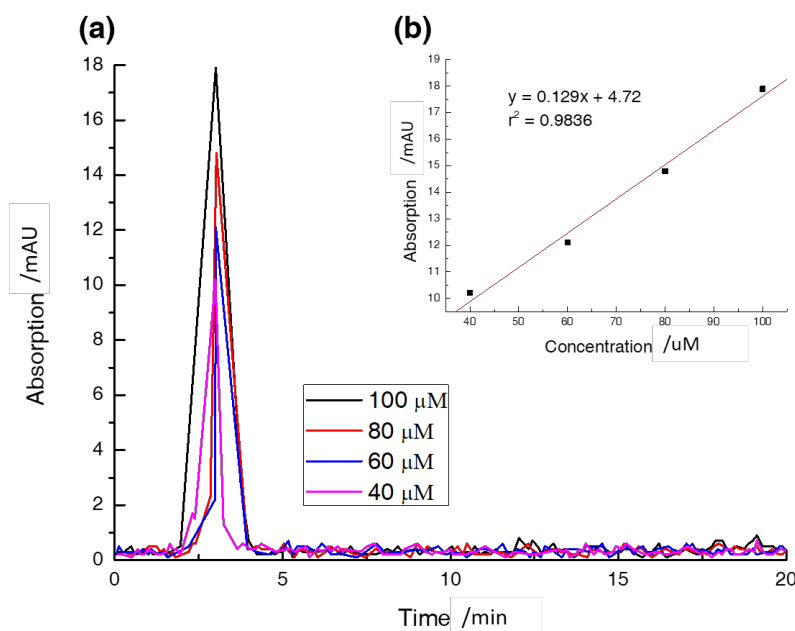


Figure 2.15: HPLC UV calibration plot (220 nm wavelength) of G solution . The solvent was acidic mobile phase (95 vol% water, 4.9 vol% acetonitrile and 0.1 vol% TFA). (a) UV absorption spectra; (b) calibration line.

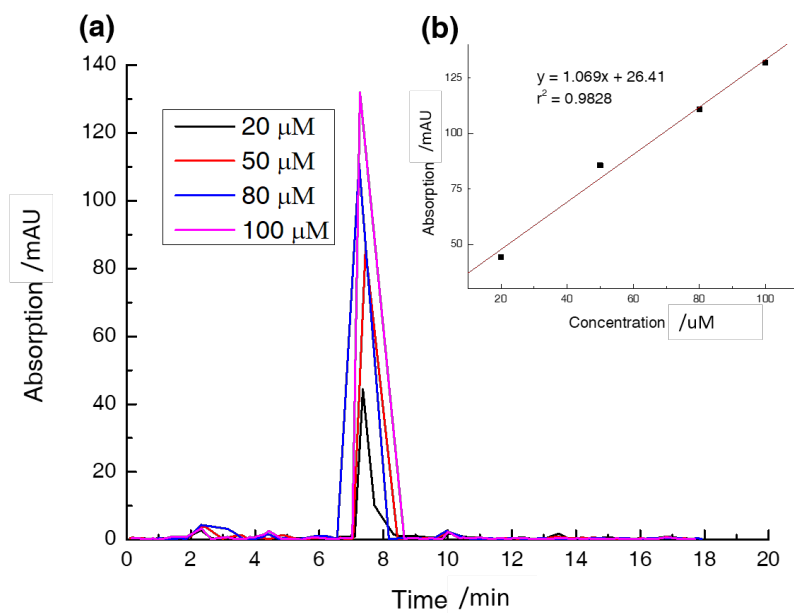


Figure 2.16: HPLC UV calibration plot (220 nm wavelength) of **F** solution. The solvent was acidic mobile phase (95 vol% water, 4.9 vol% acetonitrile and 0.1 vol% TFA). (a) UV absorption spectra; (b) calibration line.

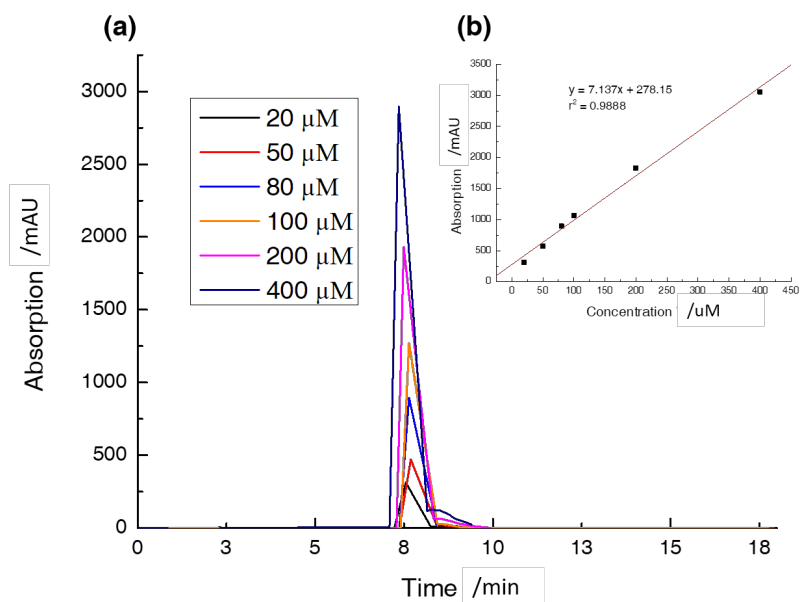


Figure 2.17: HPLC UV calibration plot (220 nm wavelength) of **W** solution. The solvent was acidic mobile phase (95 vol% water, 4.9 vol% acetonitrile and 0.1 vol% TFA). (a) UV absorption spectra; (b) calibration line.

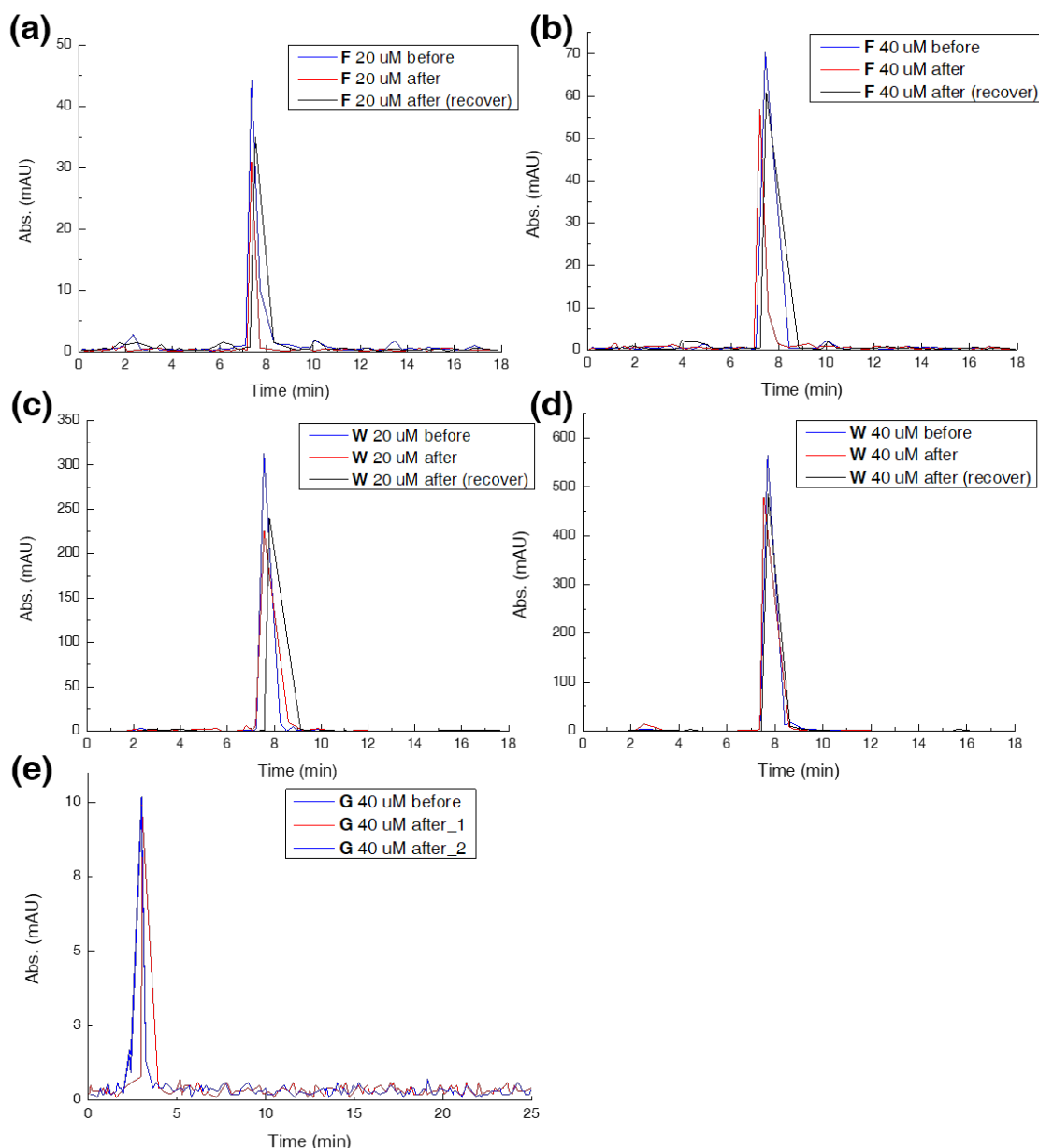


Figure 2.18: Target peptides **F** at 20 μ M (a) and 40 μ M (b), **W** at 20 μ M (c) and 40 μ M (d), as well as control peptide **G** at 40 μ M (e) before and after mixing with CBC-MNPs. 1.5 mL peptide solutions in acidic mobile phase were mixed with 1.5 mg CBC-MNPs. The decreases of concentration for solutions of **F** and **W** at both 20 and 40 μ M were similar, around 12 μ M according to calculation. While remained unchanged for solutions of **G**. After recycling of the CBC-MNPs, a subsequent separation cycle showed almost no loss in the separation efficiency, suggesting good recoverability (a-d).

The absorption of the mixture solutions of **W** and **G**, **F** and **G**, cannot be analysed by HPLC, as the absorption of the solutions of **W** and **F** are 10 – 50 times larger than that of

G. After the reduction of MV^{2+} to MV^{+} by sodium dithionite, the UV absorptions of the recovered peptides were measured by HPLC. The separation efficiency of the recovered CBC-MNPs showed small decrease, which might be due to the weight loss during the washing of CBC-MNPs.

2.4.13 Quantification of the peptide separation using CBC-MNPs

The calculation results are shown in Table 2.4.

Table 2.4: Calculation of the peptide separation using CBC-MNPs

	c(pep) [μ M]	$\Delta Abs.$ [mAU]	$\Delta c(\text{pep})$ [μ M]	$\Delta n(\text{pep})$ [nmol]	Av. $\Delta n(\text{pep})$ [μ mol/g]
F	20	13.4	12.6	18.9	12.5 ± 0.1
	40	13.3	12.4	18.6	
W	20	87.9	12.3	18.5	12.2 ± 0.2
	40	85.5	12.0	18.0	

note: c stands for concentration, "pep" stands for peptides, "Av." stands for average.

The calculation is similar to the section 2.4.11. Take the calculation of 1.5 mg catenanes added to 1.5 mL 20 μ M **F** solution as an example.

$$\Delta Ab.(\mathbf{F}) = 44.4\text{mAU} - 30.9\text{mAU} = 13.5\text{mAU}$$

According to the HPLC UV-vis calibration plot of **F** solution, the calibration equation is:

$$y = 1.069x + 26.41$$

so the change of concentration of **F** solution is:

$$\Delta c(\mathbf{F}) = \frac{\Delta Ab.(\mathbf{F})}{1.069} = \frac{13.5}{1.069} = 12.6\mu\text{M}$$

The change of mole of **F**:

$$\Delta n(\mathbf{F}) = \Delta c(\mathbf{F}) \times Volume = 12.6\mu\text{M} \times 1.5\text{mL} = 18.9\text{nmol}$$

The $\Delta n(\mathbf{F})$ measured in 20 μM and 40 μM are averaged to 18.75 nmol. So the average decrease of $n(\mathbf{F})$ by adding per mg catenane is:

$$\Delta n(\mathbf{F}) = \frac{18.75 \text{ nmol}}{1.5 \text{ mg}} = 12.5 \text{ nmol/mg}$$

Calculation procedures are similar as for \mathbf{W} , instead of using calibration equation of \mathbf{W} :

$$y = 7.137x + 278.15$$

Chapter 3

Advanced Molecular Sensing Exploiting Catenane-Engineered Nanostructures

Surface-enhanced Raman scattering (SERS) spectroscopy is a powerful and versatile finger-printing method for ultrasensitive detection of chemicals and biomolecules. The sensitivity arises from highly localised plasmonic field enhancements or hot-spots generated in metallic nanostructures with sharp features or narrow gaps. In this work, we report a highly stable free-standing molecular sensor that exploits a self-assembly of catenane-engineered nanostructure. CB[8] is tethered onto a spiky $\gamma\text{-Fe}_2\text{O}_3\text{@Au}$ nanoparticle (NP) surface to collect target analytes from aqueous media. These target analytes can be detected with a high sensitivity (down to low micromolar concentrations), on account of the high SERS enhancement (on the order of 10^8) of the spiky NPs. Additionally, through the incorporation of magnetic cores, the spiky NPs can be separated from aqueous phase by simple magnetic separation. This molecular nanosensor provides a powerful SERS substrate that shows great promise in the detection of a variety of chemicals, biomolecules, controlled substances and auxiliary diagnostics of various diseases.

This work has been submitted in the following peer-reviewed journal articles:

- **Ren, X.;** Clarke, D. E.; Kamp, M.; Wu, Y.; Chikkaraddy, R.; Nijs, B. D.; Liu, J.; Barrow, S. J.; Yu, Z.; Baumberg, J. J.*; Scherman, O. A.*, "Advanced molecular sensor exploiting catenane-engineered nanostructures", *submitted*.

3.1 Introduction

Ultrasensitive detection of target analytes with high specificity and sensitivity is of fundamental importance in a broad range of scientific and technological fields, ranging from analytical chemistry,⁹ biomolecular diagnostics,¹² pharmaceutical drugs¹³ to environmental monitoring.¹ Among various techniques, surface-enhanced Raman scattering (SERS) spectroscopy shows the greatest promise in the detection of trace amounts of molecules as sensing capabilities can reach analyte concentrations down to the few or even single molecule regime.^{1,4,7,8} To reach such high sensitivity SERS signals, metallic substrates are typically designed with sharp features, a high surface roughness or small nanogaps to obtain highly localised intense plasmonic hot-spots providing the required field enhancements.^{1,4,5,8,22,45,46,181} Top-down methods for such metallic nanostructures are generally too expensive, as substrates are difficult to be reused, or lack the ability to reproducibly generate a large number of precise nanoscale features required for quantitative SERS measurements.^{1,4,5,8,45,46} As a result, most common SERS substrate designs reported in literature exploit a form of bottom-up approach for growing the desired metallic nanostructures.^{1,5,22,45,46,181} Most of the successful quantitative approaches rely on colloidal nanoparticle synthesis combined with a self-assembly step to generate precisely controlled plasmonic hot-spots.^{53,139,140,182,183} Such SERS-based sensing techniques have demonstrated efficient and quantitative detection of analytes at clinical levels and hence hold great promise for use in medical applications.^{53,139,140}

However, challenges still remain in this research field, namely, the limited scope of detectable molecule species and also the potential barrier generated by the charge-stabilised colloids used for self-assembled substrates.^{1,4,5,45,46,53,139,140,182,183} Analytes must be able to adsorb efficiently on the SERS substrate and be positioned in or near the plasmonic hot-spots. Consequently, SERS substrates are often characterised using a relatively dense layer of thiolated or aminated molecules which can adsorb chemically or by electrostatic interactions to the metal surface, i.e. silver (Ag) and gold (Au) surfaces.^{1,4,5,8,45,46} For analytes without a clear metal binding group (here referred to as "inert"), SERS signals become weaker as a result of fewer molecules binding to the substrate.^{1,4,5,8,45,46} A range

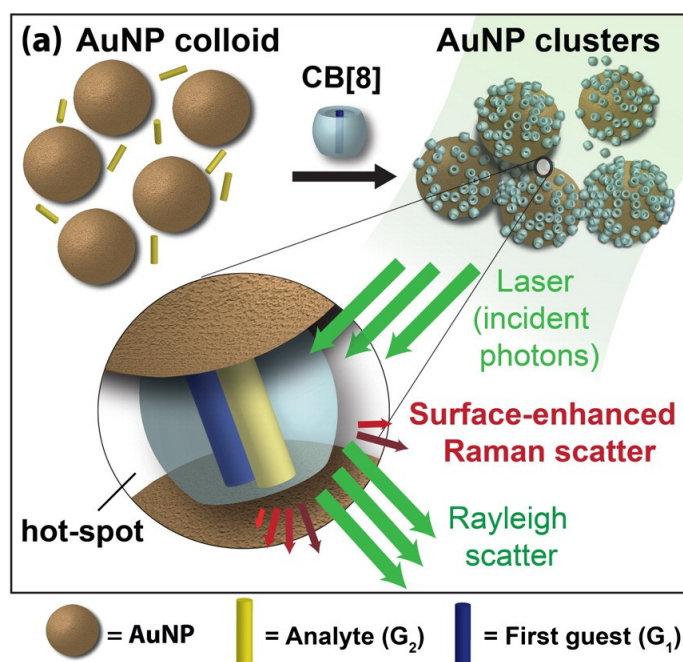


Figure 3.1: Schematic of host-guest SERS analysis using ternary complexation: CB[8] aggregates Au NPs and localises the analyte (G_2) in the hot-spots for SERS analysis. (Note: The Au NPs are not drawn to scale with the analytes.) Adapted from reference.⁵³

of solutions have been presented to trap "inert" analytes in the plasmonic hot-spots, including dense partition layers,⁵⁷ antibody receptors,⁵⁰ and macromolecular cages consisting of cyclodextrins^{71,74} or cucurbit[n]urils (CB[n]s: where $n = 5, 6, 7$ or 8).^{28,51–56} The latter, CB[n], is of particular interest here as it not only exhibits strong and selective encapsulation of various guest molecules into its barrel-shaped cavity, but also functions as a precise rigid spacer between nanoparticles (NPs).^{53,76–78} The larger homologue CB[8] can simultaneously sequester two guest molecules to form ternary complexes, allowing for tailoring of the chemical environment of its cavity to trap specific analytes.^{53,76–78,113}

When combined with citrate-capped metallic NPs, CB[n]s readily self-assemble the NPs into chains and fractal-like aggregates on account of the strong binding affinity of their carbonyl-fringed portals to the metallic surface, forming a powerful SERS substrate to detect a wide variety of "inert" molecules (as shown in Figure 3.1.)^{28,51–56} However, when left uninhibited, as with most self-assembly processes, CB[n] will continue to aggregate the metallic structures leading to colloidal instabilities.^{28,51–55,122,140} As a

consequence, measurements have to be taken within 60 minutes of the substrate's preparation.^{53,140} In addition, *in situ* measurements may involve environments that affect such self-assembly processes. For example, the possible displacement of analytes in the nanogap by non-analyte moieties can give rise to fluctuating backgrounds and hence the need for advanced data interpretation techniques, e.g. Principle Component Analysis.^{53,55,140} Therefore, it is of great benefit to design SERS substrates that can provide the same levels of detection and functionality but eliminate the need for aggregation.

Herein, we present catenane-functionalised magnetic spiky NPs (**CBCat**) as an alternative of self-assembled colloids for advanced molecular sensing. A viologen derivative, 1,1'-bis(4-mercaptobutyl)-4,4'-bipyridine (HS-MV-SH or **G**₁), was used to thread and immobilise CB[8] host onto metallic SERS substrate (as illustrated in Figure 3.2). The remaining hydrophobic cavity of CB[8] scavenges and sequesters target analytes from aqueous media, binding them near the metallic surface for SERS detection. It is well recognized that the morphology of NPs plays an important role in the magnitude of SERS enhancement.^{1,4,6,8,9} The overall SERS enhancement factor increases with shape as follows: nanospheres < nanorods < nanocubes < nanogap (dimers, aggregates) <= nanostars, attributed to the number of intrinsic hot-spots per NP.^{1,5,6,27-29} The reliable fabrication of dimers in solution is challenging and requires careful placement of the analyte into the ultra-small hot-spots with right position and orientation.^{28,29} Spiky NPs, on the other hand, can provide a large number of hot-spots within a single structure.¹⁸⁴⁻¹⁸⁸ Our molecular sensor was deliberately designed to have a spiky architecture, resulting in high SERS enhancements (on the order of 10⁸). We demonstrate the detection of various target analytes, in particular, a commonly illegal stimulant molecule (1,5-pentamethylene-1H-tetrazole), using the developed catenane molecular sensor. All the analytes can be detected with high sensitivities.

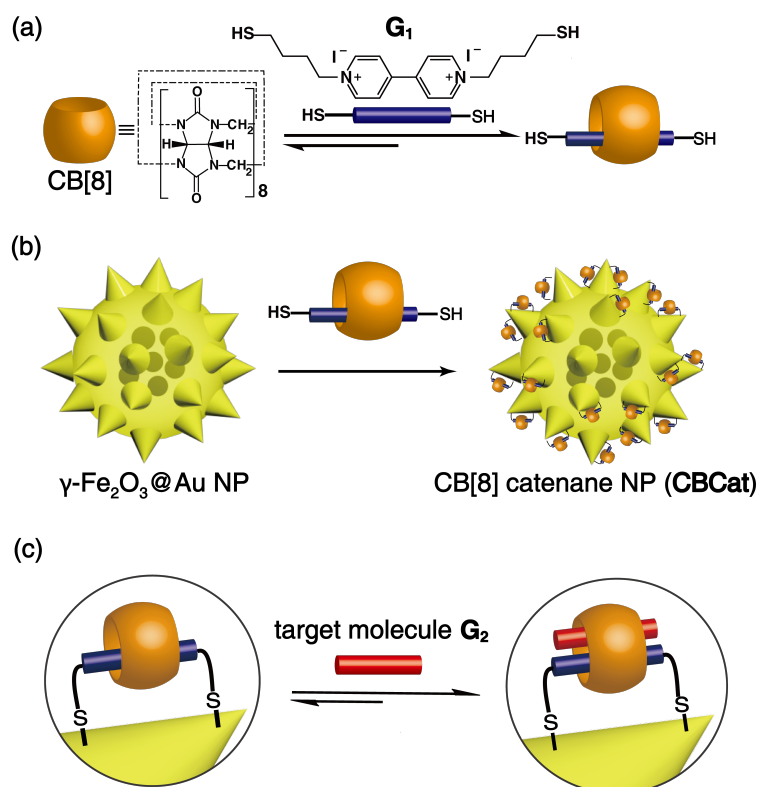


Figure 3.2: (a) Complexation between CB[8] and HS-MV-SH; (b) surface-bound CB[8] catenane on spiky $\gamma\text{-Fe}_2\text{O}_3\text{@Au}$ NP (**CBCat**) prepared by immobilising HS-MV-SH@CB[8] inclusion complexes onto spiky NPs. (c) capture of target molecules from aqueous media into CB[8] cavity for SERS detection.

3.2 Results and Discussion

3.2.1 Trials of CB[8] catenanes on spherical Au NPs

To start with, CB[8] catenanes on spherical magnetic Au NPs were investigated. The spherical $\gamma\text{-Fe}_2\text{O}_3\text{@Au}$ NP cores were synthesised according to the Lyon's iterative hydroxylamine seeding method (149 ± 28 nm).¹⁸⁹ Both the TEM images (obtained after the magnetic attraction and separation, Figure 3.3b) and STEM-EDX elemental analysis by line-scan (Figure 3.3c) across the central NP confirm the incorporation of the $\gamma\text{-Fe}_2\text{O}_3$ NPs inside Au. However, CB[8] catenanes prepared on spherical $\gamma\text{-Fe}_2\text{O}_3\text{@Au}$ NP cores could not obtain clear SERS signals, due to the low field enhancements, as shown in Figure 3.4. Therefore, magnetic Au NP cores of a spiky shape was facilitated to obtain highly

localised intense plasmonic hot-spots providing the required field enhancements.

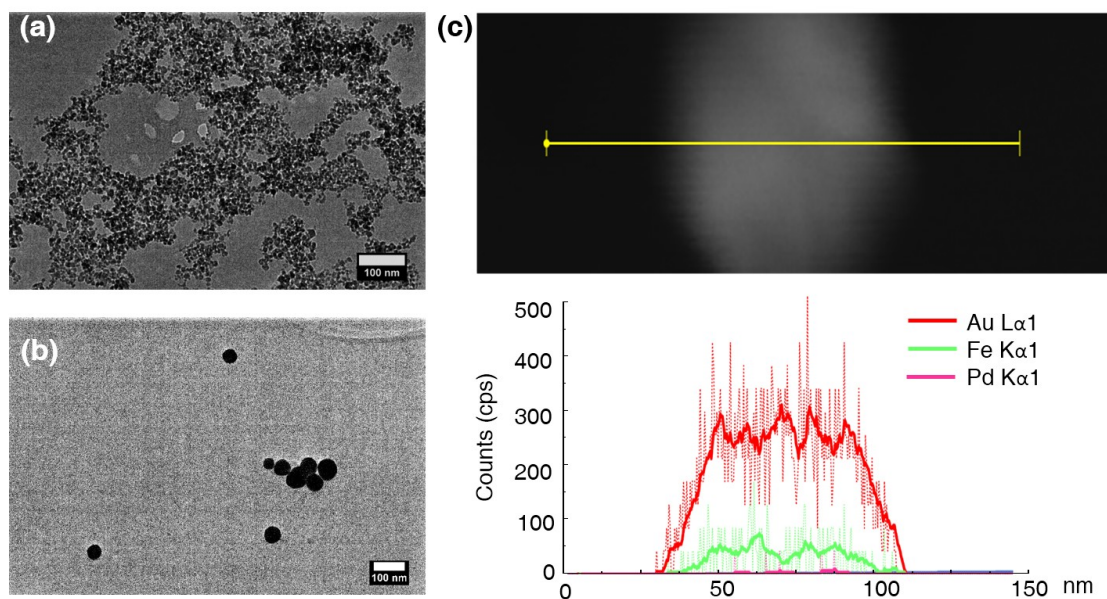


Figure 3.3: (a) TEM image of $\gamma\text{-Fe}_2\text{O}_3$ NPs (7 ± 2 nm, zeta potential of -68.8 mV measured by DLS at pH=12); (b) TEM image of spherical $\gamma\text{-Fe}_2\text{O}_3\text{@Au}$ NPs (149 ± 28 nm, zeta potential of -50.4 mV at pH=12); (c) STEM-EDX elemental analysis by line-scan across the central NP, where the counts of Au element are much higher than Fe since it covers outside.

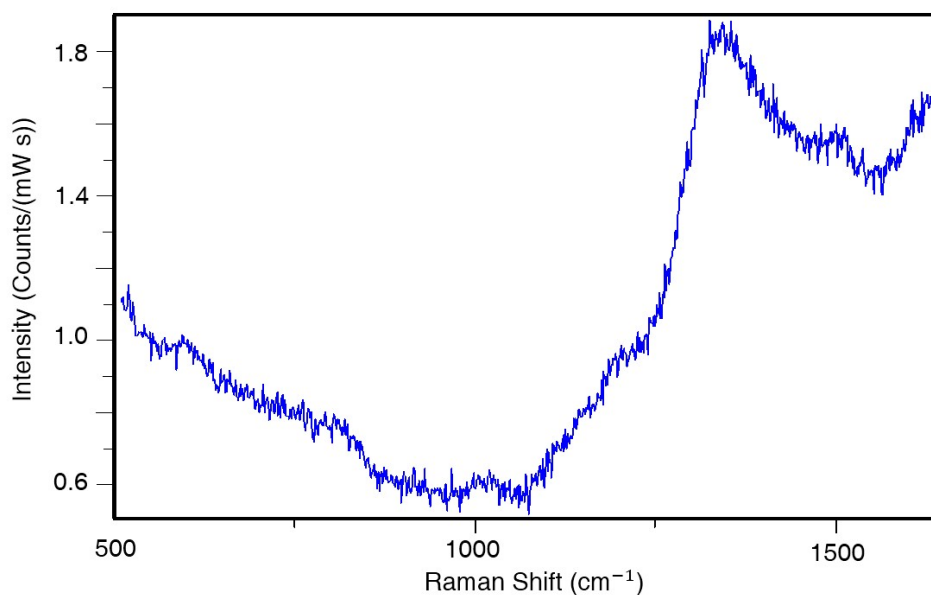


Figure 3.4: SERS spectrum of the CB[8] catenanes on spherical $\gamma\text{-Fe}_2\text{O}_3\text{@Au}$ NP cores irradiated at 785 nm, where no clear signal could be obtained.

3.2.2 Synthesis and characterisation of spiky $\gamma\text{-Fe}_2\text{O}_3\text{@Au}$ NP core

The spiky Au NP was grown around $\gamma\text{-Fe}_2\text{O}_3$ NPs no larger than 10 nm (to retain superparamagnetism of the maghemite), adding magnetic properties to the CBCat which allow for *in situ* manipulation and retrieval of the SERS substrates. The spiky $\gamma\text{-Fe}_2\text{O}_3\text{@Au}$ NP core was synthesised by a modified Lyon's iterative hydroxylamine seeding method.¹⁸⁹ TEM images clearly show the spiky shape of the $\gamma\text{-Fe}_2\text{O}_3\text{@Au}$ NP (130 ± 20 nm, Figure 3.5a). UV-vis absorption spectrum of the spiky $\gamma\text{-Fe}_2\text{O}_3\text{@Au}$ NPs show a new absorption peak around 530 nm, indicating the coating of Au (Figure 3.5b).

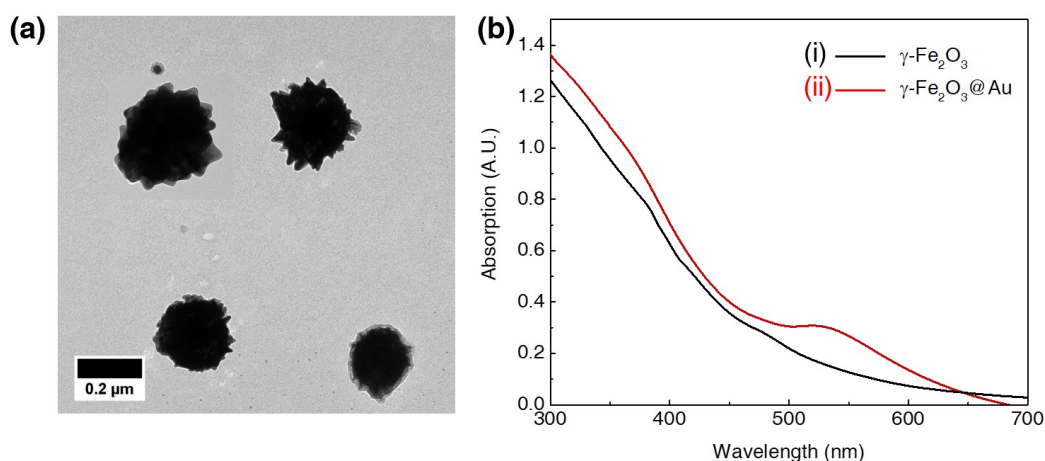


Figure 3.5: (a) TEM image of the spiky $\gamma\text{-Fe}_2\text{O}_3\text{@Au}$ NPs (130 ± 20 nm, zeta potential of -42.6 mV measured by DLS at pH=12); (b) UV-vis absorption spectra of the $\gamma\text{-Fe}_2\text{O}_3$ NP solution (i) and spiky $\gamma\text{-Fe}_2\text{O}_3\text{@Au}$ NP solution (ii). The shoulder at 530 nm in (ii) is due to the absorption of Au, indicating the successful coating of Au.

The incorporation of $\gamma\text{-Fe}_2\text{O}_3$ NPs inside Au was further confirmed by STEM-EDX element analysis (Figure 3.6). The counts of Au element in STEM-EDX line-scan over the central spiky NP is around ten times higher than that of Fe, indicating Au covers the outside region (Figure 3.6a). In addition, as shown in Figure 3.7, after attraction by a magnet, most of the spiky NPs were collected to the corner with dramatic decline of the SERS signals.

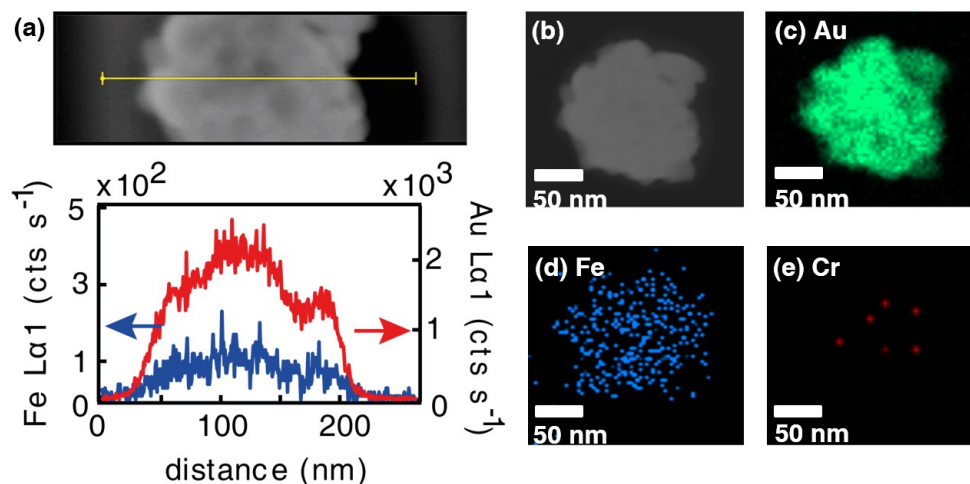


Figure 3.6: (a) STEM-EDX elemental analysis by line-scan across the central spiky NP, where the counts of Au element are much higher than Fe, suggesting that γ - Fe_2O_3 NPs are covered by Au; (b) HAADF-STEM (High-Angle Annular Dark-Field Scanning Transmission Electron Microscopy) image and corresponding EDX mapping data of the spiky γ - Fe_2O_3 @Au NPs : (c) for Au element, (d) for Fe and (e) for background control (Cr).

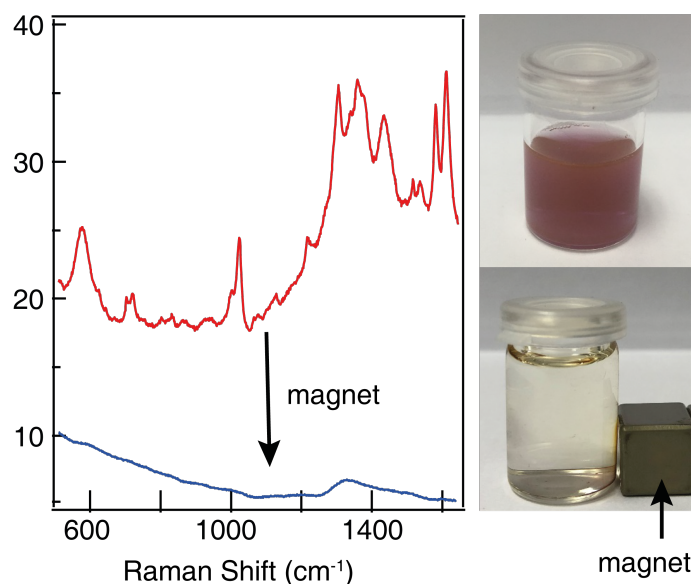


Figure 3.7: SERS spectra and pictures of spiky NP dispersions before and after applying a magnetic field for 15 min.

3.2.3 Preparation of CB[8] catenanes on spiky magnetic Au NPs (CBCat)

The surface-bound CB[8] catenanes on spiky $\gamma\text{-Fe}_2\text{O}_3\text{@Au}$ NPs (**CBCat**) were prepared by immobilising HS-MV-SH (G_1)@CB[8] inclusion complexes onto the spiky NPs *via* a gold-sulfur conjugation, as illustrated in Figure 3.8. G_1 was chosen as the first guest to tether CB[8], on account of its strong binding affinity towards CB[8] (association constant K_a of $3.3 \times 10^5 \text{ M}^{-1}$, Figure 3.9).¹¹³ The zeta potential of spiky NPs switched from -42.6 mV to $+34.9 \text{ mV}$ after the functionalisation with G_1 @CB[8] complexes, suggesting the immobilisation of positively charged MV^{2+} onto NP surface. The surface density of immobilised CB[8] was $0.9 \pm 0.2 \text{ nm}^{-2}$, quantified by ITC and UV-vis titration (see the Experimental Appendix for details).

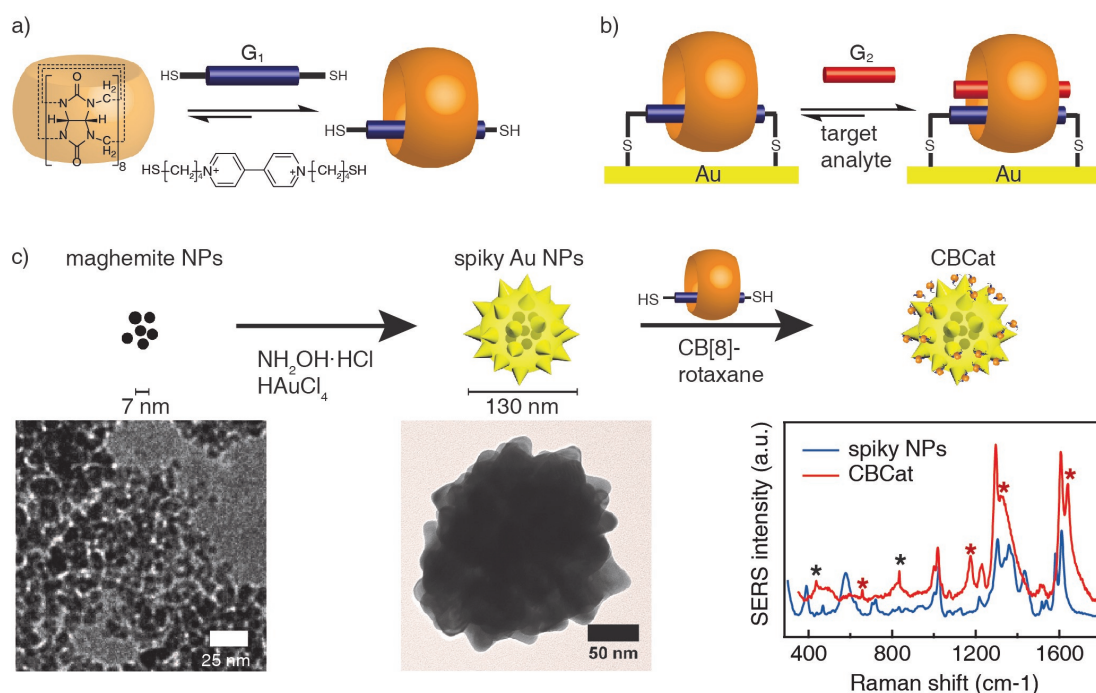


Figure 3.8: (a) Complexation between CB[8] and HS-MV-SH (G_1); (b) capture of target molecules from aqueous media into CB[8] cavity on the NP surface for SERS detection; (c) schematic illustration of the preparation of spiky cores and **CBCat**, as well as corresponding TEM images and SERS spectra. The SERS signature peaks of CB[8] and G_1 can be clearly observed after the immobilisation of G_1 @CB[8] inclusion complexes onto the NP surface (highlighted with asterisks, black for CB[8] and red for G_1). (Note: spectra are normalised and offset for clarity.)

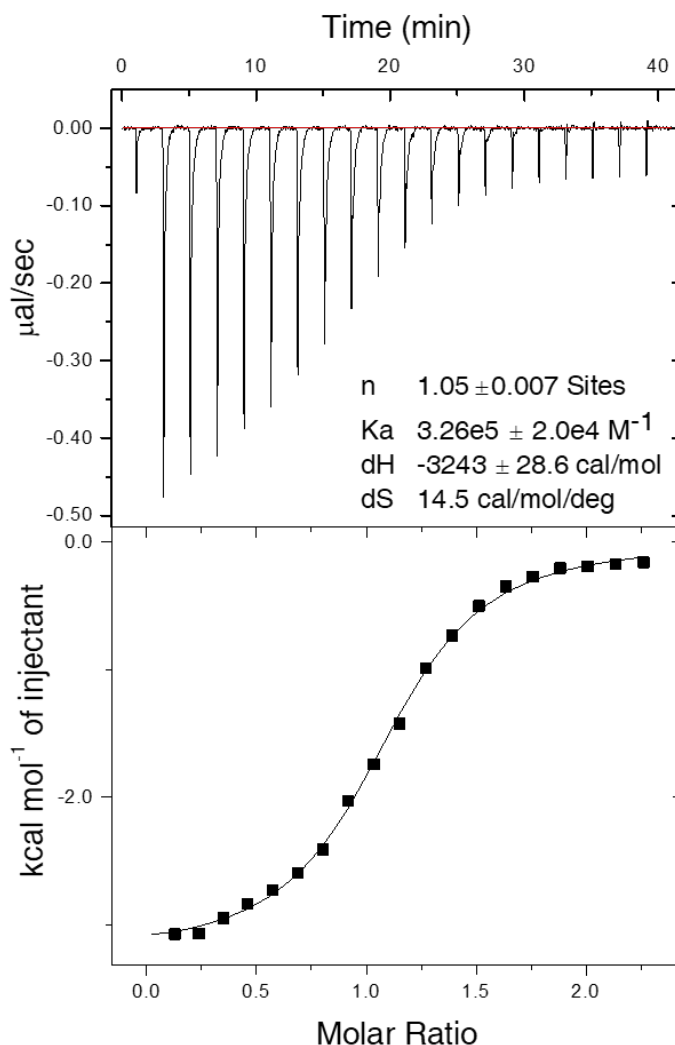


Figure 3.9: ITC titration result shows a strong complexation between HS-MV-SH and CB[8]. 1 mM HS-MV-SH was injected into 0.05 mM CB[8] in phosphate buffer solution (50 mM, pH=6.8) at 25 °C.

Significant Raman signal enhancement occurs on hot-spots, usually located on the sharp corners and edges of noble metal nanostructures, or nanoscale junctions between two adjacent noble metal NPs.^{1,4,5,8,45,46} Therefore, the high anisotropy and relatively large number of intrinsic hot-spots per NP of the **CBCat** make it an ideal SERS substrate, with substantially high electromagnetic field enhancements. As shown in Figure 3.10, **CBCat** shows intense SERS signals, with signature peaks of both CB[8] and **G**₁. The signals at 436 and 835 cm⁻¹ have been assigned to the ring scissor and ring deformation

modes of CB[8] respectively.⁵¹ The peaks at 652, 1175, 1322, and 1642 cm^{-1} are signature peaks of G_1 ^{53,190} (see the Experimental Appendix for powder Raman spectra of G_1 and surfactant sodium citrate). In particular, the peak at 652 cm^{-1} corresponding to the stretching vibration mode of the carbon-sulphur bond, which is too weak to be observed from powder non-SERS Raman spectrum but it can be clearly observed in **CBCat**, corroborating the immobilisation of G_1 @CB[8] on the NP surface.¹⁹⁰ The SERS enhancement factor (EF) calculated from the experimental data is $(2.3 \pm 0.1) \times 10^8$ (Experimental Appendix 3.4.10). Theoretical modelling with three dimensional Finite Difference Time Domain (3D-FDTD) was also applied to simulate the local electromagnetic field distribution irradiated with monochromatic light at 785 nm (Figure 3.11a). The simulation results show that the strongest localised field occurs at the gap between spikes (EF of 10^8), spreading from the central highest to the spikes (10^4). The modelled SERS EF is on the order of 10^8 and is consistent with the experimental results obtained. In addition, the modelled SERS EF of **CBCat** is 4-5 orders of magnitude higher than that of spherical $\gamma\text{-Fe}_2\text{O}_3$ @Au NPs (Figure 3.11b). This is in agreement with our experimental observation of catenane structures on spherical $\gamma\text{-Fe}_2\text{O}_3$ @Au NPs, where no SERS signal was observed (Figure 3.4).

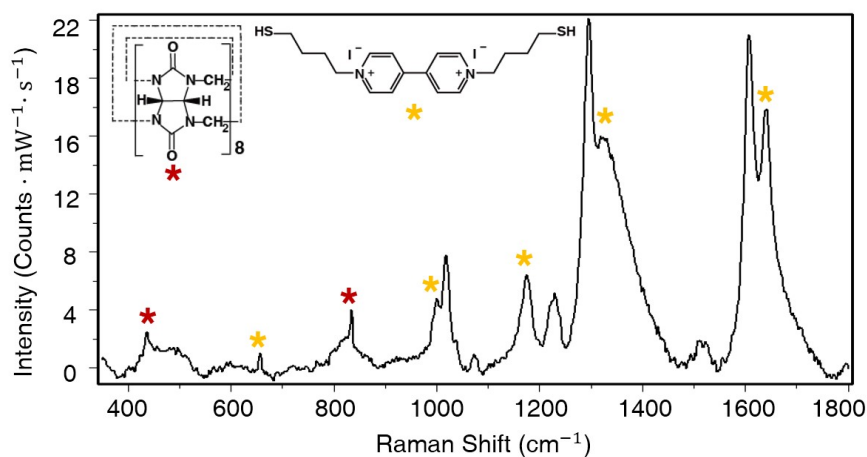


Figure 3.10: SERS spectrum of **CBCat** at the excitation wavelength of 785 nm, where the red and yellow stars highlight the signature peaks of CB[8] and HS-MV-SH (G_1) respectively. Other peaks correspond to the surfactant sodium citrate.

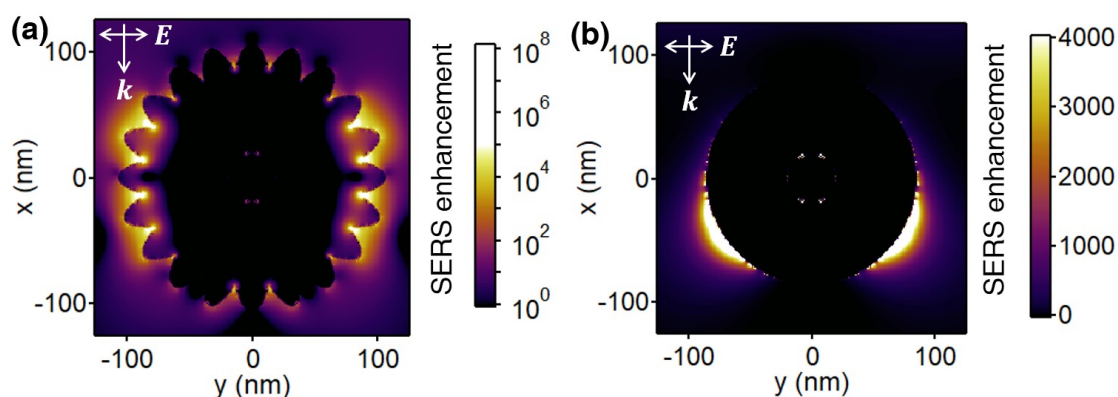


Figure 3.11: (a) The 3D-FDTD modelled local electric field enhancement of **CBCat** at the XY plane, irradiated from the top at 785 nm. The modelled field enhancement factor (EF) is up to 10^8 , which is in good agreement with the experimental obtained EF; (b) the 3D-FDTD modelled EF of spherical γ - Fe_2O_3 @Au NPs, which is approximately 10^5 lower than **CBCat**.

The **CBCat** is very stable in aqueous solution and no obvious change of the **CBCat** SERS spectrum has been observed over 90 days (Figure 3.12), suggesting no irreversible aggregation of the NPs has occurred over the extended period.

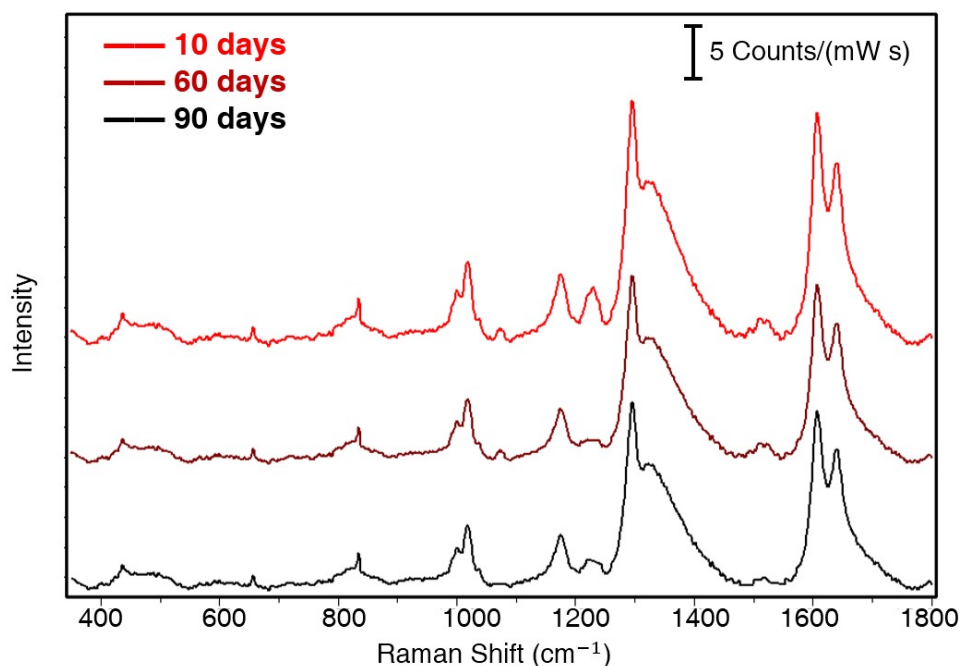


Figure 3.12: SERS spectra of **CBCat** over 90 days, where few changes were observed, suggesting good colloidal stability of the **CBCat**.

3.2.4 Detection of target analytes

The electron deficient nature of G_1 facilitates the subsequent inclusion of electron rich aromatic molecules in CB[8], forming ternary complexes of $[G_2 \cdot G_1]@CB[8]$.⁵³ Therefore, $G_1@CB[8]$ complexes immobilised on the **CBCat** surface can serve as "receptors" to collect analytes, from aqueous media into hot-spots to perform SERS detection. A variety of aromatic compounds were investigated (G_2), including dopamine (i), 2-naphthol (ii), phloroglucinol (iii), 4-(phenylazo)-phenol (iv), tetrathiafulvalene (v) and indole (vi). SERS signals from the analytes can be clearly identified in all SERS assays (Figure 3.13). Taking the detection of dopamine (Figure 3.13 (i)) as an example, **CBCat** (48 mg L^{-1}) was added to a dopamine solution ($30 \text{ }\mu\text{M}$) and irradiated at 785 nm. Signature peaks of dopamine are clearly observed, with peaks at 580, 983 and 1643 cm^{-1} mainly attributed to the aromatic ring deformation and O-H scissoring, a peak at 1107 cm^{-1} mainly attributed to the C-C-H bending and N-H twisting, a peak at 1463 cm^{-1} attributed to the aromatic C=C stretching and C-H scissoring, and a peak at 1294 cm^{-1} mainly attributed to the phenolic C-O stretching.¹⁹¹ Analogous to the detection of other aromatic compounds, where signature SERS peaks are all observed and highlighted in Figure 3.13 (ii)-(vi) (see the Experimental Appendix for powder Raman Spectra of G_2 s and binding constants of ternary complexes $[G_2 \cdot G_1]@CB[8]$). In comparison, SERS detection assays were also carried out on a CB[7] catenanes on spiky $\gamma\text{-Fe}_2\text{O}_3@Au$ NPs (**CB7Cat**), using which none of the analytes could be detected (Figure 3.14). Unlike CB[8], CB[7] can only accommodate one guest molecule in its cavity, thus the tethered CB[7] was occupied by G_1 and there was no extra space for analytes to go inside. The analytes did not possess metal binding groups and could not adsorb on the spiky NP surface, thus could not be detected.

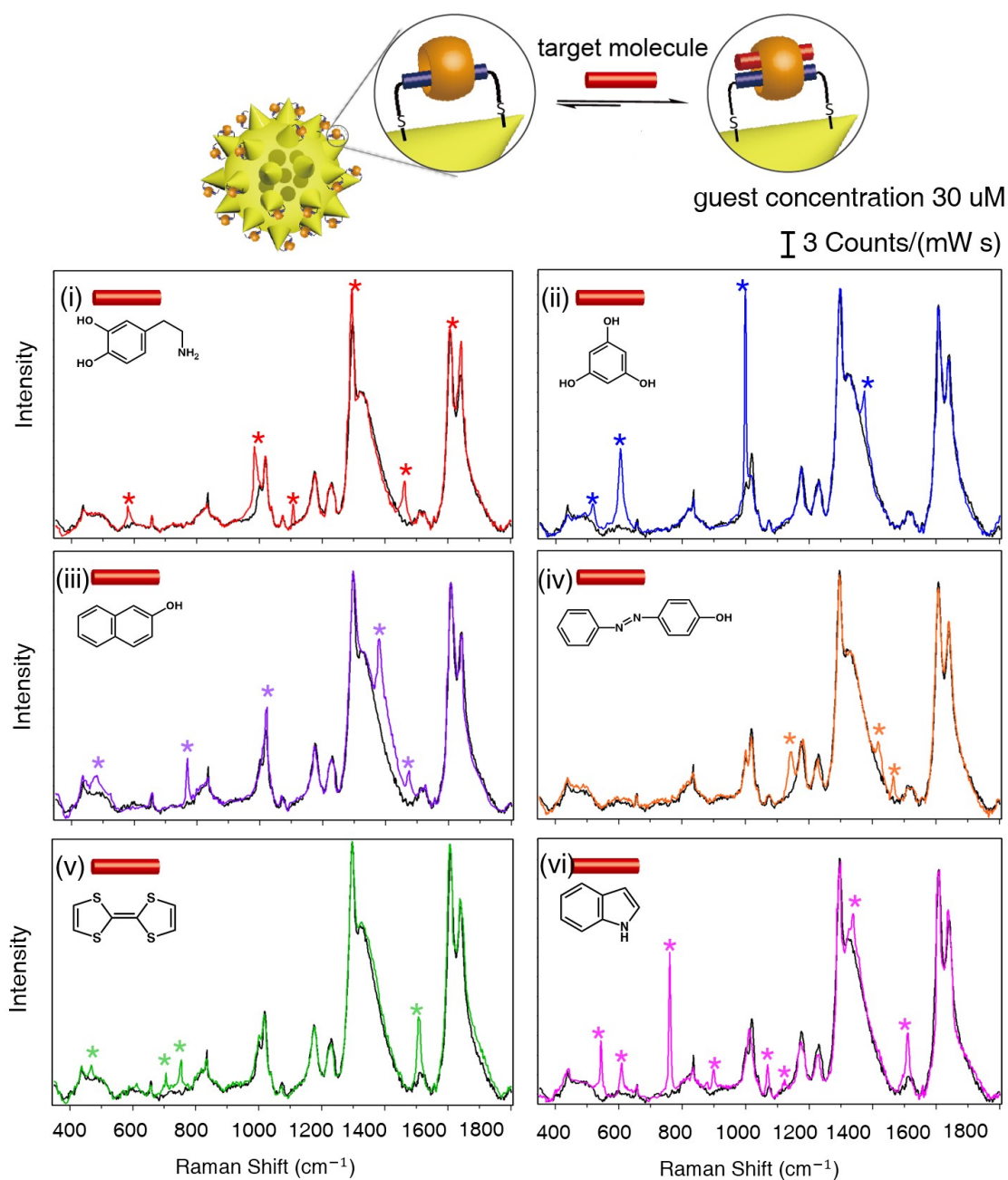


Figure 3.13: SERS spectra of the detection of target guest molecules (G_2 , 30 μM) using CBCat (48 mg L^{-1}). Spectra are stacked with the SERS spectrum of solely CBCat (black) for comparison. Signature peaks of all guest molecules can be clearly observed and are highlighted with asterisks in the figures. Chemical structures of electron-rich aromatic second guests (G_2) are listed in the figures: dopamine (i), 2-naphthol (ii), phloroglucinol (iii), 4-(phenylazo)-phenol (iv), tetrathiafulvalene (v) and indole (vi).

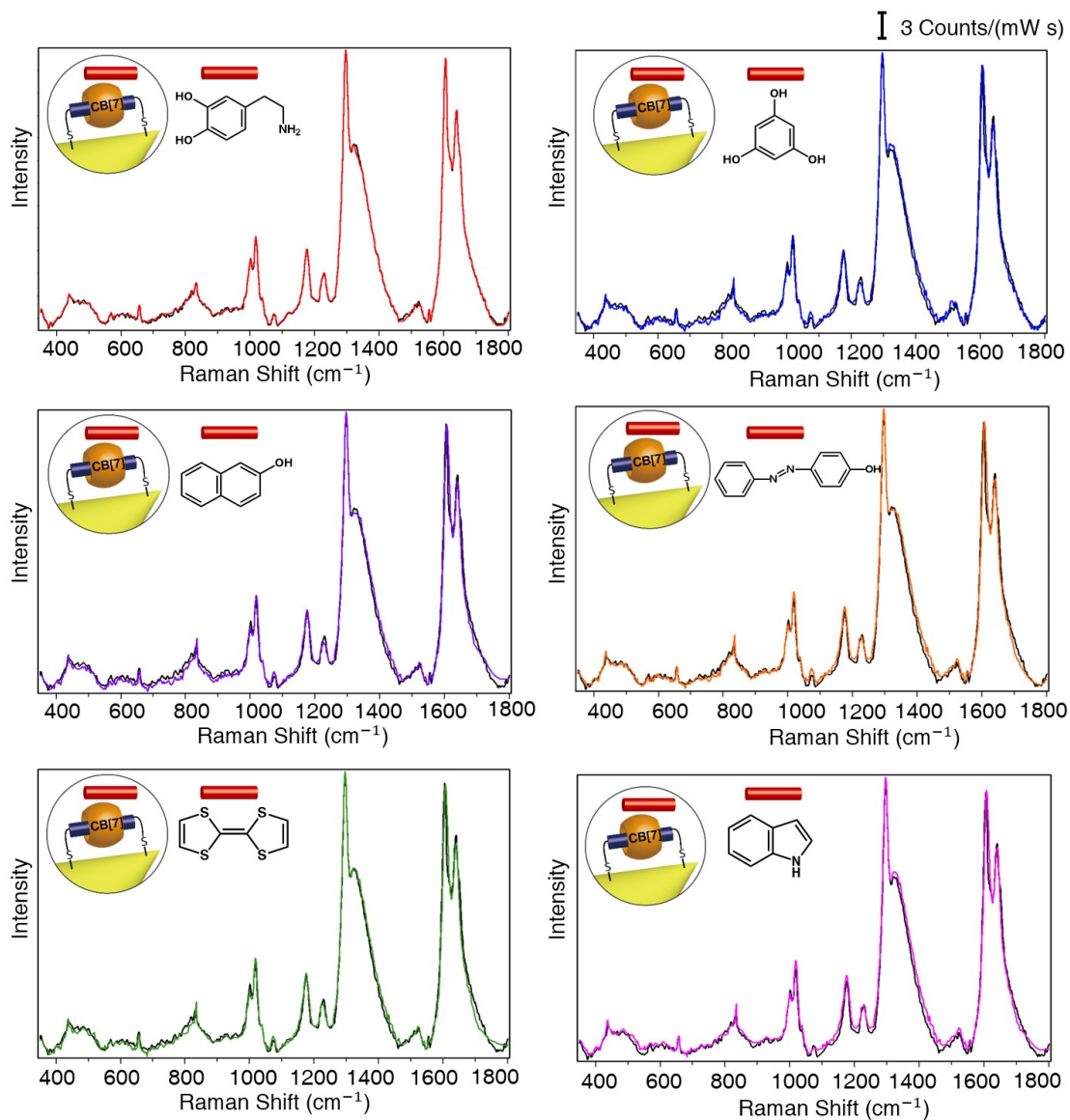


Figure 3.14: SERS spectra of **CB7Cat** with target guest molecules (30 μM), where nearly no difference of the SERS spectra before and after mixing with the targets were observed. Spectra are stacked with the SERS spectrum of solely **CB7Cat** (black) for comparison. CB[7] can only encapsulate one guest molecule in its cavity, therefore, there was no extra space in CB[7]'s cavity for target molecules to accommodate in **CB7Cat**.

3.2.5 Detection of controlled substances

CBCat is promising for the detection of various biomolecules and chemicals, including some controlled substances (e.g. illegal stimulant). The abuse of illegal stimulant is of increasing concern in many countries and a rapidly growing problem particularly in modern competitive sports. Methods for dope analyses typically involves colourimetry,¹⁹² electrochemistry,¹⁹³ fluorescence assays,¹⁹⁴ gaschromatographic mass spectrometry (GC-MS) and high-performance liquid chromatography (HPLC).¹⁹⁵ However, such methods are limited by complicated preparation and high cost.¹⁹⁶ In this regard, there is a growing demand for a simple, fast, sensitive and cheap analysis method to detect stimulants in competitive sports.¹⁹⁶ CB[n] derivatives are capable of selectively sequestering various aromatic dope molecules; therefore, the **CBCat**, which combines the selectivity of supramolecular chemistry and the sensitivity of SERS, is promising for the detection of dopes. Here, we demonstrate that 1,5-pentamethylene-1H-tetrazole, a commonly abused dope, can be detected by the **CBCat** with a high sensitivity (down to 100 ng/mL, Figure 3.15 (ii)). In addition, the use of different aqueous media (phosphate buffer solution at pH 7.4, urine control) shows little influence on the detection capability of the **CBCat** system, as shown in Figure 3.15 (iii-iv).

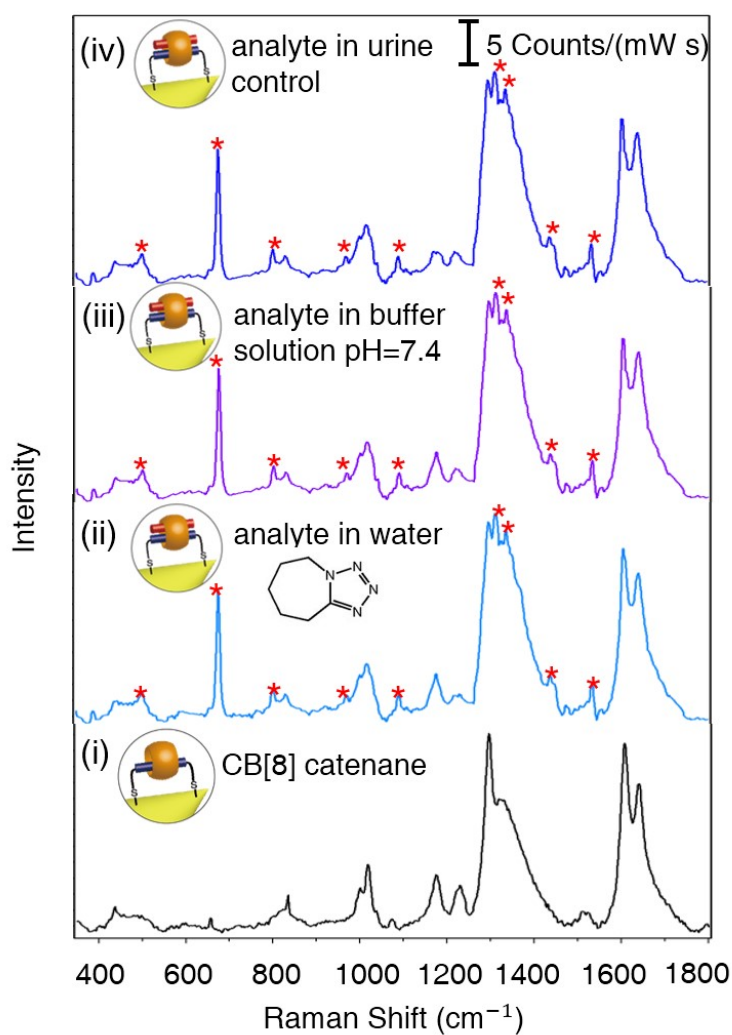


Figure 3.15: SERS spectra of controlled substance (1,5-pentamethylene-1H-tetrazole) detection using **CBCat** in different media: water (ii), phosphate buffer solution pH=7.4 (iii) and ClinChek[®] urine control lyophil (iv). The signature peaks of the stimulant molecule could be observed clearly in all solutions, showing few differences.

3.3 Conclusion and Outlook

In conclusion, we have demonstrated an advanced molecular sensor exploiting a catenane-engineered nanostructure, by tethering CB[8] onto the surface of spiky γ -Fe₂O₃@Au NPs. The deliberately designed spiky shapes contribute to a high SERS enhancement factor (in the magnitude of 10⁸) and enable target analytes to be detected with high level of sensitivity (down to 30 μ M). The incorporation and immobilisation of macrocyclic host molecule CB[8] on the molecular sensor allows for a greater variety of analyte molecules to be detected *via* SERS techniques. Moreover, this molecular sensor shows improved colloidal stability, acting as a free-standing sensor in water, aqueous buffer or biological system. The embedding of magnetic cores is promising for the easy magnetic separation of the substrate from aqueous phase. We envisage that this stable and sensitive molecular sensor will provide a useful platform for the detection of controlled substances and auxiliary diagnostics of various diseases.

3.4 Experimental Appendix

3.4.1 Materials and general methods

All the starting materials were purchased from Alfa Aesar and Sigma Aldrich and used as received unless stated otherwise. CB[7] and CB[8] were prepared according to literature.⁷⁷

¹H NMR (400 MHz) spectra were recorded using a Bruker Advance QNP 400. DLS and zeta potential measurements were performed on a Malvern Zeta-sizer NS90. UV-*vis* spectra were obtained on a Varian Cary 4000 UV-*vis* spectrometre. Titration experiments were carried out on a MicrocalTM ITC₂₀₀ (isothermal titration calorimetry). TEM and STEM-EDX images were obtained on a FEI Philips Tecnai20 TEM (Specifications: accelerating voltage 100 keV, double tilt specimen holder, SIS imaging software and CCD camera). Samples were prepared by applying one drop of the metallic NP solutions onto a Holey R carbon coated copper TEM grid (400 mesh), followed by drying overnight at room temperature. Extinction measurements for the nanoparticles were monitored with an Ocean

Optics 650-USB Red Tide spectrometre and SERS spectra were recorded on a Renishaw inVia Raman microscope (Specifications: 137 mW, 785 nm, 120 μm focal spot diameter and a dark noise level of less than 80 rms at 9 ms, per scan.)

3.4.2 Synthesis and characterisation of HS-MV-SH

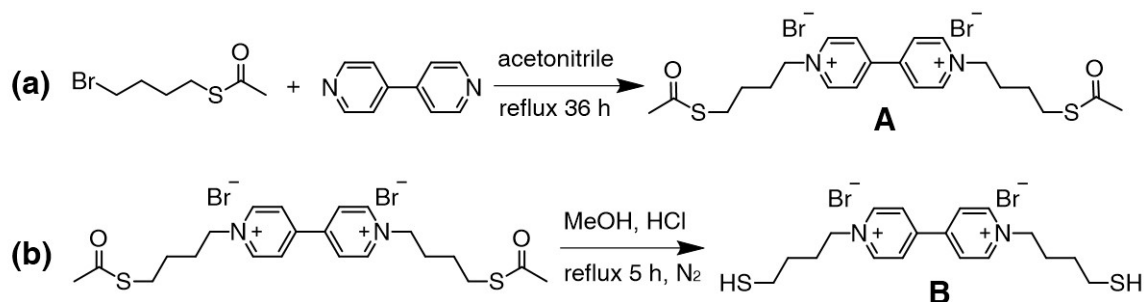


Figure 3.16: Reaction scheme of the synthesis of 1,1'-bis(4-mercaptobutyl)-4,4'-bipyridine (HS-MV-SH.)

(a) A solution of S-(4-bromobutyl) ethanethioate (4.66 g, 14.2 mmol) and 4,4'-bipyridine (0.44 g, 2.85 mmol) in acetonitrile (15 mL) was refluxed at 80 °C for 36 h, whereupon it became orange with abundant yellow precipitate. The mixture was then cooled to room temperature, sonicated and filtered. The precipitate was washed with cold ethanol (2x10 mL), cold dichloromethane (DCM, 2x10 mL) and cold diethyl ether (DEE, 2x10 mL). The crude product was purified by recrystallisation from boiling ethanol and dried in vacuum oven overnight. The product obtained (**A**) was a yellow powder (1.12 g, yield of 68%). ¹H NMR (400 MHz, D₂O), 9.03 (*d*, 4H), 8.88 (*d*, 4H), 4.98 (*t*, 4H), 3.12 (*t*, 4H), 2.28 (*s*, 6H), 2.01 (*m*, 4H), 1.87 (*m*, 4H). Mass Spectra, *m/z* = 418.65 g/mol.

(b) Hydrochloric acid (1.25 M, 4 mL) in methanol was added to the solution of **A** (12 mM in 16 mL methanol). The mixture was heated to reflux at 65 °C for 5 h, and then cooled to room temperature, drying by rotary evaporation. The product obtained (**B**) was a yellow solid (0.4 mg, yield of 83%), which was then stored under nitrogen. ¹H NMR (400 MHz, D₂O), 9.03 (*d*, 4H), 8.86 (*d*, 4H), 4.97 (*t*, 4H), 2.53 (*t*, 4H), 2.01 (*m*, 4H), 1.79 (*m*, 4H), 1.42 (*s*, 2H). Mass Spectra, *m/z* = 334.2 g/mol.

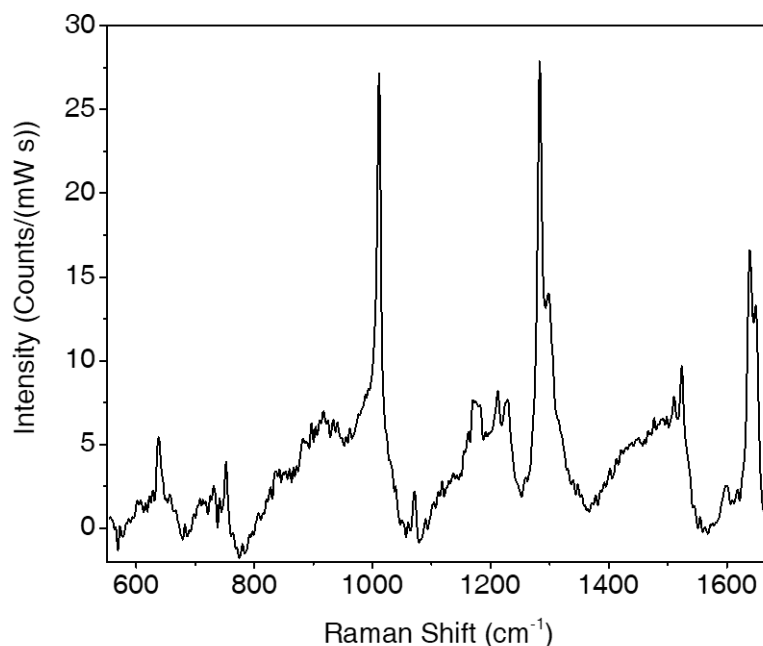


Figure 3.17: Powder Raman spectrum of solid HS-MV-SH, where the signature peaks at 638, 752, 1011, 1283, 1524 and 1639 cm⁻¹ were observed.

3.4.3 Preparation of spiky γ -Fe₂O₃@Au NPs

The spiky γ -Fe₂O₃@Au NPs were synthesised by a modified Lyon's iterative hydroxylamine seeding method.^{189,197}

Firstly, γ -Fe₂O₃ NPs were synthesised by the oxidation of freshly prepared Fe₃O₄ NPs using 0.01 M HNO₃ under heating at 90-100°C for 30 min and dispersed in TMAOH (tetramethylammonium hydroxide pentahydrate, 250 mL, 0.1 M) after washing with copious water.¹⁸⁹ The γ -Fe₂O₃ NPs (7.0 mL, 1.1 mM) were then mixed with sodium citrate solution (7.0 mL, 0.1 M) for 10 min to exchange adsorbed OH⁻ with citrate anions, followed by dilution using deionised water to 140 mL. Subsequently, NH₂OH·HCl solution (0.7 mL, 80.0 M) and HAuCl₄ (7.0 mL, 1.0 mg mL⁻¹) were added dropwise under stirring for total 50 min, respectively. The addition of NH₂OH·HCl and HAuCl₄ was repeated for another 2 times, with at least 10 min between additions. The clear yellow solution became blue at first addition and further changed to garnet after three iterative additions. After 5 h stirring, the solution was washed with copious amounts of water *via* centrifugation

at 10000 rcf.

3.4.4 Preparation of CB[8] catenanes on spiky γ -Fe₂O₃@Au NPs (CBCat)

CBCat was prepared by the immobilisation of HS-MV-SH@CB[8] inclusion complexes onto the surface of spiky γ -Fe₂O₃@Au NPs. Firstly, CB[8] (5.1 mg, 3 μ mol) and HS-MV-SH (2.5 mg, 5 μ mol) were dissolved in 5 mL deionised water and sonicated for 5-10 min. After that, the complex solution was mixed with 5 mL prepared spiky γ -Fe₂O₃@Au NP solution (96 mg/L), followed by 10 min sonication (concentrations were obtained by UV-vis titration). The mixture solution was then dialysed in 10 mM ADA (1-adamantylamine) solution for 3-5 days to eliminate unfixed CB[8]. The CB[7] catenane control NP (**CB7Cat**) was prepared by the same method using CB[7] instead.

3.4.5 Molecular detection using CBCat by SERS

To confirm the formation of CB[8] catenane structure on spiky NPs, SERS measurements of solely HS-MV-SH functionalised spiky NPs, CB[8] catenanes on spiky NPs (**CBCat**), and CB[7] catenanes on spiky NPs (**CB7Cat**) followed by a series of guests detection were carried out. None of the guests could be detected using **CB7Cat** since CB[7] can only encapsulate one guest molecule in its cavity (in this case HS-MV-SH) and there was no extra space for another guest. On the contrary, the target guests could be clearly detected by **CBCat** on account of CB[8]'s capability to encapsulate two guests in its cavity in the meantime, confirming the formation of CB[8] catenane structures on spiky NPs. Note: sufficient dialysis using ADA was performed to eliminate unfixed CB[8] in the last step of catenane preparation.

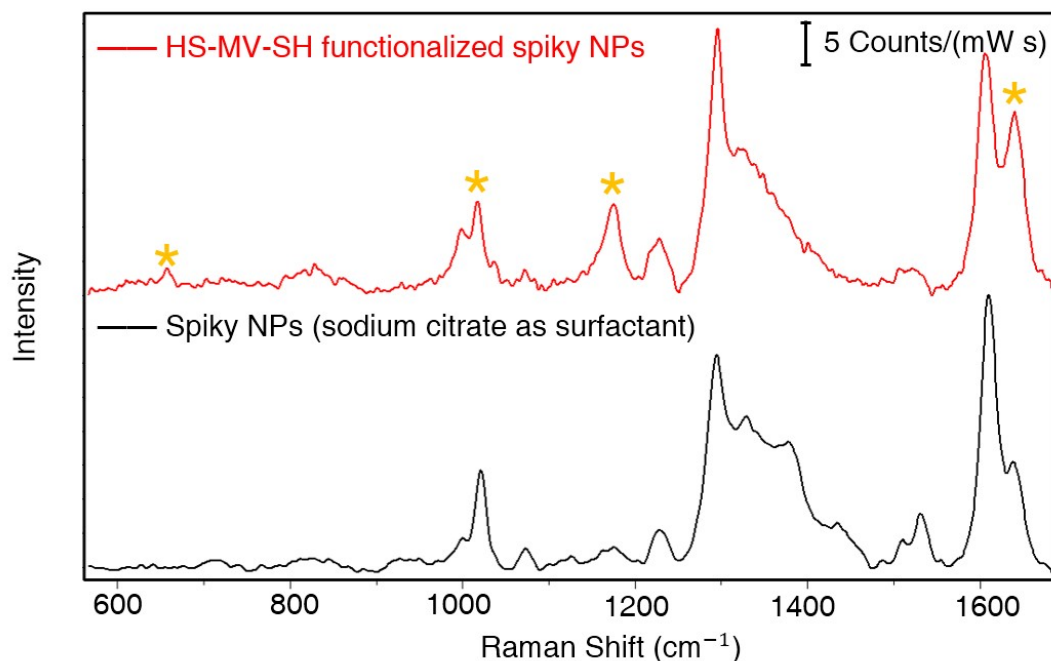


Figure 3.18: SERS spectra of spiky $\gamma\text{-Fe}_2\text{O}_3\text{@Au}$ NPs (black, sodium citrate as surfactant) and HS-MV-SH functionalised spiky $\gamma\text{-Fe}_2\text{O}_3\text{@Au}$ NPs (red), where the signature peaks of HS-MV-SH were clearly observed and marked with yellow asterisks (*). In particular, as shown in the black spectrum, signature peaks of sodium citrate at 1019 (stretching of CCO), 1072 (symmetric stretching of CC), 1226 (stretching of CCO), 1292 (stretching of CO and deformation of OH), 1425 (stretching of CO and deformation of OH), and 1609 cm^{-1} (asymmetric stretching of CO_2^-) were observed.^{198–200} After functionalisation using HS-MV-SH (red spectrum), new peaks at 657 (stretching of C-S near gold surface), 1012 (stretching of N-R and deformation of C-H), 1176 (stretching of N-R and deformation of C-H), and 1641 cm^{-1} (vibration of MV ring part) were observed,^{190,198,199} confirming the immobilisation of HS-MV-SH on the NP surface. (See Figure 3.17, 3.24 and 3.23 for powder Raman spectra of HS-MV-SH, sodium citrate and MVCl_2 .)

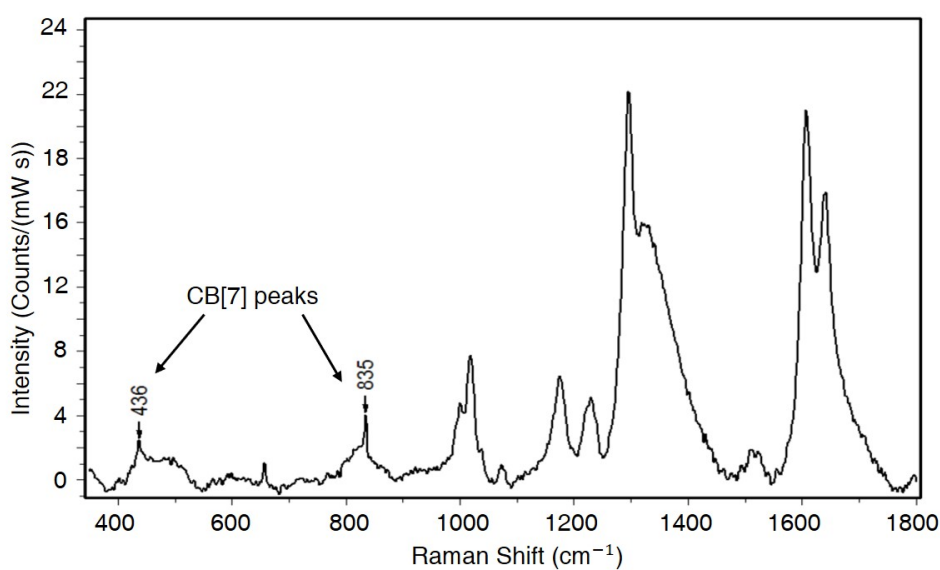


Figure 3.19: SERS spectrum of CB[7] catenanes on spiky $\gamma\text{-Fe}_2\text{O}_3\text{@Au}$ NPs (**CB7Cat**), almost the same with **CBCat** (Figure 3.10).

3.4.6 Powder Raman spectra of investigated molecules

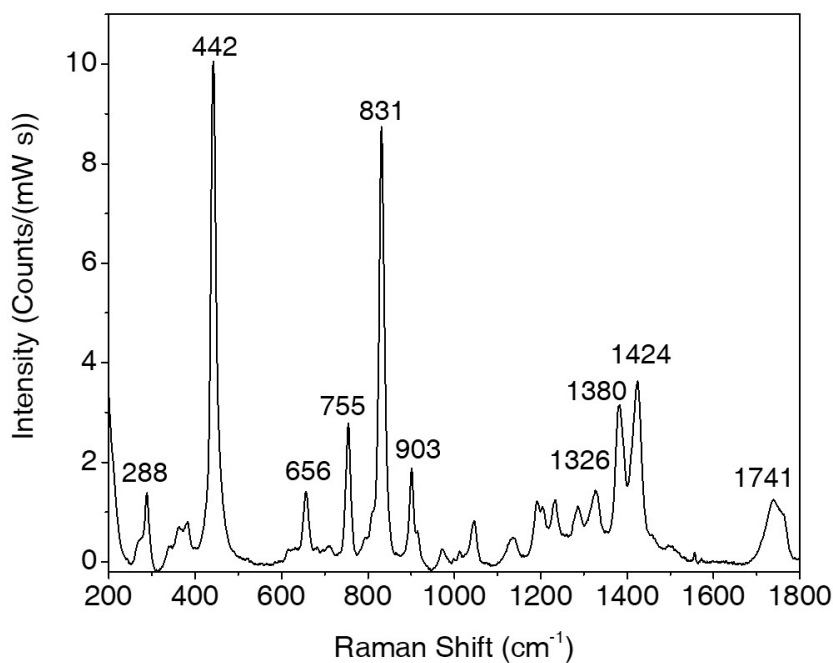


Figure 3.20: Raman spectrum of solid CB[7].

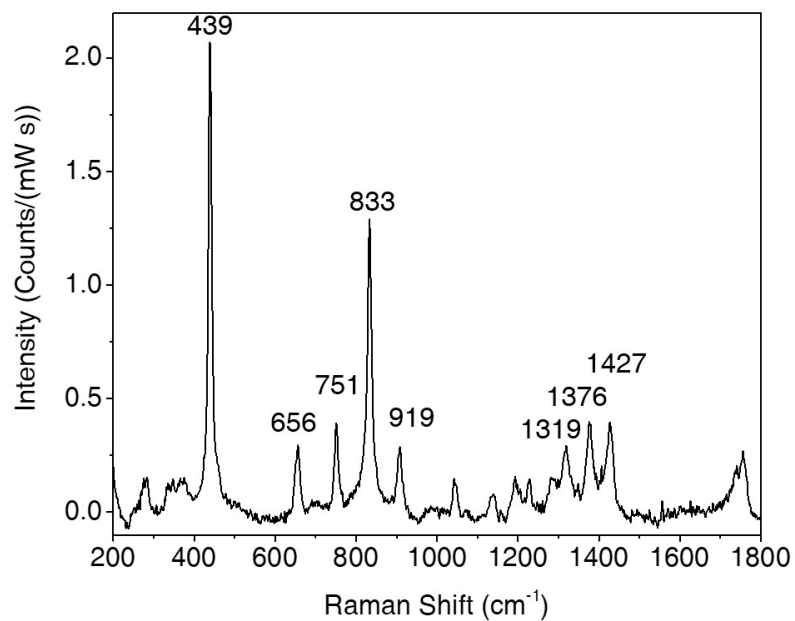


Figure 3.21: Raman spectrum of solid CB[8].

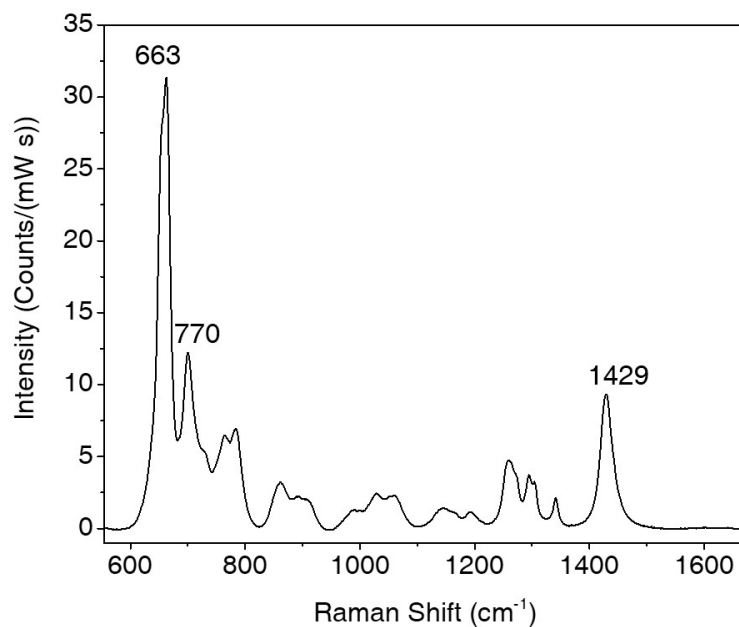


Figure 3.22: Raman spectrum of pure HS(CH₂)₃SH.

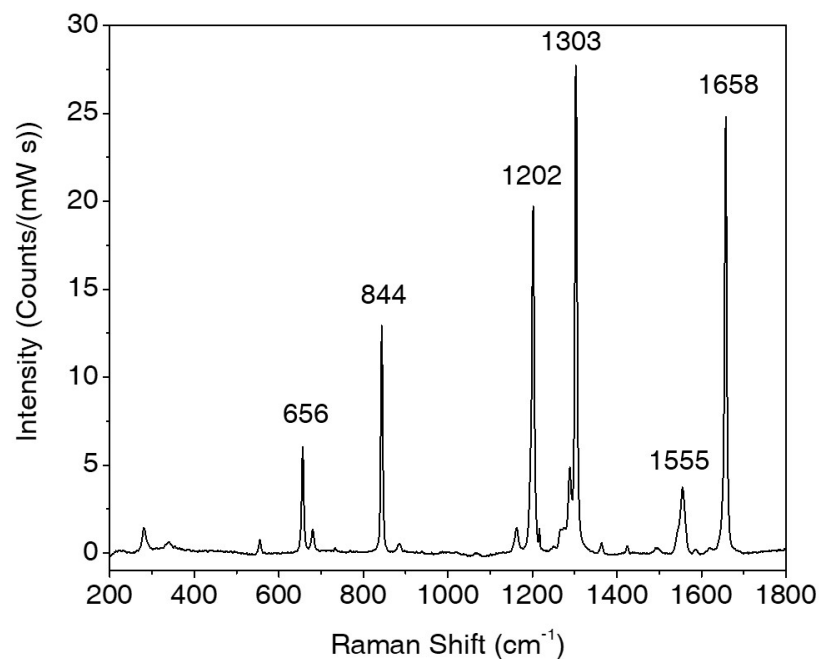


Figure 3.23: Raman spectrum of solid $MVCl_2$.

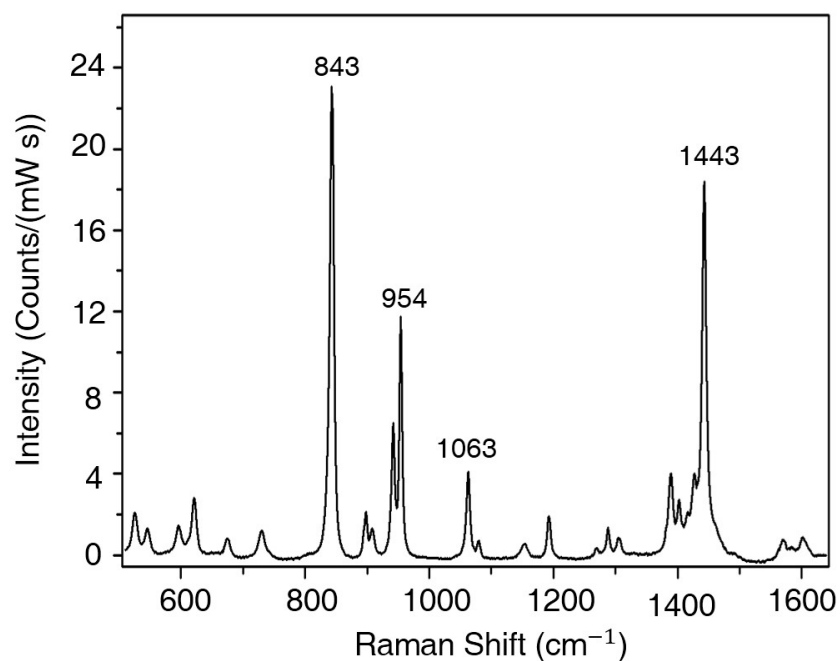


Figure 3.24: Raman spectrum of solid sodium citrate.

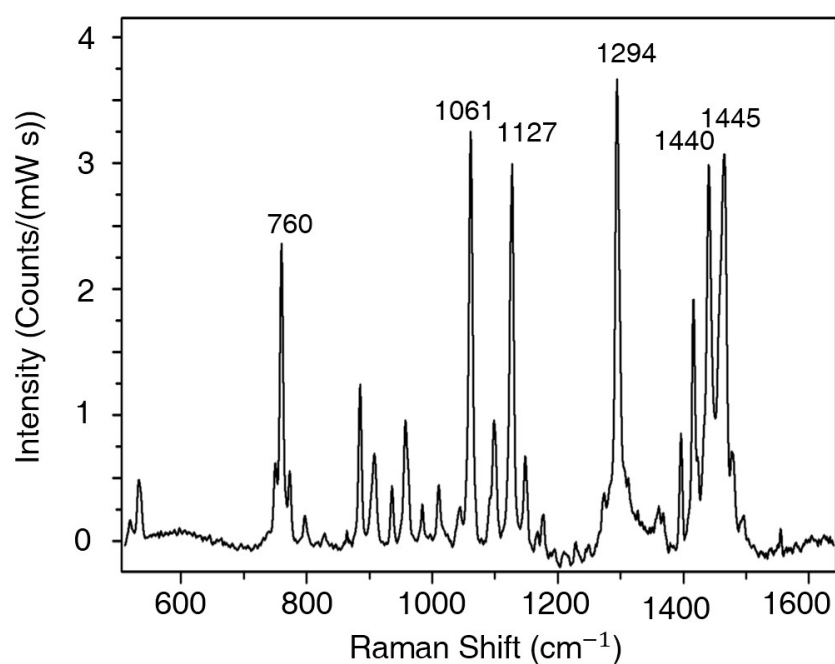


Figure 3.25: Raman spectrum of solid cetyl trimethylammonium bromide (CTAB).

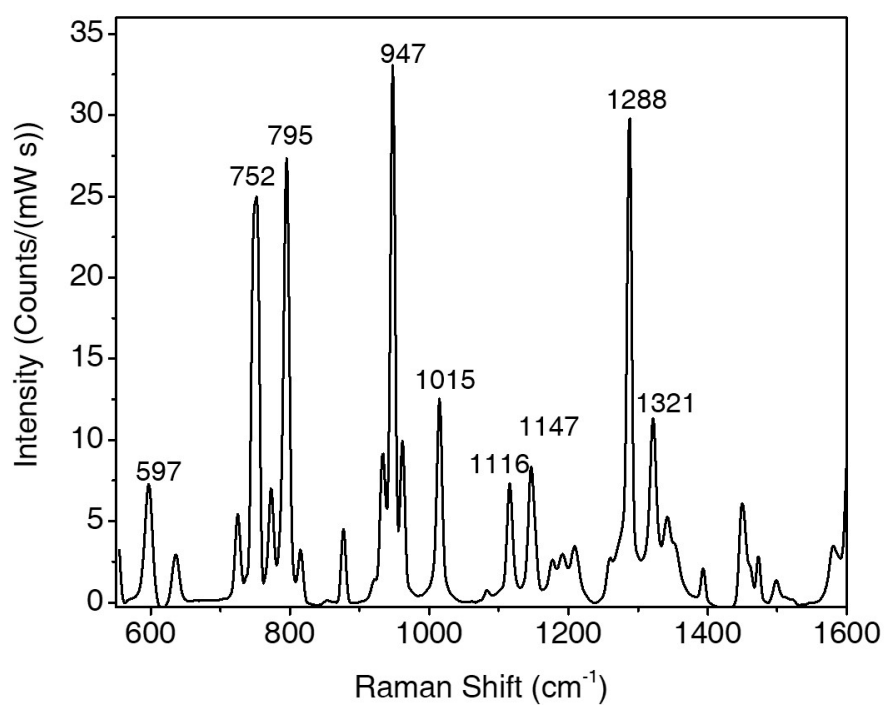


Figure 3.26: Raman spectrum of solid dopamine.

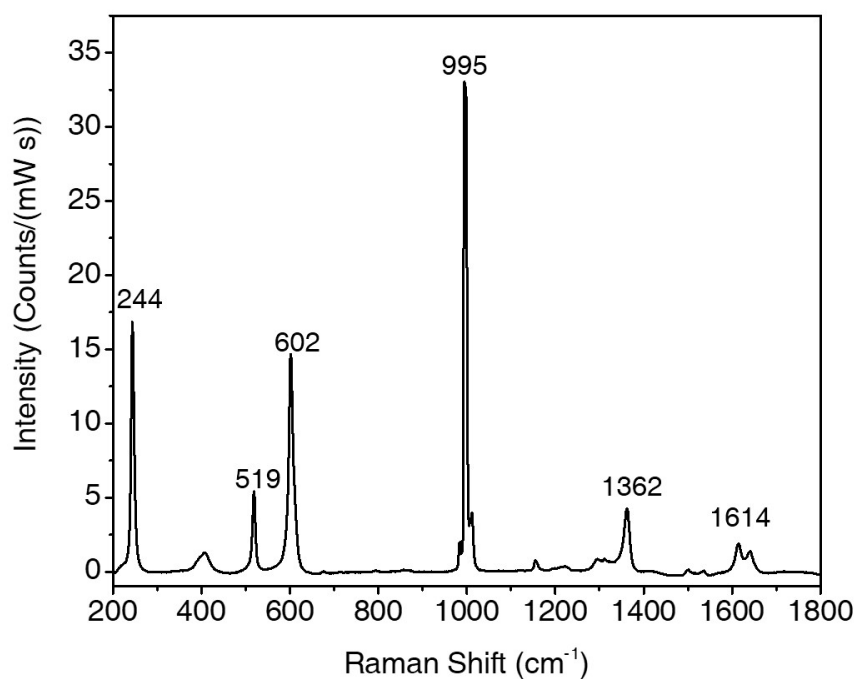


Figure 3.27: Raman spectrum of solid phloroglucinol.

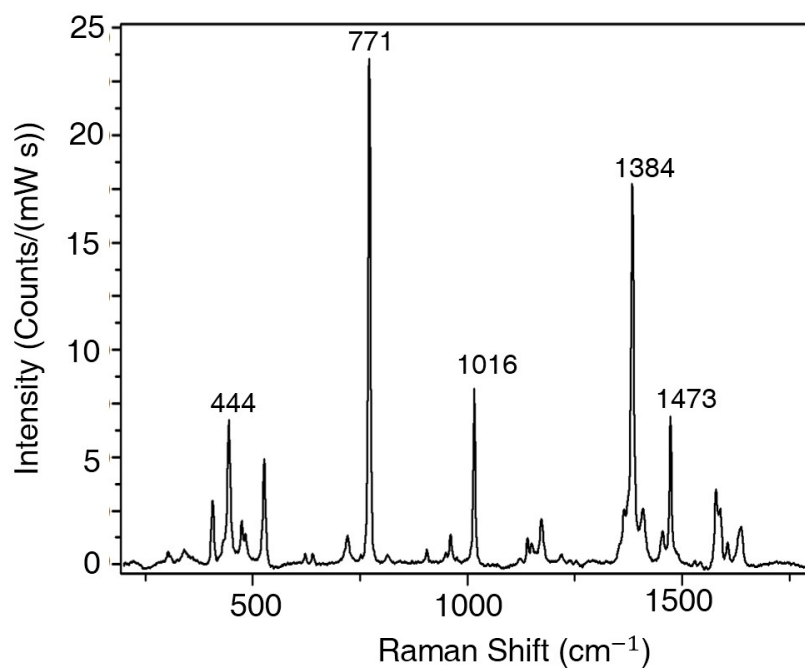


Figure 3.28: Raman spectrum of solid 2-naphthol.

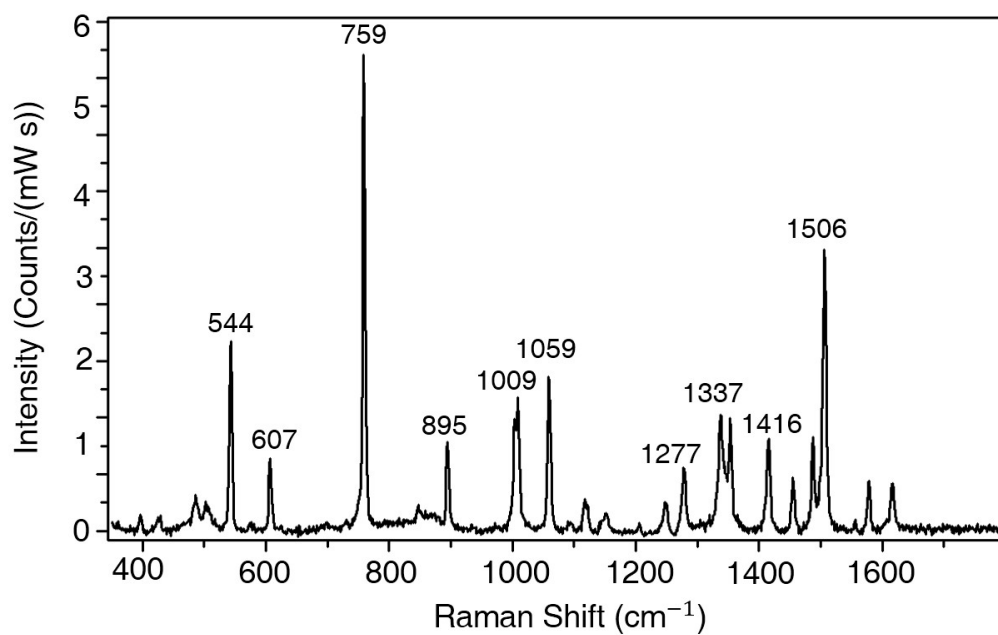


Figure 3.29: Raman spectrum of solid indole.

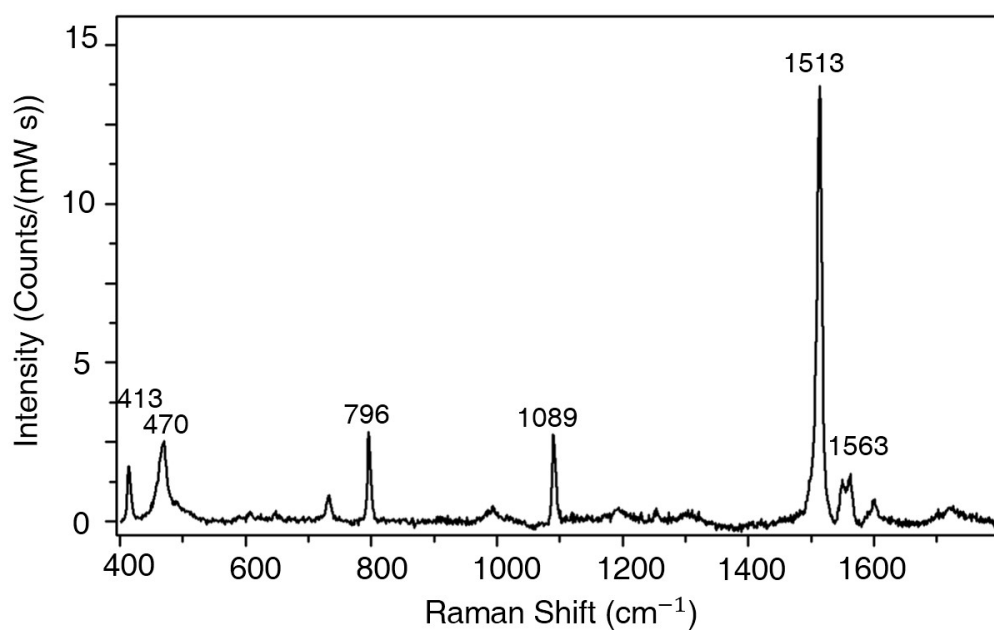


Figure 3.30: Raman spectrum of solid tetrathiafulvalene.

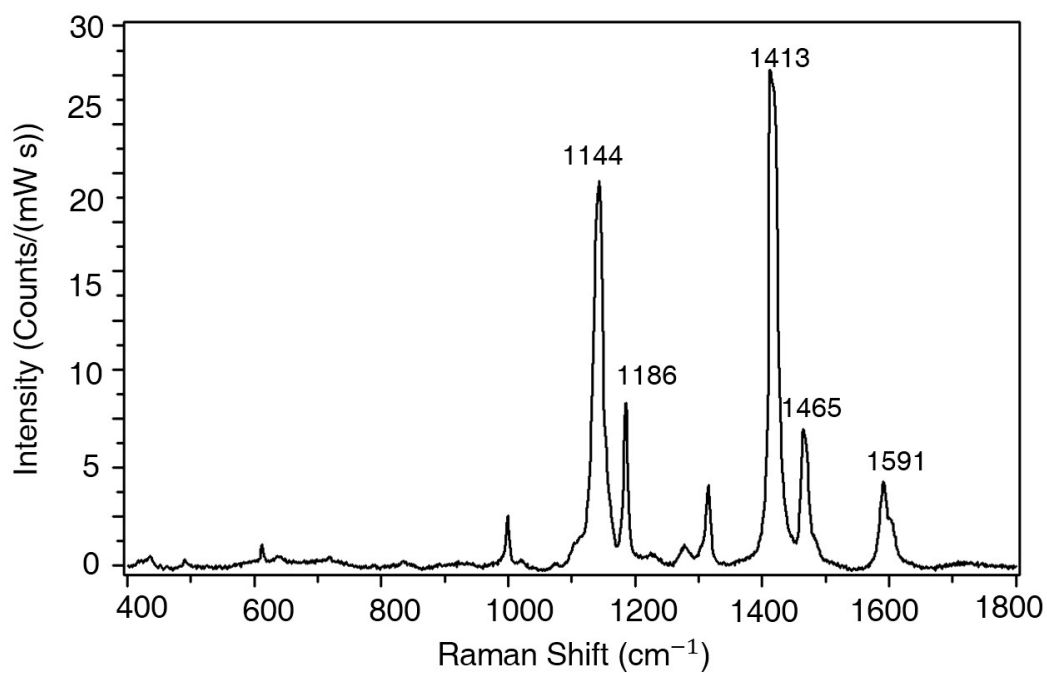


Figure 3.31: Raman spectrum of solid 4-(phenylazo)phenol.

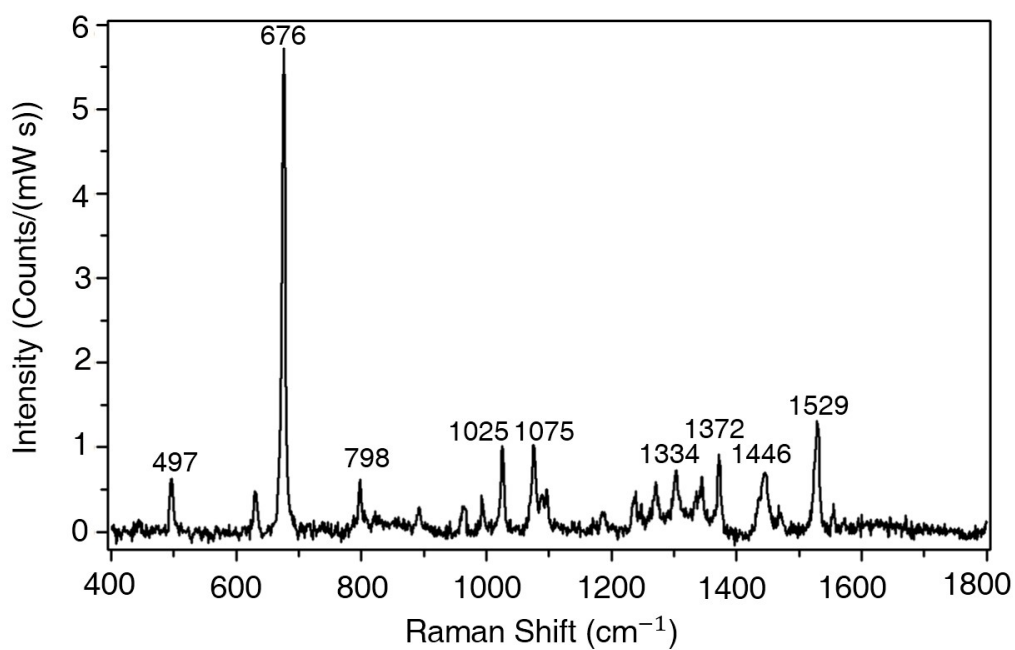


Figure 3.32: Raman spectrum of solid 1,5-pentamethylene-1H-tetrazole.

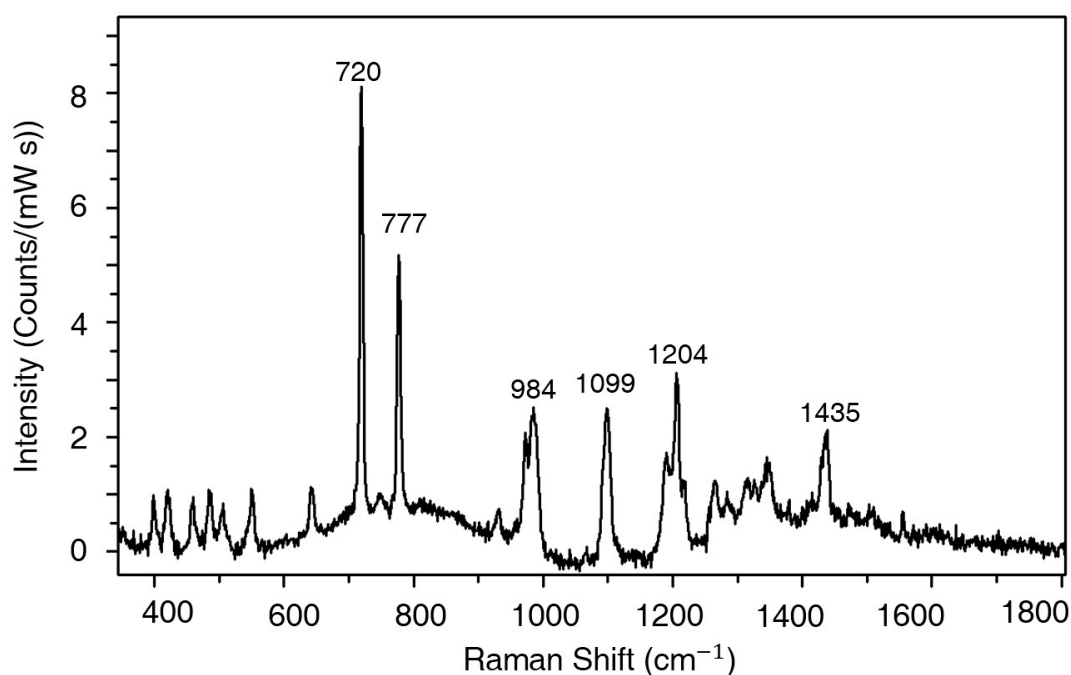


Figure 3.33: Raman spectrum of solid ADA.

3.4.7 Binding constants of ternary complexes

Binding constants of ternary complexes $[G_2 \cdot G_1]@CB[8]$ reported in literature and measured by ITC are listed in Table 3.1. 20 μM G_2 was injected into 0.2 mM HS-MV-SH@CB[8] in buffer solution at 25 °C. 50 mM sodium acetate buffer, pH=4.6, was used.

Table 3.1: Binding constants (K_a) of ternary complexes

G_2	K_a (M^{-1})
dopamine	10^4 - 10^5 ^{53,140}
phloroglucinol	$(5.1 \pm 0.3) \times 10^{2201}$
2-naphthol	$(8.9 \pm 0.6) \times 10^{5201}$
indole	$(6.1 \pm 4.4) \times 10^4$
tetrathiafulvalene	$(1.07 \pm 0.04) \times 10^5$
4-(phenylazo)phenol	$(4.9 \pm 0.3) \times 10^{5202}$
1,5-pentamethylene-1H-tetrazole	$(4.1 \pm 0.9) \times 10^4$

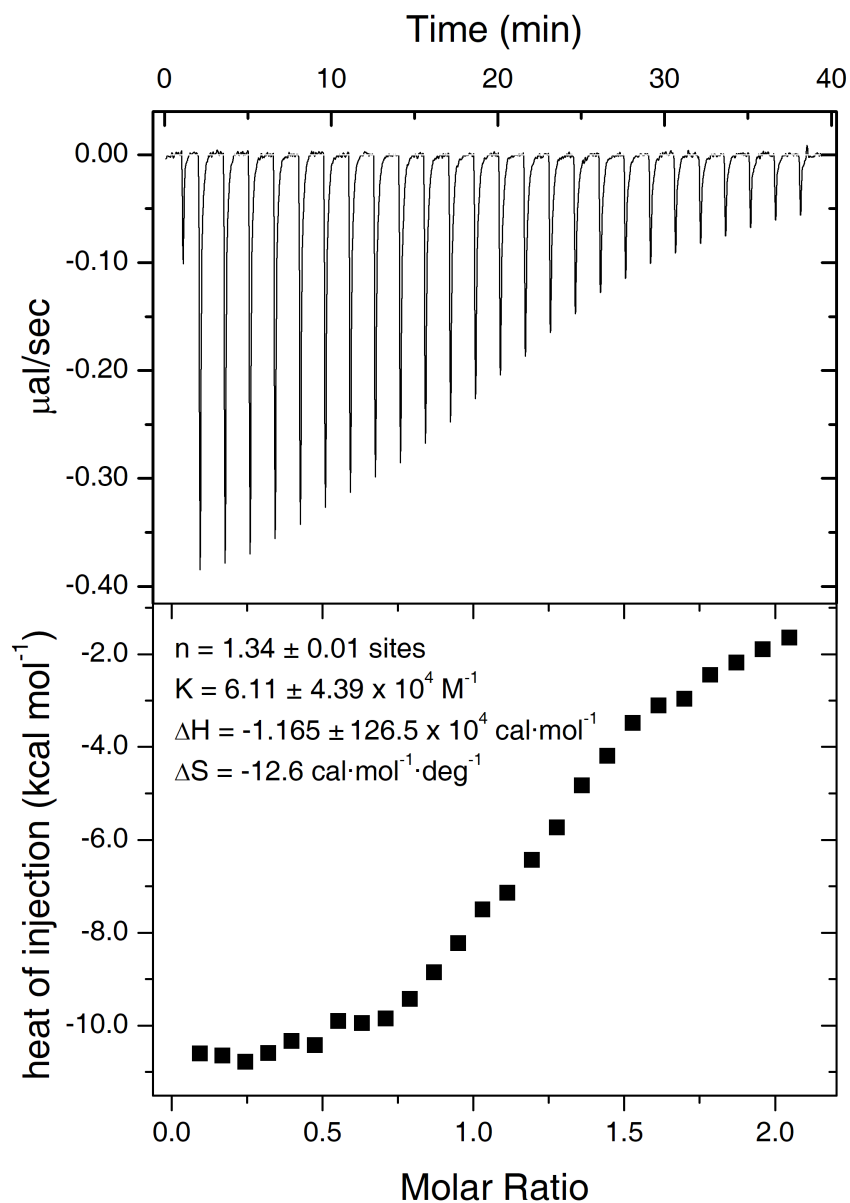


Figure 3.34: ITC result of the complexation between indole and HS-MV-SH@CB[8]. 200 μM indole was injected into 20 μM HS-MV-SH@CB[8] in buffer solution at 25 $^{\circ}\text{C}$. 50 mM sodium acetate buffer, pH=4.6, was used.

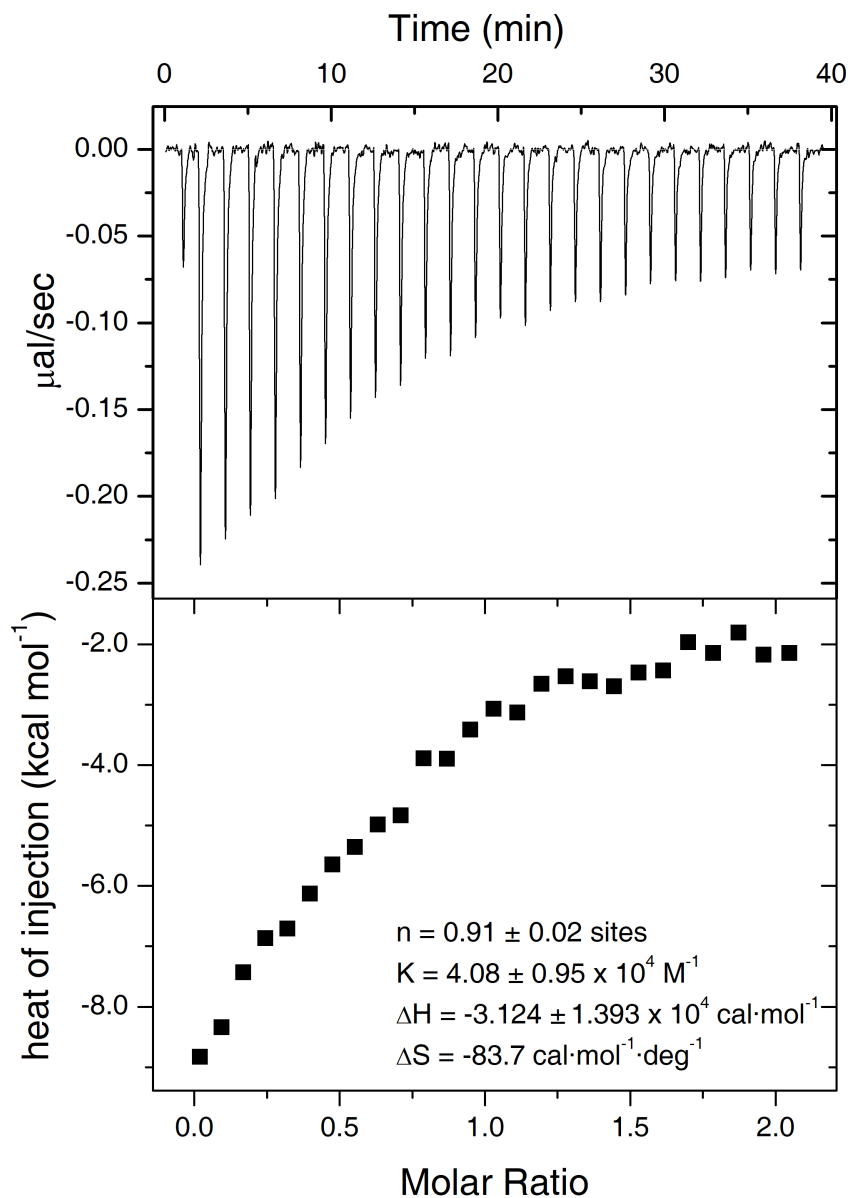


Figure 3.35: ITC result of the complexation between 1,5-pentamethylene-1H-tetrazole and HS-MV-SH@CB[8]. 200 μM 1,5-pentamethylene-1H-tetrazole was injected into 20 μM HS-MV-SH@CB[8] in buffer solution at 25 °C. 50 mM sodium acetate buffer, pH=4.6, was used.

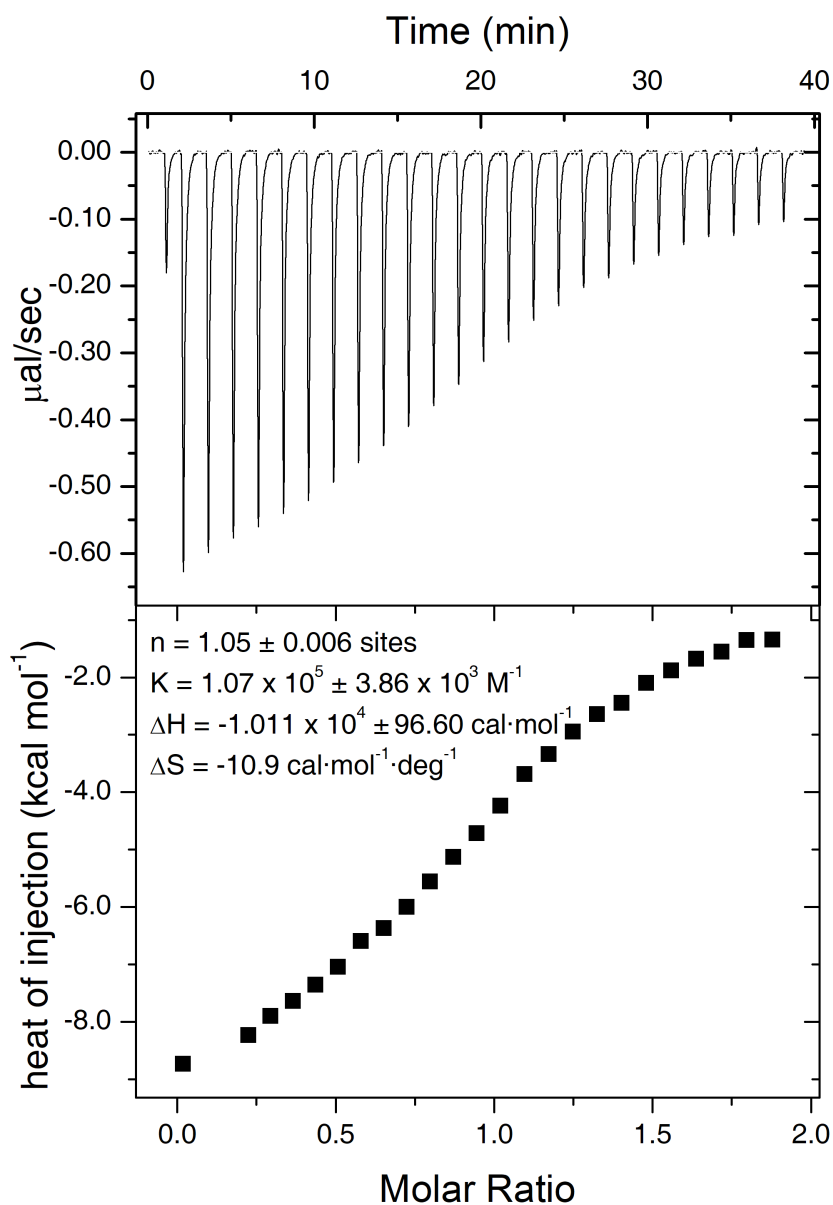


Figure 3.36: ITC result of the complexation between tetrathiafulvalene and HS-MV-SH@CB[8]. 200 μM tetrathiafulvalene was injected into 20 μmM HS-MV-SH@CB[8] in buffer solution at 25 $^{\circ}\text{C}$. 50 mM sodium acetate buffer, pH=4.6, was used.

3.4.8 UV-vis study of spherical Au NPs aggregation

UV-vis spectroscopy and zeta potential studies proved that spherical Au NPs would only aggregate with CB[8], but remained stable when mixed with HS-MV-SH or HS-MV-SH@CB[8] complex solutions, suggesting that HS-MV-SH bond only with single Au NP at the investigated concentrations.

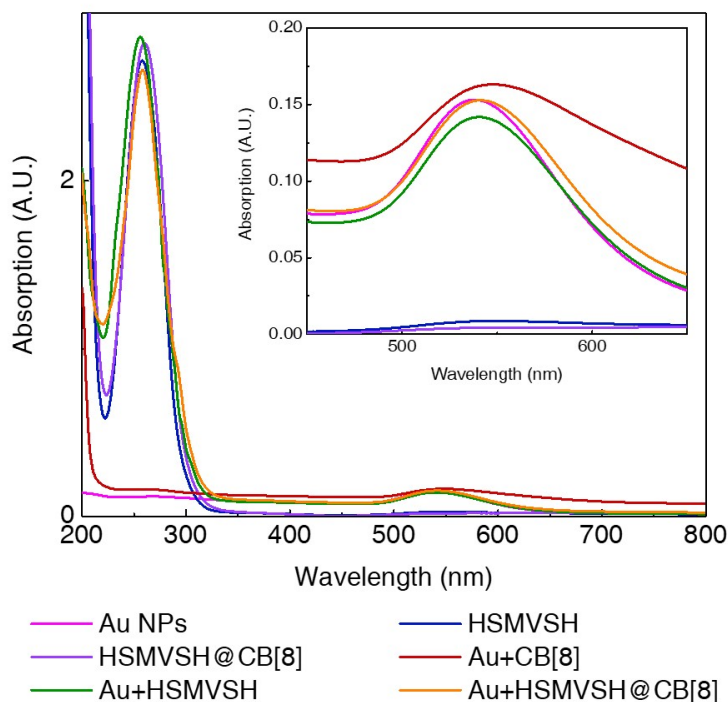


Figure 3.37: The UV-vis absorption spectra of Au NP solution, HS-MV-SH solution, HS-MV-SH@CB[8] complex solution, and Au NP with CB[8], HS-MV-SH and HS-MV-SH@CB[8] complex solutions, respectively. Au NP solution was purchased from BBITM (60 nm, 56.8 mg/L, spherical) and the concentrations of HS-MV-SH and CB[8] were 1 mM and 0.6 mM respectively in each solution. Together with the zeta potential results (Table 3.2), it can be concluded that at the investigated concentrations, Au NPs would only aggregate when mixed with CB[8], but remained stable when mixed with HS-MV-SH or HS-MV-SH@CB[8] complex.

Table 3.2: Results of zeta potential study

	zeta potential [mV]	state of aggregation
Au NP solution	-29.4	stable
Au NP with CB[8] solution	+0.42	aggregated
Au NP with HS-MV-SH solution	+33.9	stable
Au NP with HS-MV-SH@CB[8] solution	+34.9	stable

3.4.9 Quantification of CB[8] surface density on spiky $\gamma\text{-Fe}_2\text{O}_3\text{@Au}$ NP

The surface density of CB[8] on spiky $\gamma\text{-Fe}_2\text{O}_3\text{@Au}$ NPs in **CBCat** was quantified using the same method as CB[8] catenanes on silica NPs,²⁰³ by ITC and UV-vis titration experiments. Briefly, **CBCat** was mixed with a guest molecule solution (concentration **A**), after sonication and centrifugation, **CBCat** was separated and the concentration of the supernatant solution (**B**) was measured by UV-vis and/or ITC. The surface density of CB[8] can then be deducted from a series of titration experiments based on the concentration decrease of the guest molecule solution (**A** - **B**). The calculation procedures are shown as follows.

For 1400 μL **CBCat** solution (48 mg/L), second guest molecule (dopamine, 1.5 mL) showed concentration decrease of 290 ± 50 nM.

The mass of **CBCat** NP added:

$$m(\text{CBCat}) = 48\text{mg/L} \times 1400\mu\text{L} = 67.2\mu\text{g}$$

The change of mole of dopamine in 1.5 mL:

$$\Delta n(\text{dopamine}) = \Delta c(\text{dopamine}) \times \text{Volume} = 590 \pm 50\text{nM} \times 1.5\text{mL} = 0.435 \pm 0.068\text{nmol}$$

which is equal to the mole of CB[8] in 67.2 μg **CBCat** added.

The total volume of NPs in 67.2 μg **CBCat**:

$$V_{\text{total}} = \frac{m}{\rho} = \frac{67.2\mu\text{g}}{11.37\text{g/cm}^3} = 5.91 \times 10^{-12}\text{m}^3$$

where ρ is the average density of spiky $\gamma\text{-Fe}_2\text{O}_3\text{@Au}$ NP, 11.37 g/cm³.

The volume of a single **CBCat** NP is:

$$V_{single} = \frac{4}{3}\pi r^3 = \frac{4}{3} \times \pi \times \left(\frac{133nm}{2}\right)^3 = 1.23 \times 10^6 nm^3$$

where r is the radius of the **CBCat** NP, which is equal to 133 nm/2 =66.5 nm, according to DLS and TEM image results. Note: the calculation of spiky NPs was simplified as spherical NPs in this calculation procedure.

The total number of the **CBCat** NP in 67.2 μ g **CBCat** is:

$$N = \frac{V_{total}}{V_{single}} = \frac{5.91 \times 10^{15} nm^3}{1.23 \times 10^6 nm^3} = 4.80 \times 10^9$$

The total surface area of the **CBCat** nanoparticle in 67.2 μ g **CBCat** is:

$$S = 4\pi r^2 N = 4 \times \pi \times 133^2 nm^2 \times 4.80 \times 10^9 = 2.66 \times 10^{14} nm^2$$

The average number of CB[8] in 67.2 μ g **CBCat** is:

$$N(CB[8]) = n(CB[8])NA = n(dopamine)NA = (2.62 \pm 0.41) \times 10^{14}$$

So the surface density of CB[8] on the spiky NP in **CBCat** is:

$$\frac{N(CB[8])}{S} = \frac{2.62 \pm 0.41 \times 10^{14}}{2.66 \times 10^{14} nm^2} = 0.9 \pm 0.2 nm^{-2}$$

3.4.10 Calculation of SERS enhancement factor

SERS enhancement factor (EF) was calculated by two methods: 3D-FDTD simulation (10^8 , Figure 3.11) and experimental measurements. The calculation of EF based on experimental measurements are shown as follows.

The most widely used definition equation for the average SERS EF is:

$$EF = \frac{I_{SERS}/N_{Surf}}{I_{RS}/N_{Vol}}$$

where $N_{Vol} = c_{RS}V$ is the average number of molecules in the scattering volume (V) for the Raman (non-SERS) measurement, and N_{Surf} is the average number of adsorbed molecules in the scattering volume for the SERS experiments.²⁰⁴ The methyl viologen peak at around 1280 cm^{-1} was chosen to calculate the SERS EF in this case. For the **CBCat** (48 mg/L, 330 μL , 30 s exposure time), 30000 ± 500 counts was obtained. For HS-MV-SH non-SERS Raman measurement (1 M, 330 μL , 120 s), 1700 ± 100 counts was obtained using the same laser power at 138 mW.

$$I_{SERS} = \frac{30000 \pm 500 \text{ counts}}{30 \text{ s}} = 1000 \pm 17 \text{ cps}$$

$$I_{RS} = \frac{1700 \pm 100 \text{ counts}}{120 \text{ s}} = 14.17 \pm 0.83 \text{ cps}$$

$$N_{Vol} = 1 \text{ M} \times 330 \mu\text{L} \times NA = 1.98 \times 10^{20}$$

$$N_{Surf} = \frac{N(\text{CB}[8]) \times 330 \mu\text{L}}{1400 \mu\text{L}} = \frac{2.62 \pm 0.41^{14} \times 330 \mu\text{L}}{1400 \mu\text{L}} = (6.2 \pm 1.0) \times 10^{13}$$

where $N(\text{CB}[8])$ is the number of CB[8] in 1400 μL **CBCat** (calculated in the previous section).

Therefore,

$$EF = \frac{1000 \pm 17 \text{ cps} / 6.2 \pm 1.0 \times 10^{13}}{14.17 \pm 0.83 \text{ cps} / 1.98 \times 10^{20}} = (2.25 \pm 0.20) \times 10^8$$

Chapter 4

γ -Fe₂O₃@Au Nanoraspberry Particles for High-performance SERS

Preparation of composite material structures for high-performance surface-enhanced Raman scattering (SERS) spectroscopy is of great interest for sensing applications. Various nanostructures have been developed to improve SERS signals, among which nanoraspberry particles have attracted great attention on account of their high curvature surface and precisely localised plasmonic interactions. Conventional preparation of nanoraspberry particles is generally based on a template-assisted method, attaching smaller nanoparticles onto the core particles with connecting ligands. These methods, however, suffer from various limitations, for example, low yields, inhomogeneity and instability. We demonstrate a facile preparation of a monodispersed γ -Fe₂O₃@Au magnetic nanoraspberry particles using a one-pot seeded growth method. The obtained nanoraspberry particles show excellent colloidal stability and high enhancement factors (on the order of 10¹⁰). By immobilising a dense layer of macrocyclic cucurbit[n]urils onto the nanoraspberry surface, it could act as a molecular sensor to detect analytes in solution with high sensitivities. This nanoraspberry-based molecular sensor provides a powerful platform for SERS detection in various fields, such as chemical and biomolecule analysis, and pre-clinical/clinical diagnosis.

This work has been submitted in the following peer-reviewed journal articles:

- **Ren, X.;** Wu, Y.; Kamp, M.; Liu, J.; Chikkaraddy, R.; Nijs, B. D.; Yu, Z.; Baumberg, J. J.*; Scherman, O. A.* “ γ -Fe₂O₃@Au core-shell magnetic nanoraspberry particles for high-performance SERS”, *submitted*.

4.1 Introduction

Surface-enhanced Raman scattering (SERS) spectroscopy is a powerful analytical technique widely used in various fields, including surface science,^{10,11} biomolecule analysis²⁰⁵ and material characterisation.^{5,206} Vibrational fingerprint information of analytes can be obtained with high sensitivity and specificity, even down to single-molecule level.^{5,207} One of the main challenges in realising efficient SERS detection is the preparation of composite material architectures exhibiting precisely localised plasmonic interactions.^{5,206,208} Hence, great efforts have been devoted to the preparation and optimisation of SERS substrates for high field enhancements, greater ease of use and high colloidal stability.^{5,53,205,206} The required plasmonic SERS-active nanostructures are generally fabricated using coinage-metal (e.g. Au, Ag, or Cu) on account of their ability to support surface plasmons, the collective oscillating modes of the conduction electrons at metal/dielectric interfaces.^{5,14} Controlled assembly of metallic nanoparticles (NPs) into dimers,^{209,210} trimers,²¹¹ and tailoring the NP shape into nanotriangle,²¹² nanostar,²¹³ nanoraspberry (or core-satellite nanoassemblies)^{11,214,215} have been developed to improve SERS signals. Among these nanostructures, nanoraspberry particles hold great potential as SERS substrate of ultrahigh sensitivity, on account of their highly enhanced electromagnetic fields in the gaps between the NP building blocks, which allow for great penetration of the electromagnetic field into the dielectric environment.^{5,214}

The predominant approach to fabricate nanoraspberry structures in solution is template-assisted method using organic (peptides,^{214,217} viruses,²¹⁸ polystyrene^{215,219}) or inorganic particles (silica,^{220,221} metals^{208,210,222,223}) as cores and attaching smaller inorganic NPs (Au, Ag NPs) with linkers such as DNAs^{210,216,224} and multithiols.^{11,225} Figure 4.1 shows an example of nanoraspberry structures prepared by DNA conjugates. The DNA-linked nanoraspberry particles provide easier control over the interparticle distance, but the intra-assembly gap distance reaches tens of nanometres since the DNA linkers require a certain minimal length to ensure proper base pairing.^{11,208,226} In addition, the distance between core and satellites is difficult to specify due to the non-specific adsorption of nitrogenous bases of DNA onto Au NPs; therefore, the nanoraspberry particles obtained

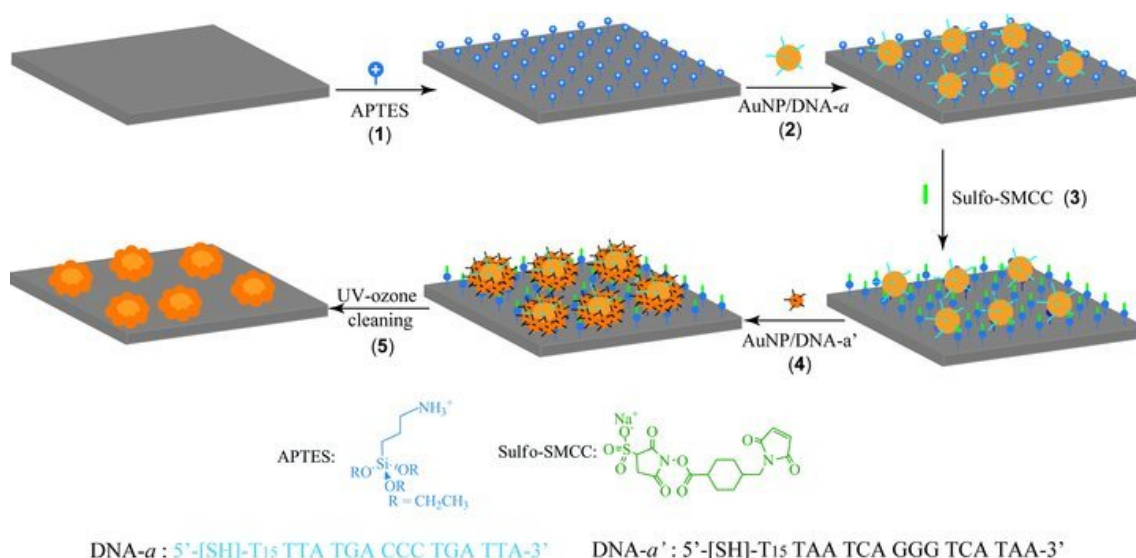


Figure 4.1: A schematic representation of the hierarchical self-assembly procedure for the fabrication of core-satellite plasmonic nanostructures: (1) APTES functionalisation of a glass substrate; (2) electrostatic immobilisation of 30 nm AuNP-DNA conjugates onto the APTES-modified substrate surface; (3) neutralisation of surface-confined amino groups by the formation of covalent amide bonds with sulfo-SMCC; (4) hybridisation of 20 nm AuNP-DNA conjugates onto the 30 nm AuNPs, forming the core-satellite nanoparticle assemblies; and (5) removal of the surface-confined molecules through UV-ozone cleaning, yielding pristine gold surfaces. Adapted from reference.²¹⁶

from this method are usually not suitable as high-performance SERS substrates.^{11,208,226,227}

Other methods using small molecules as linkers (e.g. multithiols) shorten the intra-assembly gaps. However, these methods suffer from various limitations, for example, colloidal instability, low yields, assemblies with unlinked NPs mixtures and harsh post separation conditions (e.g. high salt concentrations, nonpolar organic solvents, and high viscosity reagents).^{11,208,215,228–230}

Herein, we report a facile one-pot synthesis of γ -Fe₂O₃@Au magnetic nanoraspberry particles (NRSP) with high stability and homogeneity, as illustrated in Figure 4.2. The rough surface contributes to a significantly high SERS enhancement factor (on the order of 10^{10}), allowing this nanostructure for the applications in high-performance SERS detection. Embedding supraparamagnetic γ -Fe₂O₃ NPs provides facile magnetic separation of the NRSP from the detection media. Moreover, by complexing a dense layer of the macrocyclic host cucurbit[*n*]uril (CB[*n*]) onto the NRSP surface, it can further act

as a molecular sensor to detect analytes in solution with high sensitivities. We demonstrate the effective SERS detection of various electron rich and electron deficient analytes using CB[7] and CB[8]-functionalised NRSP. In particular, the detection of a controlled substance (ephedrine) with the sensitivity down to $350 \mu\text{g}\cdot\text{L}^{-1}$ has been demonstrated, reaching the standard of real-life ephedrine urine detection.

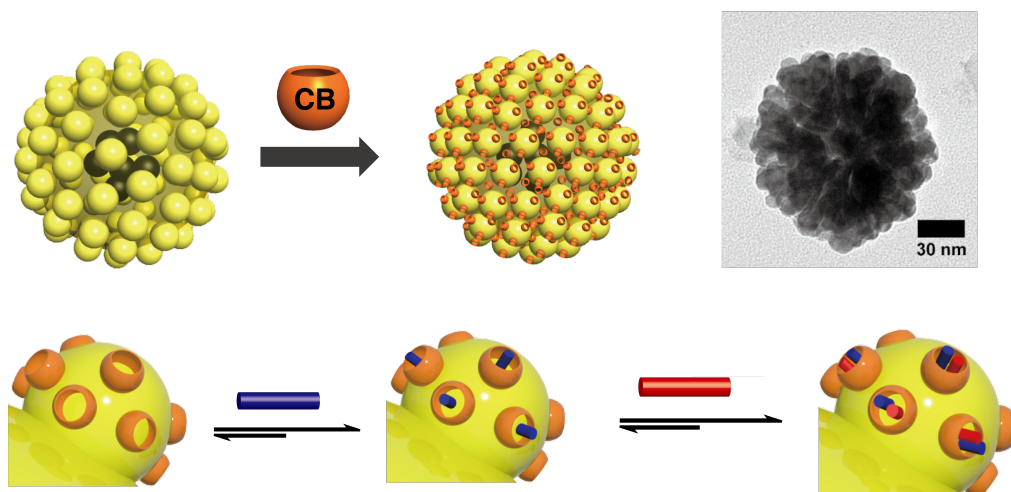


Figure 4.2: A schematic representation of the γ -Fe₂O₃@Au magnetic nanoraspberry particles (NRSP) and its application in SERS sensing after complexation with a dense layer of CB[*n*]s.

4.2 Results and Discussion

4.2.1 Synthesis and characterisation of γ -Fe₂O₃@Au nanoraspberry particles

The γ -Fe₂O₃@Au nanoraspberry particles (NRSP) were synthesised by a one-pot seeded growth method, using γ -Fe₂O₃ NPs of 7 ± 2 nm as the seeds, growing in a growth solution containing chloroauric acid (HAuCl₄), ascorbic acid as the reducing agent, silver nitrate as the catalyst and cetyltrimethylammonium bromide (CTAB) as the stabiliser (see the Experimental Appendix for details). After heating at 100 °C for 45 min, NRSP of great homogeneity was obtained, as shown in the TEM images Figure 4.3. NRSP of various sizes ranging from 30 to 150 nm can be obtained by adjusting the volume fraction of seed NPs (Figure 4.3).

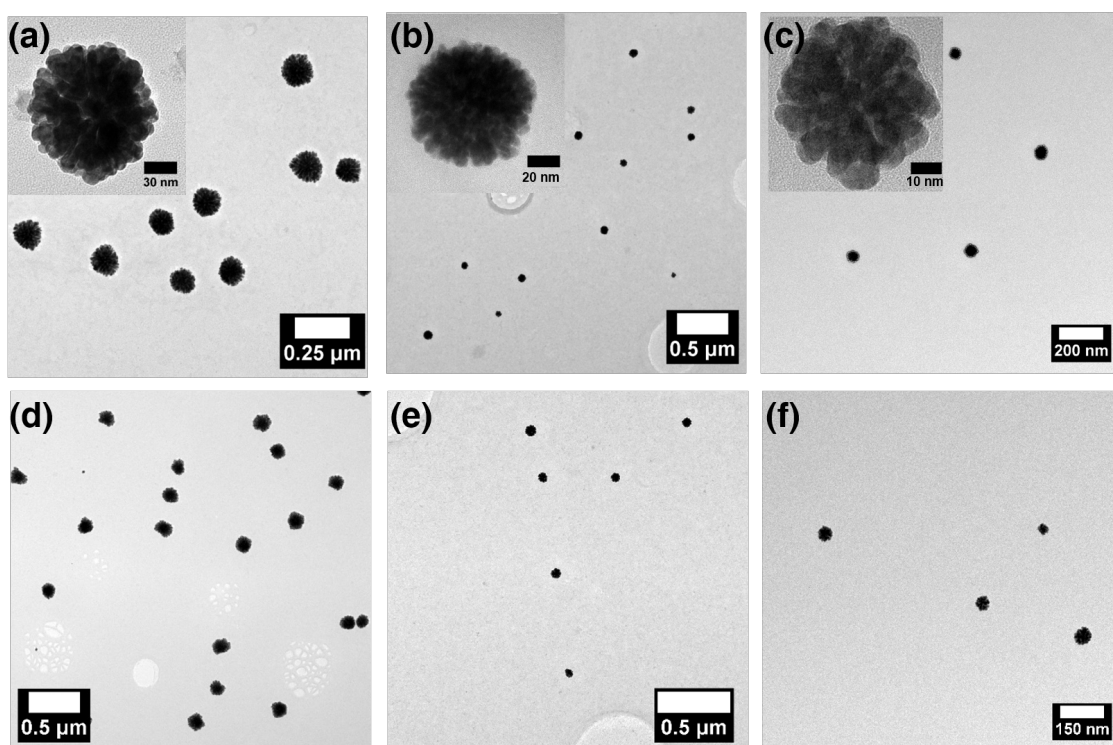


Figure 4.3: TEM images of different overall sizes NRSP: 123 ± 5 nm (a, d), 59 ± 7 nm (b, e) and 31 ± 3 nm (c, f), where the overall size was adjusted by controlling the amount of seed NPs (2 mg, 3 mg and 4 mg added respectively).

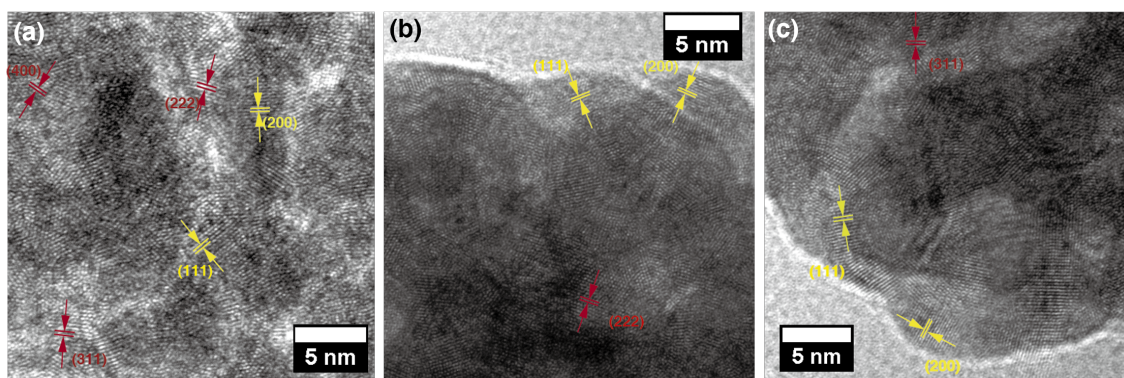


Figure 4.4: HRTEM images of the NRSP (123 ± 5 nm), where γ -Fe₂O₃ lattices (311), (222) and (400) are observed in the core region (JCPDS card No. 39-1346). Au lattices (111) and (220) are also observed (JCPDS card No. 04-0784). The knobs of the NRSP are of the similar size (5-10 nm).

High resolution TEM (HRTEM) and scanning transmission electron microscopy (STEM) with energy dispersive X-ray (EDX) were performed to further investigate the composition and growth mechanism of the NRSP. As shown in the HRTEM images (Figure 4.4),

γ -Fe₂O₃ lattices (311), (222) and (400) are mainly observed in the central region and Au lattices (111) and (220) are observed across the NRSP. STEM-EDX map and line scans (Figure 4.5) also suggest the dispersion of γ -Fe₂O₃ in the central region and Au on the outside. In addition, both of the TEM and HRTEM images show that the knobs of different sized NRSP are of similar size (5-10 nm), which is also testified by the STEM 3D tomography reconstruction images (Figure 4.6) and UV-vis-NIR spectra (Figure 4.7). NRSP of different sizes show similar UV-vis-NIR absorption peaks around 530 nm, the same as a 7 nm Au NP solution, suggesting that the absorption is attributed to the knobs on the NRSP surface.²³¹

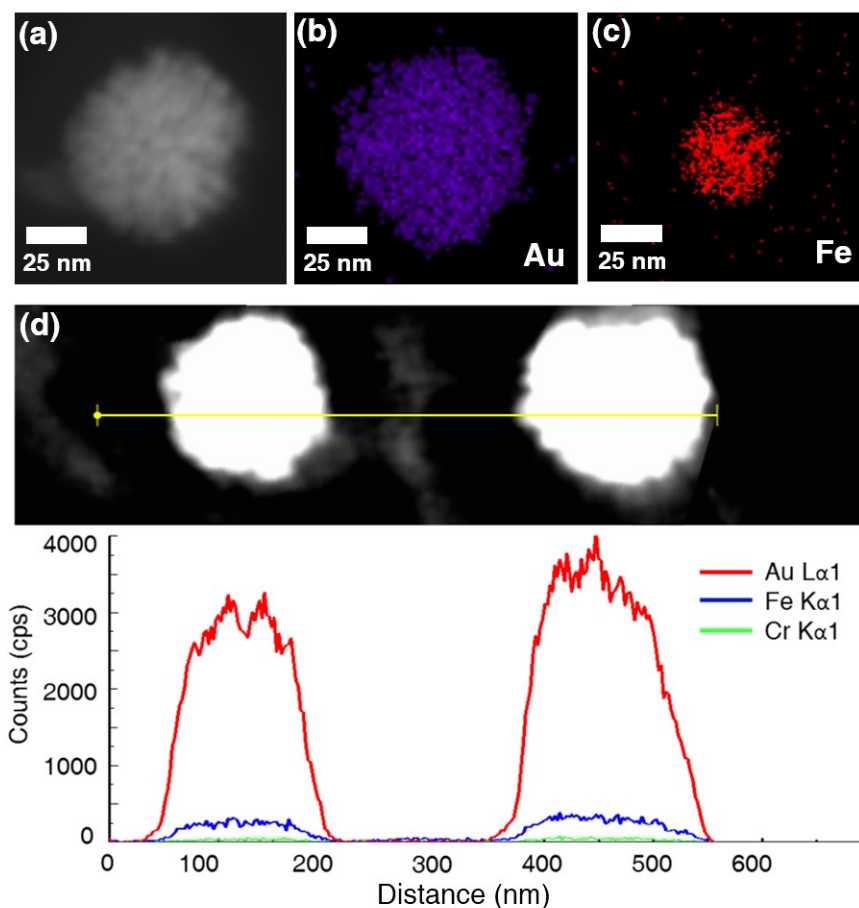


Figure 4.5: (a) STEM image of the NRSP; (b, c) Au and Fe STEM maps of the NRSP; (d) STEM line scan of the NRSP, where Cr was recorded as the background control. Au shows higher counts than Fe since it covers outside.

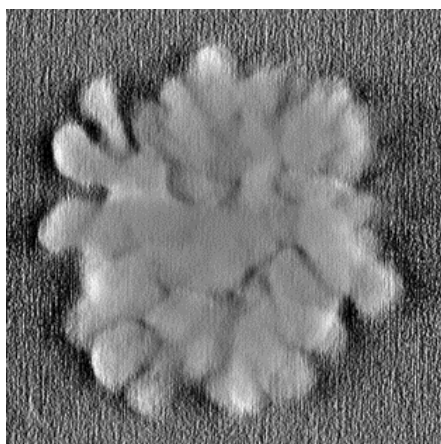


Figure 4.6: 3D tomography reconstruction image of the NRSP obtained from HAADF-STEM (high-angle annular dark-field scanning transmission electron microscopy).

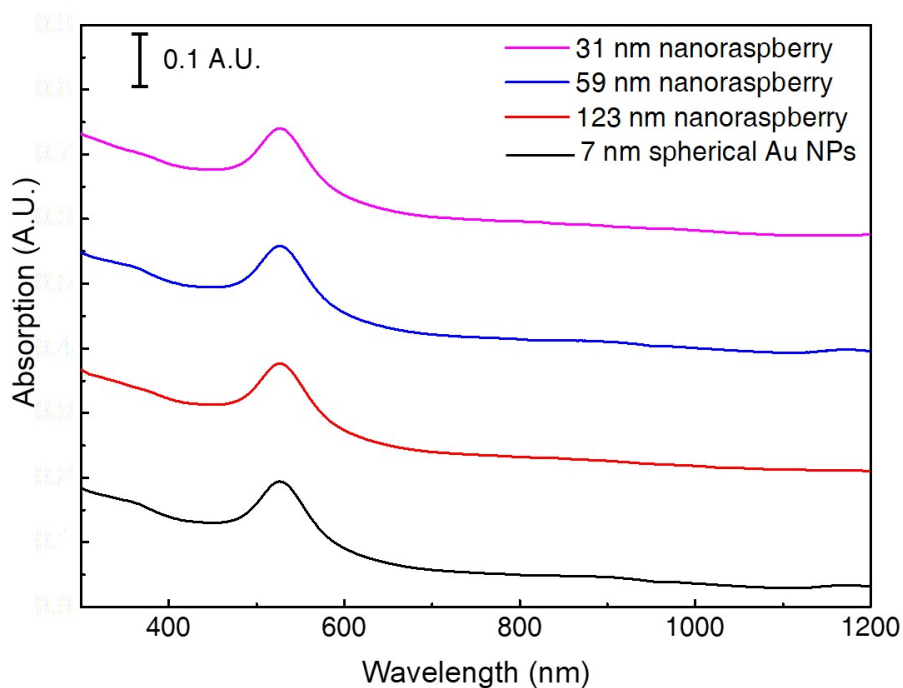


Figure 4.7: UV-vis-NIR absorption spectra of different overall sizes NRSP and 7 nm Au NP solution at the same concentration, showing similar absorption peak around 530 nm.

The hypothesised growth mechanism, a modified Turkevich mechanism,^{232,233} is proposed in Figure 4.8. In addition, the NRSP shows excellent colloidal stability and mag-

netic responsiveness. SERS spectra of the NRSP stored over 80 days were recorded to investigate the colloidal stability of the NRSP (Figure 4.9). No obvious change of the SERS peaks (stemming from surface ligands) was observed, suggesting no irreversible aggregation and great colloidal stability of the NRSP. Figure 4.10 shows the SERS spectra and photographs of the NRSP before and after applying a magnetic field, where the NRSP was collected in a corner by a magnet and SERS peaks dramatically decayed.

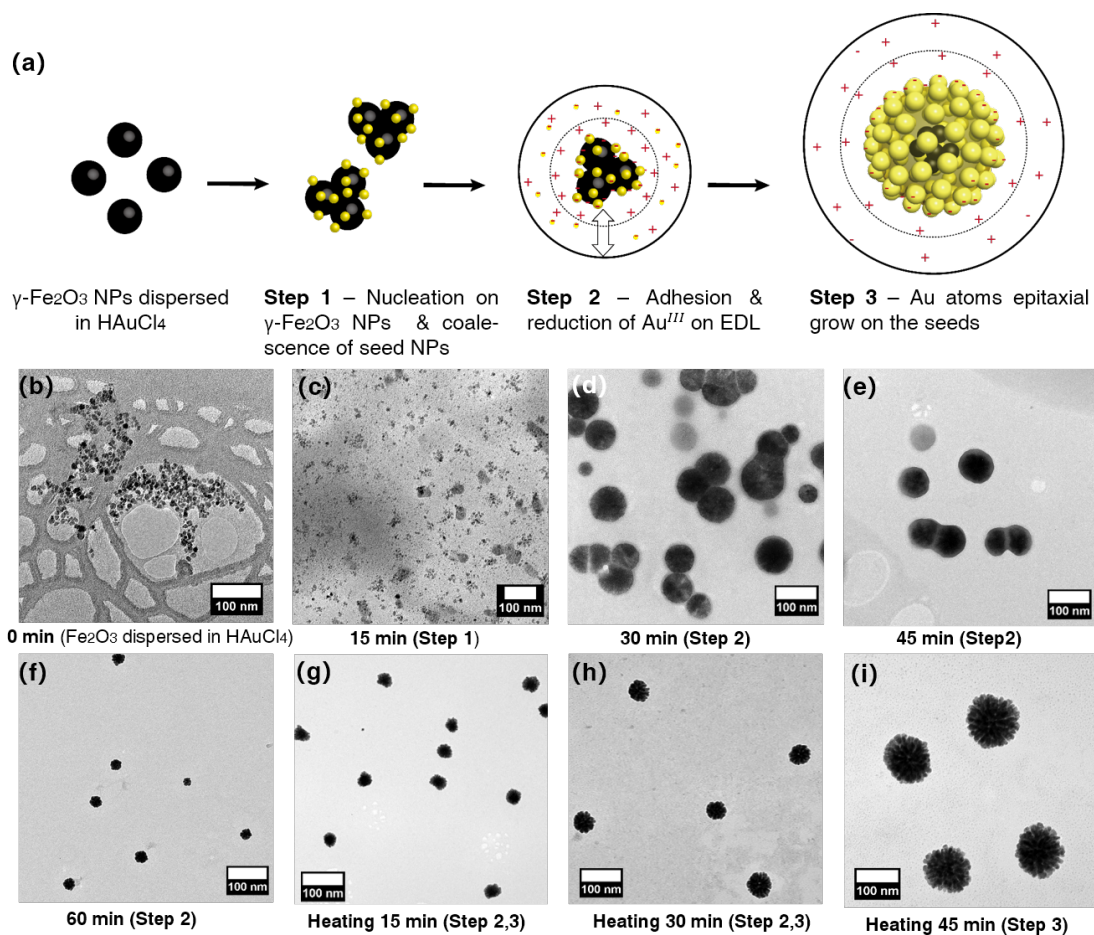


Figure 4.8: (a) Schematic illustration of the hypothesised growth mechanism. Step 1 corresponds to a growth due to coalescence whereby a fast reduction occurs immediately after mixing the γ -Fe₂O₃ NPs and HAuCl₄ solutions. The first step can also be described as a nucleation process with subsequent growth due to aggregation. Step 2 is interpreted as a growth by diffusion, whereby gold ions adhere to the electronic double layer (EDL), reduced and grown onto the existing particles. In the step 3, the reduction rate increases tremendously, leading to a fast reduction of the remaining gold salt and the reduced gold grows epitaxially onto the existing particles.^{232,233} (b-i) TEM images of the NRSP formation progress, with a interval time of 15 min.

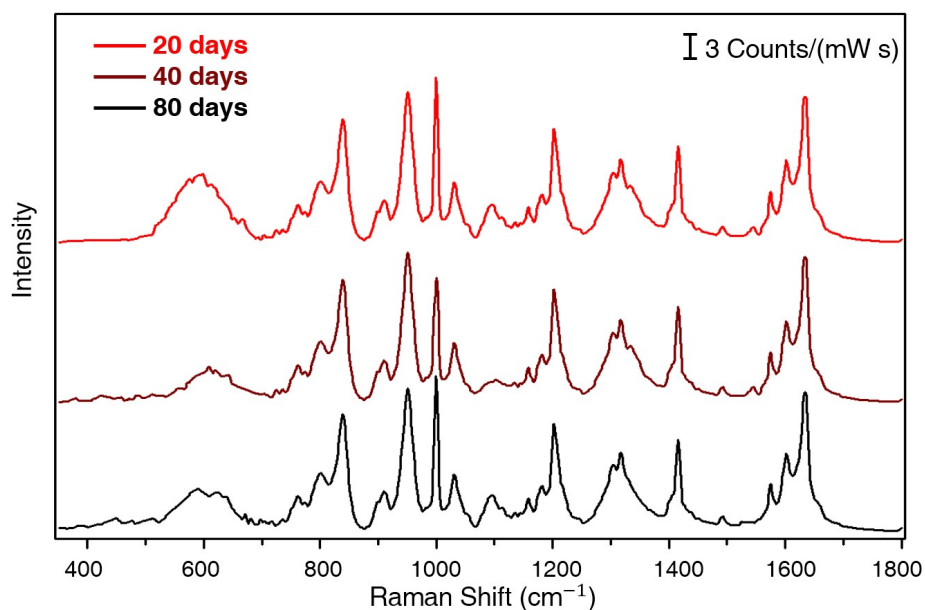


Figure 4.9: SERS spectra of the NRSP stored over 80 days, where few differences were observed, suggesting good stability of the nanoraspberry structure.

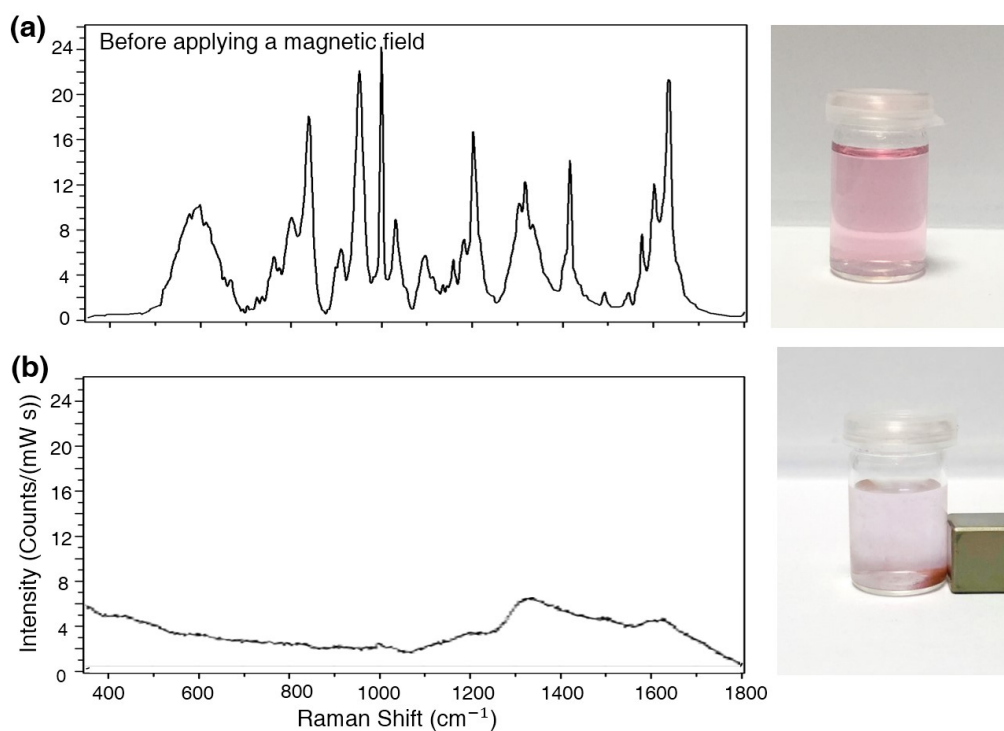


Figure 4.10: SERS spectra and photographs of the NRSP before (a) and after (b) applying a magnetic field, where the NRSP was collected in a corner using a magnet and SERS peaks disappeared.

Theoretical modelling with three dimensional finite difference time domain (3D-FDTD) was used to simulate the local electromagnetic field distribution under monochromatic light at 785 nm. The simulation result (Figure 4.11a) shows that the strongest localised electromagnetic field occurs at the crevices between knobs. High field enhancement of the NRSP, on the order of 10^{10} , was obtained, consistent with the experimental results. In addition, the simulated SERS enhancement factor (EF) of NRSP is a factor of 10^6 - 10^7 higher than that of spherical γ -Fe₂O₃@Au NPs (Figure 4.11b), confirming the superiority of the NRSP architecture over spherical shape NPs as SERS substrate.

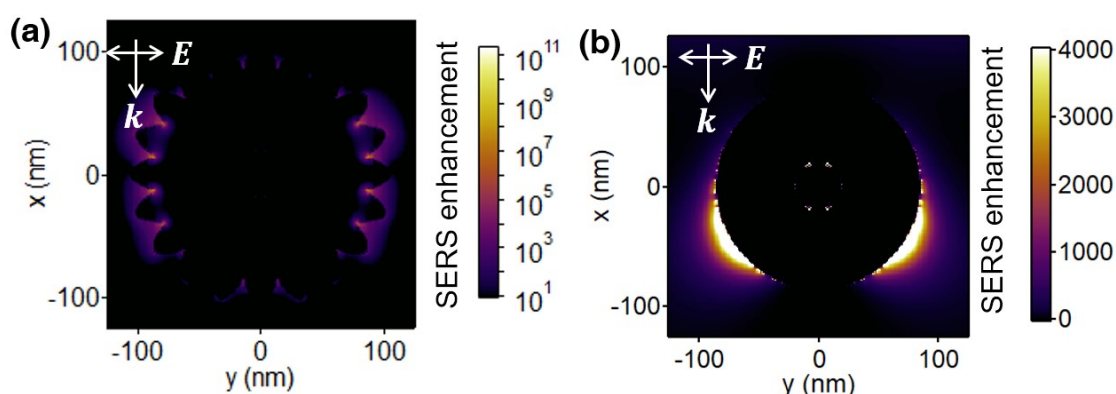


Figure 4.11: (a) The 3D-FDTD simulated local electromagnetic field enhancement of the NRSP at the XY plane, irradiated from the top at 785 nm. The simulated SERS EF is on the order of 10^{10} , which is in good consistent with the experiment obtained EF; (b) the 3D-FDTD simulated EF of spherical γ -Fe₂O₃@Au NP, which is approximately 10^7 lower than the NRSP.

4.2.2 Detection of target analytes using CB[7]-functionalised NRSP

By immobilising a dense layer of cucurbit[*n*]urils (CB[*n*]s) onto the NRSP surface, it can act as a high-performance SERS substrate for the detection of a variety of molecules, as illustrated in Figures 4.12. CB[*n*] is a family of barrel-shaped macrocyclic receptors exhibiting strong and selective encapsulation of various guest molecules into its cavity (K_a up to 10^{15}).^{53,76–78,113} In addition, CB[*n*] portal can bind strongly towards metallic surfaces.^{53,77,113} While the smaller homologues CB[5], CB[6] and CB[7] can encapsulate one guest molecule,^{53,76–78,113} CB[8] with a larger cavity volume can simultaneously accommodate two guest molecules.^{53,76–78,113} This work investigates CB[7]-

functionalised NRSP (CB[7]-NRSP, CB[8]-NRSP): CB[7]-NRSP could detect electron-deficient molecules (e.g. methyl viologen, indole); CB[8]-NRSP could also detect electron-rich molecules (e.g. dopamine, 2-naphthol, phloroglucinol, azobenzene) when complexed with a first guest molecule methyl viologen dichloride (MVCl₂). CB[n]-functionalised NRSP demonstrates high detection sensitivity (down to a few micromolar), meanwhile overcoming the limitation of most conventional SERS substrates which can only be applied to thiolated or aminated molecules.^{5,45}

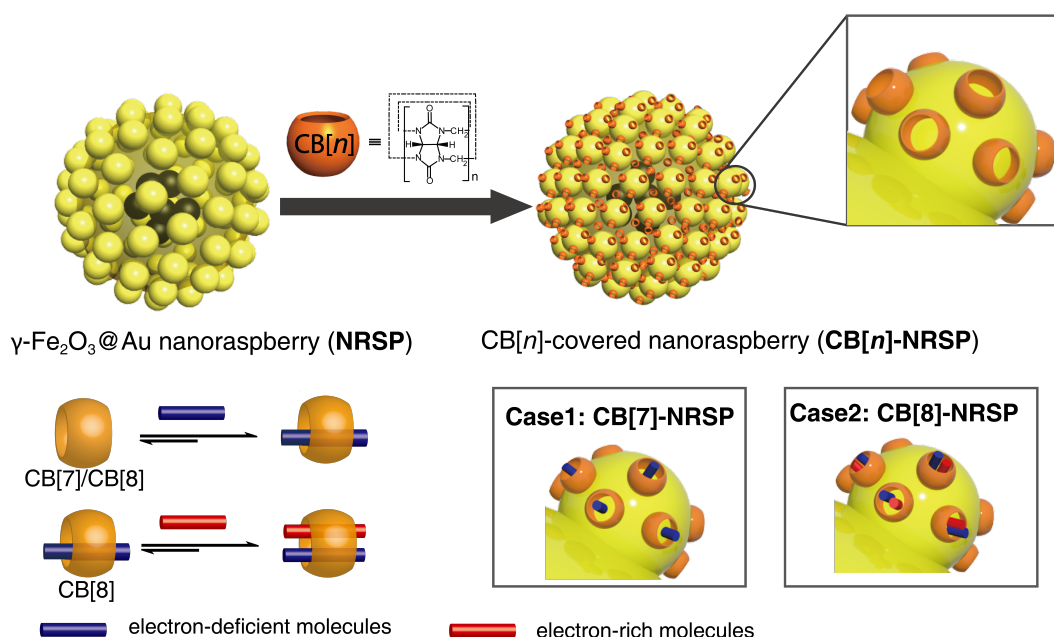


Figure 4.12: Schematic illustration of CB[n]-functionalised nanoraspberry particles (CB[n]-NRSP), electron-deficient molecules detection with CB[7]/CB[8]-functionalised NRSP and electron-rich molecules detection with CB[8]-functionalised NRSP.

As shown in Figure 4.13 (i) and (ii), both NRSP and CB[n]-NRSP show intense SERS signals. After functionalising NRSP with CB[7], the signature peaks of CB[7] at 443, 620 and 775 cm⁻¹ were clearly observed.⁵¹ Meanwhile, sodium citrate peaks at 598, 763, 801, 839, 951 and 1097 cm⁻¹ decreased greatly, which may be due to the partial displacement of sodium citrate by CB[7] (see the Experimental Appendix 3.4.6 for powder Raman spectra of CB[7] and surfactant sodium citrate). Aromatic compounds MVCl₂ and indole were investigated for SERS detection assays. CB[7]-NRSP (68 mg·L⁻¹) was added to MVCl₂

and indole solutions respectively (1:1 by volume), followed by the irradiation at 785 nm. Signature peaks of both analytes can be clearly identified (marked with asterisks in Figure 4.12 (iii) and (iv), see the Experimental Appendix 3.4.6 for powder Raman spectra of MVCl₂ and indole).^{53,190} Control experiments using NRSP alone without the immobilisation of CB[7] were also carried out, where none of above analytes could be detected since they were not able to reach the hot-spots uncombined with CB[7] (Figure 4.14).

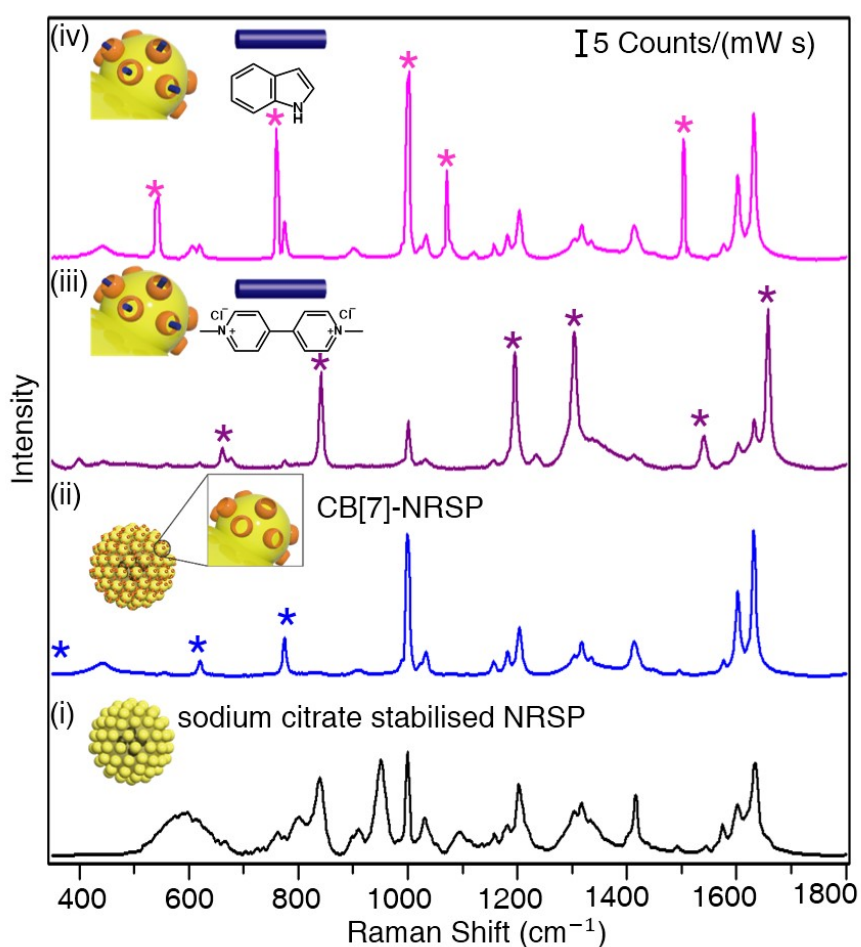


Figure 4.13: (i) SERS spectra of sodium citrate stabilised NRSP, irradiated at 785 nm; (ii) SERS spectra of CB[7]-NRSP (NRSP with 1 mM CB[7] 1:50 by volume, optimised condition obtained by titration); (iii) and (iv) detection of analytes (10 μ M) using CB[7]-NRSP (68 mg·L⁻¹). Signature peaks of both analytes can be clearly observed and are highlighted with asterisks in the figures. (Note: spectra are stacked and offset for clarity.)

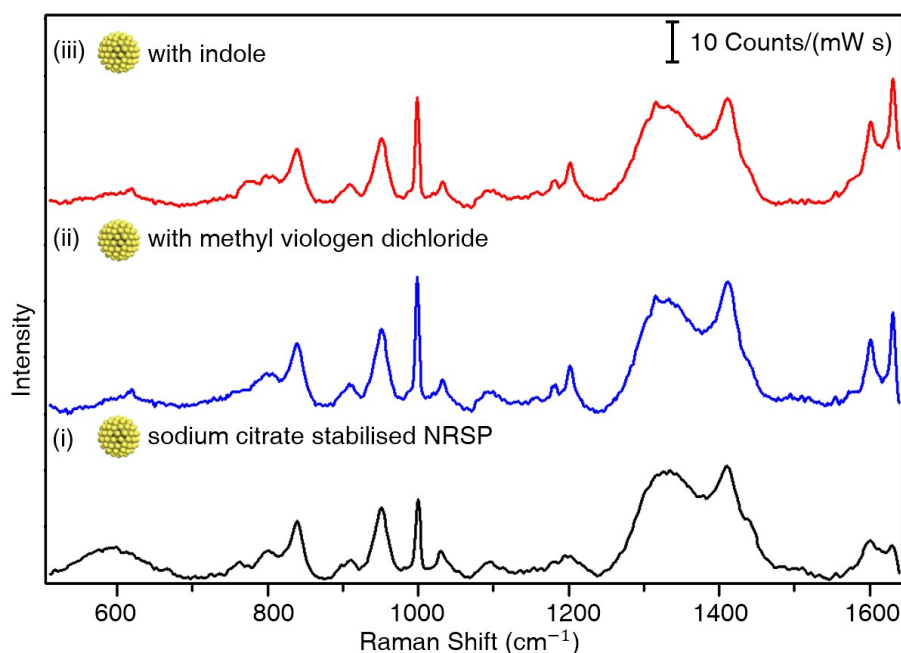


Figure 4.14: SERS spectra of NRSP with target analytes without the functionalisation of CB[7], where none of the analytes could be detected. This proves that target analytes could not attach to the NRSP surface for SERS measurements without the assistance of CB[*n*]. (Note: spectra are stacked and offset for clarity.)

4.2.3 Detection of target analytes using CB[8]-functionalised NRSP

We also investigated the detection of a variety of electron-rich analytes using CB[8]-NRSP (e.g. phloroglucinol, 2-naphthol, 4-(phenylazo)phenol, tetrathiafulvalene and dopamine), as listed in Figure 4.15. CB[8] was complexed with a first guest molecule MVCl₂ and then immobilised on the NRSP surface to form MVCl₂@CB[8]-NRSP. The MVCl₂@CB[8] complexes on the NRSP surface act as receptors for the electron-rich analytes and bring them into the hot-spots for detection. Analytes were detected with high sensitivities and signature peaks of all tested analytes were clearly identified (Figure 4.15 and the Experimental Appendix 3.4.6 for powder Raman spectra). Control experiments using NRSP alone and CB[8]-NRSP uncombined with MVCl₂ to detect electron-rich analytes were examined, where no signature peaks of any analytes could be observed in both cases (Figure 4.16 and 4.17). These suggest that the electron-rich analytes cannot go into the CB[8]'s cavity without the assistance of the electron-deficient molecule MVCl₂.^{53,76–78,113}

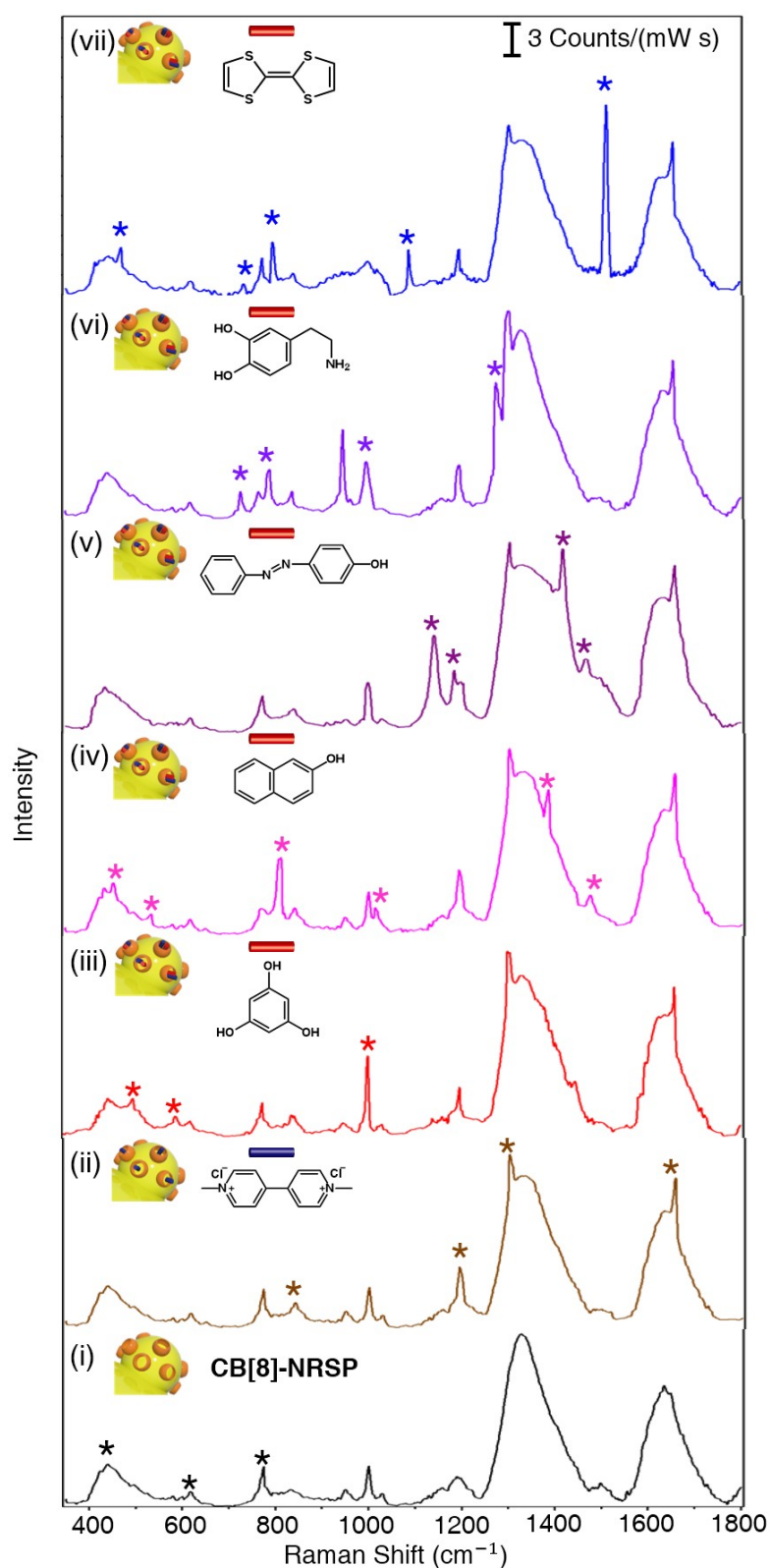


Figure 4.15: SERS spectra of (i) CB[8]-functionalised NRSP (CB[8]-NRSP, NRSP with 0.2 mM CB[8] 1:3 by volume); (ii) CB[8]-NRSP detected MVCl₂ (10 μM), (iii-vii) MVCl₂@CB[8]-NRSP detected electron-rich molecules phloroglucinol, 2-naphthol, 4-(phenylazo)phenol, dopamine and tetrathiafulvalene (10 μM), respectively. Signature peaks of the target analytes were clearly observed and marked with asterisks (*). 110

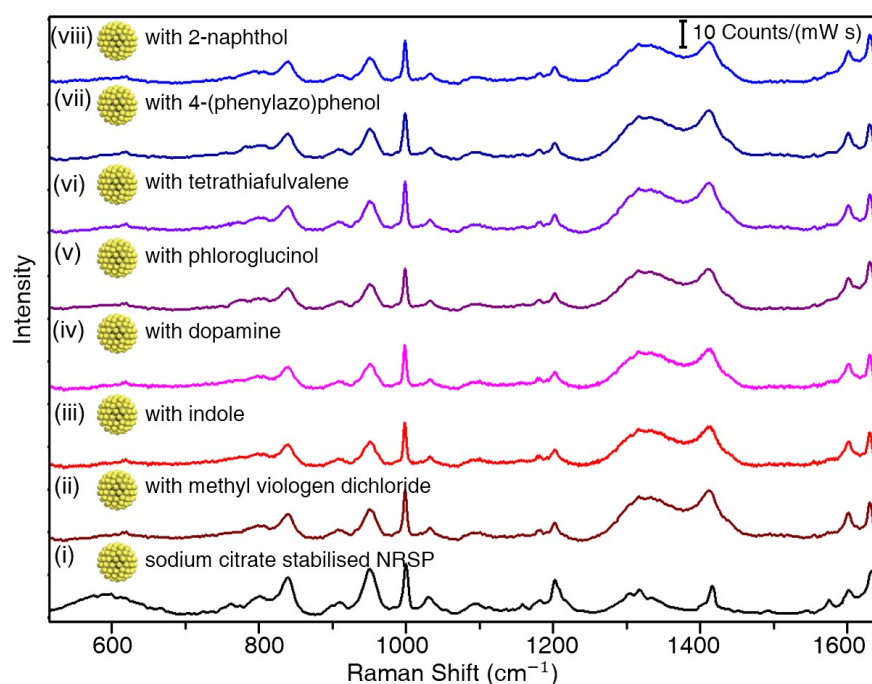


Figure 4.16: SERS spectra of NRSP with target analytes, where none of the analyte could be detected. This proves that target analytes could not attach to the NRSP surface for SERS measurement without the assistance of CB[n].

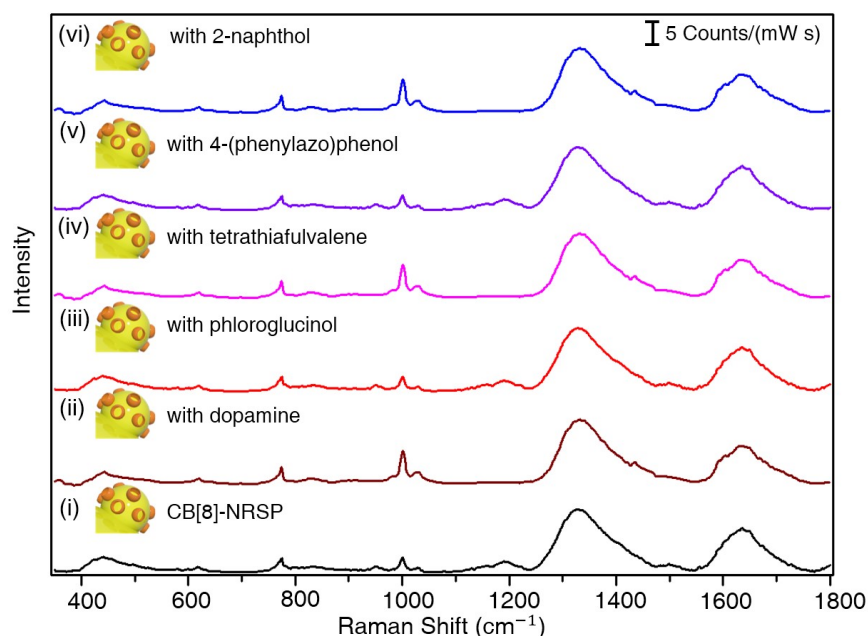


Figure 4.17: SERS spectra of CB[8]-NRSP with electron rich target analytes without MVCl₂, where none of the analyte could be detected. This suggests that electron rich target analytes could not go into CB[8]'s cavity without the existence of the electron deficient MVCl₂.

4.2.4 Detection of ephedrine

CB[n]-NRSP can be applied to the detection of controlled substances and various biomolecules as it shows significant field enhancements with high detection sensitivity and stability. As a showcase, we investigated the detection of ephedrine using our CB[7]-NRSP. Ephedrine is an energising-stimulating substance which can excite the central nervous system of human beings.²³⁴⁻²³⁶ For this reason, ephedrine is in the banned list of the International Olympic Committee. Conventional detection methods of ephedrine include high-performance liquid chromatography (HPLC),²³⁵ capillary electrophoresis (CE),²³⁴ and gas chromatography-mass spectrometry (GC-MS).²³⁶ However, these methods require qualified technicians and are time-consuming and expensive.²³⁴⁻²³⁶ CB[n]-NRSP, in this case, provides a simple, rapid and effective method to detect the presence of ephedrine in aqueous media. As shown in Figure 4.18 (ii), ephedrine could be clearly detected down to 350 $\mu\text{g}\cdot\text{L}^{-1}$, which reaches the standard of real-life detection (typically, abusers or poisoned patients possess 300-3000 $\mu\text{g}\cdot\text{L}^{-1}$ in blood, plasma or urine).²³⁴⁻²³⁶ Different aqueous media (e.g. phosphate buffer solution at pH 7.4, urine control) did not interfere the detection ability of the CB[n]-NRSP system (Figure 4.18), allowing for its potential application in real-life athletes urine test.

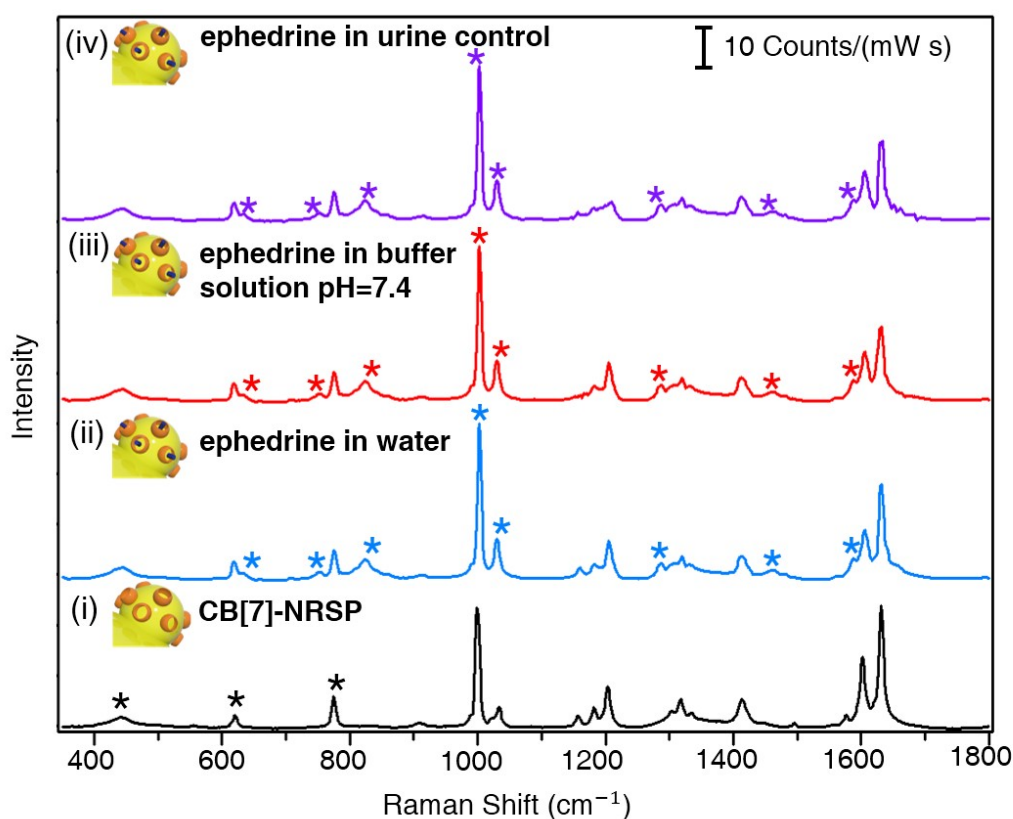


Figure 4.18: SERS spectra of ephedrine ($350 \mu\text{g}\cdot\text{L}^{-1}$) detection using CB[7]-NRSP in different media (water, phosphate buffer solution pH=7.4, ClinChek[®] urine control lyophil). The signature peaks of ephedrine could be observed clearly in all solutions and marked with asterisks, showing few differences.

4.3 Conclusion and Outlook

In conclusion, we have demonstrated a facile one-pot synthesis of γ -Fe₂O₃@Au nanoraspberry particles. The obtained nanoraspberry particles are monodispersed, highly stable, and of good magnetic responsiveness on account of the incorporation of the magnetic cores. The curvature surface contributes to a high SERS enhancement factor (on the order of 10^{10}), making it advantageous for a high-performance SERS substrate. By immobilising a dense layer of macrocyclic host molecule CB[*n*]s onto the surface of nanoraspberry particles, they could act as a stable free-standing molecular sensor for a variety of electron-deficient and electron-rich molecules. The CB[*n*]s immobilised on the nanoraspberry surface act as molecular receptors and bring the target analytes into the hot-spots. As a result, analytes could be detected with high sensitivity and specificity.

We envisage that this stable and monodispersed nanoraspberry will provide a powerful high-performance substrate for SERS detection of various biomolecules, chemicals and illegal drugs.

4.4 Experimental Appendix

4.4.1 Materials and general methods

All the starting materials were purchased from Alfa Aesar and Sigma Aldrich and used as received unless stated otherwise. CB[7] and CB[8] were prepared according to literature protocols.⁷⁷

¹H NMR (400 MHz) spectra were recorded using a Bruker Advance QNP 400. DLS and zeta potential measurements were performed on a Malvern Zeta-sizer Nano-S90. UV-vis-NIR spectra were obtained on a Agilent Cary 7000 UV-vis-NIR spectrometre. Titration experiments were carried out on a MicrocalTM ITC₂₀₀ (isothermal titration calorimetry). TEM and high resolution TEM images were obtained by a FEI Philips Tecnai20 transmission electron microscope (specifications: accelerating voltage 100 keV, double tilt specimen holder, SIS imaging software and CCD camera). Samples were prepared by applying one drop of the metallic NP solutions onto a Holey R carbon coated copper TEM grid (400 mesh), followed by drying overnight at room temperature. STEM-EDX and 3D tomography images were carried out on a VG HB501 scanning transmission electron microscopy with EELS (electron energy loss spectrum). Extinction measurements for the nanoparticles were monitored with an Ocean Optics 650-USB Red Tide spectrometre and SERS spectra were recorded on a Renishaw inVia Raman microscope (Specifications: 138 mW, 785 nm, 120 μ m focal spot diameter and a dark noise level of less than 80 rms at 9 ms, per scan.)

4.4.2 Synthesis of γ -Fe₂O₃ nanoparticles

The γ -Fe₂O₃ NPs were synthesised by a modified Massart's method.^{237,238} FeCl₃·6 H₂O (0.32 mol) and FeCl₂·4 H₂O (0.16 mol) in 3.5 L deionised water were mixed with 300 mL

ammonium hydroxide solution (8.6 M) at room temperature, resulting in the mixture turning black immediately. The nanoparticles were collected with a permanent neodymium magnet and the supernatant was discarded after 15 min. The nanoparticles were then suspended in 400 mL nitric acid solution (2 M) under stirring for 15 min. After collection of the nanoparticles and removal of the supernatant, 600 mL ferric nitrate solution (0.33 M) was added and stirred at 90 °C for 30 min. After that, they were peptised with 400 mL nitric acid (2 M) for 15 min at room temperature, rinsed with acetone (200 mL) for 5 times and dispersed in 500 mL deionised water. The pH value of the final γ -Fe₂O₃ NP suspension was tuned to be 4.0, and a concentration of 61.5 g·L⁻¹ was confirmed by titration. The average particle size obtained from TEM images was 7 ± 2 nm and zeta potential of -68.8 mV.

4.4.3 Synthesis of γ -Fe₂O₃@Au nanoraspberry particles

γ -Fe₂O₃@Au nanoraspberry particles were synthesised by a one-pot seeded growth method. The seed solution was prepared by dispersing 2 mg of the above γ -Fe₂O₃ NPs in 500 μ L sodium citrate solution (2.5 mM), followed by sonication for 20 min. The growth solution was prepared as follows: 300 μ L AgNO₃ (2 mM) was added in 5 mL cetyltrimethyl ammonium bromide (CTAB) clear solution (0.2 M), sonicated for 30 min and then mixed with 5 mL HAuCl₄ (7 mM) under a vortex mixer for 15 s. After that, 300 μ L ascorbic acid (80 mM) was added to the mixture, agitated by a vortex mixer and kept still for 15 min. Finally, 250 μ L of the seed solution was added to the growth mixture and mixing briefly by hand, remaining still without turbulence at room temperature for 30 min. The mixture was heated at 100 °C for 45 min to obtain the magnetic γ -Fe₂O₃@Au nanoraspberry (68 mg·L⁻¹). The surfactant was exchanged by repetitive washing with 0.2 M sodium citrate.

4.4.4 Modification of growth conditions

A series of experiments were carried out to investigate the optimum synthesis condition and the growth mechanism.

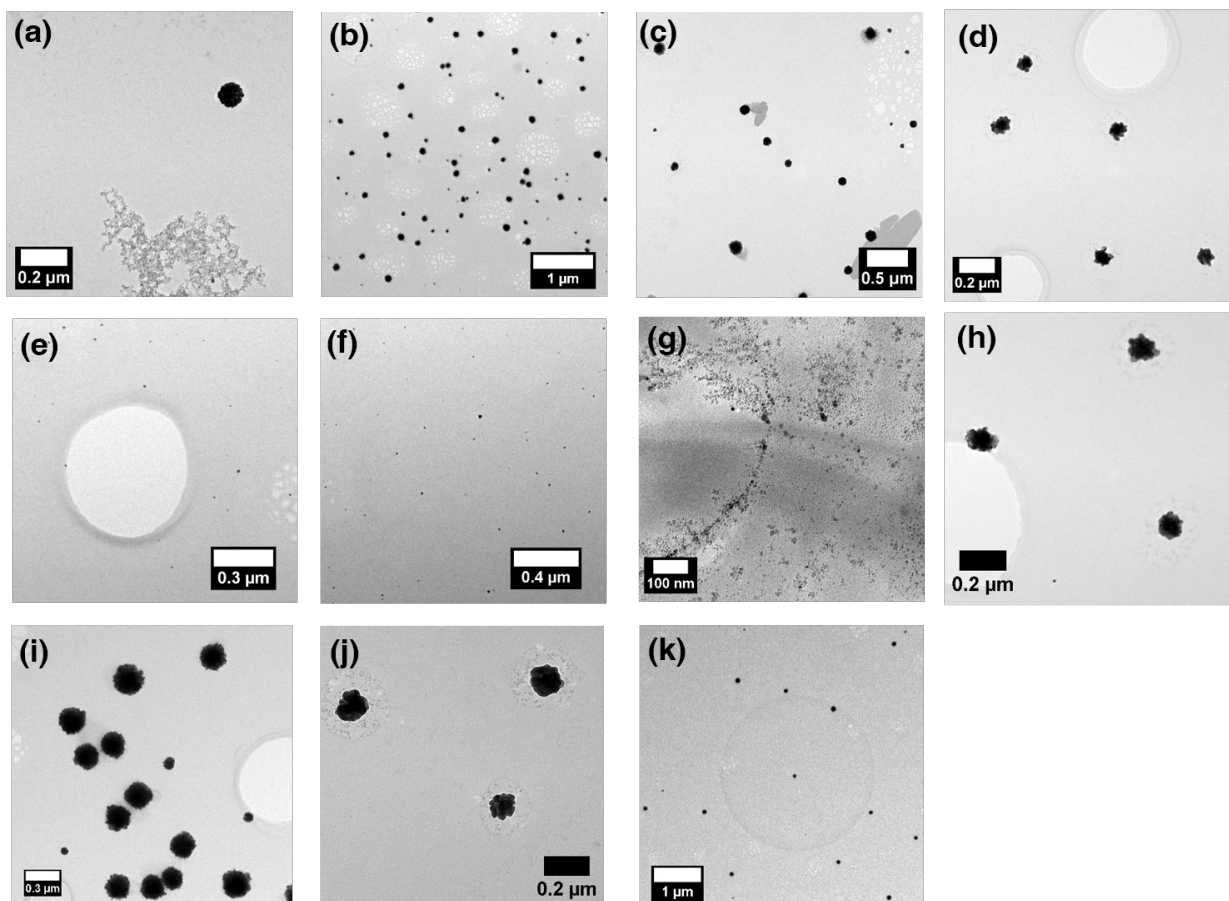


Figure 4.19: (a) Lower HAuCl₄ concentration in the growth solution (6.2 mM) resulted in the leaking of free γ -Fe₂O₃ NPs; (b) extended time in the growth solution preparation procedures led to the existence of free Au NPs; (c) 0.1 M NaOH was added 15 min after the mixing of seed and growth solutions, leading to inhomogeneous nanoraspberries; (d) 0.2 M sodium citrate was used as the stabiliser during the growth process, resulting in NPs of irregular shapes; (e, f) growth solutions without the addition of seeds after 7 d and 14 d, where the formation of nanoraspberry was not observed; (g) NaBH₄ was used as the reducing agent, where Au NPs were formed before the addition of seed solution, leading to the mixture of γ -Fe₂O₃ and Au NPs. (h) AgNO₃ was not added in the growth solution, leading to slightly irregular shape of the nanoparticles; (i, j) modification of ascorbic acid concentration (150 mM, 50 mM) to assist the shape control; (k) Au NPs (around 7 nm) was used as the seed NPs, where spherical NPs were formed in the end.

4.4.5 Surfactant exchange

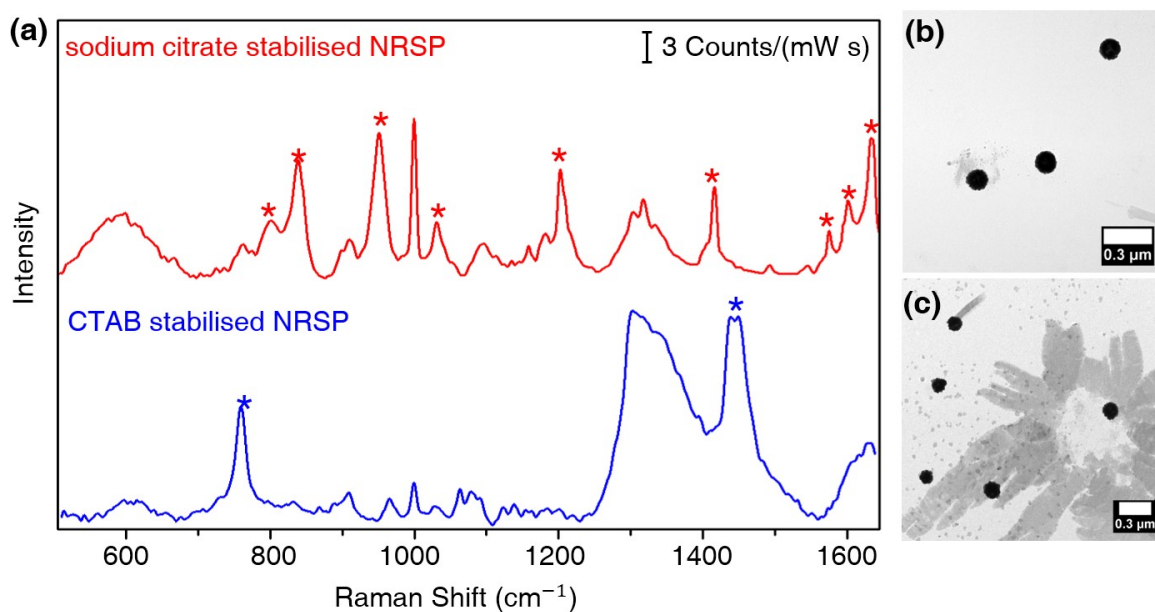


Figure 4.20: (a) SERS spectra of the NRSP stabilised with CTAB (blue) and after exchanging CTAB using sodium citrate (red). TEM images of the NRSP stabilized with sodium citrate (b) and CTAB (c). The precipitation of CTAB could be observed from the TEM image (c).

4.4.6 Detection of target analytes using CB[7]-functionalised NRSP

CB[7]-functionalised nanoraspberry particles (CB[7]-NRSP) are capable of detecting electron deficient molecules (e.g. MVCl₂) with high sensitivity. The addition sequence of the analyte and CB[7] was also investigated, where no difference of adding MVCl₂ to CB[7]-NRSP and adding MVCl₂@CB[7] complex to NRSP was observed at the same concentration.

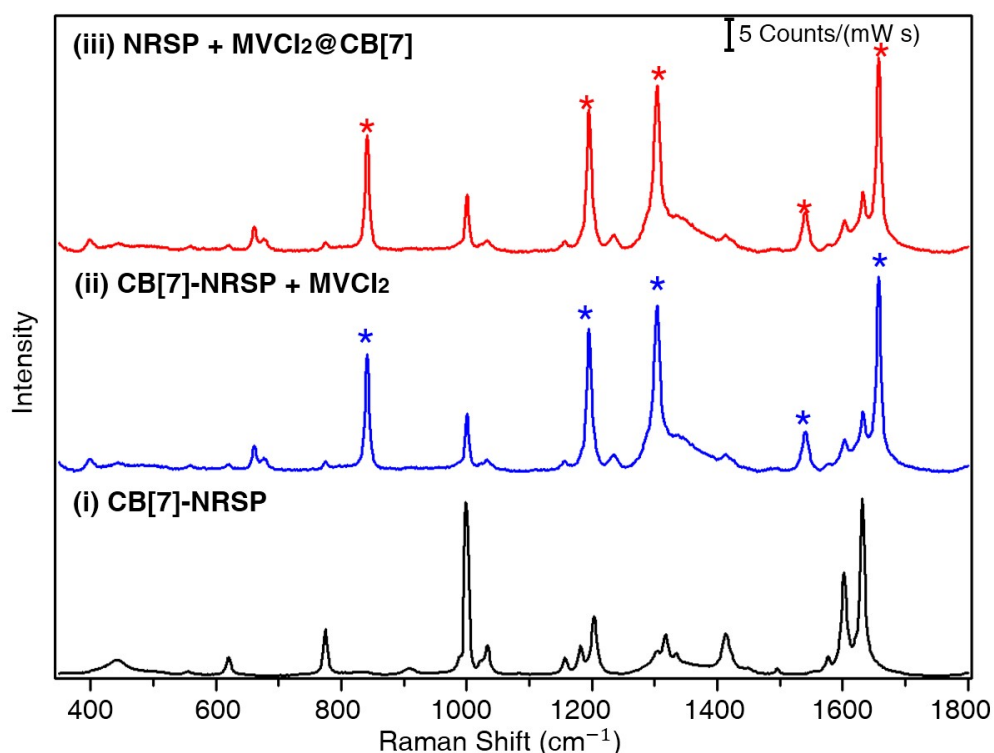


Figure 4.21: SERS spectra of (i) CB[7]-functionalised nanoraspberry (CB[7]-NRSP, NRSP with 1 mM CB[7] 1:50 by volume, condition optimised by titration); (ii) 200 μ M MVCl₂ added to CB[7]-NRSP solution (1:10 by volume); (iii) 20 μ M MVCl₂@ 1 mM CB[7] complex added to NRSP solution (50:1 by volume). The signature peaks were marked with asterisks (*). No obvious difference of (ii) and (iii) was observed.

4.4.7 Guest displacement

Guest displacement study using adamantane amine (ADA) to displace MVCl₂ in the cavity of CB[7] on CB[7]-NRSP, which further confirms that the analytes were encapsulated in the CB[7] cavity for detection instead of sitting in the crevice of the surface knobs.

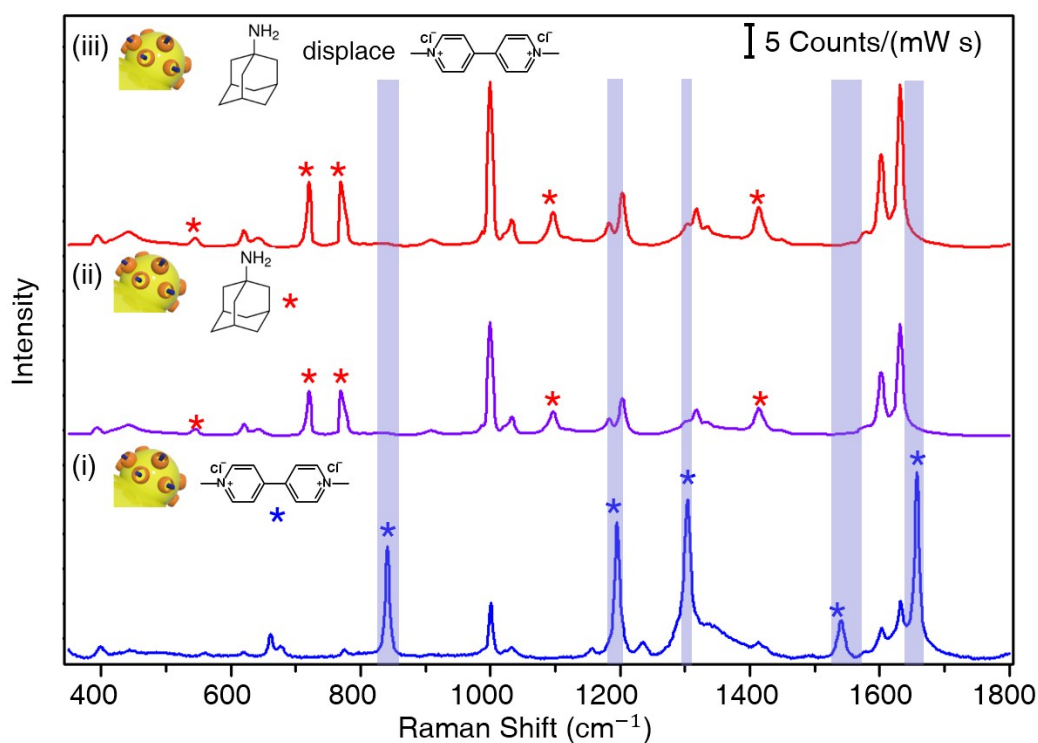


Figure 4.22: SERS spectra of (i) CB[7]-NRSP with MVCl₂ (30 μ M); (ii) CB[7]-NRSP with ADA (30 μ M); (iii) guest displacement using ADA (300 μ M) to displace MVCl₂ in the cavity of CB[7] on CB[7]-NRSP.

4.4.8 Powder Raman spectra of investigated molecules

Powder Raman spectra of CB[7], CB[8], sodium citrate, CTAB, MVCl₂, indole, dopamine, phloroglucinol, 2-naphthol, tetrathiafulvalene, 4-(phenylazo)phenol and ADA can be found in the Experimental Appendix 3.4.6.

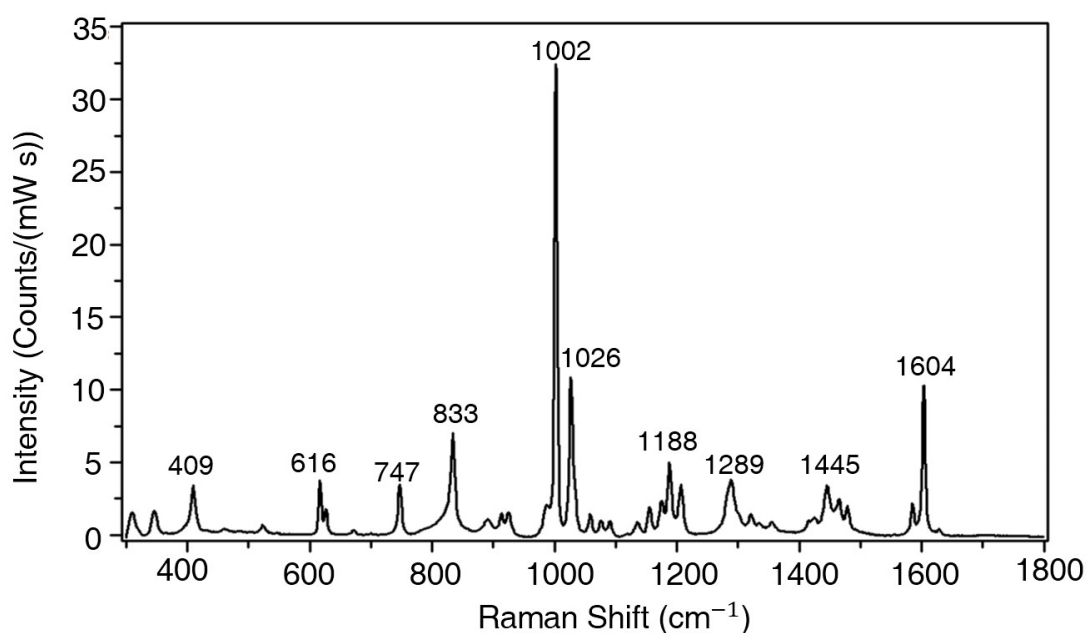


Figure 4.23: Raman spectrum of solid ephedrine.

4.4.9 Binding constants of complexes

Binding constants of G_1 @CB[7] complex reported in literature and measured by ITC are listed as follows. Binding constants of dopamine, phloroglucinol, 2-naphthol, indole, tetrathiafulvalene and 4-(phenylazo)phenol towards MVCl₂@CB[8] can be found in the Table 3.1.

Table 4.1: Binding constants (K_a) of tested analytes with CB[7]

G_1 with CB[7]	K_a (M ⁻¹)
MVCl ₂	$1.2 \times 10^5 - 1.3 \times 10^{7113}$
indole	$(6.7 \pm 0.5) \times 10^{5201}$
ephedrine	$(4.7 \pm 1.0) \times 10^{5201}$

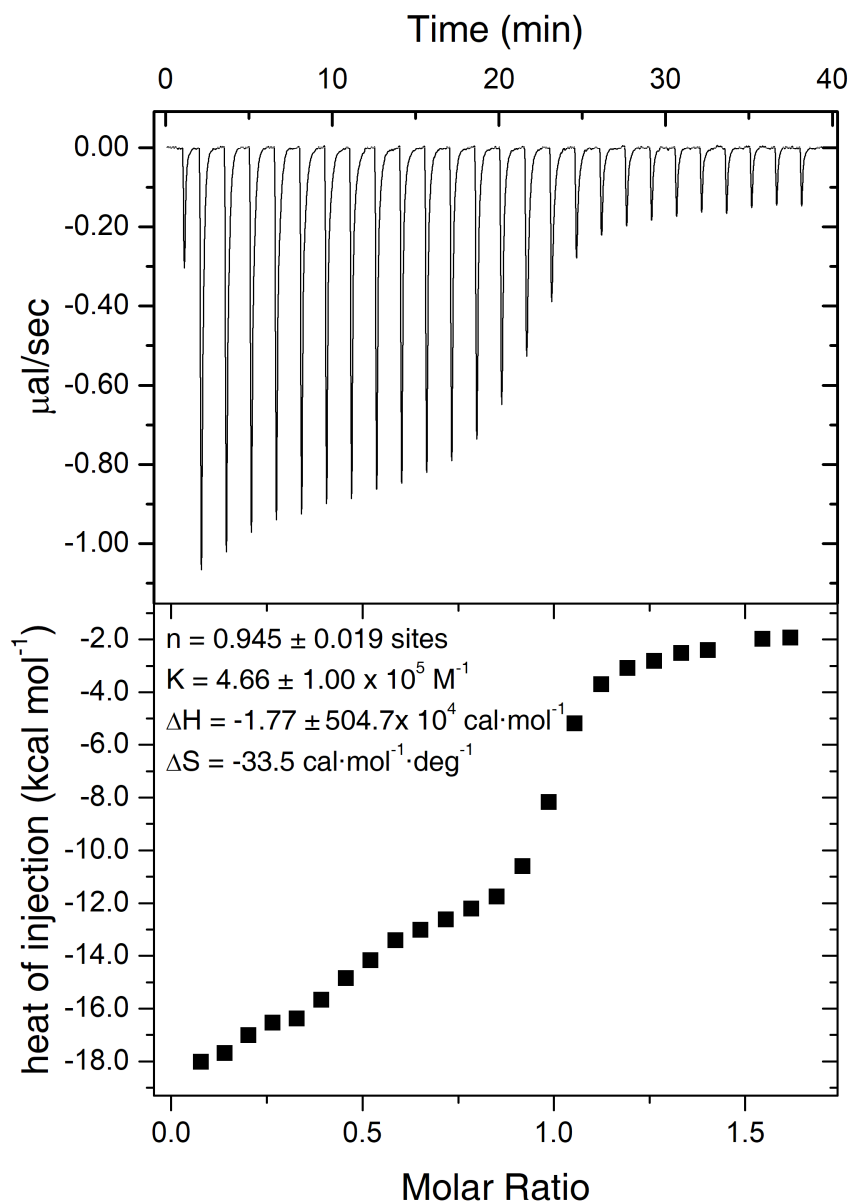


Figure 4.24: ITC result of the complexation between ephedrine and CB[7]. 500 μM ephedrine was injected into 50 μM CB[7] in buffer solution at 25 $^{\circ}\text{C}$. 50 mM sodium acetate buffer, pH=4.6, was used.

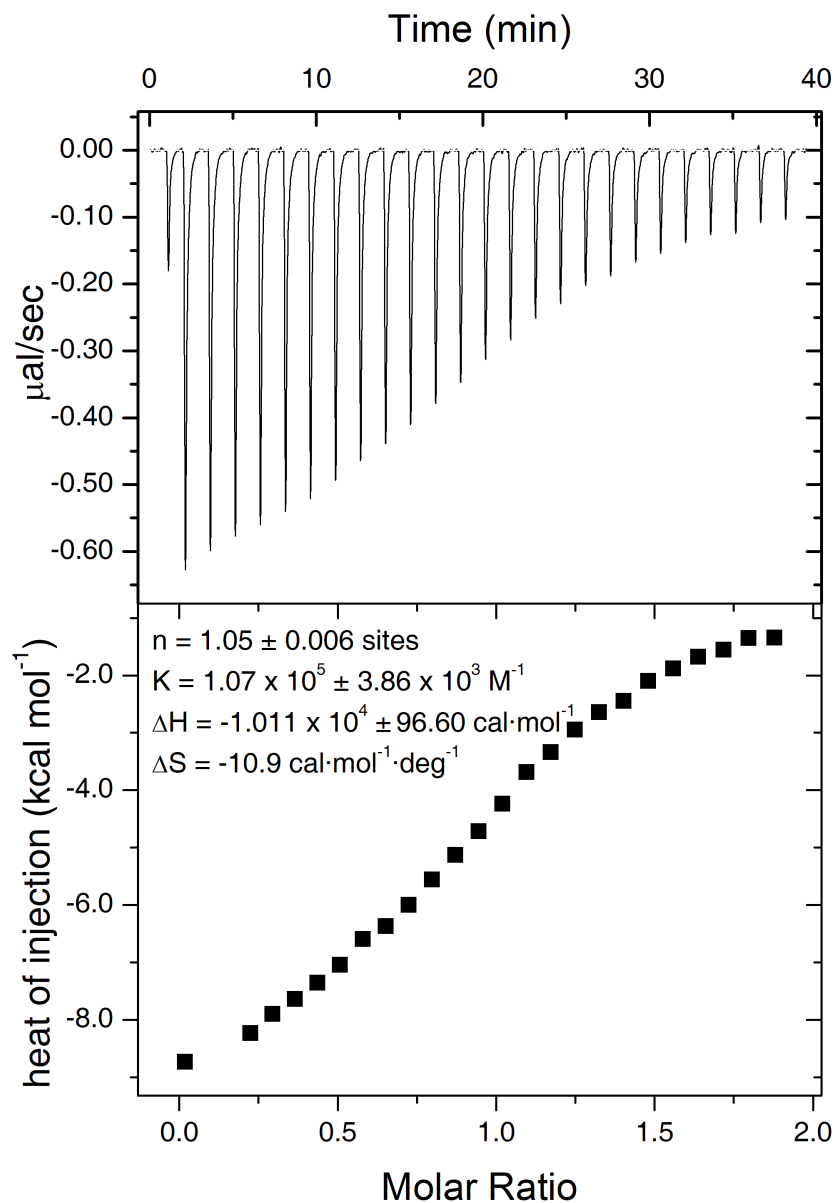


Figure 4.25: ITC result of the complexation between tetrathiafulvalene and MVCl₂@CB[8]. 200 μ M tetrathiafulvalene was injected into 20 μ M MVCl₂@CB[8] in buffer solution at 25 °C. 50 mM sodium acetate buffer, pH=4.6, was used.

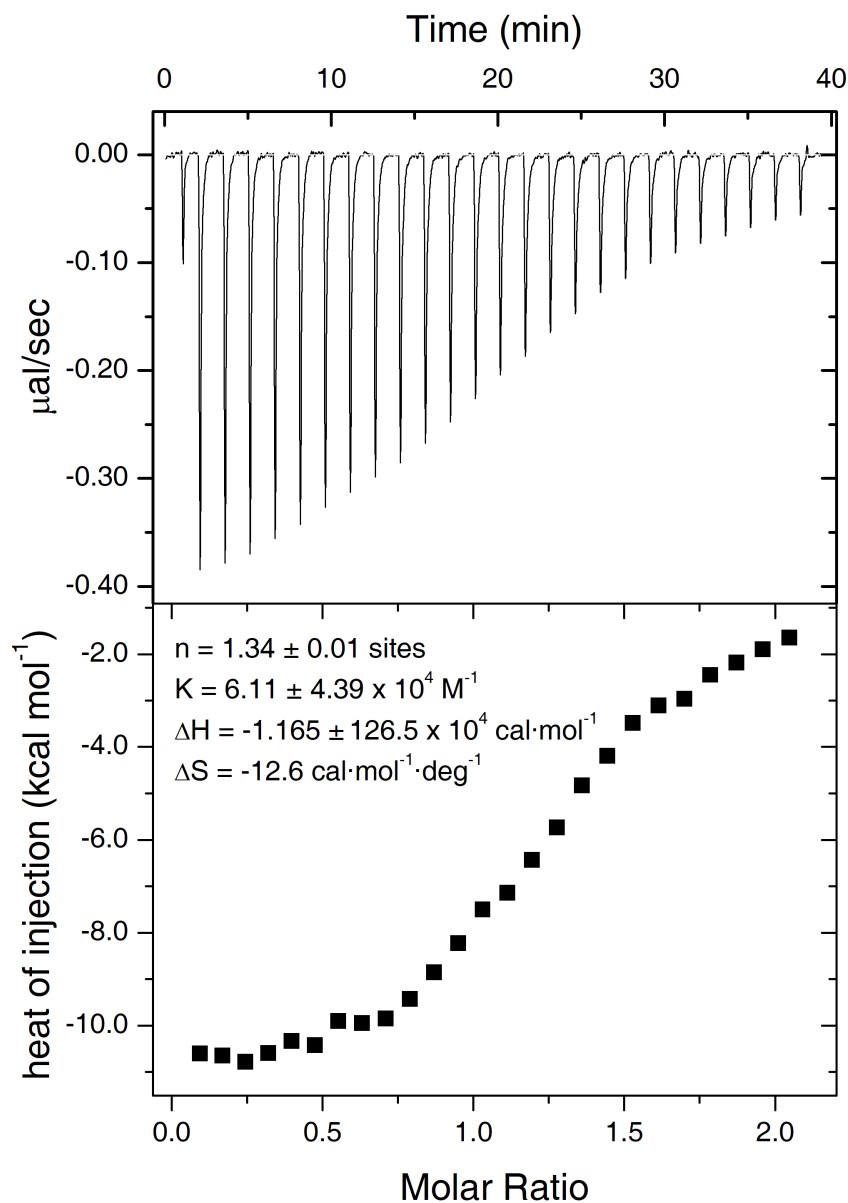


Figure 4.26: ITC result of the complexation between indole and MVCl₂@CB[8]. 200 μM indole was injected into 20 μM MVCl₂@CB[8] in buffer solution at 25 $^{\circ}\text{C}$. 50 mM sodium acetate buffer, pH=4.6, was used.

4.4.10 Calculation of SERS enhancement factor

SERS enhancement factor (EF) was calculated by two methods: 3D-FDTD simulation (10¹⁰, Figure 4.11) and experimental measurements. The calculation of EF based on experimental measurements are shown as follows.

The most widely used definition equation for the average SERS EF is:

$$EF = \frac{I_{SERS}/N_{Surf}}{I_{RS}/N_{Vol}}$$

where $N_{Vol} = c_{RS}V$ is the average number of molecules in the scattering volume (V) for the Raman (non-SERS) measurement, and N_{Surf} is the average number of adsorbed molecules in the scattering volume for the SERS experiments.²⁰⁴ Methyl viologen peak at around 1280 cm⁻¹ was chosen to calculate the SERS EF in this case. For the CB[7]-functionalised nanoraspberry (68 mg/L, 306 μ L, 15 s exposure time), 60000 \pm 2500 counts was obtained. For MVCl₂ non-SERS Raman measurement (1 M, 330 μ L, 120 s), 1700 \pm 100 counts was obtained using the same laser power 138 mW.

$$I_{SERS} = \frac{60000 \pm 2500 \text{ counts}}{15 \text{ s}} = 4000 \pm 167 \text{ cps}$$

$$I_{RS} = \frac{1700 \pm 100 \text{ counts}}{120 \text{ s}} = 14.17 \pm 0.83 \text{ cps}$$

$$N_{Vol} = 1 \text{ M} \times 330 \mu\text{L} \times NA = 1.98 \times 10^{20}$$

N_{Surf} was calculated from ITC titration experiments. Briefly, CB[7]-NRSP (NRSP: 1mM CB[7] 1: 50 by volume) was centrifuged and the concentration of the remaining CB[7] in the supernatant solution was titrated by ITC. The surface density of CB[7] can then be deducted from a series of titration experiments based on the concentration decrease of CB[7]. The calculation procedures are shown as follows.

15 mL NRSP was freeze dried, re-dispersed in 50 μ L of sodium citrate (2.5 M) solution and mixed with 2.5 mL of CB[7] (1 mM) solution. After sonication (5 min) and centrifug-

gation (13000 rpm, 20 min), the concentration of the remaining CB[7] in the supernatant solution was titrated by ITC ($993.15 \pm 0.85 \mu\text{M}$). Therefore, the concentration decrease of CB[7] in $2550 \mu\text{L}$ CB[7]-NRSP was $6.85 \pm 0.15 \mu\text{M}$.

The total number of CB[7] adhered to the NRSP surface in $2550 \mu\text{L}$ examined solution was:

$$N(\text{CB}[7])_{2550} = n(\text{CB}[7])N_A = (6.85 \pm 0.15) \times 10^{-6} \text{M} \times 2550 \times 10^{-6} \text{L} \times 6.02 \times 10^{23} = (1.05 \pm 0.23) \times 10^{16}$$

In the SERS detection measurement, $6 \mu\text{L}$ of NRSP was used. Therefore, the number of CB[7] in the CB[7]-NRSP was:

$$N(\text{CB}[7])_6 = \frac{N(\text{CB}[7])_{2550} \times 6}{2550 \times 300} = (4.21 \pm 0.09) \times 10^{12}$$

So:

$$N_{\text{Surf}} = (4.21 \pm 0.09) \times 10^{12}$$

Therefore, SERS enhancement factor for CB[7]-NRSP is:

$$EF_{\text{CB}[7]-\text{NRSP}} = \frac{4000 \pm 167 \text{cps} / (4.21 \pm 0.09) \times 10^{14}}{14.17 \pm 0.83 \text{cps} / 1.98 \times 10^{20}} = (1.33 \pm 0.15) \times 10^{10}$$

Similar for the calculation of SERS enhancement for CB[8]-NRSP, where N_{Surf} was calculated to be $(6.8 \pm 1.7) \times 10^{11}$ based on the ITC titration experiment.

$$I_{\text{SERS}} = \frac{18000 \pm 1300 \text{counts}}{15 \text{s}} = 1200 \pm 87 \text{cps}$$

Therefore, SERS enhancement factor for CB[8]-NRSP is:

$$EF_{\text{CB}[8]-\text{NRSP}} = \frac{1200 \pm 87 \text{cps} / (6.8 \pm 1.7) \times 10^{11}}{14.17 \pm 0.83 \text{cps} / 1.98 \times 10^{20}} = (2.47 \pm 0.75) \times 10^{10}$$

Chapter 5

Cucurbit[7]uril-based High-performance Catalytic Microreactors

Catalytic microreactors manufactured using microfluidic devices have received significant research interest in recent years. However, little attention has been paid to immobilising metallic nanoparticles (NPs) on microchannel walls for high efficiency catalytic reactions. We demonstrate a facile preparation of cucurbit[n]uril-based catalytic microreactors, where metallic NPs are immobilised onto microchannels via supramolecular complexation with methyl viologen@cucurbit[7]uril (CB[7]). This microreactor exhibits remarkable catalytic activity owing to substantially high surface area to volume ratio of the microchannels and metallic NPs. Superior to most conventional heterogeneous catalytic reactions, separation post reaction and complicated recycling steps of the catalysts are not required. Moreover, CB[7] can complex a variety of metallic NPs to its portal, providing a multifunctional high-performance in situ catalytic platform.

This work has been published in the following peer-reviewed journal articles:

- **Ren, X.**; Yu, Z.; Wu, Y.; Liu, J.; Abell, C.; Scherman, O.A.*, "Cucurbit[7]uril-based high-performance catalytic microreactor", *Nanoscale*, in press.

5.1 Introduction

Microfluidics have received much attention over the past few decades in a broad range of fields,^{239–242} including chemistry,^{243,244} biology,^{245,246} pharmaceuticals,²⁴⁷ physics²⁴⁸ and materials science.²⁴⁹ In particular, flow chemistry using microfluidic devices have attracted great interests, on account of a variety of distinct advantages.^{247,250,251} For instance, significant surface area to volume ratio in a microreactor (10,000 to 50,000 m⁻¹) can dramatically enhance the mass transport efficiency of reactants and products.²⁵⁰ In addition, a small channel diameter (10–1000 μm) results in largely improved heat transfer for isothermal catalytic reactions, allowing high selectivity towards desired products.^{247,250,252} Catalytic microreactors are one of the most popular topics in flow chemistry.^{250,253} Various approaches to fabricate catalytic microreactors have been reported,^{253–259} among which the most advantageous has been functionalisation of the microchannel surface using catalysts.^{206,260} This surface functionalisation approach could substantially minimise the mass transfer resistance, avoiding adverse pressure drops or blockages of the microchannels, problems commonly observed in other approaches.^{247,250} However, investigation on surface functionalised catalytic microreactors has mainly focused until now on the immobilisation of organocatalysts^{261,262} and organometallic catalysts.^{263,264} Less effort has been devoted to immobilising metallic nanoparticles (NPs) onto microchannel surfaces.^{247,264,265} The state-of-the-art approaches to prepare such microreactors suffer from shortcomings of high temperature and harsh conditions,^{247,250,264,266} as well as inevitable leaking of the metallic NPs due to fragile attachment.^{206,247,265}

Herein, we demonstrate a facile fabrication route to multifunctional catalytic microreactors based on cucurbit[*n*]uril (CB[*n*]) host-guest chemistry (illustrated in Figure 5.1). CB[*n*]s are a family of symmetric barrel-shaped host molecules, which are capable of selectively encapsulating small guest molecules in their cavity (K_a up to 10¹⁵ M⁻¹).^{78,267,268} Moreover, the portal of CB[*n*] exhibits strong binding affinity towards various metallic NPs (e.g. gold, palladium, platinum, copper and silver).^{119,165} By functionalising the microchannel with methyl viologen (MV)-silane@CB[*n*] complexes, a variety of metallic NPs could be readily loaded and immobilised onto the microchannel wall. This CB[*n*]-

based catalytic microreactors exhibit higher catalytic activity than most single-site heterogeneous NP catalysts supported by mesoporous silica,^{269–271} carbon,^{270–272} polymer networks,^{270,271,273,274} and other substrates,^{270,271,275,276} while avoiding the inconvenience of post-reaction catalyst separation as well as leaching.^{269–276}

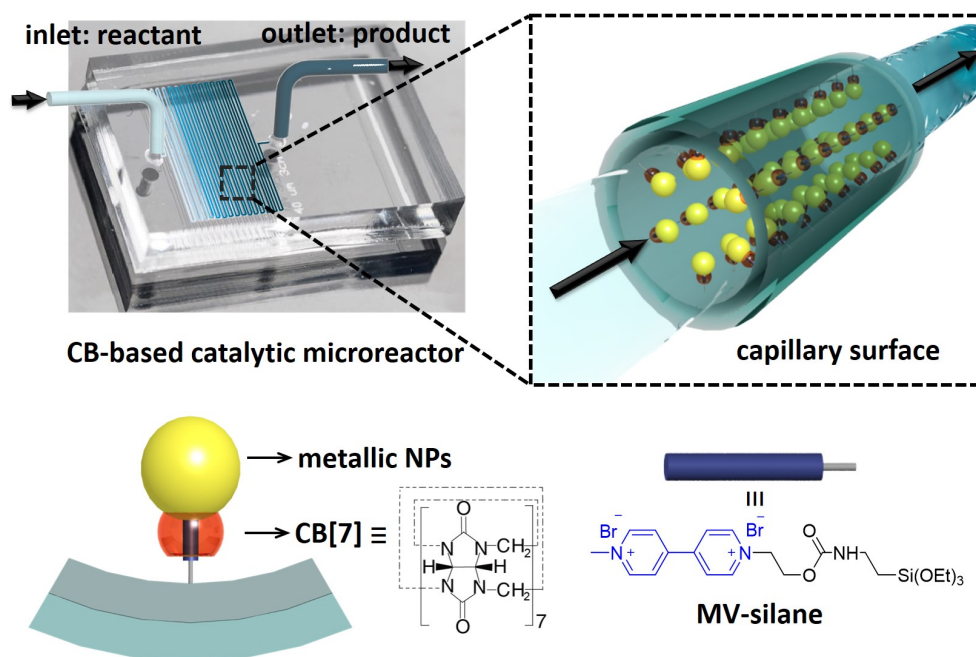


Figure 5.1: Schematic illustration of cucurbit[7]uril-based high-performance catalytic microreactor.

5.2 Results and Discussion

5.2.1 Fabrication of the catalytic microreactor

The microfluidic devices were prepared through well-established soft lithography using polydimethylsiloxane (PDMS).²⁴² The CB[*n*]-based *in situ* catalytic microreactors were fabricated in two steps. First, after activation of the microchannel by oxygen plasma, an aqueous solution of MV-silane@CB[7] inclusion complex was injected into the microchannel at a flow rate of $300 \mu\text{L}\cdot\text{h}^{-1}$ for 2 h. The methyl viologen groups formed strong 1:1 inclusion complexes with CB[7], with an association constant K_a of $3.3 \times 10^5 \text{ M}^{-1}$ (Figure 5.2). Meanwhile, the silane moieties on the MV-silane covalently attached and be-

came immobilised onto the activated microchannels. The second step was the flow of the metallic NP solution into the microchannel at a flow rate of $200 \mu\text{L}\cdot\text{h}^{-1}$ for 1 h. The PDMS microchannel can be made with different geometries or length depending on the requirement for the particular catalytic reaction (Figure 5.3). Au ($6.8 \pm 2.1 \text{ nm}$, Figure 5.4a) and Pd NPs ($3.7 \pm 0.8 \text{ nm}$, Figure 5.4b) were chosen as example metallic NPs to immobilise inside the microchannels on account of their excellent catalytic activity.^{277,278}

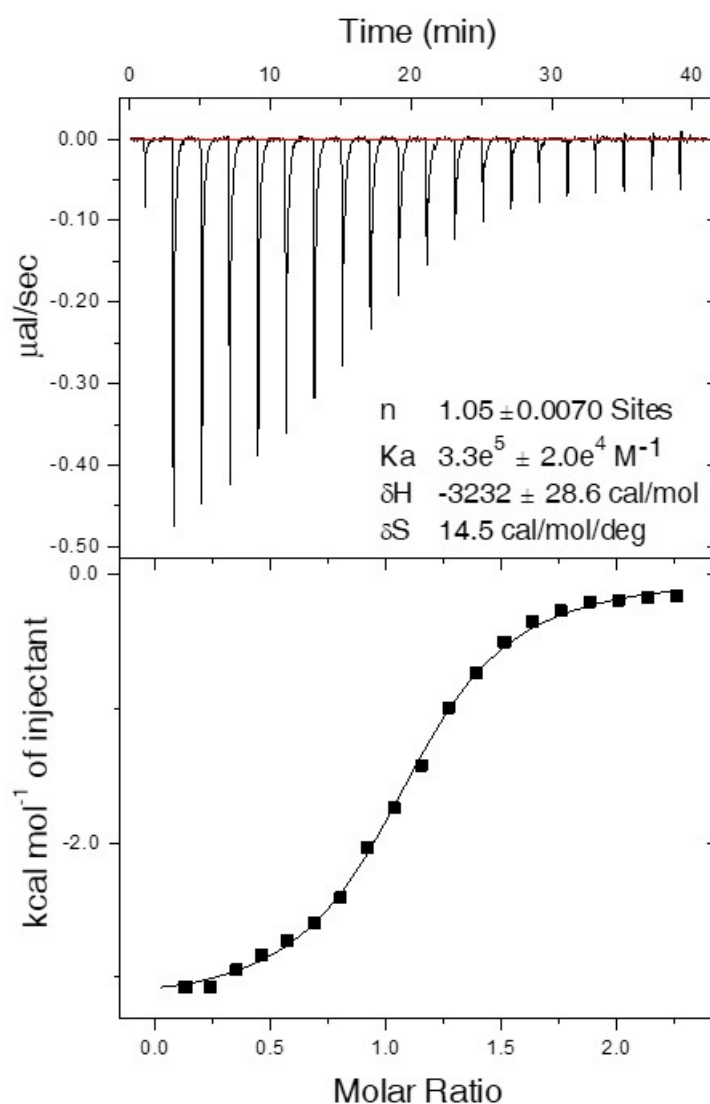


Figure 5.2: ITC result of the complexation between MV-silane and CB[7]. 1 mM MV-silane was injected into 0.05 mM CB[7] in buffer solution at 25 °C. 50 mM sodium acetate buffer, pH=4.6, was used.

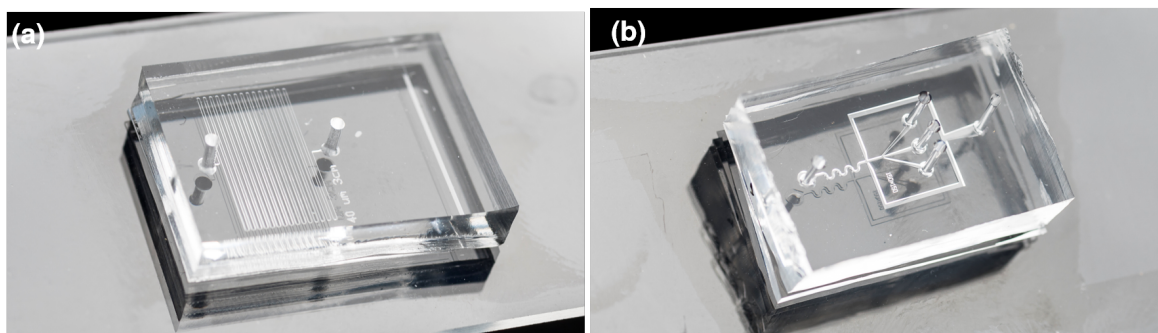


Figure 5.3: (a) and (b) Pictures of example PDMS microchannels with various channel shapes and length. In this work, Au/Pd microreactors utilized the PDMS microchannels (a) with 40 μm diameter and 3 cm length.

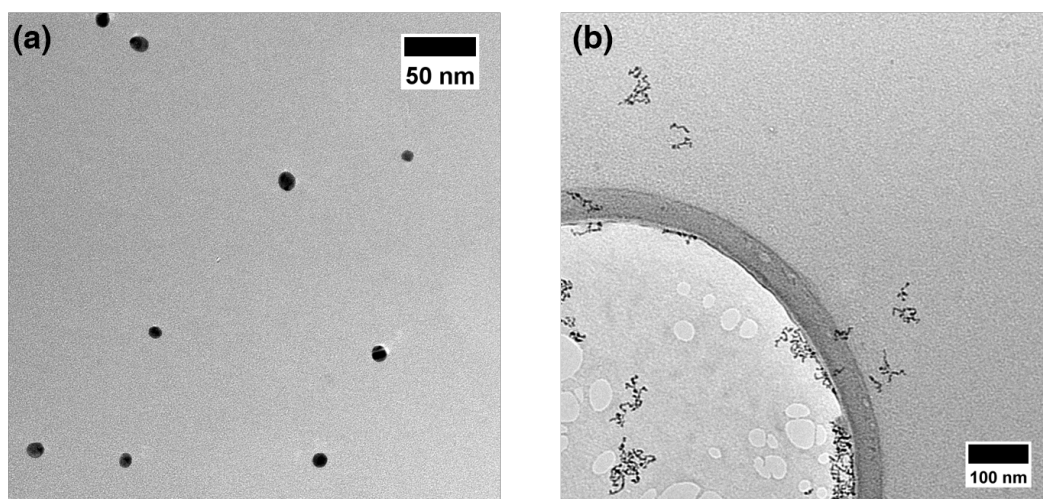


Figure 5.4: TEM images of (a) Au NPs (6.8 ± 2.1 nm) and (b) Pd NPs (3.7 ± 0.8 nm)

5.2.2 Characterisation of the catalytic microreactor

Figure 5.5b and c show SEM images of the internal channel of the CB[7]-based Au NP catalytic microreactor. The loaded Au NPs can be clearly observed suggesting their immobilisation. AFM images of the Au NP microreactor are shown in Figure 5.5d-f. According to the 3D view and topography images, Au NPs formed a monolayer inside the microreactor. The height of Au NPs in the AFM profile (Figure 5.5f) is consistent with the size of the Au NPs obtained from TEM (6.8 ± 2.1 nm, Figure 5.4a).

In addition, control channels (blank microchannel, channel **A**, **B** and **C**) were also examined to confirm the importance of MV-silane@CB[7] inclusion complex. Control chan-

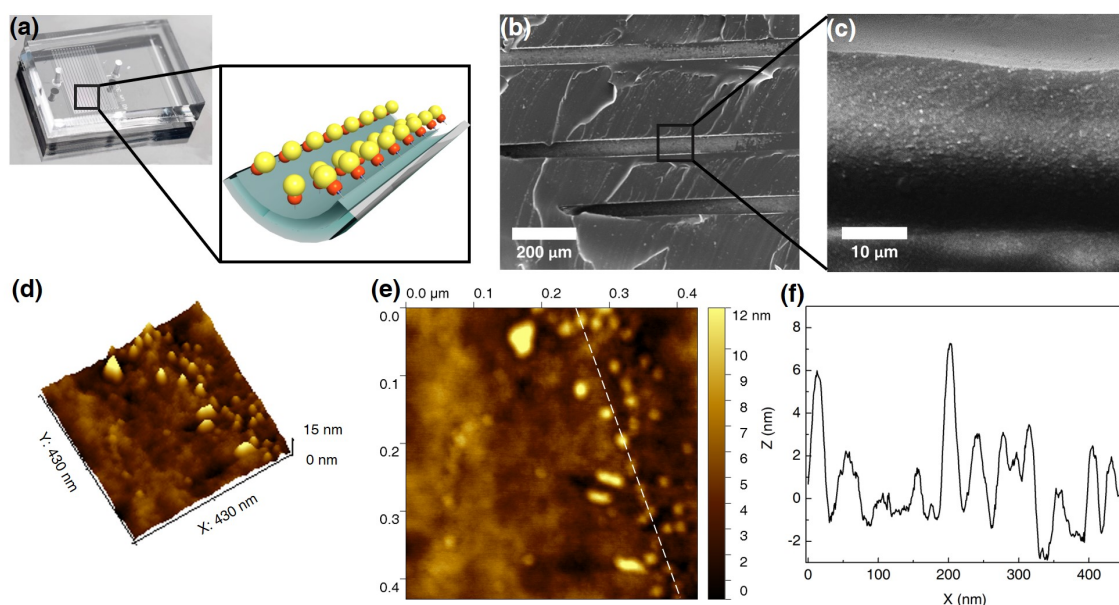


Figure 5.5: (a) Illustration of the internal structure of the microreactors; (b) and (c) SEM images of the internal surface of CB[7]-based Au NP catalytic microreactor, where the immobilisation of Au NPs was clearly observed; (d) AFM 3D view of the Au NP microreactor internal surface; (e) AFM topography image of the Au NP microreactor internal surface; (f) profile of the dashed line in (e), where the height of Au NPs are consistent with the size of Au NPs obtained from TEM (6.8 ± 2.1 nm).

nels **A** and **B** were prepared by solely injecting MV-silane or CB[7] solutions in the first step, followed by the injection of metallic NPs. Control channel **C** was prepared by just injecting metallic NPs without the injection of MV-silane@CB[7] inclusion complex solutions. As seen in Figure 5.6c and 5.8, control **A** shows severe agglomeration of metallic particles on a scale of micrometres. Control **B** (Figure 5.6d and 5.9) and **C** (Figure 5.6e) resemble the blank channel (Figure 5.6b and 5.7), since all the NPs were flushed out of the microchannels.

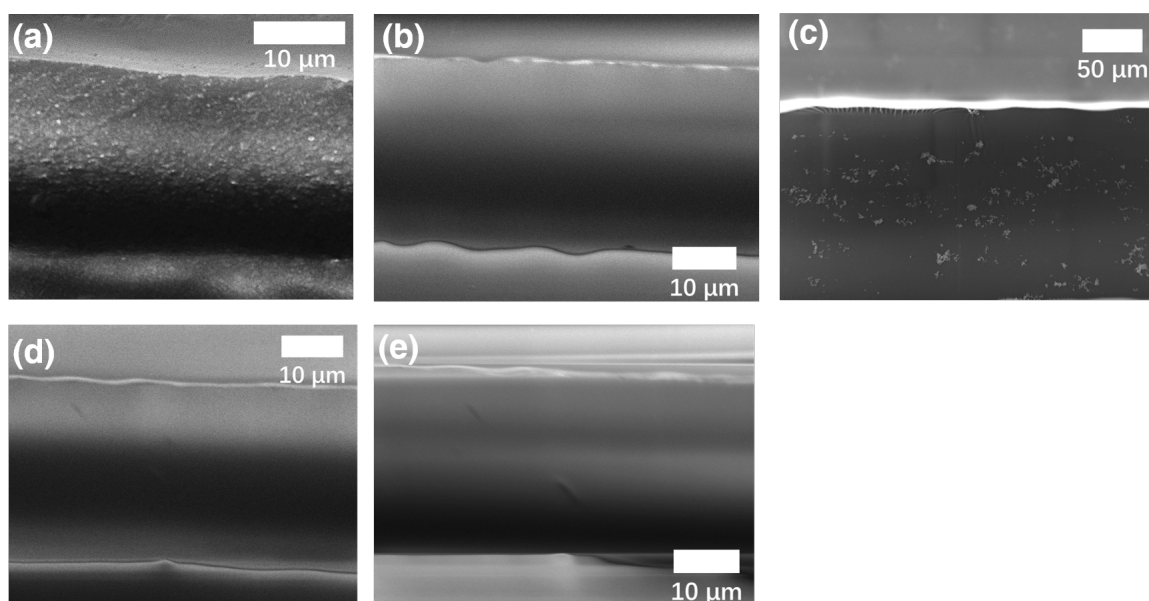


Figure 5.6: SEM images of (a) CB[7]-based Au NP catalytic microreactor, (b) blank PDMS microchannel, (c) control channel A, (d) control channel B, (e) control channel C. Note: Control channels A and B were prepared by solely injecting MV-silane or CB[7] solutions, followed by metallic NP solutions. Control channel C was prepared by just injecting metallic NPs.

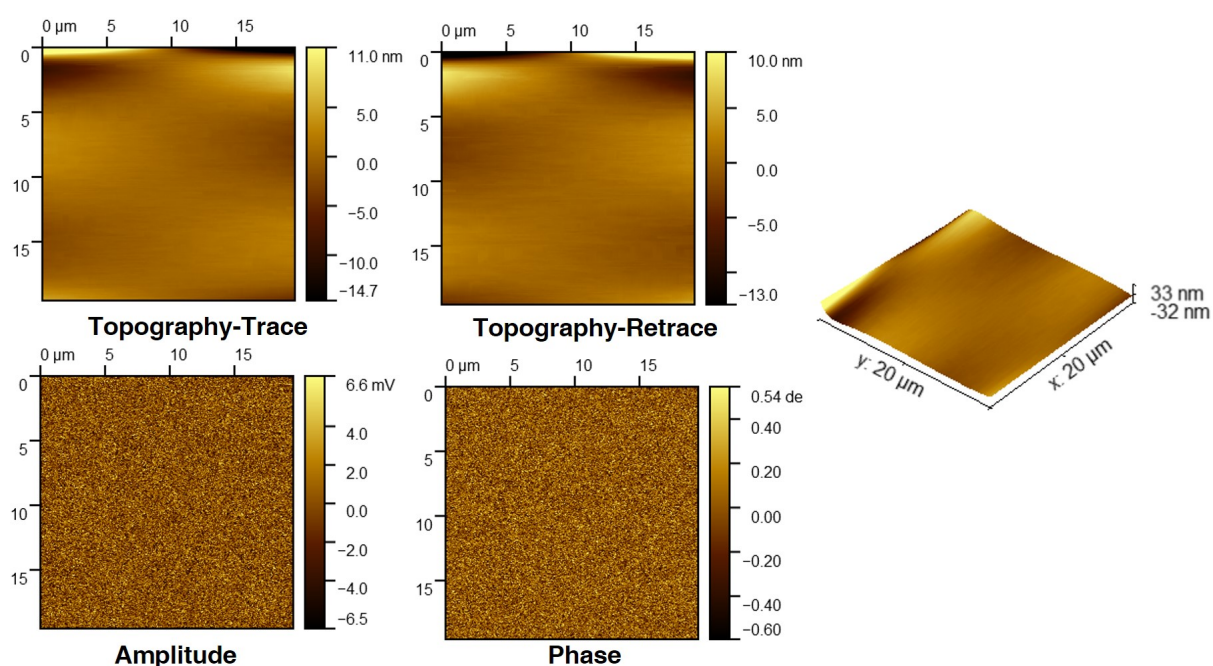


Figure 5.7: AFM images of blank PDMS microchannels (roughness = 0.06 nm).

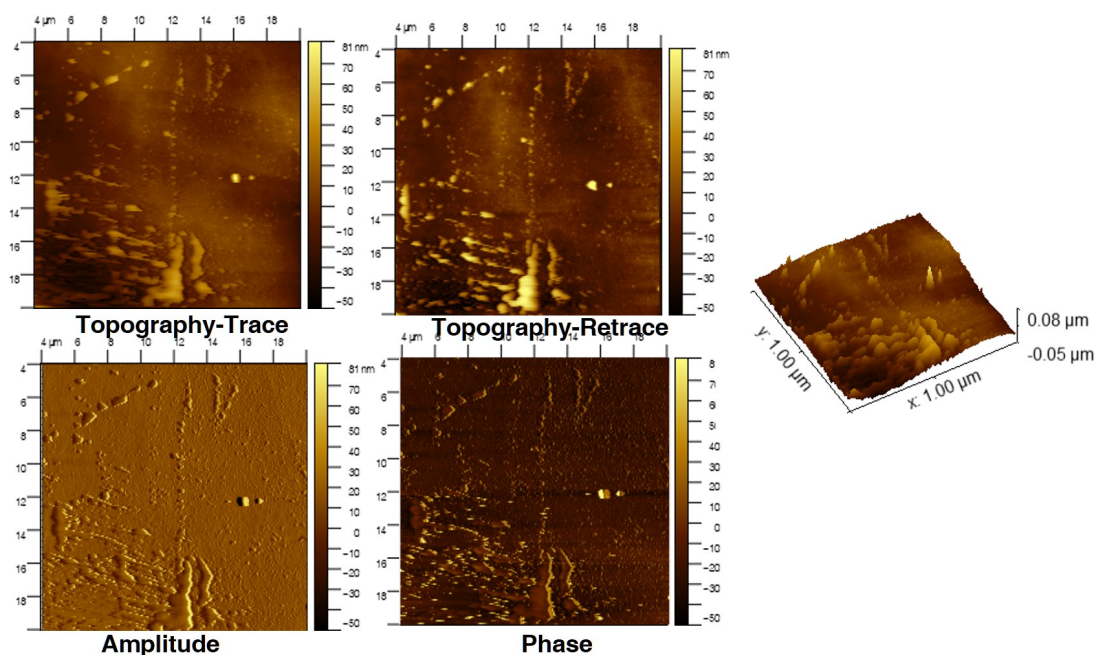


Figure 5.8: AFM images of Au NP control channel (A, just injecting MV-silane and then metallic NP solutions, but without CB[7] solutions), where serious agglomeration of Au particles was observed. Roughness = $0.12 \mu\text{m}$.

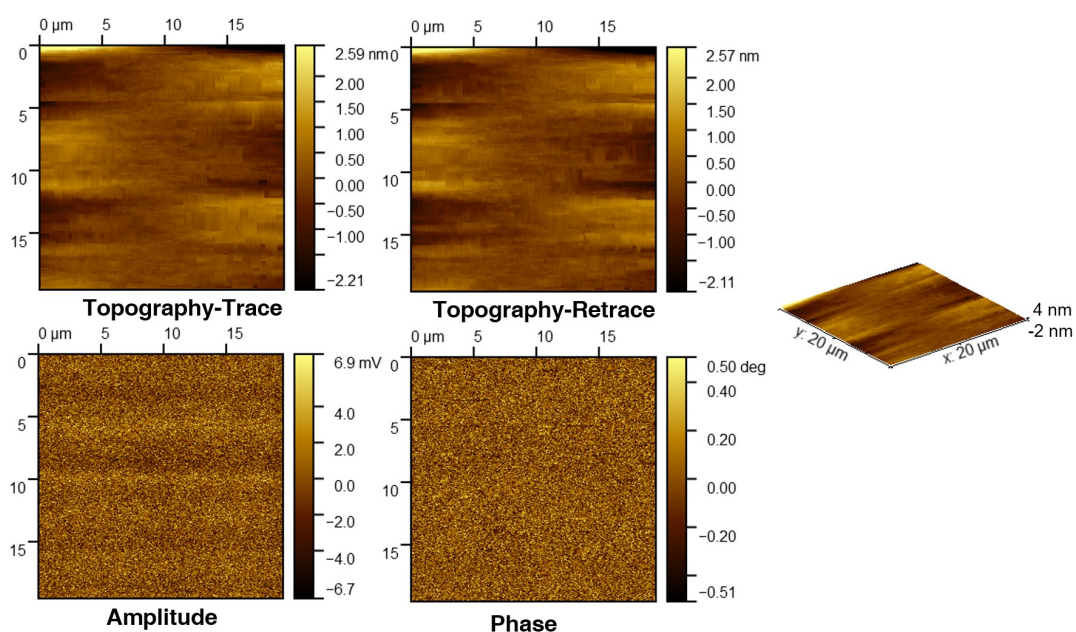


Figure 5.9: AFM images of Au NP control channel (B, prepared by just injecting CB[7] and then metallic NP solutions, but without the injection of MV-silane solutions), where no Au NPs were observed.

Moreover, it was observed that by increasing the concentration of injected Au NP solutions (e.g. from 1 *wt%* to 5 *wt%*), the density of the immobilised Au NPs increased (from 0.11 ± 0.06 to $0.20 \pm 0.05 \text{ nm}^{-2}$, Figure 5.10).

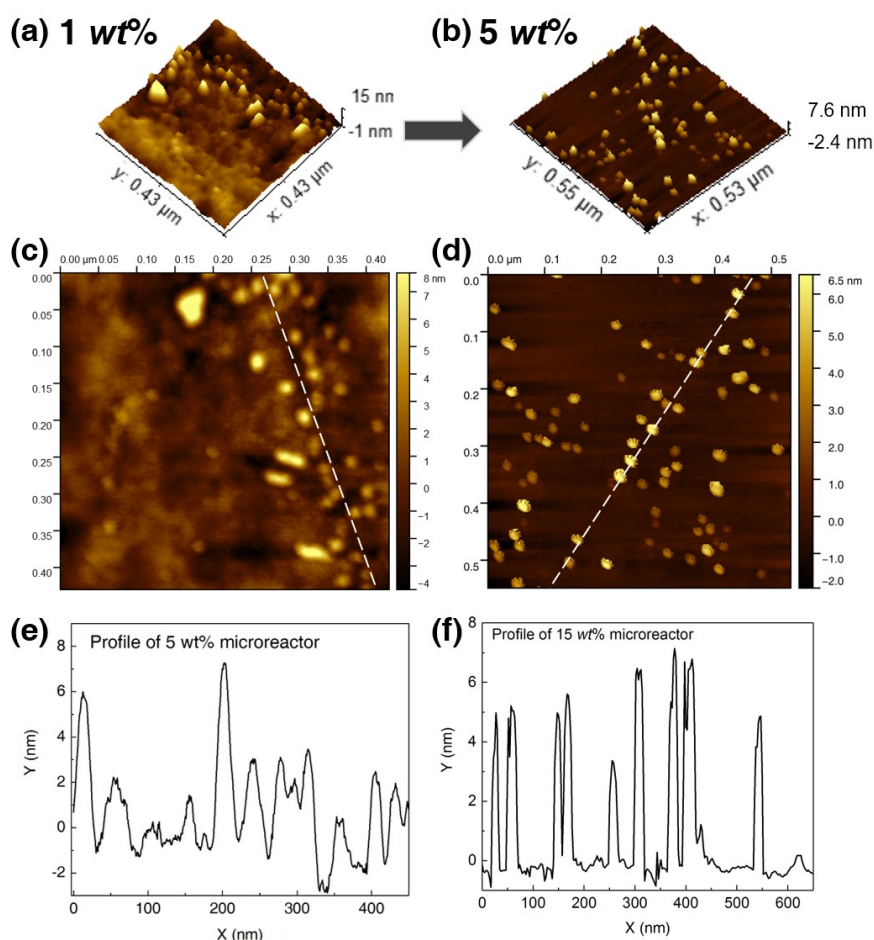


Figure 5.10: AFM 3D view images (a, b) and topography images (c, d) of Au NP catalytic microreactors prepared using 1 *wt%* and 5 *wt%* Au NP solutions, respectively. (e, f) show the profiles of the dashed lines indicated in (c, d) respectively. An increase of the loading NP density using increased concentration was observed.

The immobilisation of Pd NPs in a CB[7]-based catalytic microreactor was also confirmed by SEM (Figure 5.11) and AFM (Figure 5.12), with the immobilised Pd NP density of $0.15 \pm 0.07 \text{ nm}^{-2}$ deposited from a 1 *wt%* solution.

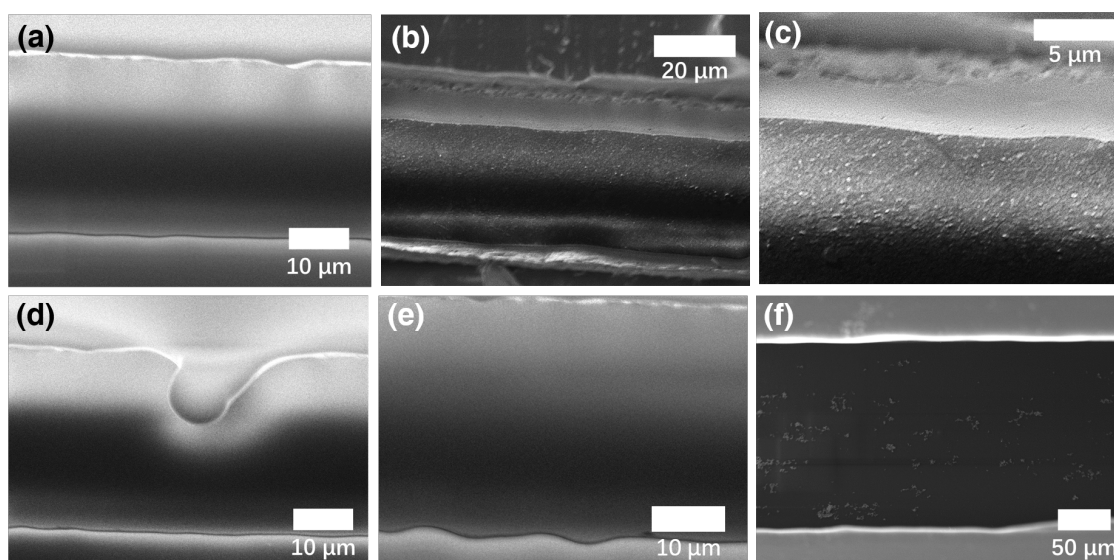


Figure 5.11: SEM images of (a) blank PDMS microchannel, (b) CB[7]-based Pd NP catalytic microreactor, (c) zoom in image of (b), (d) control channel C, (e) control channel B, (f) control channel A, where agglomerates in micrometre scale (no catalytic activity) were observed.

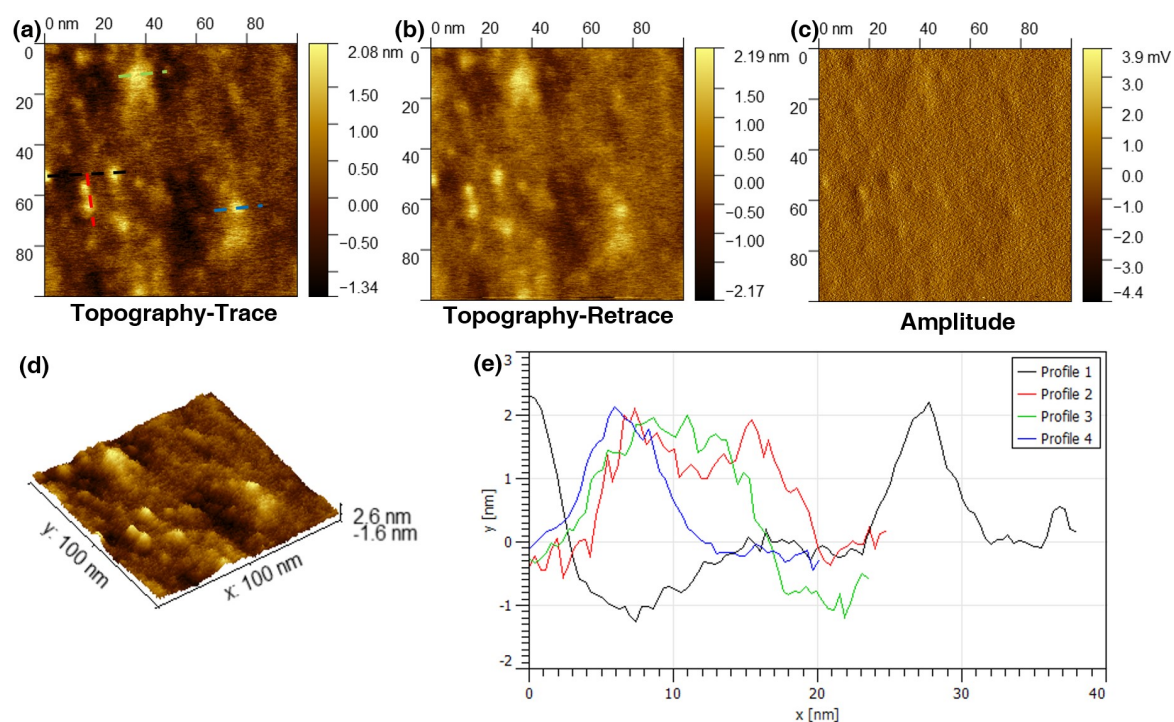


Figure 5.12: AFM images of Pd NP catalytic microreactor, where good immobilisation of Pd NPs was observed. (a) AFM topography images (trace); (b) AFM topography image (retrace); (c) AFM amplitude image; (d) AFM 3D view image; (e) profile of the dashed lines indicated in (a).

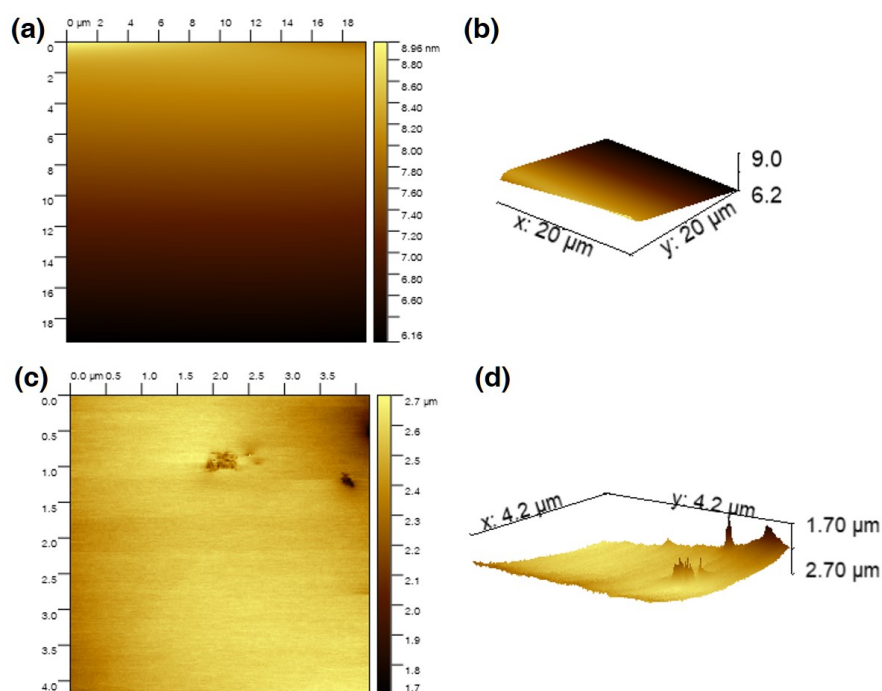
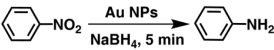
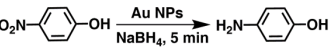
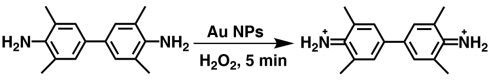
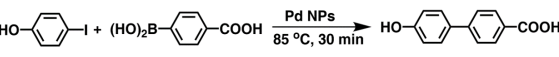
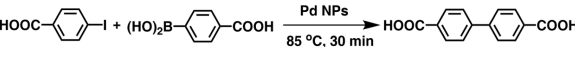
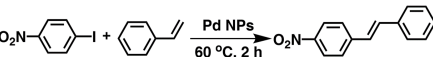


Figure 5.13: Topography and 3D view AFM images of Pd control channels. (a, b) were prepared by only injecting Pd NPs, where no NP was observed in the microchannel. (c, d) were prepared by only injecting MV-silane and Pd NP solutions, without CB[7] solutions. The agglomerates up to micrometre scale were observed, however, showing no catalytic activity.

5.2.3 Catalytic activity investigation

The catalytic activity of the Au NP microreactor with a density of $0.11 \pm 0.06 \text{ nm}^{-2}$ was examined with three reactions: reduction of nitrobenzene and 4-nitrophenol, as well as the catalytic oxidation of 3,3',5,5'-tetramethylbenzidine (TMB), as illustrated in Table 5.1 and Figure 5.14. To investigate the importance of the MV-silane@CB[7] complexes immobilised on the wall of the microreactor, control experiments were carried out using: (i) blank PDMS microchannel, (ii) control channel (prepared without the injection of CB[7] solution) and (iii) the reaction carried out using "bench" conditions.

Table 5.1: Summary of representative reactions catalysed by CB[7]-based Au NPs or Pd NPs catalytic microreactors.

Entry	Reaction Mode	Yield (%)	TOF ^a (s ⁻¹)
	microreactor	99 ^b	$(1.7 \pm 0.1) \times 10^2$
	control channel ^c	0 ^d	0
	bench ^e	50	$(4.2 \pm 0.2) \times 10^{-3}$
	microreactor	99	$(1.8 \pm 0.1) \times 10^2$
	control channel	0 ^f	0
	bench	60	$(5.0 \pm 0.3) \times 10^{-3}$
	microreactor	99	$(2.5 \pm 0.1) \times 10^2$
	control channel	0	0
	bench	0	0
	microreactor	99 ^g	$(1.3 \pm 0.1) \times 10^4$
	control channel	0	0
	bench	40	$(1.0 \pm 0.1) \times 10^3$
	microreactor	99	$(1.3 \pm 0.1) \times 10^4$
	control channel	0	0
	bench	50	$(1.3 \pm 0.1) \times 10^3$
	microreactor	85	$(7.2 \pm 0.1) \times 10^2$
	control channel	0	0
	bench	10	$(7.1 \pm 0.1) \times 10^{-4}$

^a Turnover frequency (TOF) suggests remarkable catalytic activity of the microreactors, which is much above most relevant industrial reactions (TOF sit in between 10^{-2} to 10^2 s⁻¹).²⁷⁹ Moreover, the TOF of the microreactors remained unchanged for more than 300 h at a flow rate of $200 \mu\text{L h}^{-1}$. ^b Au NP reactions in microchannels were carried out at a flow rate of $200 \mu\text{L h}^{-1}$. The yield was determined from UV-vis absorption analysis. ^c Control channels were prepared by only injecting and flowing MV-silane and metallic NP solutions through the microchannel sequentially, but without CB[7] solutions. ^d The first run gave rise to 50% yield; however, this quickly decreased to 0% in the subsequent reaction cycles due to severe leaking of the particles. ^e Bench reactions were carried out under approximately similar conditions, using free metallic NPs as the catalyst instead. ^f The first run gave rise to 60% yield; however, later reaction cycles quickly decreased to 0% yield. ^g Pd NP reactions in microchannels were carried out at a flow rate of $100 \mu\text{L h}^{-1}$. The yield was determined from HPLC analysis.

The catalytic reduction of nitrobenzene by NaBH₄ in the presence of Au NPs is a typical test reaction yielding aniline, which is an important chemical widely used in the fine chemicals, agrochemical and pharmaceutical industries.²⁸⁰ As shown in Figure 5.14a and Figure 5.16, the microreactor gave rise to 99% yield in 5 min, while 0% yield was observed for the reaction in the blank microchannel and only 50% for the reaction carried out on the bench with approximately similar conditions. Importantly, 50% yield was

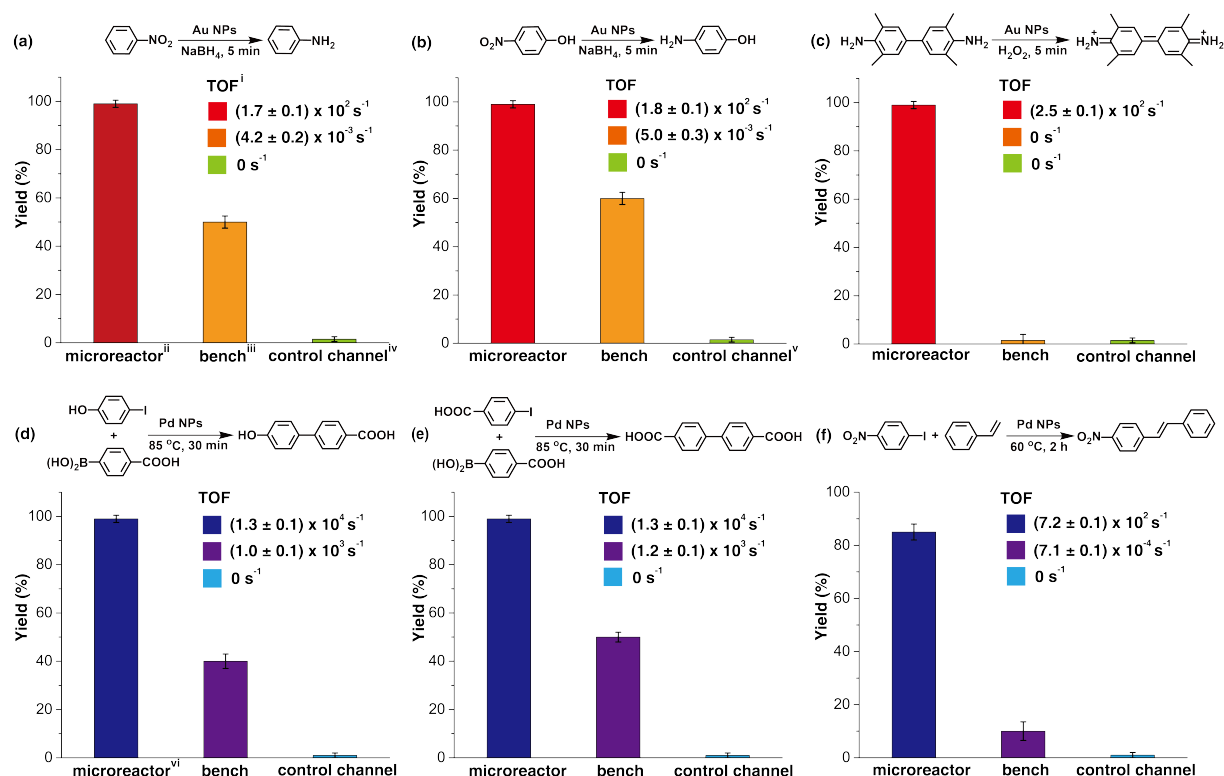


Figure 5.14: Summary of representative reactions catalysed by CB[7]-based Au/Pd NP catalytic microreactors. (a), (b) and (c) show the yield and turnover frequency (TOF) of three typical reactions catalysed by the Au NP microreactor, control channel and reactions on bench. (d), (e) and (f) show the results for Pd NP catalysed reactions, demonstrating the versatility of the microreactor. The microreactors led to high purity products with high yield (85% to 99%) in all reactions, while the bench reaction gave rise to comparably low yield products (10% to 60%) with various byproducts. The control channel showed almost no catalytic ability due to leaching of catalysed particles during the reactions.

observed in the control channel on the first run; however, this quickly decreased to 0% in the subsequent reaction cycles. This initial moderate level of catalytic activity might be explained by the formation of Au agglomerates arising from electrostatic attraction between the positively charged MV groups and the negatively charged Au NP surface (Figure 5.6c and 5.8). Au agglomerates leaked out in the presence of salt during the reaction, leading to deactivation of the control channel.^{281,282} In contrast, CB[7]-based Au NP catalytic microreactors, where the Au NPs were immobilised with the CB[7] portals did not leak out from the microchannel during the reaction,^{119,165} capable of maintaining the same yield for more than 300 h at a flow rate of 200 $\mu\text{L}\cdot\text{h}^{-1}$. The catalytic reduction

of 4-nitrophenol by NaBH_4 in the presence of Au NPs leading to 4-aminophenol, an important reactive intermediate for the photographic and pharmaceutical industries,²⁸³ led to similar results as the previous reaction (Figure 5.14b and Figure 5.17). Oxidation of the aromatic amine TMB in the presence of Au NPs by hydrogen peroxide, which is a highly sensitive method for the detection of H_2O_2 in biological fluids was also tested.²⁸⁴ Figure 5.14c and Figure 5.18 show that Au NPs microreactors efficiently catalysed the oxidation of TMB, giving rise to 99% yield in 5 min at a flow rate of $200 \mu\text{L}\cdot\text{h}^{-1}$. A solution colour change from colourless in the inlet tube to blue in the outlet tube was clearly observed. In contrast, both the control channel and bench reactions showed 0% conversion. The turnover frequency (TOF) of the three reactions described above in the Au NP microreactors were calculated to be 171 ± 2 , 178 ± 4 and $256 \pm 6 \text{ s}^{-1}$, respectively, which are 10^5 greater than the TOF for reactions on the bench (Table 5.1); moreover, these TOF values are much higher than most single-site Au NP heterogeneous catalysts,^{269,270,273,275} demonstrating excellent catalytic activity. Additionally, no detectable loss in the catalytic activity (TOF) was observed upon continuous operation for 300 h.

Three typical Pd NP catalysed cross coupling reactions were examined for the CB[7]-based Pd NP microreactor, as depicted Table 5.1, Figure 5.14d-e and Figure 5.19 to 5.21. Interestingly, only the reactions in the microreactors led to pure products with high yield (99% for both Suzuki reactions and 85% for the Heck reaction), while reactions in both the blank microchannel and control channel did not yield any product. The bench reaction showed comparably low yield (40-50% for the Suzuki reactions and 10% for the Heck reaction), all with various by-products. The high catalytic activity of the microreactors are attributed to the significant surface area to volume ratio of the NPs and the microchannel. The higher purity observed of the products may be due to the small channel diameter, which contributes to enhanced heat transfer, allowing high selectivity for desired products.^{247,250,252} The Pd microreactor gives rise to higher TOF than most single-site heterogeneous Pd catalysts (10 - 10^5 times).^{271,272,274,276} TOF for both of the Suzuki reactions in the microreactors were $(1.3 \pm 0.1) \times 10^4 \text{ s}^{-1}$, and the TOF for the Heck reaction was $719 \pm 2 \text{ s}^{-1}$, at a flow rate of $100 \mu\text{L h}^{-1}$. Similarly, no loss in catalytic activity was

observed upon continuous operation for 300 h.

5.3 Conclusion and Outlook

By taking advantage of the strong binding affinity of the CB[7] portal towards metallic NPs, as well as CB[7]'s ability to encapsulate small guest molecules such as viologen derivatives in its cavity, we have successfully fabricated CB[7]-based metallic NP catalytic microreactors. The metallic NPs were immobilised as a monolayer inside microchannels *via* supramolecular inclusion complexes (MV-silane@CB[7]) and subsequent attachment to the carbonyl portal of the sequestered CB[7]. This microreactor exhibits several advantages. For instance, no further separation or recycling of the catalysts are required. More importantly, the substantially high surface area to volume ratio of both the microchannel and metallic NPs contribute to remarkable activity of the catalytic microreactor. All catalytic reactions investigated with the Au NP and Pd NP microreactors exhibited high yield with high TOF (up to 10^4 s^{-1}), significantly higher than most single-site heterogeneous NP catalysts^{269–276} and are above the values of relevant industrial applications (TOF values in the range of 10^{-2} to 10^2 s^{-1}).²⁷⁹ This CB[7]-based attachment methodology provides a powerful multifunctional platform for high performance flow chemistry, holding great promise in a variety of catalytic reactions.

5.4 Experimental Appendix

5.4.1 Materials and general methods

All the starting materials were purchased from Sigma Aldrich and used as received unless stated otherwise. CB[7] was prepared according to literature protocols.⁷⁷

¹H NMR (400 MHz) spectrum was recorded using a Bruker Advance QNP 400. The binding constant of MV-silane and CB[7] was measured using MicrocalTM ITC₂₀₀ (isothermal titration calorimetry). TEM images were obtained by a FEI Philips Tecnai 20 TEM under an accelerating voltage of 100 kV. Samples were prepared by applying one drop of the metallic NP solutions onto a Holey R carbon coated copper TEM grid (400 mesh),

followed by drying overnight at room temperature. SEM images were obtained by a TESCAN MIRA3 FEG-SEM using a beam voltage of 5 kV under in-beam SE detector. Samples were prepared by cutting the microchannels from the middle, sticking onto SEM stubs and coating with 5 nm Chromium under vacuum using Quorum Technologies Q150T ES turbo-pumped sputter coater. AFM images were recorded using an Agilent Technologies 5500 AFM under AAC mode (acoustic intermittent contact mode). The AFM probes were purchased from Bruker Nano Inc. (MSNL, back layer of the cantilevers coated by 45 ± 5 nm Au). F triangle probes, with a spring constant of 0.6 N/m, resonant frequency of 125 kHz, tip radius of 20 nm by average and 60 nm at the maximum, were used. The AFM samples were prepared by carefully cutting the channels through the middle, then cutting it into square pieces with a thickness of around 1 mm. UV-vis spectra were obtained on a Varian Cary 4000 UV-vis spectrometre. High-performance Liquid Chromatography (HPLC) was performed on a Varian 940-LC system. The Agilent Eclipse Plus C18 5 μ m 4.6 \times 150 mm column was used to analyse the resultant products. The gradient applied was from 95 : 5 water (0.1% trifluoroacetic acid): acetonitrile to 100% acetonitrile.

5.4.2 Preparation of metallic catalyst nanoparticles

The metallic catalyst NPs were synthesised by rapid reduction of corresponding high valence metallic acids/salts in the presence of sodium borohydride. The Au NPs were synthesised by firstly mixing 1 *wt*% sodium citrate (2 mL) with 1 *wt*% chloroauric acid (1 mL) in 100 mL water, stirring and cooling in an ice bath for 10 min. Then 0.1 M sodium borohydride (10 mL, pre-cooled) was added rapidly, stirring for 1 h. Similarly, the Pd NPs were synthesised by the rapid addition of sodium borohydride (0.1 M, 4 mL, pre-cooled) to the cooled mixtures of 1 *wt*% sodium citrate (2 mL) with 10 mM sodium tetrachloropalladate (1 mL) in 100 mL water.

5.4.3 Synthesis and characterisation of MV-silane

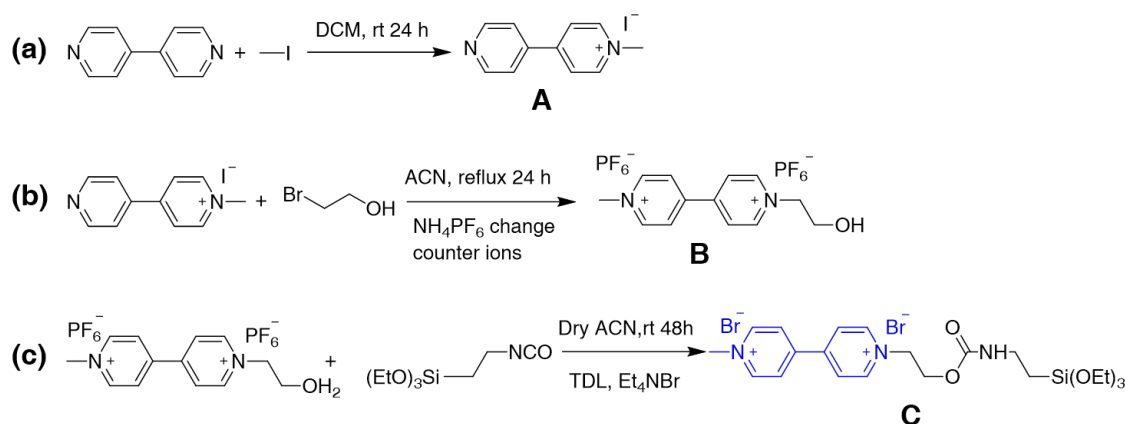


Figure 5.15: Reaction scheme of the synthesis of 1-(4,4-diethoxy-8-oxo-3,9-dioxa-7-aza-4-silaundecan-11-yl)-1'-methyl-[4,4'-bipyridine]-1,1'-dium (MV-silane).

(a) 4,4'-bipyridine (20 g, 128 mmol) was dissolved in 200 mL dichloromethane (DCM). Methyl iodide (10 mL, 162 mmol) was well dispersed in 100 mL DCM, and then added dropwise to the bipyridine solution, allowing reaction at room temperature (rt) for 24 h. The product 1-methyl-4-(4-pyridinyl)pyridinium iodide (**A**, MV⁺) was separated and washed with copious DCM, and then air dried (34.3 g, yield 79 %).

(b) MV⁺ (**A**) (6.0 g, 20 mmol) was dissolved and refluxed in 300 mL acetonitrile (ACN). 2-bromoethanol (12.5 g, 100 mmol) was firstly dispersed in 15 mL ACN, and then added in to the MV⁺ solution, refluxing for 24 h. The resultant products were separated and washed with copious ACN, then dissolved in 15 mL water and were exchanged counter ions with ammonium hexafluorophosphate (4.16 g, 25.5 mmol) to obtain C₁₃H₁₆N₂O²⁺ · 2 PF₆⁻ (**B**).

(c) **B** (0.9 g, 1.8 mmol) and 3-(triethoxysilyl)propyl isocyanate (4.45 g, 18 mmol) were dissolved in 20 mL dry ACN, with the addition of catalytic amount of dibutyltin dilaurate (TDL), stirring for 48 h under nitrogen. After that, tetraethylammonium bromide (2.3 g, 10.9 mmol, dissolved in 3 mL dry ACN) was added in the resultant solution, stirring for 2 h. Then the product was separated and washed with ACN and copious diethyl ether (**C**, 1.36 g, yield 60%). ¹H NMR (400 MHz, DMSO), 9.17 (*d*, 4H, J_{AB}=0.52Hz), 8.65 (*d*, 4H, J_{BA}=0.52Hz), 7.03 (*t*, 1H, J_{AB}= 2.01Hz), 5.02 (*t*, 2H, J_{BC}=0.52 Hz), 4.50 (*t*, 2H,

$J_{AC}=1.26\text{Hz}$), 4.45 (s, 3H), 3.78 (q, 6H), 2.89 (t, 2H, $J_{AB}=1.68\text{Hz}$), 1.21 (t, 9H, $J_{BC}=0.31\text{Hz}$), 0.9 (t, 2H, $J_{AC}=0.99\text{Hz}$). ^{13}C NMR (400 MHz, DMSO), δ = 158.73, 150.87, 145.43, 126.95, 63.93, 59.98, 58.43, 48.83, 29.76, 20.45, 18.32 ppm. Mass Spectra, m/z = 449.3423 g/mol.

5.4.4 Preparation of PDMS microfluidic devices

The microfluidic device was produced *via* standard soft lithography by pouring poly-(dimethylsiloxane) (PDMS, 20 g) along with a crosslinker (Sylgard 184 elastomer kit, Dow Corning, pre-polymer : crosslinker = 10 : 1 by weight) onto a silicon wafer patterned with SU-8 photoresist.^{242,285,286} It was then placed in vacuum for half an hour to remove dissolved gas. The PDMS was allowed to solidify at 90 °C for 12 h before being peeled off, after which inlets and outlets were generated using a biopsy punch. The enclosed microfluidic channels were formed by attaching the moulded PDMS replica onto a clean glass slide after exposure to oxygen plasma for 10 s in a Femto plasma cleaner.

The microchannels could be fabricated to various shapes and length (Figure 5.3 as example), to satisfy the requirement of certain catalytic reactions, such as various inlets or gas protection. In this work, the PDMS microchannels with 40 μm diameter and 3 cm length was utilised.

5.4.5 Preparation of CB[7]-based catalytic microreactors

The CB[7]-based Au NPs catalytic microreactors were prepared as follows:

(1) The blank PDMS microfluidic channels were activated by oxygen plasma for 10 s, after which the MV-silane@CB[7] solution (2.5 mM MV-silane, 1 mM CB[7], in 50 : 50 water : ethanol solvent) was injected and flowed through the microchannel at a flow rate of 300 $\mu\text{L h}^{-1}$ for 2 h, followed by washing with water for 1 h at the same rate.

(2) The prepared Au NPs solution was injected and flowed through the microchannel at a rate of 200 $\mu\text{L h}^{-1}$ for 1 h, followed by washing with water for 1 h at the same rate.

The CB[7]-based Pd NPs catalytic microreactors were prepared in the same approach, injecting the prepared Pd NPs solution in step (2) instead. Note that all the solutions were filtered using 200 nm filter tips before being injected into the microchannels to avoid

blockage of the microchannels.

Control channels (A and B) were prepared by solely injecting MV-silane or CB[7] solutions in step (1). Control channel (C) was prepared by just conducting step (2), but without the injection of MV-silane@CB[7] inclusion complex solutions.

5.4.6 Au NP catalytic microreactors reaction conditions

5.4.6.1 Reduction of nitrobenzene by NaBH_4

6 mL deionised water, 0.5 mL 1 mM nitrobenzene and 2 mL 50 mM NaBH_4 were mixed, injected and flowed through the microreactor, control channel (A) and blank microchannel, all at a flow rate of $200 \mu\text{L h}^{-1}$. The bench reaction was carried out at the same experimental condition, using Au NP ($6.8 \pm 2.1 \text{ nm}$, 1 wt% 100 μL) as the catalyst instead. The resultant products were analysed using UV-vis spectroscopy. Yield was deduced from the reactant absorption peak (nitrobenzene, 270nm). The microreactor can be operated continuously for 300 h without detectable loss of the yield and TOF.

5.4.6.2 Reduction of nitrophenol by NaBH_4

Similar to previous reaction, the products were analysed using UV-vis spectroscopy.

5.4.6.3 Oxidation of TMB by H_2O_2

The mixture of 3,3',5,5'-tetramethylbenzidine (TMB, 1 mM, in 3 mL ethanol/water 1 : 1 solvent) and H_2O_2 (4 M in 3 mL water) was injected and flowed through the microreactor, control channel (A) as well as blank microchannel, at a flow rate of $200 \mu\text{L h}^{-1}$. A solution colour change from colourless in the inlet tube to blue in the outlet tube was clearly observed in the catalytic microreactor. The resultant products were analysed using UV-vis spectroscopy. Yield was deduced from the product absorption peak (oxidized TMB, 652 nm). The microreactor can be operated continuously for 300 h without detectable loss of the yield and TOF.

5.4.7 Pd NP catalytic microreactors reaction conditions

5.4.7.1 Suzuki reaction 1

4-iodophenol (100 mM) and potassium carbonate (200 mM) in 10 mL ethanol/water 1 : 1 solvent was preheated at 85 °C and mixed with 4-carboxyphenylboronic acid (150 mM in 10 mL ethanol/water 1 : 1 solvent). The reaction mixture was injected and flowed through the preheated microreactor and control channel (A) at a flow rate of 100 $\mu\text{L h}^{-1}$, heating and reacting at 85 °C for 30 min. The bench reaction was carried out using Pd NP (3.7 ± 0.8 nm, 1 wt% 100 μL) to catalyse 2 mL reaction mixture at 85 °C for 30 min. The resultant products were analysed using HPLC. The yield was deduced from HPLC calibration line of the reactant (4-iodophenol). The microreactor can be operated continuously for 300 h without detectable loss of the yield and TOF.

5.4.7.2 Suzuki reaction 2

Similar to previous reaction, the products were analysed using HPLC. The yield was deduced from HPLC calibration line of the reactant (4-iodobenzoic acid).

5.4.7.3 Heck reaction

1-iodo-4-nitrobenzene (13.3 mM), styrene (16.6 mM), potassium carbonate (26.6 mM) and tetrabutylammonium bromide (0.8 mM) were dissolved in 7.5 mL water/DMF 1 : 2 solvent and preheated at 60 °C. The reaction mixture was injected and flowed through the preheated microreactor and control channel (A) at a flow rate of 100 $\mu\text{L h}^{-1}$, heating and reacting at 60 °C for 2 h. The bench reaction was carried out using Pd NP (3.7 ± 0.8 nm, 1 wt% 100 μL) to catalyse 2 mL reaction mixture at 60 °C for 4 h. The resultant products were analysed using HPLC. The yield was deduced from HPLC calibration line of the reactant (1-iodo-4-nitrobenzene). The microreactor can be operated continuously for 300 h without detectable loss of the yield and TOF.

5.4.8 UV-vis and HPLC spectra for examined reactions

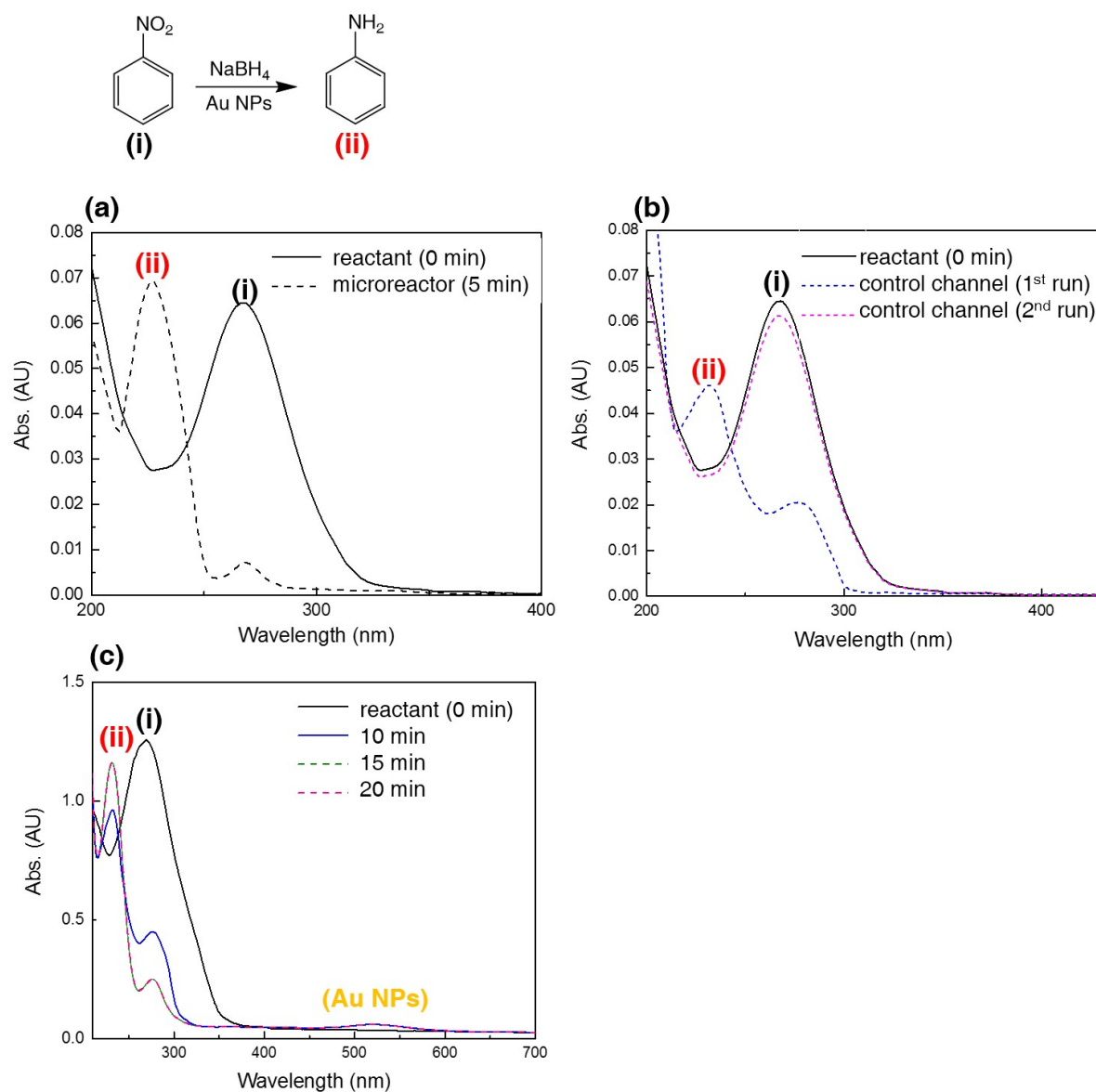


Figure 5.16: UV-vis spectra of (a) Au NP catalytic microreactor before and after reaction, yielding 99% after 5 min. (b) Au NP control channel: the first run gave 50% yield, then subsequent reaction cycles gave 0% yield. (c) The bench reaction with Au NPs led to a yield of 50% after 5 min and 99% after 15 min. No further increase of the product peak (ii) was observed after 15 min. The peak at 530 nm was caused by the remaining Au NPs in the reaction solution. The Au NPs used for the bench reaction were difficult to be separated and recycled for further use.

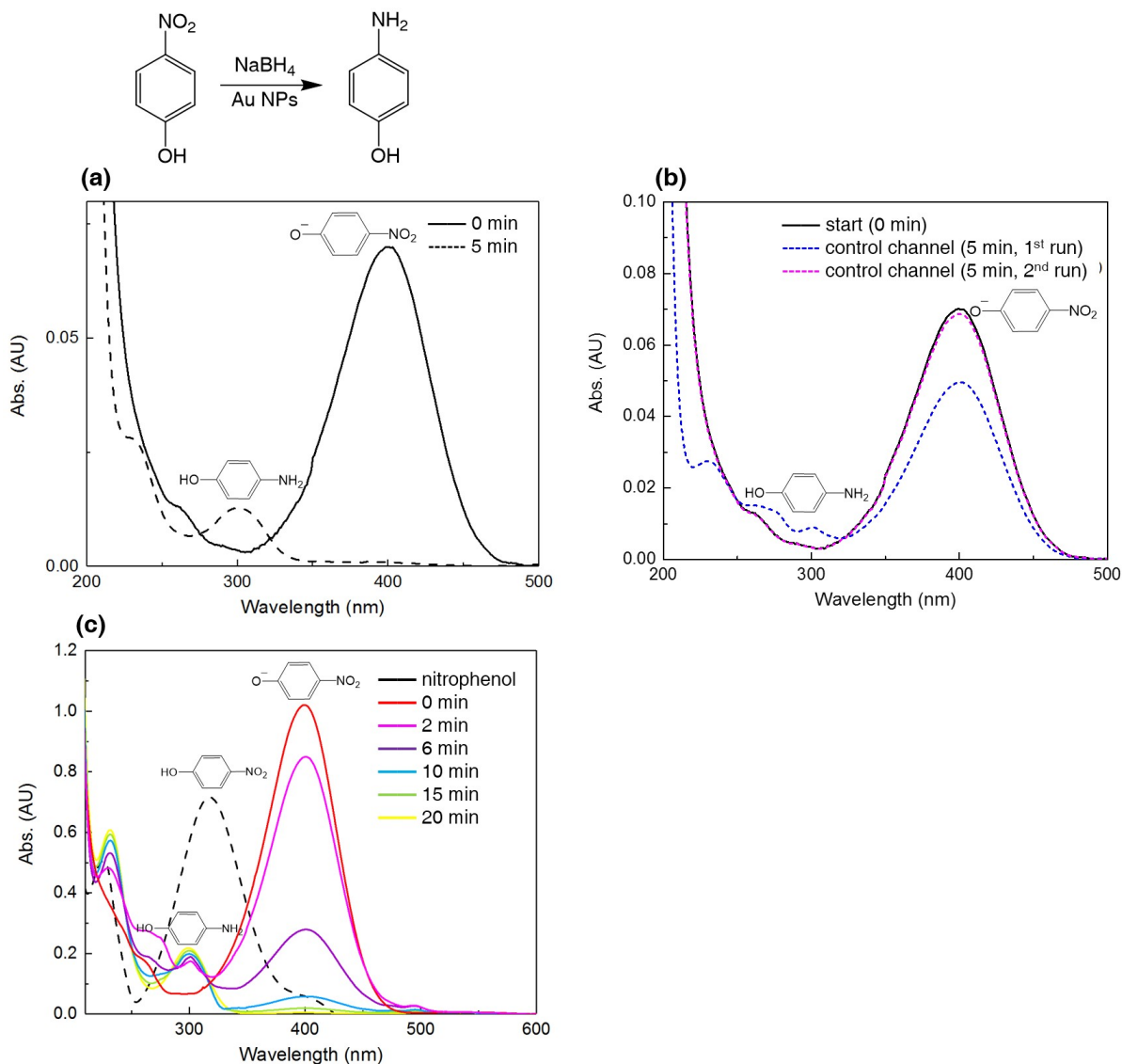


Figure 5.17: UV-vis spectra of (a) Au NP catalytic microreactor before and after reaction, yielding product in 99% after 5 min. (b) Au NP control channel: the first run gave 60% yield (the blue dashed line); however, the yield quickly decreased to 0% in subsequent reaction cycles (the pink dashed line). (c) The bench reaction with Au NPs led to a yield of 60% after 5 min and 99% till 20 min. The Au NPs used for the bench reaction were difficult to be separated and recycled for further use.

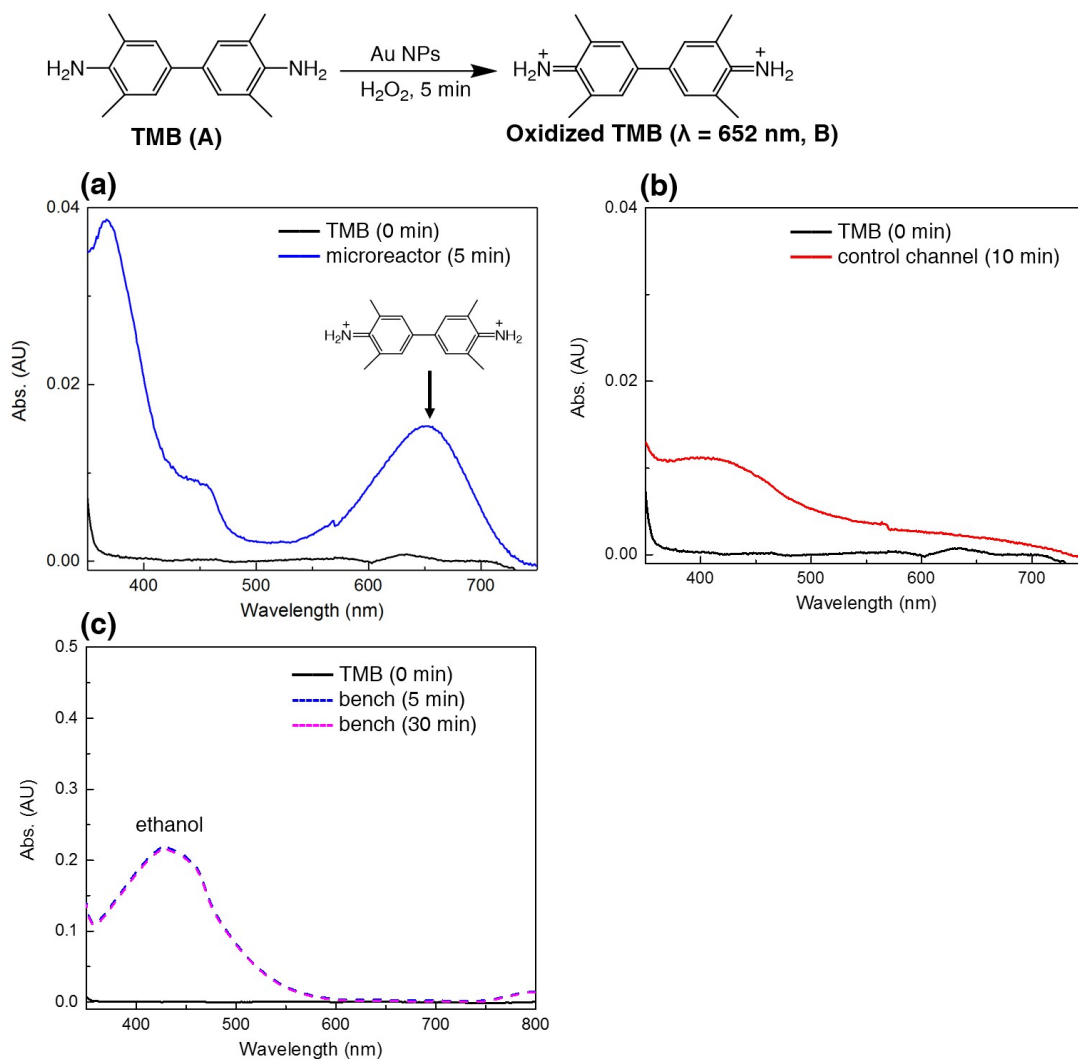


Figure 5.18: UV-vis spectra of (a) Au NP catalytic microreactor before and after reaction, yielding 99% after 5 min. (b) control channel did not produce any product after 10 min. (c) The bench reaction with Au NPs did not produce any product after 5 min and even 30 min. The wide peak around 400 nm came from the ethanol solvent.

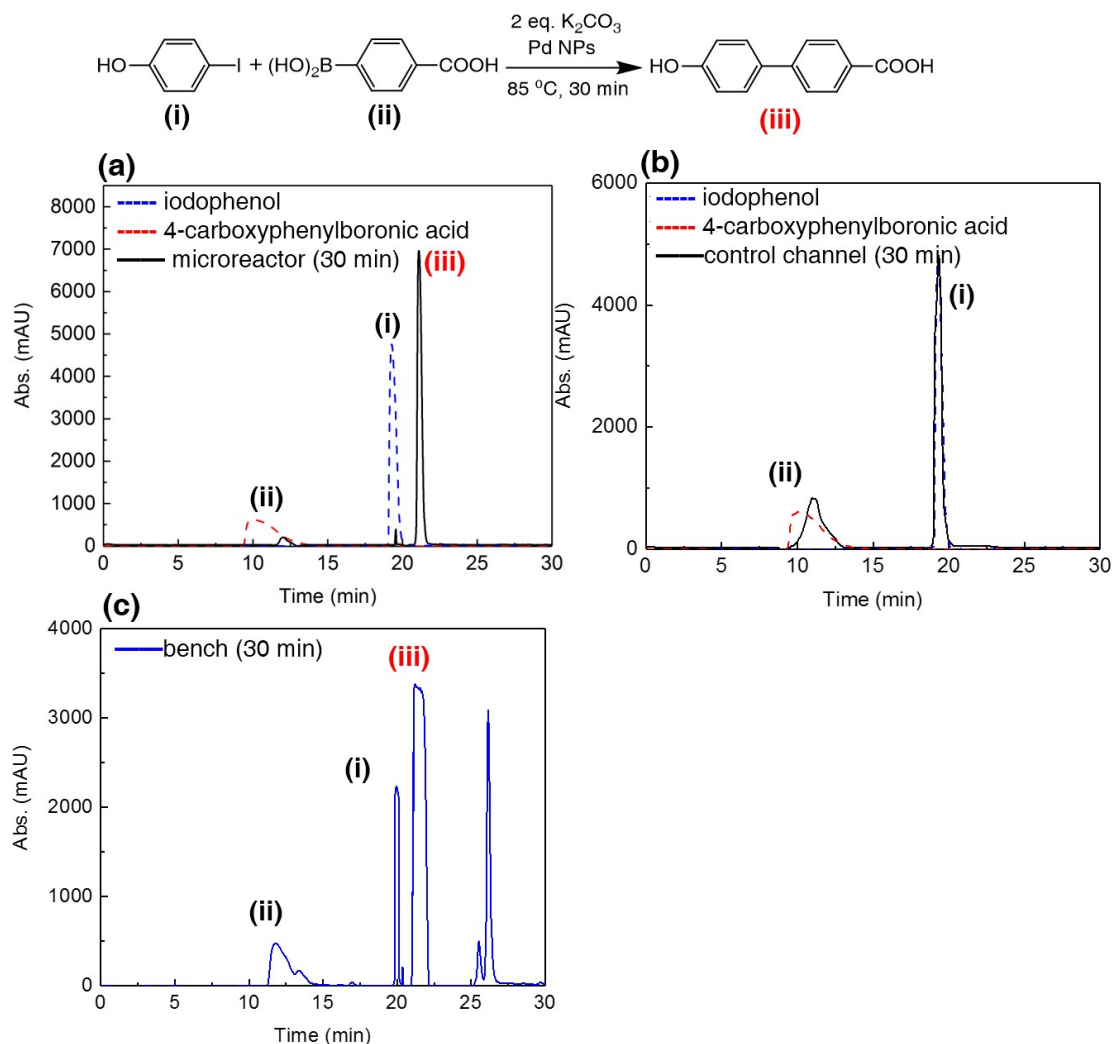


Figure 5.19: HPLC spectra of (a) reactants (dashed lines) and after reaction in Pd NP catalytic microreactor for 30 min, leading to 99% yield (solid line). (b) The Pd NP control channel did not yield any product after 30 min. Only the peaks of the reactants were observed. (c) The bench reaction with Pd NPs gave 40% yield after 30 min, however, with various byproducts (peaks between 25 to 30 min). The Pd NPs used in the bench reaction were difficult to be separated and recycled for further use.

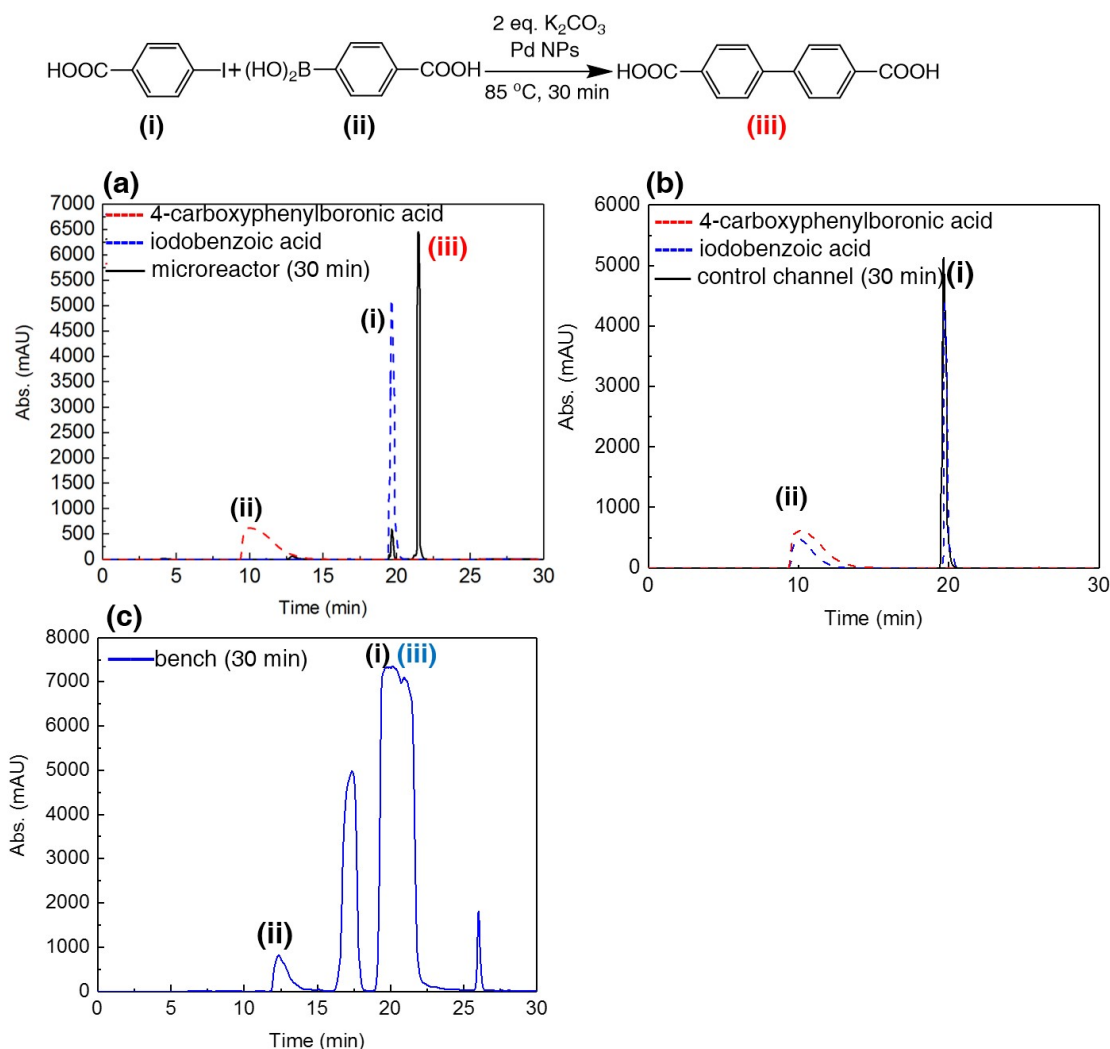


Figure 5.20: HPLC spectra of (a) reactants (dashed lines) and after reaction in Pd NP catalytic microreactor for 30 min, leading to 99% yield (solid line). (b) The Pd NP control channel did not produce any product after 30 min. Only the peaks of the reactants were observed. (c) The bench reaction with Pd NPs gave 50% yield after 30 min, however, with various byproducts (peaks at 17 and 27 min). The Pd NPs used in the bench reaction were difficult to be separated and recycled for further use.

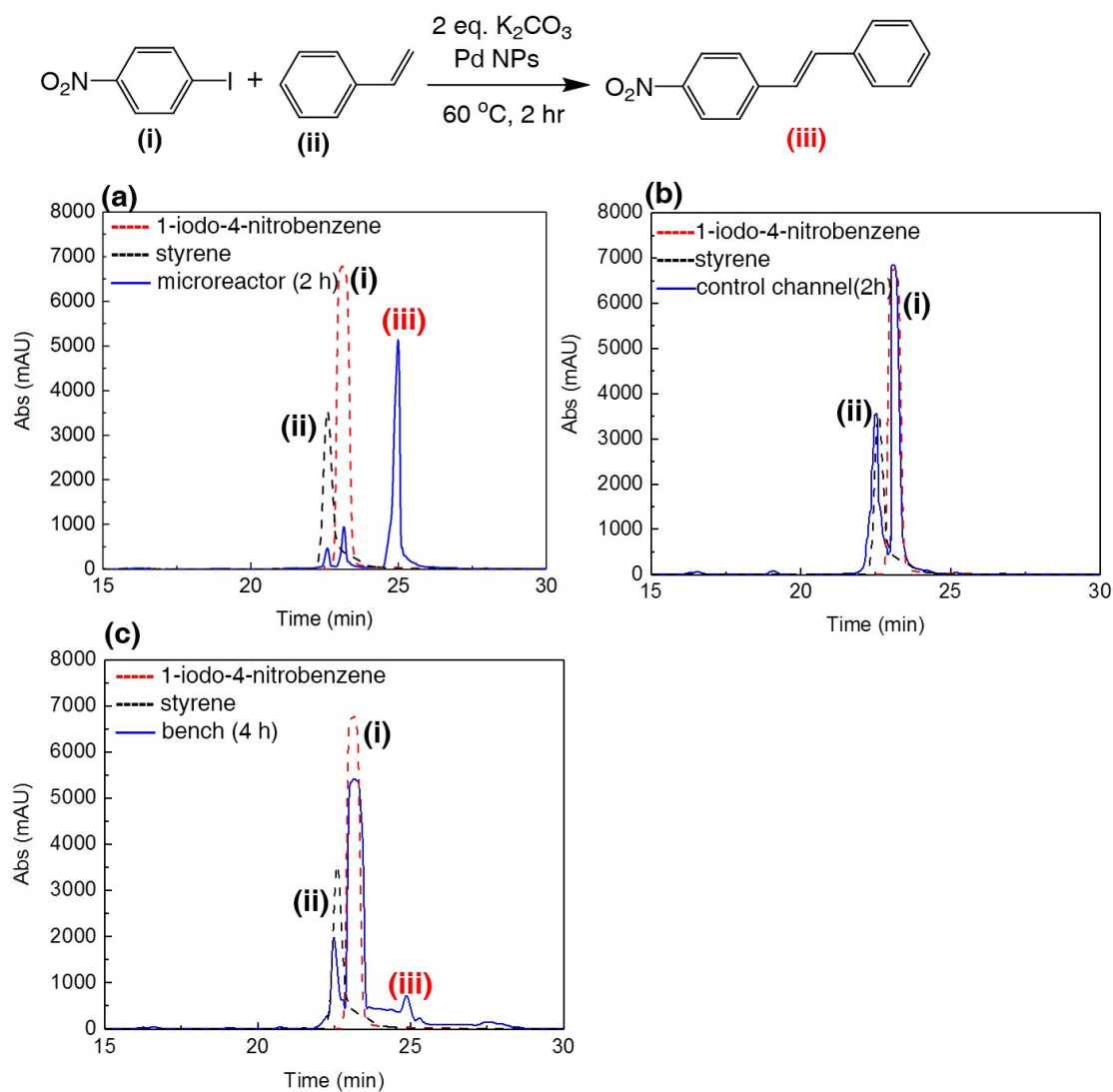


Figure 5.21: HPLC spectra of (a) reactants (dashed lines) and after reaction in Pd NP catalytic microreactor for 2 h, leading to 85% yield (solid line). (b) The Pd NP control channel did not produce any product after 2 h. The peaks remained the same with the reactants. (c) The bench reaction with Pd NPs gave 10% yield after 4 h.

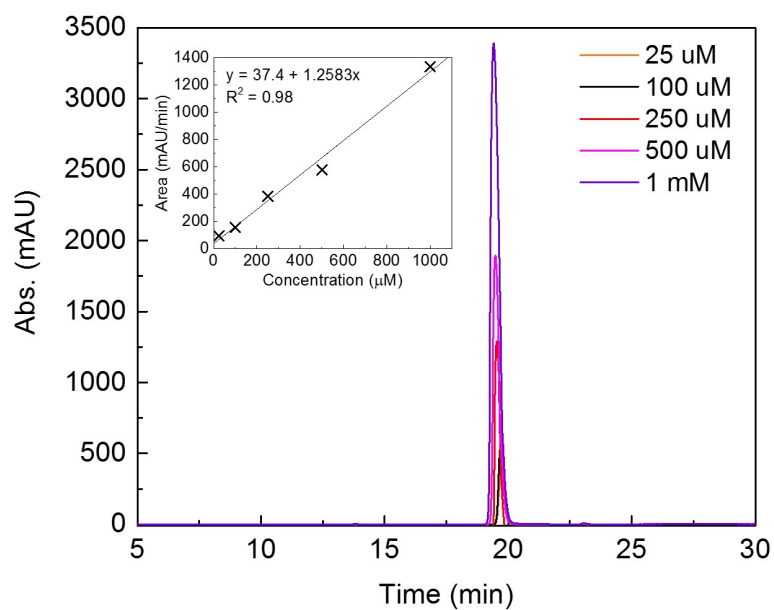


Figure 5.22: HPLC calibration line of 4-iodophenol.

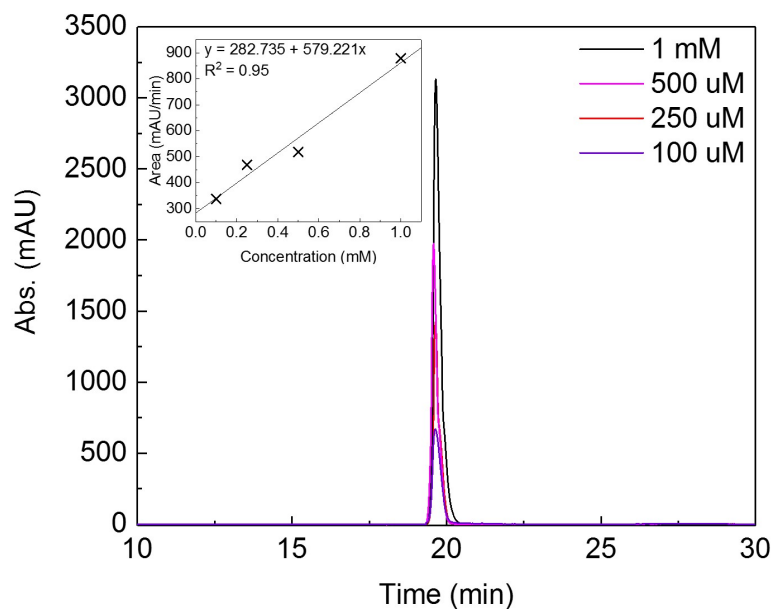


Figure 5.23: HPLC calibration line of 4-iodobenzoic acid.

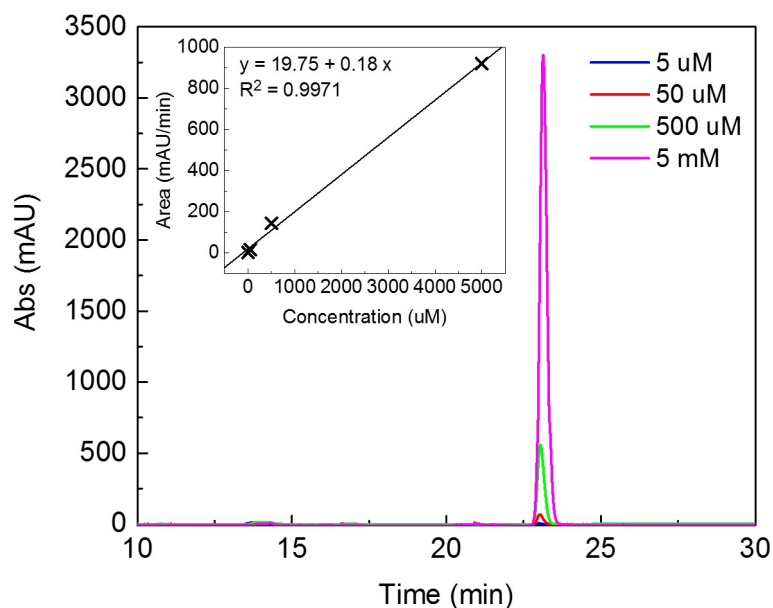


Figure 5.24: HPLC calibration line of 1-iodo-4-nitrobenzene.

5.4.9 Turnover frequency calculation

Turnover frequency (TOF) is the total number of moles transformed into the desired product by one mole of active site per second. The larger the TOF, the more active the catalyst.²⁸⁷

$$TOF = \frac{\text{Moles of product}}{\text{Moles of catalyst} \times \text{Reaction time}}$$

The TOF for Au NP catalytic microreactor catalysing the reduction of nitrobenzene was calculated as follows:

$$\text{Concentration of reactant} = \frac{1\text{mM} \times 0.5\text{mL}}{8.5\text{mL}} = 58.8 \mu\text{M}$$

$$\text{Moles of reactant} = 58.8\mu\text{M} \times 200\mu\text{L/h} \times 5\text{min} = 3.56 \times 10^{-10} \text{ mol}$$

$$\text{Moles of product} = (99\% \pm 1\%) \times \text{moles of reactant} = (3.52 \pm 0.04) \times 10^{-10} \text{ mol}$$

Number of catalyst in the microreactor with a diameter of 40 μm diameter and length of 3 cm = $\pi d \times 3 \text{ cm} \times \text{density of the immobilised NPs}$ = 4.14×10^9

$$\text{Mole of catalyst} = 4.14 \times 10^9 \div N_A = 6.89 \times 10^{-15}$$

So

$$\text{TOF} = \frac{(3.52 \pm 0.04) \times 10^{-10} \text{mol}}{6.89 \times 10^{-15} \times 300 \text{s}} = 171 \pm 2$$

TOF for other reactions were calculated by the same method.

Chapter 6

Conclusion and Outlook

Cucurbit[*n*]uril (CB[*n*])-engineered nanostructures have been applied in various areas, ranging from SERS sensing, catalysis, drug delivery to pollutant detection. This thesis mainly discussed highly stable and sensitive SERS substrates exploiting CB[*n*]-engineered nanostructures, including CB[8] catenanes on spiky magnetic gold nanoparticles (Au NPs) and CB[8] functionalised nanoraspberry particles. A few other applications of CB[*n*]-engineered nanostructures such as peptide separation and catalysis have also been discussed.

Chapter 2 introduced a novel and facile method for the preparation of surface-bound CB[8] catenanes on silica NPs, which is the first reported work about CB[*n*]-related catenane structures on NPs. CB[8] can simultaneously sequester two guest molecules in its cavity. Immobilised on the NP surface, it can act as a nanoscale molecular receptor for certain aromatic molecules such as perylene bis(diimide), naphthol and aromatic amino acids. The simple and efficient peptide separation approach using this surface-bound CB[8] catenane on magnetic NPs, whereby the target peptides could be selectively captured and separated from a peptide mixture and released by the single-electron reduction of MV^{2+} , was also demonstrated. Moreover, the CB[8] catenane NPs can be readily recycled after use on account of the incorporated magnetic cores. The introduction of CB[8] catenane structures onto NPs allows for single molecule recognition on a micromolar scale, providing potential opportunities in biological sensing and separation, as well as nanostructure tailoring. One of the promising research directions is utilising

these CB[8] catenane NPs for the preparation of core-shell NPs, by interacting with a polymer molecule (e.g. hydroxyethyl cellulose) possessing certain guest moieties (e.g. naphthol). Another potential application is the complexation of CB[8] catenane NPs with poly(N-isopropylacrylamide) or polystyrene micelles for the controlled releasing of drug molecules activated by temperature or pH.

Following the same concept, chapter 3 demonstrated an advanced molecular sensor exploiting a catenane-engineered nanostructure, by tethering CB[8] onto the surface of spiky $\gamma\text{-Fe}_2\text{O}_3\text{@Au}$ NPs. The deliberately designed spiky shapes contribute to a high SERS enhancement factor (on the order of 10^8) and enable target analytes to be detected with high sensitivities. The immobilisation of CB[8] on the molecular sensor allows for a greater variety of analyte molecules to be detected *via* SERS techniques. Moreover, this molecular sensor shows improved colloidal stability, acting as a free-standing sensor in water, aqueous buffer or biological system. The detection of a drug molecule, 1,5-pentamethylene-1H-tetrazole, was demonstrated. This stable and sensitive molecular sensor provides a useful platform for the detection of controlled substances and auxiliary diagnostics of various diseases. One of the potential applications is encapsulating the spiky catenane NPs into microfluidic droplets to detect the cell release, followed by the sorting of cells according to their released chemicals.

In chapter 4, a new type of CB[n]/Au SERS substrate was described. The emerging facile one-pot synthesis of $\gamma\text{-Fe}_2\text{O}_3\text{@Au}$ magnetic nanoraspberry particles was introduced. The obtained nanoraspberry particles were monodispersed, highly stable, and of good magnetic responsiveness on account of the incorporation of the magnetic cores. Moreover, the curvature surface contributes to a high SERS enhancement factor (on the order of 10^{10}), making it advantageous for a high-performance SERS substrate. By complexing a dense layer of CB[n] onto the surface of nanoraspberry NPs *via* its portal, they could act as a stable molecular sensor for a variety of electron-deficient and electron-rich molecules. The detection of ephedrine with high sensitivities was demonstrated. This stable and monodispersed nanoraspberry provides a powerful high-performance substrate for SERS detection of various biomolecules, chemicals and illegal drugs. One of the promising

applications is the nanoraspberry-on-mirror geometry, which might lead to extremely highly enhanced fields in the gaps between the nanoraspberry particles and Au surface.

Chapter 5 introduced CB[7]-based metallic NP catalytic microreactors, where metallic NPs were immobilised as a monolayer inside microchannels *via* supramolecular inclusion complexes (MV-silane@CB[7]). The high surface area to volume ratio of both the microchannel and metallic NPs contribute to remarkable activity of the catalytic microreactor. All catalytic reactions investigated with the Au NP and Pd NP microreactors exhibited high yield with high turnover frequencies (TOF up to 10^4 s^{-1}), significantly higher than most single-site heterogeneous NP catalysts^{269–276} and above the values of relevant industrial applications (TOF values in the range of 10^{-2} to 10^2 s^{-1}).²⁷⁹ This CB[7]-based attachment methodology provides a powerful multifunctional platform for high performance flow chemistry, holding great promise in a variety of catalytic reactions, as well as sensing applications. One promising research direction is the preparation of a CB[*n*]-based microchannel sensor for trace amount molecule detection. A similar attachment methodology was applied. The microchannel was first functionalised with (3-mercaptopropyl)trimethoxysilane, followed by the injection of Au NPs (100 nm) which were then immobilised by the thiol moieties onto the microchannel surface. CB[*n*] (*n*=7,8) solutions were injected, after which Au NPs (60 nm) solutions were injected again to create the plasmonic junctions. This approach takes advantage of the microchannel to create CB[*n*]-bridged metallic NP clusters under controlled conditions, thus avoiding the instability of the substrates system. A detection sensitivity down to 1 nM was achieved, however conditions still need to be modified to achieve even higher sensitivities.

In conclusion, the functionalising of CB[*n*] macromolecular structures onto nanoscale substrates establishes an exceptional interface between the molecular engineering and nanoscience. The host-guest complexation of CB[*n*] with guest molecules and the strong binding affinity of CB[*n*]'s portal with metallic interfaces provide controlling of the nano-constructs in the molecular level. CB[*n*]-engineered nano-construct has proven itself as a versatile tool in various applications such as separation science, molecular sensing and catalysis.

Bibliography

- [1] Alvarez Puebla, R. A.; Liz Marzán, L. M. *Chem. Soc. Rev.* **2012**, *41*, 43–51.
- [2] Sharma, B.; Frontiera, R. R.; Henry, A.-I.; Ringe, E.; Van Duyne, R. P. *Mater. Today Chem.* **2012**, *15*, 16–25.
- [3] Fan, M.; Andrade, G. F.; Brolo, A. G. *Anal. Chim. Acta* **2011**, *693*, 7–25.
- [4] Schlucker, S. *Angew. Chem. Int. Ed.* **2014**, *53*, 4756–4795.
- [5] Ding, S.-Y.; You, E.-M.; Tian, Z.-Q.; Moskovits, M. *Chem. Soc. Rev.* **2017**, *46*, 4042–4076.
- [6] Mosier-Boss, P. A. *Nanomater.* **2017**, *7*, 142.
- [7] Zhang, H.; Wang, C.; Sun, H.; Fu, G.; Chen, S.; Zhang, Y.; Chen, B.; Anema, J. R.; Yang, Z.; Li, J.; Tian, Z. *Nat. Commun.* **2017**, *8*, 15447.
- [8] Zong, C.; Xu, M.; Xu, L.; Wei, T.; Ma, X.; Zheng, X.; Hu, R.; Ren, B. *Chem. Rev.* **2018**, *118*, 4946–4980.
- [9] Yang, S.; Dai, X.; Stogin, B. B.; Wong, T. S. *Proc. Natl. Acad. Sci. U.S.A.* **2016**, *113*, 268–273.
- [10] Mulvihill, M. J.; Ling, X. Y.; Henzie, J.; Yang, P. J. *Am. Chem. Soc.* **2009**, *132*, 268–274.
- [11] Yoon, J. H.; Lim, J.; Yoon, S. *ACS Nano* **2012**, *6*, 7199–7208.
- [12] Kelley, S. O.; Mirkin, C. A.; Walt, D. R.; Ismagilov, R. F.; Toner, M.; Sargent, E. H. *Nat. Nanotechnol.* **2014**, *9*, 969.

-
- [13] Reiner, E. J.; Clement, R. E.; Okey, A. B.; Marvin, C. H. *Anal. Bioanal. Chem.* **2006**, 386, 791–806.
- [14] Stiles, P. L.; Dieringer, J. A.; Shah, N. C.; Van Duyne, R. P. *Annu. Rev. Anal. Chem.* **2008**, 1, 601–626.
- [15] Nie, S.; Emory, S. R. *Science* **1997**, 275, 1102–1106.
- [16] Liao, P.; Bergman, J.; Chemla, D.; Wokaun, A.; Melngailis, J.; Hawryluk, A.; Economou, N. *Chem. Phys. Lett.* **1981**, 82, 355–359.
- [17] Tian, Z.-Q.; Ren, B.; Li, J.-F.; Yang, Z.-L. *Chem. Commun.* **2007**, 3514–3534.
- [18] Blatchford, C.; Campbell, J.; Creighton, J. *Surf. Sci.* **1981**, 108, 411–420.
- [19] Freeman, R. G.; Grabar, K. C.; Allison, K. J.; Bright, R. M.; Davis, J. A.; Guthrie, A. P.; Hommer, M. B.; Jackson, M. A.; Smith, P. C.; Walter, D. G. *Science* **1995**, 267, 1629–1632.
- [20] Haynes, C. L.; Van Duyne, R. P. *J. Phys. Chem. B* **2003**, 107, 7426–7433.
- [21] Wang, H.; Brandl, D. W.; Nordlander, P.; Halas, N. J. *Acc. Chem. Res* **2007**, 40, 53–62.
- [22] Li, J. F.; Huang, Y. F.; Ding, Y.; Yang, Z. L.; Li, S. B.; Zhou, X. S.; Fan, F. R.; Zhang, W.; Zhou, Z. Y.; Ren, B.; Wang, Z. L.; Qun, T. Z. *Nature* **2010**, 464, 392.
- [23] Fleischmann, M.; Hendra, P. J.; McQuillan, A. J. *Chem. Phys. Lett.* **1974**, 26, 163–166.
- [24] Jeanmaire, D. L.; Van Duyne, R. P. *J. Electroanal. Chem.* **1977**, 84, 1–20.
- [25] Nikoobakht, B.; El-Sayed, M. A. *Chem. Mater.* **2003**, 15, 1957–1962.
- [26] Xia, Y.; Xiong, Y.; Lim, B.; Skrabalak, S. E. *Angew. Chem. Int. Ed.* **2009**, 48, 60–103.
- [27] Yang, Y.; Liu, J.; Fu, Z.-W.; Qin, D. J. *Am. Chem. Soc.* **2014**, 136, 8153–8156.
- [28] Chikkaraddy, R.; de Nijs, B.; Benz, F.; Barrow, S. J.; Scherman, O. A.; Rosta, E.; Demetriadou, A.; Fox, P.; Hess, O.; Baumberg, J. J. *Nature* **2016**, 535, 127.

-
- [29] Chikkaraddy, R.; Turek, V.; Kongsuwan, N.; Benz, F.; Carnegie, C.; Van De Goor, T.; de Nijs, B.; Demetriadou, A.; Hess, O.; Keyser, U. F.; Baumberg, J. J. *Nano Lett.* **2017**,
- [30] Andreou, C.; Hoonejani, M. R.; Barmi, M. R.; Moskovits, M.; Meinhart, C. D. *ACS Nano* **2013**, *7*, 7157–7164.
- [31] Yang, S.; Dai, X.; Stogin, B. B.; Wong, T.-S. *Proc. Natl. Acad. Sci. USA* **2016**, *113*, 268–273.
- [32] Hatab, N. A.; Eres, G.; Hatzinger, P. B.; Gu, B. J. *Raman Spec.* **2010**, *41*, 1131–1136.
- [33] Ma, Z.; Tian, L.; Qiang, H. J. *Nanosci. Nanotechnol.* **2009**, *9*, 6716–6720.
- [34] Toderas, F.; Baia, M.; Baia, L.; Astilean, S. *Nanotechnol.* **2007**, *18*, 255702.
- [35] Lee, S. J.; Baik, J. M.; Moskovits, M. *Nano Lett.* **2008**, *8*, 3244–3247.
- [36] Zhai, J.; Wang, Y.; Zhai, Y.; Dong, S. *Nanotechnol.* **2009**, *20*, 055609.
- [37] Oh, M. K.; Yun, S.; Kim, S. K.; Park, S. *Anal. Chim. Acta* **2009**, *649*, 111–116.
- [38] Li, X.; Xu, W.; Zhang, J.; Jia, H.; Yang, B.; Zhao, B.; Li, B.; Ozaki, Y. *Langmuir* **2004**, *20*, 1298–1304.
- [39] Yue, W.; Wang, Z.; Yang, Y.; Chen, L.; Syed, A.; Wong, K.; Wang, X. *J. Micromech. Microeng.* **2012**, *22*, 125007.
- [40] Abu Hatab, N. A.; Oran, J. M.; Sepaniak, M. J. *ACS Nano* **2008**, *2*, 377–385.
- [41] Wu, D.-Y.; Li, J.-F.; Ren, B.; Tian, Z.-Q. *Chem. Soc. Rev.* **2008**, *37*, 1025–1041.
- [42] Zhang, C.; Yi, P.; Peng, L.; Lai, X.; Chen, J.; Huang, M.; Ni, J. *Sci. Rep.* **2017**, *7*, 39814.
- [43] Mahajan, S.; Abdelsalam, M.; Suguwara, Y.; Cintra, S.; Russell, A.; Baumberg, J.; Bartlett, P. *Phys. Chem. Chem. Phys.* **2007**, *9*, 104–109.
- [44] Wu, D.-Y.; Ren, B.; Jiang, Y.-X.; Xu, X.; Tian, Z.-Q. *J. Phys. Chem. A* **2002**, *106*, 9042–9052.

- [45] Bantz, K. C.; Meyer, A. F.; Wittenberg, N. J.; Im, H.; Kurtulus, O.; Lee, S. H.; Lindquist, N. C.; Oh, S. H.; Haynes, C. L. *Phys. Chem. Chem. Phys.* **2011**, *13*, 11551–11567.
- [46] Tao, C.; An, Q.; Zhu, W.; Yang, H.; Li, W.; Lin, C.; Xu, D.; Li, G. *Chem. Commun.* **2011**, *47*, 9867–9869.
- [47] Alvarez Puebla, R. A.; Arceo, E.; Goulet, P. J.; Garrido, J. J.; Aroca, R. F. *J. Phys. Chem. B* **2005**, *109*, 3787–3792.
- [48] Álvarez-Puebla, R. A.; Contreras-Cáceres, R.; Pastoriza-Santos, I.; Pérez-Juste, J.; Liz-Marzán, L. M. *Angew. Chem. Int. Ed.* **2009**, *121*, 144–149.
- [49] Contreras-Cáceres, R.; Abalde-Cela, S.; Guardia-Girós, P.; Fernández-Barbero, A.; Pérez-Juste, J.; Alvarez-Puebla, R. A.; Liz-Marzán, L. M. *Langmuir* **2011**, *27*, 4520–4525.
- [50] He, L.; Rodda, T.; Haynes, C. L.; Deschaines, T.; Strother, T.; Diez-Gonzalez, F.; Labuza, T. P. *Anal. Chem.* **2011**, *83*, 1510–1513.
- [51] Mahajan, S.; Lee, T. C.; Biedermann, F.; Hugall, J. T.; Baumberg, J. J.; Scherman, O. A. *Phys. Chem. Chem. Phys.* **2010**, *12*, 10429–10433.
- [52] Taylor, R. W.; Lee, T. C.; Scherman, O. A.; Esteban, R.; Aizpurua, J.; Huang, F. M.; Baumberg, J. J.; Mahajan, S. *ACS Nano* **2011**, *5*, 3878–3887.
- [53] Kasera, S.; Biedermann, F.; Baumberg, J. J.; Scherman, O. A.; Mahajan, S. *Nano Lett.* **2012**, *12*, 5924–5928.
- [54] Jones, S. T.; Taylor, R. W.; Esteban, R.; Abo Hamed, E. K.; Bomans, P. H.; Sommerdijk, N. A.; Aizpurua, J.; Baumberg, J. J.; Scherman, O. A. *Small* **2014**, *10*, 4298–4303.
- [55] De Nijs, B.; Kamp, M.; Szab, I.; Barrow, S. J.; Benz, F.; Wu, G.; Carnegie, C.; Chikkaraddy, R.; Wang, W.; Deacon, W. M. B. *Faraday Discuss* **2017**, *205*, 505–515.
- [56] Kim, N. H.; Hwang, W.; Baek, K.; Rohman, M. R.; Kim, J.; Kim, H. W.; Mun, J.; Lee, S. Y.; Yun, G.; Murray, J. J. *Am. Chem. Soc.* **2018**, *140*, 4705–4711.

- [57] Yonzon, C. R.; Haynes, C. L.; Zhang, X.; Walsh, J. T.; Van Duyne, R. P. *Anal. Chem.* **2004**, *76*, 78–85.
- [58] Camden, J. P.; Dieringer, J. A.; Zhao, J.; Van Duyne, R. P. *Acc. Chem. Res.* **2008**, *41*, 1653–1661.
- [59] Jones, C. L.; Bantz, K. C.; Haynes, C. L. *Anal. Bioanal. Chem.* **2009**, *394*, 303–311.
- [60] Bantz, K. C.; Haynes, C. L. *Vib. Spectrosc.* **2009**, *50*, 29–35.
- [61] Yin, P.-G.; Chen, Y.; Jiang, L.; You, T.-T.; Lu, X.-Y.; Guo, L.; Yang, S. *Macromol. Rapid Commun.* **2011**, *32*, 1000–1006.
- [62] Qian, X.; Li, J.; Nie, S. *J. Am. Chem. Soc.* **2009**, *131*, 7540–7541.
- [63] Gupta, M. K.; Chang, S.; Singamaneni, S.; Drummy, L. F.; Gunawidjaja, R.; Naik, R. R.; Tsukruk, V. V. *Small* **2011**, *7*, 1192–1198.
- [64] Kozlovskaya, V.; Kharlampieva, E.; Khanal, B. P.; Manna, P.; Zubarev, E. R.; Tsukruk, V. V. *Chem. Mater.* **2008**, *20*, 7474–7485.
- [65] Wu, W.; Mitra, N.; Yan, E. C.; Zhou, S. *ACS Nano* **2010**, *4*, 4831–4839.
- [66] Sanles-Sobrido, M.; Rodríguez-Lorenzo, L.; Lorenzo-Abalde, S.; González-Fernández, Á.; Correa-Duarte, M. A.; Alvarez-Puebla, R. A.; Liz-Marzán, L. M. *Nanoscale* **2009**, *1*, 153–158.
- [67] Culha, M.; Stokes, D.; Allain, L. R.; Vo-Dinh, T. *Anal. Chem.* **2003**, *75*, 6196–6201.
- [68] Kang, T.; Yoo, S. M.; Yoon, I.; Lee, S. Y.; Kim, B. *Nano Lett.* **2010**, *10*, 1189–1193.
- [69] Vo-Dinh, T.; Houck, K.; Stokes, D. *Anal. Chem.* **1994**, *66*, 3379–3383.
- [70] Isola, N. R.; Stokes, D. L.; Vo-Dinh, T. *Anal. Chem.* **1998**, *70*, 1352–1356.
- [71] Abalde-Cela, S.; Hermida-Ramón, J. M.; Contreras-Carballada, P.; De Cola, L.; Guerrero-Martínez, A.; Alvarez-Puebla, R. A.; Liz-Marzán, L. M. *ChemPhysChem* **2011**, *12*, 1529–1535.

- [72] Xu, J. Y.; Wang, J.; Kong, L. T.; Zheng, G. C.; Guo, Z.; Liu, J. H. *J. Raman Spectrosc.* **2011**, *42*, 1728–1735.
- [73] Xie, Y.; Wang, X.; Han, X.; Xue, X.; Ji, W.; Qi, Z.; Liu, J.; Zhao, B.; Ozaki, Y. *Analyst* **2010**, *135*, 1389–1394.
- [74] Strickland, A. D.; Batt, C. A. *Anal. Chem.* **2009**, *81*, 2895–2903.
- [75] Del Puerto, E.; Sánchez-Cortés, S.; García-Ramos, J. V.; Domingo, C. *Chem. Commun.* **2011**, *47*, 1854–1856.
- [76] Lagona, J.; Mukhopadhyay, P.; Chakrabarti, S.; Isaacs, L. *Angew. Chem. Int. Ed.* **2005**, *44*, 4844–4870.
- [77] Kim, J.; Jung, I.-S.; Kim, S.-Y.; Lee, E.; Kang, J.-K.; Sakamoto, S.; Yamaguchi, K.; Kim, K. J. *Am. Chem. Soc.* **2000**, *122*, 540–541.
- [78] Ren, X.; Wu, Y.; Clarke, D. E.; Liu, J.; Wu, G.; Scherman, O. A. *Chem. Asian J.* **2016**, *11*, 2382–2386.
- [79] Kyba, E. P.; Helgeson, R. C.; Madan, K.; Gokel, G. W.; Tarnowski, T. L.; Moore, S. S.; Cram, D. J. *J. Am. Chem. Soc.* **1977**, *99*, 2564–2571.
- [80] Gao, H.; Miles, M. S.; Meyer, B. M.; Wong, R. L.; Overton, E. B. *J. Environ. Monit.* **2012**, *14*, 2164–2169.
- [81] König, B. *J. Prakt. Chem-Chem. ZTG.* **1995**, *337*, 339–346.
- [82] Hu, J.; Cheng, Y.; Wu, Q.; Zhao, L.; Xu, T. *J. Phy. Chem. B* **2009**, *113*, 10650–10659.
- [83] Gutsche, C.; Stoddart, J. *RSC. Cam.* **1989**, *1*.
- [84] Samanta, A.; Tesch, M.; Keller, U.; Klingauf, J.; Studer, A.; Ravoo, B. J. *J. Am. Chem. Soc.* **2015**, *137*, 1967–1971.
- [85] Pedersen, C. J. *Org. Synth.* **1972**, *66*–66.
- [86] Gokel, G. W.; Leevy, W. M.; Weber, M. E. *Chem. Rev.* **2004**, *104*, 2723–2750.

- [87] Day, A.; Arnold, A. P.; Blanch, R. J.; Snushall, B. J. *Org. Chem.* **2001**, *66*, 8094–8100.
- [88] Day, A. I.; Blanch, R. J.; Arnold, A. P.; Lorenzo, S.; Lewis, G. R.; Dance, I. *Angew. Chem. Int. Ed.* **2002**, *41*, 275–277.
- [89] Liu, S.; Ruspic, C.; Mukhopadhyay, P.; Chakrabarti, S.; Zavalij, P. Y.; Isaacs, L. *J. Am. Chem. Soc.* **2005**, *127*, 15959–15967.
- [90] Thatiparti, T. R.; Shoffstall, A. J.; von Recum, H. A. *Biomaterials* **2010**, *31*, 2335–2347.
- [91] Cadogan, A.; Gao, Z.; Lewenstam, A.; Ivaska, A.; Diamond, D. *Anal. Chem.* **1992**, *64*, 2496–2501.
- [92] Das, D.; Scherman, O. A. *Isr. J. Chem.* **2011**, *51*, 537–550.
- [93] Lee, J. W.; Samal, S.; Selvapalam, N.; Kim, H.-J.; Kim, K. *Accts. Chem. Res.* **2003**, *36*, 621–630.
- [94] Freeman, W.; Mock, W.; Shih, N. *J. Am. Chem. Soc.* **1981**, *103*, 7367–7368.
- [95] Behrend, R.; Meyer, E.; Rusche, F. *Justus Liebigs Ann. Chem.* **1905**, *339*, 1–37.
- [96] Cheng, X.-J.; Liang, L.-L.; Chen, K.; Ji, N.-N.; Xiao, X.; Zhang, J.-X.; Zhang, Y.-Q.; Xue, S.-F.; Zhu, Q.-J.; Ni, X.-L. *Angew. Chem. Int. Ed.* **2013**, *125*, 7393–7396.
- [97] Huang, W.-H.; Zavalij, P. Y.; Isaacs, L. *J. Am. Chem. Soc.* **2008**, *130*, 8446–8454.
- [98] Jiao, D.; Zhao, N.; Scherman, O. A. *Chem. Commun.* **2010**, *46*, 2007–2009.
- [99] Masson, E.; Ling, X.; Joseph, R.; Kyeremeh-Mensah, L.; Lu, X. *RSC Adv.* **2012**, *2*, 1213–1247.
- [100] Sindelar, V.; Moon, K.; Kaifer, A. E. *Org. Lett.* **2004**, *6*, 2665–2668.
- [101] Monhaphol, T. K.; Andersson, S.; Sun, L. *Chem. Eur. J.* **2011**, *17*, 11604–11612.
- [102] Deroo, S.; Rauwald, U.; Robinson, C. V.; Scherman, O. A. *Chem. Commun.* **2009**, 644–646.

- [103] Appel, E. A.; Biedermann, F.; Rauwald, U.; Jones, S. T.; Zayed, J. M.; Scherman, O. A. *J. Am. Chem. Soc.* **2010**, *132*, 14251–14260.
- [104] Assaf, K. I.; Nau, W. M. *Chem. Soc. Rev.* **2015**, *44*, 394–418.
- [105] Lü, J.; Lin, J.-X.; Cao, M.-N.; Cao, R. *Coord. Chem. Rev.* **2013**, *257*, 1334–1356.
- [106] Biedermann, F.; Vendruscolo, M.; Scherman, O. A.; De Simone, A.; Nau, W. M. *J. Am. Chem. Soc.* **2013**, *135*, 14879–14888.
- [107] Biedermann, F.; Uzunova, V. D.; Scherman, O. A.; Nau, W. M.; De Simone, A. *J. Am. Chem. Soc.* **2012**, *134*, 15318–15323.
- [108] Zhao, J.; Kim, H.-J.; Oh, J.; Kim, S.-Y.; Lee, J. W.; Sakamoto, S.; Yamaguchi, K.; Kim, K. *Angew. Chem. Int. Ed.* **2001**, *113*, 4363–4365.
- [109] Kim, H.; Heo, J.; Jeon, W.; Lee, E.; Kim, J.; Sakamoto, S.; Yamaguchi, K.; Kim, K. *Angew. Chem. Int. Ed.* **2001**, *40*, 1526–1529.
- [110] Bush, M. E.; Bouley, N. D.; Urbach, A. R. *J. Am. Chem. Soc.* **2005**, *127*, 14511–14517.
- [111] Lan, Y.; Loh, X. J.; Geng, J.; Walsh, Z.; Scherman, O. A. *Chem. Commun.* **2012**, *48*, 8757–8759.
- [112] An, Q.; Li, G.; Tao, C.; Li, Y.; Wu, Y.; Zhang, W. *Chem. Commun.* **2008**, 1989–1991.
- [113] Barrow, S. J.; Kasera, S.; Rowland, M. J.; del Barrio, J.; Scherman, O. A. *Chem. Rev.* **2015**, *115*, 12320–12406.
- [114] Lee, T. C.; Scherman, O. A. *Chem. Commun.* **2010**, *46*, 2438–2440.
- [115] Coulston, R. J.; Jones, S. T.; Lee, T.-C.; Appel, E. A.; Scherman, O. A. *Chem. Commun.* **2011**, *47*, 164–166.
- [116] Lan, Y.; Wu, Y.; Karas, A.; Scherman, O. A. *Angew. Chem. Int. Ed.* **2014**, *53*, 2166–2169.
- [117] Premkumar, T.; Geckeler, K. *Small* **2006**, *2*, 616–620.

- [118] Premkumar, T.; Lee, Y.; Geckeler, K. E. *Chem. -Eur. J.* **2010**, *16*, 11563–11566.
- [119] Lee, T.-C.; Scherman, O. A. *Chem. Eur. J.* **2012**, *18*, 1628–1633.
- [120] Lanterna, A.; Pino, E.; Doménech-Carbó, A.; González-Béjar, M.; Pérez-Prieto, J. *Nanoscale* **2014**, *6*, 9550–9553.
- [121] Lu, X.; Masson, E. *Langmuir* **2011**, *27*, 3051–3058.
- [122] Husken, N.; Taylor, R. W.; Zigah, D.; Taveau, J. C.; Lambert, O.; Scherman, O. A.; Baumberg, J. J.; Kuhn, A. *Nano Lett.* **2013**, *13*, 6016–6022.
- [123] Herrmann, L. O.; Valev, V. K.; Tserkezis, C.; Barnard, J. S.; Kasera, S.; Scherman, O. A.; Aizpurua, J.; Baumberg, J. J. *Nat. Commun.* **2014**, *5*, 4568.
- [124] Aguirregabiria, G.; Aizpurua, J.; Esteban, R. *Opt. Express* **2017**, *25*, 13760–13772.
- [125] Lee, D.-W.; Park, K. M.; Gong, B.; Shetty, D.; Khedkar, J. K.; Baek, K.; Kim, J.; Ryu, S. H.; Kim, K. *Chem. Commun.* **2015**, *51*, 3098–3101.
- [126] Neiryneck, P.; Brinkmann, J.; An, Q.; van der Schaft, D. W.; Milroy, L.-G.; Jonkheijm, P.; Brunsveld, L. *Chem. Commun.* **2013**, *49*, 3679–3681.
- [127] Premkumar, T.; Geckeler, K. *Small* **2006**, *2*, 616–620.
- [128] Benyettou, F.; Milosevic, I.; Lalatonne, Y.; Warmont, F.; Assah, R.; Olsen, J.-C.; Jouaid, M.; Motte, L.; Platas-Iglesias, C.; Trabolsi, A. *J. Mater. Chem. B* **2013**, *1*, 5076–5082.
- [129] Benyettou, F.; Nchimi-Nono, K.; Jouiad, M.; Lalatonne, Y.; Milosevic, I.; Motte, L.; Olsen, J.-C.; Saleh, N.; Trabolsi, A. *Chem. -Eur. J.* **2015**, *21*, 4607–4613.
- [130] Benyettou, F.; Motte, L.; Traboulsi, H.; Mazher, J.; Pasricha, R.; Olsen, J.-C.; Trabolsi, A.; Guenin, E. *Chem. Eur. J.* **2018**, *24*, 2349–2353.
- [131] Kim, C.; Agasti, S. S.; Zhu, Z.; Isaacs, L.; Rotello, V. M. *Nat. Chem.* **2010**, *2*, 962.
- [132] Jones, S. T.; Zayed, J. M.; Scherman, O. A. *Nanoscale* **2013**, *5*, 5299–5302.

-
- [133] Hu, C.; Lan, Y.; Tian, F.; West, K. R.; Scherman, O. A. *Langmuir* **2014**, *30*, 10926–10932.
- [134] Hu, C.; Tian, F.; Zheng, Y.; Tan, C. S. Y.; West, K. R.; Scherman, O. A. *Chem. Sci.* **2015**, *6*, 5303–5310.
- [135] Hu, C.; Lan, Y.; West, K. R.; Scherman, O. A. *Adv. Mater.* **2015**, *27*, 7957–7962.
- [136] Esteban, R.; Taylor, R. W.; Baumberg, J. J.; Aizpurua, J. *Langmuir* **2012**, *28*, 8881–8890.
- [137] Herrmann, L. O.; Valev, V. K.; Aizpurua, J.; Baumberg, J. J. *Opt. Express* **2013**, *21*, 32377–32385.
- [138] Taylor, R. W.; Coulston, R. J.; Biedermann, F.; Mahajan, S.; Baumberg, J. J.; Scherman, O. A. *Nano Lett.* **2013**, *13*, 5985–5990.
- [139] Song, J.; Zhou, J.; Duan, H. *J. Am. Chem. Soc.* **2012**, *134*, 13458–13469.
- [140] Kasera, S.; Herrmann, L. O.; Del Barrio, J.; Baumberg, J. J.; Scherman, O. A. *Sci. Rep.* **2014**, *4*, 6785.
- [141] Sigle, D. O.; Kasera, S.; Herrmann, L. O.; Palma, A.; de Nijs, B.; Benz, F.; Mahajan, S.; Baumberg, J. J.; Scherman, O. A. *J. Phys. Chem. Lett.* **2016**, *7*, 704–710.
- [142] Aravind, P.; Rendell, R.; Metiu, H. *Chem. Phys Lett.* **1982**, *85*, 396–403.
- [143] Mock, J. J.; Hill, R. T.; Degiron, A.; Zauscher, S.; Chilkoti, A.; Smith, D. R. *Nano Lett.* **2008**, *8*, 2245–2252.
- [144] Ciraci, C.; Hill, R.; Mock, J.; Urzhumov, Y.; Fernández-Domínguez, A.; Maier, S.; Pendry, J.; Chilkoti, A.; Smith, D. *Science* **2012**, *337*, 1072–1074.
- [145] Nijs, B.; Benz, F.; Barrow, S. J.; Sigle, D. O.; Chikkaraddy, R.; Palma, A.; Carnegie, C.; Kamp, M.; Sundararaman, R.; Narang, P.; Oren, S. A.; Jeremy, B. J. *Nat. Commun.* **2017**, *8*, 994.

- [146] Gil-Ramírez, G.; Leigh, D. A.; Stephens, A. J. *Angew. Chem. Int. Ed.* **2015**, *54*, 6110–6150.
- [147] Coronado, E.; Gaviña, P.; Tatay, S. *Chem. Soc. Rev.* **2009**, *38*, 1674–1689.
- [148] Sauvage, J.-P. *Acc. Chem. Res.* **1998**, *31*, 611–619.
- [149] Collin, J.-P.; Dietrich-Buchecker, C.; Gaviña, P.; Jimenez-Molero, M. C.; Sauvage, J.-P. *Acc. Chem. Res.* **2001**, *34*, 477–487.
- [150] Collier, C. P.; Mattersteig, G.; Wong, E. W.; Luo, Y.; Beverly, K.; Sampaio, J.; Raymo, F. M.; Stoddart, J. F.; Heath, J. R. *Science* **2000**, *289*, 1172–1175.
- [151] Klajn, R.; Fang, L.; Coskun, A.; Olson, M. A.; Wesson, P. J.; Stoddart, J. F.; Grzybowski, B. A. *J. Am. Chem. Soc.* **2009**, *131*, 4233–4235.
- [152] Deng, W.-Q.; Flood, A. H.; Stoddart, J. F.; Goddard, W. A. *J. Am. Chem. Soc.* **2005**, *127*, 15994–15995.
- [153] Nakatani, Y.; Furusho, Y.; Yashima, E. *Angew. Chem. Int. Ed.* **2010**, *49*, 5463–5467.
- [154] Caballero, A.; Zapata, F.; White, N. G.; Costa, P. J.; Félix, V.; Beer, P. D. *Angew. Chem.* **2012**, *124*, 1912–1916.
- [155] Bonnet, S.; Collin, J.-P.; Koizumi, M.; Mobian, P.; Sauvage, J.-P. *Adv. Mater.* **2006**, *18*, 1239–1250.
- [156] Ashton, P. R.; Brown, C. L.; Chrystal, E. J.; Goodnow, T. T.; Kaifer, A. E.; Parry, K. P.; Philp, D.; Slawin, A. M.; Spencer, N.; Stoddart, J. F.; Williams, D. J. *Chem. Commun.* **1991**, 634–639.
- [157] Mohr, B.; Sauvage, J.-P.; Grubbs, R. H.; Weck, M. *Angew. Chem.* **1997**, *109*, 1365–1367.
- [158] Armspach, D.; Ashton, P. R.; Moore, C. P.; Spencer, N.; Stoddart, J. F.; Wear, T. J.; Williams, D. J. *Angew. Chem. Int. Ed.* **1993**, *32*, 854–858.
- [159] Li, J.; Nowak, P.; Fanlo-Virgós, H.; Otto, S. *Chem. Sci.* **2014**, *5*, 4968–4974.

- [160] Zhao, Y.-L.; Chen, Y.; Wang, M.; Liu, Y. *Org. Lett.* **2006**, *8*, 1267–1270.
- [161] Hoshino, T.; Miyauchi, M.; Kawaguchi, Y.; Yamaguchi, H.; Harada, A. *J. Am. Chem. Soc.* **2000**, *122*, 9876–9877.
- [162] Rekharsky, M. V.; Inoue, Y. *Chem. Rev.* **1998**, *98*, 1875–1918.
- [163] Appel, E. A.; del Barrio, J.; Loh, X. J.; Scherman, O. A. *Chem. Soc. Rev.* **2012**, *41*, 6195–6214.
- [164] Liu, J.; Tan, C. S. Y.; Lan, Y.; Scherman, O. A. *Macromol. Chem. Physic.* **2016**, *217*, 319–332.
- [165] Wu, Y.; Lan, Y.; Liu, J.; Scherman, O. A. *Nanoscale* **2015**, *7*, 13416–13419.
- [166] Whang, D.; Park, K.-M.; Heo, J.; Ashton, P.; Kim, K. *J. Am. Chem. Soc.* **1998**, *120*, 4899–4900.
- [167] Park, K.-M.; Kim, S.-Y.; Heo, J.; Whang, D.; Sakamoto, S.; Yamaguchi, K.; Kim, K. *J. Am. Chem. Soc.* **2002**, *124*, 2140–2147.
- [168] Day, A. I.; Xiao, X.; Zhang, Y.-Q.; Zhu, Q.-J.; Xue, S.-F.; Tao, Z. *J. Inclusion Phenom. Mol. Recognit. Chem.* **2011**, *71*, 281–286.
- [169] Ko, Y. H.; Kim, K.; Kang, J.-K.; Chun, H.; Lee, J. W.; Sakamoto, S.; Yamaguchi, K.; Fetting, J. C.; Kim, K. *J. Am. Chem. Soc.* **2004**, *126*, 1932–1933.
- [170] Hamers, C.; Kocian, O.; Raymo, F. M.; Stoddart, J. F. *Adv. Mat.* **1998**, *10*, 1366–1369.
- [171] Evans, N. H.; Rahman, H.; Leontiev, A. V.; Greenham, N. D.; Orłowski, G. A.; Zeng, Q.; Jacobs, R. M.; Serpell, C. J.; Kilah, N. L.; Davis, J. J.; D., B. P. *Chem. Sci.* **2012**, *3*, 1080–1089.
- [172] Nadai, C.; Whelan, C.; Perollier, C.; Clarkson, G.; Leigh, D.; Caudano, R.; Rudolf, P. *Surf. Sci.* **2000**, *454*, 112–117.
- [173] Daniel, M.-C.; Astruc, D. *Chem. Rev.* **2004**, *104*, 293–346.

- [174] Tian, F.; Cziferszky, M.; Jiao, D.; Wahlstrom, K.; Geng, J.; Scherman, O. A. *Langmuir* **2010**, *27*, 1387–1390.
- [175] Reczek, J. J.; Kennedy, A. A.; Halbert, B. T.; Urbach, A. R. *J. Am. Chem. Soc.* **2009**, *131*, 2408–2415.
- [176] Sonzini, S.; Ryan, S. T.; Scherman, O. A. *Chem. Commun.* **2013**, *49*, 8779–8781.
- [177] Hunter, R. J. *Zeta potential in colloid science: principles and applications*; Academic press, 2013; Vol. 2.
- [178] Biedermann, F.; Elmaleh, E.; Ghosh, I.; Nau, W. M.; Scherman, O. A. *Angew. Chem. Int. Ed.* **2012**, *124*, 7859–7863.
- [179] Ryan, S. T.; Del Barrio, J.; Ghosh, I.; Biedermann, F.; Lazar, A. I.; Lan, Y.; Coulston, R. J.; Nau, W. M.; Scherman, O. A. *J. Am. Chem. Soc.* **2014**, *136*, 9053–9060.
- [180] Stöber, W.; Fink, A.; Bohn, E. J. *Colloid Interface Sci.* **1968**, *26*, 62–69.
- [181] Alvarez-Puebla, R. A.; Agarwal, A.; Manna, P.; Khanal, B. P.; Aldeanueva-Potel, P.; Carbó-Argibay, E.; Pazos-Pérez, N.; Vigderman, L.; Zubarev, E. R.; Kotov, N. A.; Liz-Marzán, L. M. *Proc. Nat. Acad. Sci. U. S. A.* **2011**, *108*, 8157–8161.
- [182] Yap, F. L.; Thoniyot, P.; Krishnan, S.; Krishnamoorthy, S. *Acs Nano* **2012**, *6*, 2056–2070.
- [183] Cecchini, M. P.; Turek, V. A.; Paget, J.; Kornyshev, A. A.; Edel, J. B. *Nat. Mater.* **2013**, *12*, 165.
- [184] Aldeanueva-Potel, P.; Carbó-Argibay, E.; Pazos-Pérez, N.; Barbosa, S.; Pastoriza-Santos, I.; Alvarez-Puebla, R. A.; Liz-Marzán, L. M. *ChemPhysChem* **2012**, *13*, 2561–2565.
- [185] Garcia-Leis, A.; Garcia-Ramos, J. V.; Sanchez-Cortes, S. J. *Phys. Chem. C* **2013**, *117*, 7791–7795.

-
- [186] Su, Q.; Ma, X.; Dong, J.; Jiang, C.; Qian, W. *ACS Appl. Mater. Interfaces* **2011**, *3*, 1873–1879.
- [187] Guerrero-Martínez, A.; Barbosa, S.; Pastoriza-Santos, I.; Liz-Marzán, L. M. *Curr Opin Colloid Interface Sci.* **2011**, *16*, 118–127.
- [188] Indrasekara, A. D. S.; Meyers, S.; Shubeita, S.; Feldman, L.; Gustafsson, T.; Fabris, L. *Nanoscale* **2014**, *6*, 8891–8899.
- [189] Lyon, J. L.; Fleming, D. A.; Stone, M. B.; Schiffer, P.; Williams, M. E. *Nano Lett.* **2004**, *4*, 719–723.
- [190] Tang, X.; Schneider, T.; Buttry, D. A. *Langmuir* **1994**, *10*, 2235–2240.
- [191] Wang, P.; Xia, M.; Liang, O.; Sun, K.; Cipriano, A. F.; Schroeder, T.; Liu, H.; Xie, Y. *Anal. Chem.* **2015**, *87*, 10255–10261.
- [192] Zhang, J.; Wang, L.; Pan, D.; Song, S.; Boey, F. Y.; Zhang, H.; Fan, C. *small* **2008**, *4*, 1196–1200.
- [193] Shen, B.; Li, J.; Cheng, W.; Yan, Y.; Tang, R.; Li, Y.; Ju, H.; Ding, S. *Microchim. Acta* **2015**, *182*, 361–367.
- [194] He, J.; Wu, Z.; Zhou, H.; Wang, H.; Jiang, J.; Shen, G.; Yu, R. *Anal. Chem.* **2010**, *82*, 1358–1364.
- [195] Munoz, E. M.; Lorenzo Abalde, S.; Gonzalez-Fernandez, A.; Quintela, O.; Lopez Rivadulla, M.; Riguera, R. *Biosens. Bioelectron.* **2011**, *26*, 4423–4428.
- [196] Jang, Y.; Jang, M.; Kim, H.; Lee, S. J.; Jin, E.; Koo, J. Y.; Hwang, I. C.; Kim, Y.; Ko, Y. H.; Hwang, I. *Chem* **2017**, *3*, 641–651.
- [197] Quaresma, P.; Osorio, I.; Doria, G.; Carvalho, P. A.; Pereira, A.; Langer, J.; Araujo, J. P.; Pastoriza Santos, I.; Liz Marzan, L. M.; Franco, R. *RSC Adv.* **2014**, *4*, 3659–3667.

- [198] Poizat, O.; Sourisseau, C.; Mathey, Y. *J. Chem. Soc., Faraday Trans. 1* **1984**, *80*, 3257–3274.
- [199] Regis, A.; Corset, J. *J. Chim. Phys.* **1981**, *78*, 687–693.
- [200] Morasso, C.; Mehn, D.; Vanna, R.; Bedoni, M.; Forvi, E.; Colombo, M.; Prospero, D.; Gramatica, F. *Mater. Chem. Phys.* **2014**, *143*, 1215–1221.
- [201] Rauwald, U.; Biedermann, F.; Deroo, S.; Robinson, C. V.; Scherman, O. A. *J. Phys. Chem. B* **2010**, *114*, 8606–8615, PMID: 20550146.
- [202] Huang, H.; Juan, A.; Katsonis, N.; Huskens, J. *Tetrahedron* **2017**, *73*, 4913–4917.
- [203] Ren, X.; Wu, Y.; Clarke, D. E.; Liu, J.; Wu, G.; Scherman, O. A. *Chem. Asian J.* **2016**, *11*, 2382–2386.
- [204] Le Ru, E.; Blackie, E.; Meyer, M.; Etchegoin, P. G. *J. Phys. Chem. C* **2007**, *111*, 13794–13803.
- [205] Lim, D. K.; Jeon, K. S.; Hwang, J. H.; Kim, H.; Kwon, S.; Suh, Y. D.; Nam, J. M. *Nat. Nanotechnol.* **2011**, *6*, 452.
- [206] Zhang, L.; Liu, Z.; Wang, Y.; Xie, R.; Ju, X.; Wang, W.; Lin, L.; Chu, L. *Chem. Eng. J.* **2017**, *309*, 691–699.
- [207] Le Ru, E. C.; Etchegoin, P. G. *Annu. Rev. Phys. Chem.* **2012**, *63*, 65–87.
- [208] Prasad, J.; Zins, I.; Branscheid, R.; Becker, J.; Koch, A. H.; Fytas, G.; Kolb, U.; Sonnichsen, C. *J. Phys. Chem. C* **2015**, *119*, 5577–5582.
- [209] Sonnichsen, C.; Reinhard, B. M.; Liphardt, J.; Alivisatos, A. P. *Nat. Biotechnol.* **2005**, *23*, 741.
- [210] Chou, L. Y.; Zagorovsky, K.; Chan, W. C. *Nat. Nanotechnol.* **2014**, *9*, 148–155.
- [211] Wustholz, K. L.; Henry, A.-I.; McMahon, J. M.; Freeman, R. G.; Valley, N.; Pirotti, M. E.; Natan, M. J.; Schatz, G. C.; Duyne, R. P. V. *J. Am. Chem. Soc.* **2010**, *132*, 10903–10910.

- [212] Zhou, H.; Yu, F.; Guo, C. F.; Wang, Z.; Lan, Y.; Wang, G.; Fang, Z.; Liu, Y.; Chen, S.; Sun, L.; Ren, Z. *Nanoscale* **2015**, *7*, 9153–9157.
- [213] Li, A.; Tang, L.; Song, D.; Song, S.; Ma, W.; Xu, L.; Kuang, H.; Wu, X.; Liu, L.; Chen, X.; Chuanlai, X. *Nanoscale* **2016**, *8*, 1873–1878.
- [214] Holler, R. P.; Dulle, M.; Thoma, S.; Mayer, M.; Steiner, A. M.; Forster, S.; Fery, A.; Kuttner, C.; Chanana, M. *ACS Nano* **2016**, *10*, 5740–5750.
- [215] Qian, Z.; Hastings, S. P.; Li, C.; Edward, B.; McGinn, C. K.; Engheta, N.; Fakhraai, Z.; Park, S.-J. *ACS Nano* **2015**, *9*, 1263–1270.
- [216] Zheng, Y.; Thai, T.; Reineck, P.; Qiu, L.; Guo, Y.; Bach, U. *Adv. Funct. Mater.* **2013**, *23*, 1519–1526.
- [217] Song, C.; Zhao, G.; Zhang, P.; Rosi, N. L. *J. Am. Chem. Soc.* **2010**, *132*, 14033–14035.
- [218] Fontana, J.; Dressick, W. J.; Phelps, J.; Johnson, J. E.; Rendell, R. W.; Sampson, T.; Ratna, B. R.; Soto, C. M. *Small* **2014**, *10*, 3058–3063.
- [219] Sheikholeslami, S. N.; Alaeian, H.; Koh, A. L.; Dionne, J. A. *Nano Lett.* **2013**, *13*, 4137–4141.
- [220] Muhlig, S.; Cunningham, A.; Scheeler, S.; Pacholski, C.; Burgi, T.; Rockstuhl, C.; Lederer, F. *ACS Nano* **2011**, *5*, 6586–6592.
- [221] Radziuk, D.; Schuetz, R.; Masic, A.; Moehwald, H. *Phys. Chem. Chem. Phys.* **2014**, *16*, 24621–24634.
- [222] Fan, J. A.; Wu, C.; Bao, K.; Bao, J.; Bardhan, R.; Halas, N. J.; Manoharan, V. N.; Nordlander, P.; Shvets, G.; Capasso, F. *Science* **2010**, *328*, 1135–1138.
- [223] Ruan, Q.; Shao, L.; Shu, Y.; Wang, J.; Wu, H. *Adv. Opt. Mater.* **2014**, *2*, 65–73.
- [224] Sebba, D. S.; Lazarides, A. A. *J. Phys. Chem. C* **2008**, *112*, 18331–18339.
- [225] Waldeisen, J. R.; Wang, T.; Ross, B. M.; Lee, L. P. *Acs Nano* **2011**, *5*, 5383–5389.

-
- [226] Wang, Z.; Zhang, J.; Ekman, J. M.; Kenis, P. J.; Lu, Y. *Nano Lett.* **2010**, *10*, 1886–1891.
- [227] Maye, M. M.; Kumara, M. T.; Nykypanchuk, D.; Sherman, W. B.; Gang, O. *Nat. Nanotechnol.* **2010**, *5*, 116.
- [228] Wang, Y.; Chen, G.; Yang, M.; Silber, G.; Xing, S.; Tan, L. H.; Wang, F.; Feng, Y.; Liu, X.; Li, S.; Chen, H. *Nat. Commun.* **2010**, *1*, 87.
- [229] Chen, G.; Wang, Y.; Tan, L. H.; Yang, M.; Tan, L. S.; Chen, Y.; Chen, H. *J. Am. Chem. Soc.* **2009**, *131*, 4218–4219.
- [230] Bai, L.; Ma, X.; Liu, J.; Sun, X.; Zhao, D.; Evans, D. G. *J. Am. Chem. Soc.* **2010**, *132*, 2333–2337.
- [231] Sebastian, V.; Lee, S.-K.; Jensen, K. F. *Nanoscale* **2014**, *6*, 13228–13235.
- [232] Polte, J.; Ahner, T. T.; Delissen, F.; Sokolov, S.; Emmerling, F.; Thunemann, A. F.; Kraehnert, R. *J. Am. Chem. Soc.* **2010**, *132*, 1296–1301.
- [233] Turkevich, J.; Stevenson, P. C.; Hillier, J. *Faraday discuss.* **1951**, *11*, 55–75.
- [234] Nikolelis, D. P.; Drivelos, D. A.; Simantiraki, M. G.; Koinis, S. *Anal. Chem.* **2004**, *76*, 2174–2180.
- [235] Kim, T.; Truong, T.; Thanh, G. V. *Tetrahedron* **2010**, *66*, 5277–5282.
- [236] Plotka, J. M.; Morrison, C.; Adam, D.; Biziuk, M. *Anal. Chem.* **2012**, *84*, 5625–5632.
- [237] R. Massart, *IEEE Trans. Magn.* **1981**, *17*, 1247–1248.
- [238] Liu, J.; Detrembleur, C.; Debuigne, A.; Gillet, M. C. D. P.; Mornet, S.; Elst, L. V.; Laurent, S.; Labrugere, C.; Duguet, E.; Jerome, C. *Nanoscale* **2013**, *5*, 11464–11477.
- [239] Craighead, H. *Nature* **2006**, *442*, 387–393.
- [240] Hogan, J. *Nature* **2006**, *442*, 351–352.
- [241] Amstad, E.; Spaepen, F.; Brenner, M. P.; Weitz, D. A. *Lab Chip* **2017**, *17*, 1475–1480.

- [242] Yu, Z.; Zhang, J.; Coulston, R. J.; Parker, R. M.; Biedermann, F.; Liu, X.; Scherman, O. A.; Abell, C. *Chem. Sci.* **2015**, *6*, 4929–4933.
- [243] Liu, D.; Zhang, H.; Cito, S.; Fan, J.; Makila, E.; Salonen, J.; Hirvonen, J.; Sikanen, T. M.; Weitz, D. A.; Santos, H. A. *Nano Lett.* **2017**, *17*, 606–614.
- [244] Wagner, O.; Thiele, J.; Weinhart, M.; Mazutis, L.; Weitz, D. A.; Huck, W. T.; Haag, R. *Lab Chip* **2016**, *16*, 65–69.
- [245] Velasco Casquillas, G.; Le Berre, M.; Piel, M.; Tran, P. T. *Nano Today* **2010**, *5*, 28–47.
- [246] Xie, X. et al. *Nano Lett.* **2017**, *17*, 2015–2020.
- [247] Xu, B.; Zhang, Y.; Wei, S.; Ding, H.; Sun, H. *ChemCatChem* **2013**, *5*, 2091–2099.
- [248] Joanicot, M.; Ajdari, A. *Science* **2005**, *309*, 887–888.
- [249] Song, Y.; Hormes, J.; Kumar, C. S. *Small* **2008**, *4*, 698–711.
- [250] Munirathinam, R.; Huskens, J.; Verboom, W. *Adv. Synth. Catal.* **2015**, *357*, 1093–1123.
- [251] Mashaghi, S.; Abbaspourrad, A.; Weitz, D. A.; van Oijen, A. M. *Trends Analyt. Chem.* **2016**, *82*, 118–125.
- [252] Fukuyama, T.; Rahman, M. T.; Sato, M.; Ryu, I. *Synlett* **2008**, *2008*, 151–163.
- [253] Ryoo, H. I.; Lee, J. S.; Park, C. B.; Kim, D. P. *Lab Chip* **2011**, *11*, 378–380.
- [254] Park, C. P.; Kim, D. P. *J. Am. Chem. Soc.* **2010**, *132*, 10102–10106.
- [255] Wiles, C.; Watts, P.; Haswell, S. J. *Tetrahedron* **2005**, *61*, 5209–5217.
- [256] Ayats, C.; Henseler, A. H.; Dibello, E.; Pericaas, M. A. *ACS Catal.* **2014**, *4*, 3027–3033.
- [257] Hashimoto, K.; Kumagai, N.; Shibasaki, M. *Org. Lett.* **2014**, *16*, 3496–3499.
- [258] Michrowska, A.; Mennecke, K.; Kunz, U.; Kirschning, A.; Grela, K. *J. Am. Chem. Soc.* **2006**, *128*, 13261–13267.
- [259] Linares, N.; Hartmann, S.; Galarneau, A.; Barbaro, P. *ACS Catal.* **2012**, *2*, 2194–2198.

- [260] Javaid, R.; Kawasaki, S. i.; Suzuki, A.; Suzuki, T. M. *Beilstein J. Org. Chem.* **2013**, *9*, 1156.
- [261] Ricciardi, R.; Huskens, J.; Verboom, W. J. *Flow Chem.* **2013**, *3*, 127–131.
- [262] Ricciardi, R.; Munirathinam, R.; Huskens, J.; Verboom, W. *ACS Appl. Mater. Interfaces* **2014**, *6*, 9386–9392.
- [263] Basavaraju, K.; Sharma, S.; Maurya, R. A.; Kim, D. P. *Angew. Chem. Int. Ed.* **2013**, *125*, 6867–6870.
- [264] Paunovic, V.; Ordonsky, V.; Dangelo, M. F. N.; Schouten, J. C.; Nijhuis, T. A. *J. Catal.* **2014**, *309*, 325–332.
- [265] Ng, J. F.; Nie, Y.; Chuah, G. K.; Jaenicke, S. *J. Catal.* **2010**, *269*, 302–308.
- [266] Zhang, R.; Elzatahry, A. A.; Al Deyab, S. S.; Zhao, D. *Nano Today* **2012**, *7*, 344–366.
- [267] Liu, J.; Lan, Y.; Yu, Z.; Tan, C. S.; Parker, R. M.; Abell, C.; Scherman, O. A. *Acc. Chem. Res.* **2017**, *50*, 208–217.
- [268] Wu, Y.; Shah, D. U.; Liu, C.; Yu, Z.; Liu, J.; Ren, X.; Rowland, M. J.; Abell, C.; Ramage, M. H.; Scherman, O. A. *Proc. Natl. Acad. Sci. U.S.A* **2017**, *10*, 201705380.
- [269] Wu, P.; Bai, P.; Yan, Z.; Zhao, G. X. *Sci. Rep.* **2016**, *6*, 18817.
- [270] Thomas, J. M.; Raja, R.; Lewis, D. W. *Angew. Chem. Int. Ed.* **2005**, *44*, 6456–6482.
- [271] Balanta, A.; Godard, C.; Claver, C. *Chem. Soc. Rev.* **2011**, *40*, 4973–4985.
- [272] Li, J.; Chen, W.; Zhao, H.; Zheng, X.; Wu, L.; Pan, H.; Zhu, J.; Chen, Y.; Lu, J. *J. Catal.* **2017**, *352*, 371 – 381.
- [273] Li, M.; Chen, G. *Nanoscale* **2013**, *5*, 11919–11927.
- [274] Zheng, G.; Kaefer, K.; Mourdikoudis, S.; Polavarapu, L.; Vaz, B.; Cartmell, S. E.; Bouleghlimat, A.; Buurma, N. J.; Yate, L.; de Lera, A. R.; Liz-Marzan, L. M.; Pastoriza-Santos, I.; Perez-Juste, J. J. *J. Phys. Chem. Lett.* **2015**, *6*, 230–238, PMID: 26263455.

- [275] Kang, H.; Kim, M.; Park, K. H. *Appl. Catal., A* **2015**, 502, 239 – 245.
- [276] Jin, M.; Zhang, H.; Xie, Z.; Xia, Y. *Angew. Chem. Int. Ed.* **2011**, 50, 7850–7854.
- [277] Zhao, M.; Deng, K.; He, L.; Liu, Y.; Li, G.; Zhao, H.; Tang, Z. *J. Am. Chem. Soc.* **2014**, 136, 1738–1741.
- [278] Ferry, A.; Schaepe, K.; Tegeder, P.; Richter, C.; Chepiga, K. M.; Ravoo, B. J.; Glorius, F. *ACS Catal.* **2015**, 5, 5414–5420.
- [279] Jens, H. *Industrial Catalysis: A Practical Approach*, 2nd ed.; Wiley-VCH: Weinheim, 2006; Chapter Homogeneously catalyzed industrial processes, pp 59–82.
- [280] Sheng, T.; Qi, Y.-J.; Lin, X.; Hu, P.; Sun, S.-G.; Lin, W.-F. *Chem. Eng. J.* **2016**, 293, 337 – 344.
- [281] Gupta, R.; Rai, B. *Sci. Rep.* **2017**, 7, 45292–45303.
- [282] Su, G.; Zhou, H.; Mu, Q.; Zhang, Y.; Li, L.; Jiao, P.; Jiang, G.; Yan, B. *J. Phys. Chem. C* **2012**, 116, 4993–4998.
- [283] Sahiner, N.; Ozay, H.; Ozay, O.; Aktas, N. *Appl. Catal., B* **2010**, 101, 137 – 143.
- [284] Rhee, S. G.; Chang, T. S.; Jeong, W.; Kang, D. *Mol. Cells* **2010**, 29, 539–549.
- [285] Qin, D.; Xia, Y.; Whitesides, G. M. *Adv. Mater.* **1996**, 8, 917–919.
- [286] Duffy, D. C.; McDonald, J. C.; Schueller, O. J.; Whitesides, G. M. *Anal. Chem.* **1998**, 70, 4974–4984.
- [287] Kozuch, S.; Martin, J. M. *ACS Catal.* **2012**, 2, 2787–2794.